The central stellar populations of brightest cluster galaxies

D.N. Viljoen, B.Sc Hons.

20569513

Dissertation submitted in partial fulfilment of the requirements for the degree *Master of Science in Physics* at the Potchefstroom Campus of the North-West University

Supervisor: Dr. S.I. Loubser

September, 2012

ABSTRACT

The majority of galaxy clusters contain a massive galaxy in the centre of the clusters that are far more luminous and massive than the other galaxies in the cluster. These galaxies are called the brightest galaxy clusters (BCGs) and the formation and evolution of these BCGs are intimately related to the formation of the host clusters. In this project, the star formation histories (SFHs) of 51 galaxies (49 BCGs and two ellipticals) were determined by using high signal-to-noise ratio, long-slit spectra. The spectra of the galaxies were fitted against the software package *ULySS* which is a stellar population synthesis code. Two stellar population models, the Pegase.HR (P.HR) and the Vazdekis/MILES were used to determine the SFHs of the galaxies, more specifically determine whether a single stellar population (SSP) or composite stellar population (CSP) provided the most probable representation of the SFHs. Additional parameters, such as the velocity dispersions of the galaxies, the redshifts, the error spectra and the wavelength range were defined to extend these models. The observed spectra were then respectively fitted against a SSP and CSP. A series of 500 Monte-Carlo simulations were then preformed to asses the relevance of the solutions and aided in the selection of the most probable SFHs of the BCGs. The χ^2-maps were then drawn to assist in the understanding of the structure of the parameter space. The SFHs of the galaxies were given in the form of stellar components characterised by the derived ages and metallicities ([Fe/H]). The derived parameters were then compared against those derived with the LICK Indices to determine whether these approaches produced consistent results. Lastly, the derived parameters were tested against the internal galaxy properties (the velocity dispersions and absolute K-band magnitudes) and the properties of the host cluster environment (the X-ray temperatures, luminosities, offsets and the presence of cooling flows (CFs)) to determine whether any correlations could be derived to shed light on the formation and evolution of the BCGs. The results indicate that the P.HR model gave the most probable representation of the SFHs of the sample. Although 55% of the sample could be represented by a single star formation epoch, the remaining 45% had a more complex SFH. The ages, derived by the P.HR and LICK Indices showed significant consistency when compared but the [Fe/H] did not because the current P.HR model does not include $\alpha-$enhancements. 14 galaxies contained CFs. No correlations could be found between the internal properties (velocity dispersion and the absolute K-band magnitudes) and the ages/[Fe/H] but it was found that clusters containing

CFs were located at higher luminosities than those without CFs. No correlations could be found between the ages/[Fe/H] and the X-ray temperatures. The intermediate aged galaxies with CFs were located closer to the centre than the old aged galaxies with CFs. These results indicated that at least some of the galaxies in the sample had a more complex SFH than first assumed and the presence of the CFs could account for some, but not all of the star formation activities in the clusters.

Keywords: galaxies: elliptical and lenticular, cD – galaxies: evolution – galaxies: formation – galaxies: general – galaxies: stellar content.

OPSOMMING

Die sentrale sterrepopulasies van die helderste galaksieswerms

Die meerderheid van die galaksieswerms het 'n massiewe galaksie in die middel van die swerm wat herlderder en groter is as die res van die galaksies wat in die swerm aangetref word. Hierdie galaksies word die helderste galaksieswerms (HGSs) genoem en die vorming en evolusie van hierdie galaksies is nouliks verwant aan die vorming van die gasheer swerm. In hierdie projek word die stervormingsgeskiedenis (SVG) van 51 galaksies (49 HGSs en twee elliptiese galaksies) ondersoek deur van hoë sein-tot-ruis verhouding, lang-spleet spektra gebruik te maak. Die spektra van die galaksies is gepas teen die sagteware pakket *ULySS*, wat 'n sterrepopulasie sintese kode is. Twee sterrepopulasie modelle, naamlik die Pegase.HR (P.HR) en Vazdekis/MILES modelle is gebruik om die SVGs van die galaksies te bepaal, meer spesifiek om te bepaal of 'n enkel sterrepopulasie (ESP) of saamgestelde sterrepopulasie (SSP) die mees waarskynlikste voorstelling van die SVGs gee. Addisionele parameters, byvoorbeeld die snelheid dispersies van die galaksies, rooiverskuiwings, fout spektra en die golflengte is gebruik om die modelle uit te brei. Die waargenome spektra is dan onderskeidelik gepas teen 'n ESP en SSP. Volgende is 'n reeks van 500 Monte-Carlo simulasies verrig om die relevansie van die oplossings te bepaal en om die mees waarskynlikste voorstelling van die HGSs se SVGs te bepaal. Die χ^2-kaarte is dan getrek met die doel om die parameter ruimte se struktuur te bepaal en beter te verstaan. Die SVGs van die galaksies word in die vorm van sterkomponente gegee wat weer gekarakteriseer word deur die ouderdomme en metaal-inhoud ([Fe/H]). Die afgeleide parameters (ouderdomme en [Fe/H]) is dan vergelyk met die waardes, bereken deur die LICK indekse, met die doel om te bepaal of die twee metodes ooreenstemmende resultate sou produseer. Laastens is die afgeleide parameters getoets teenoor die interne eienskappe van die galaksies (die snelheid dispersies en die absolute K-band magnitudes) en die eienskappe van die gasheer swerm (die X-straal temperature, luminositeite, die afstand tussen die HGS en die X-straal piek en die teenwoordigheid van verkoelingstrome (VSe)) om te bepaal of daar moontlike verbande tussen hierdie eienskappe, die ouderdomme en [Fe/H] bestaan wat moontlike leidrade kan bied om die vorming en evolusie van die HGSs te ontsyfer. Die resultate het getoon dat die P.HR model die mees waarskynlikste voorstelling van die galak-

sies se SVGs gee. 55% van die galaksies kon voorgestel word deur ’n enkele stervormingsepog terwyl die oorblywende 45% ’n meer komplekse SVGs ervaar het. Die ouderdomme, soos bepaal deur die P.HR model en die LICK indekse het goeie ooreenstemmendheid getoon, maar dit was nie die geval vir die [Fe/H] nie, omdat alfa-versterkings nie huidiglik in die P.HR model vervat is nie. 14 galaksies het VSe bevat. Geen korrelasies kon tussen die interne eienskappe van die galaksies (die snelheid dispersies en die absolute K-band magnitudes), die ouderdomme en [Fe/H] afgelei word nie. Daar is ook gevind dat die swerms wat VSe bevat, by hoër luminositeite geleë is as die swerms wat nie VSe bevat nie. Geen korrelasies kon tussen die X-straal temperature, die ouderdomme en die [Fe/H] afgelei word nie. Die intermedêre galaksies wat VSe bevat is nader aan die middelpunt van die swerms geleë as die ouer galaksies wat VSe bevat. Saamgevat toon hierdie resultate dat sommige van die HGSs ’n meer komplekse SVGs besit as wat huidiglik aanvaar word in die literatuur en dat die teenwoordigheid van VSe gedeeltelik, maar nie vir al die stervorming in die swerms verantwoordelik gehou kan word nie.

Sleutelwoorde: galaksies: algemeen – galaksies: ellipties en lensvormig, cD – galaksies: evolusie – galaksies: sterre inhoud – galaksies: vorming

ACKNOWLEDGEMENTS

Above all, I want to thank the Lord for the privilege to be able to study my life's passion and making it my career. Father, You have shown me the vastness of the Universe and with that Your endless love and grace. You have blessed me with so many opportunities to make my dreams come true and also to experience the world. In times of doubt, thank you for keeping me on my feet and inspiring me. Thank you for showing me the mysteries of the Universe but above all for showing me that even though I am a small part of Your plan, I still am a significant part of it. My soul stand in awe of Your power and love. Thank you for giving me the chances and experiences of more than one lifetime. I now know the meaning of endless love.

Now, I want to thank my fiance and the love of my life. Coenie, there are still no words to describe my love for you. I thank the Lord for the privilege to know you and share my life with you. Above all, I thank you for not being afraid of my wings and for encouraging me to pursue my dreams. You will never know how much I love you for that and the fact that you encourage me and let me be me. You are my motivation, you keep me grounded and you are the air beneath my wings in times of doubt. Without you I would not be the person I am today. You are my soulmate and you showed me the meaning of true love. I love you with all my heart, forever and a day.

To my wonderful parents, I thank you for the courage and faith you taught me as a child. Life was not an easy journey in the past, but you taught me love, faith, determination but above all kindness. Thank you for believing in me and encouraging me. Mamma, I wish I could express the gratitude I feel towards you. You taught me so many valuable lessons which will always guide me through my life. I could not ask for a better mother. Thank you for teaching me that even in rough times I still have the courage and strength to carry on. Thank you for teaching me grace and love. Daddy, you always were my rock in rough times. Thank you for all the evenings you listened to my stories and the interest you have shown in all the things I do with my life. Thank you for the support and love you have always given me and for leading me to the right paths when I lost my way. May you both always be blessed and loved. I love you both beyond measure.

To my soon to be mother and father-in-law, I thank you for welcoming me as a child in your home from the start. I truly gained a second mother and father. Thank you for the encouragement and love you have showed me over the years. You provided me with a home away from home. Thank you for believing in me and for giving me advice when I did not know the way. Thank you for dropping by to see how Coenie and I were doing. Ma San and Pa Coen, thank you for the numerous cappuccinos we shared and the weekends spent with the family. I love you both very much.

To the rest of my now very extended families, I thank you all from the bottom of my heart for all your love and believing in me. Each one of you have played an important part in my life and I treasure you all.

Now to thank the one person without whom this dissertation would not have been possible. Ilani, thank you for not only being my supervisor but also for being my mentor and keeping me on the straight and narrow. Your sense of humor definitely helped to make these past years more fun. I learned so much from you, professionally and personally. I am still amazed at everything you have accomplished in your life. Thank you for the chances you have given me to experience the world with you and for the occasional push in the right direction. You took me out of my comfort zone and that challenged me in a lot of ways. Because of that, I also have a treasure chest of my own, containing both funny and horror stories. Knowing you has enriched my life in so many ways. May you always be blessed.

Now for my friends, thank you for all the craziness and love you brought into my life. Truly, without you all I would have gone stark raving mad by now — you kept me balanced. Each one of you are unique: Barend, thank you for all the late night coffee visits and for just dropping by. Thank you for being a quiet place to reflect and for being my rock at hard times. You will move heaven and earth for those you love and that makes you an exceptional person. Walter you always will have a huge influence on my life. My wish for you is that life will always treat you with kindness and generosity. It is a privilege to call you my friend. Monica, you know the craziness we have to deal with. Thank you for balancing the scale with your daily dozes of reality. Remember that you are the constant. And lastly Robert, you are a character to say the least but still a lovable person. Hope you never lose your sense of humor. Thank you for making the department a more interesting place. Remember that you can always make it at Walt Disney for voice overs if you cannot find work as a physicist.

I also want to thank a few extra special people: Prof. R.A. Burger, thank you for the advice you have given me during some trying times and for making time to help me. Next, Mama Petro, thank you for looking after your “children” and especially for handling the financial side of my studies. Without you, the department will truly fall apart. I also want to thank Elanie and Lee-Ann for handling any adminstrational queries.

I also thank the Square Kilometre Array project for providing me with a full scholarship to complete my M.Sc. degree. This bursary enabled me to take part in two international conferences

where I presented my research and met some of the leading researchers in galaxy formation. The opinions expressed and conclusions arrived at, are those of the author and are not necessarily to be attributed to the National Research Foundation.

Dedicated to the loving memory of my grandfather. Never will I forget the guidance and patience of your love. You are truly missed! In a family mostly consisting of colorful and eccentric artists, you showed me where science could fit into our family. Thank you for encouraging my curiosity, always answering my questions and for teaching me where the answers could be found. You showed me the way towards my passion — astronomy, and for that I will always be thankful. Till we see each other again grandpappa, rest in peace and I love you.

“Ek sal jou nooit begewe en jou nooit verlaat nie.
Die Here is vir my ’n Helper, en ek sal nie vrees nie;
wat sal ’n mens aan my doen?”

Hebreeus 13: 5 – 6

“The LORD Himself goes before you and will be with you;
He will never leave you nor forsake you.
Do not be afraid;
do not be discouraged.”

Deuteronomy 31: 8

CONTENTS

ABBREVIATIONS AND ACRONYMS

Λ CDM	Lambda Cold Dark Matter
2dF	2-degree Field
2MASS	Two-Micron All Sky Survey
AGB	Asymptotic Giant Branch
AGN	Active Galactic Nuclei
BB	Big Bang
BCG	Brightest Cluster Galaxy
CCD	Charge-Coupled Device
cD	centrally Dominant
CDM	Cold Dark Matter
CF	Cooling Flow
CSP	Composite Stellar Population
CuAr	Copper-Argon
DEC	DEClination
ETG	Early Type Galaxy
FITS	Flexible Image Transport System
GADGET	GAlaxies with Dark matter and Gas intEracT
GALEX	Galaxy Evolution Explorer
GANDALF	Gas AND Absorption Line Fitting
GMOS	Gemini Multi-Object Spectrograph
GNT	Gemini North Telescope
GST	Gemini South Telescope
GT	Gemini Telescope
HB	Horizontal Branch
HDF	Hubble Deep Field
IDL	Interactive Data Language
IMF	Initial Mass Function
IR	InfraRed

IRAF	Image Reduction and Analysis Facility
ISIS	Intermediate dispersion Spectrograph and Imaging System
ISM	Interstellar Medium
ISP	Intermediate Stellar Population
KS	Kolmogorov-Smirnov
LF	Light Fraction
LOSVD	Line-Of-Sight Velocity Distribution
LSF	Line Spread Function
MATISSE	MATrix Inversion for Spectral SynthEsis
MC	Monte-Carlo
MF	Mass Fraction
MILES	Medium-resolution Isaac Newton Telescope Library of Empirical Spectra
M/L	Mass-to-Light
MS	Main-Sequence
NED	NASA/IPAC Extragalactic Database
OSP	Old Stellar Population
P.HR	Pegase.HR
PSF	Point Spread Function
RA	Right Ascension
RGB	Red Giant Branch
SDSS	Sloan Digital Sky Survey
SED	Spectral Energy Distribution
SFH	Star Formation History
SFR	Star Formation Rate
S/N	Signal-to-Noise
SSP	Single Stellar Population
STECKMAP	STEllar Content and Kinematics via Maximum A Posteriori
SGB	Super Giant Branch
TGMET	Temperature, Gravity and METallicity
TO	TurnOff
ULySS	Université de Lyon Spectroscopic analysis Software
UV	UltraViolet
VESPA	VErsatile SPectral Analysis
V/M	Vazdekis/MILES
WHT	William Herschel Telescope
YSP	Young Stellar Population

LIST OF FIGURES

LIST OF TABLES

CHAPTER 1

INTRODUCTION

"Drome en ideale is die sketse uit
die boek wat jou siel oor jou skryf."

MARSHA NORMAN

1.1 Introduction

The French astronomer, Charles Messier watched the progress of a comet on the night of April 15th, 1779 as it slowly passed between the constellations of Virgo and Coma Berenices. It was after he watched the return of Halley's Comet during 1759 that he became an enthusiastic comet seeker which led King Louis XV to give him the nickname "ferret of the comets".

It was during one of these comet "hunts" that Messier noticed three vague objects in the night sky that resembled comets from a far, but he noticed that these objects remained stationary and could be found in the same location night after night. He compiled a separate list of these stationary objects and with the help of Pierre Mechain later identified these objects as Messier objects. The earliest versions of this list contained 13 of these 109 unmoving objects that could be found in a small region on the Virgo-Coma border. Unbeknown to Messier, he discovered the very first example of a galaxy cluster. Crudely stated, these clusters of galaxies are groups of galaxies held together by their own gravity. This list gave way to the catalogue known today as the Messier Catalogue. Objects contained within this catalogue were referred to by the prefix M, followed by the catalogue number. The Messier Catalogue, as astronomers know it today, now includes nebulae, galaxies and star clusters.

The clusters found in the Universe contain samples of cosmic material. This cosmic material consists of galaxies and stars, found in a wide variety of chemical compositions and ages. But

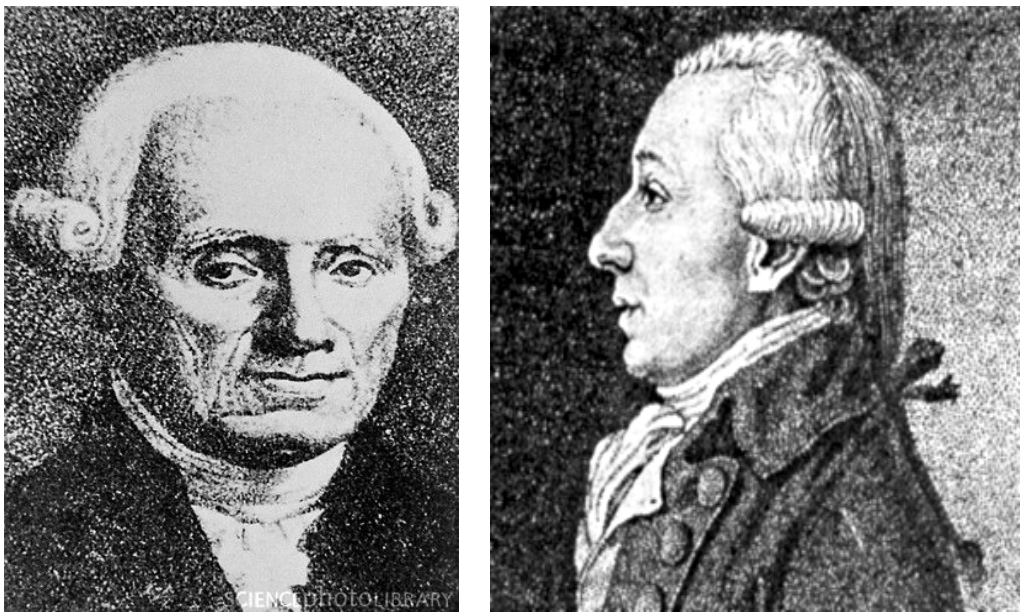

(a) Charles Messier (b) Pierre Mechain

Figure 1.1: Charles Messier, the French astronomer who created the Messier Catalogue with the help of Pierre Mechain. Credit: SCIENCE PHOTO LIBRARY.

this material contains another component: the elusive dark matter, which is thought to direct the movement of celestial bodies.

Galaxy clusters present astronomers with a unique opportunity to study the role that cluster environments play in galaxy evolution and therefore, study the Universe from the outside. But the galaxies in these clusters present rare and biased systems, as these galaxies form from the densest regions of the primordial density field (illustrated in Fig. (1.2)) and the evolutionary processes involved in these systems are expected to proceed at a faster rate than the galaxies found in regions with an average density in the Universe. Studies of galaxy evolution are further complicated by the fact that 10% of the cosmic galaxy populations are found in the local Universe and this is decreasing with increasing redshift (De Lucia, 2010).

It was only with the recent advances made in the designs and sensitivities of telescopes that large spectroscopic and photometric surveys could be undertaken to understand the role that cluster environments play in galaxy evolution. But this also presented its own difficulties: these studies each had their own definition for the cluster environment, for example to estimate the halo mass that is depended on the quality and quantity of data available. These conflicting definitions and different cosmic epoch studied, prevent the developers of galaxy formation models, such as the GAlaxies with Dark matter and Gas intEracT (GADGET) code, to put strong constraints on these models.

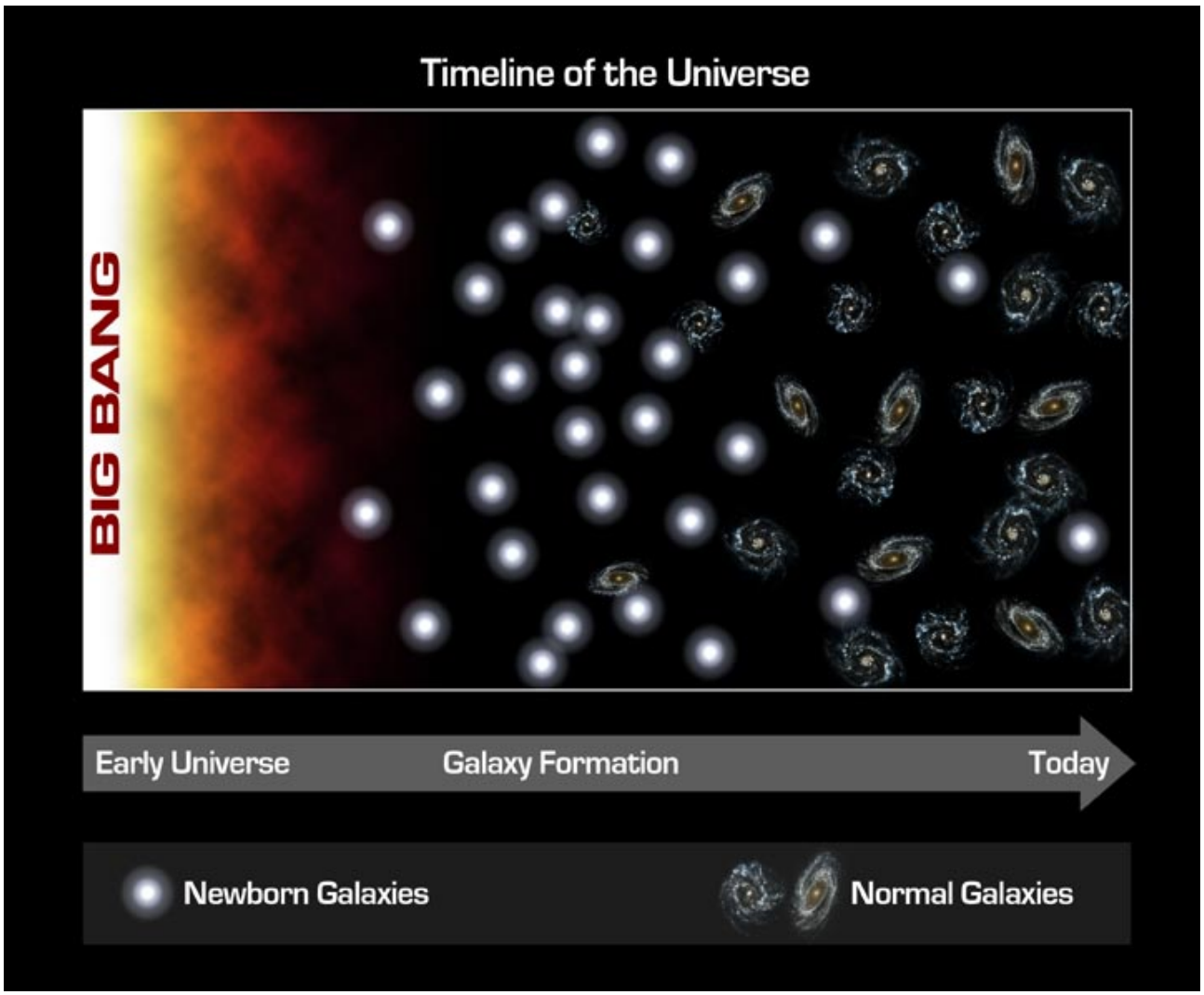

Figure 1.2: Galaxies formed frequently when the Universe was still young (indicated with the white circles). As time progressed these galaxies became older and evolved into spiral galaxies. Astronomers thought that massive, young galaxies did not form in the later Universe, but by using the GALaxy Evolution eXplorer (GALEX) software, new evidence was found to suggest that young galaxies still formed in the old Universe. These galaxies are also indicated with the white circles at the "today" side of the timeline and lead astronomers to believe that our Universe is still young and thriving. Image courtesy of NASA/JPL-CALTECH.

1.2 Purpose of this Study

Astronomers use galaxy clusters to probe the formation of the Universe because these clusters are found in the densest regions of the Universe. These densest regions are the progenitors of the first over-densities to collapse after the Big Bang (BB). One of the major questions asked by astronomers in modern cosmology is: How did galaxies form in these clusters?

Central galaxies in clusters are often the most massive early-type galaxies (ETGs) and it is an ideal place to start searching for the answer to this question. These ETGs are considered to be very unique due to the fact that these galaxies are extremely bright and contain a large fraction of the stellar mass in the present Universe. These ETGs are also diffuse with extended structures and they are located in the dominant locations in the clusters. It is due to the rather special positions of the ETGs in these clusters that astronomers find these galaxies of particular interest and use ETGs to study galaxy formation and evolution.

The stellar populations of ETGs were once thought to be straightforward and old, but due to pilot studies undertaken by Von der Linden et al. (2007) and Trager, Faber & Dressler (2008), new evidence have come to light to suggest that the star formation histories (SFHs) of these galaxies are far more complex and not that straightforward than first assumed.

In this project, a rather unique sub-class of the most massive ETGs, more specifically *brightest cluster galaxies* (BCGs) will be studied. To comply with more recent definitions given in the literature, BCGs are defined as the most luminous and massive galaxies in the Universe (Dubinski, 1998) which can be found in or very close to the densest part of the centre of the host clusters. This in turn indicates that the star formation rate (SFR) of these galaxies are lower than that of the galaxies located in less dense environments (Kauffmann et al. 2004). A study conducted by Thomas et al. (2005) indicated that the stars in massive ETGs formed very early on in the star formation epochs and therefore, it is expected that BCGs will be dominated by old stars and will not experience any further star formation activities (Liu, Mao & Meng, 2012).

The spectra of some BCGs contain emission lines and it was found by Edwards et al. (2007) that BCGs, with the presence of emission lines, were more frequently found in clusters containing cooling flows (CFs). They also found that some of the BCGs in their sample experienced recent star formation periods, which in turn indicated that the SFHs of BCGs were not that straightforward or easy to understand.

This dissertation tries to answer the following questions: (1) Can the SFHs of the BCGs in the sample be represented by a single epoch of star formation or is a more complex approach needed? More specifically, to determine whether simple or composite stellar populations are needed. (2) Are the BCGs more influenced by the internal properties of the galaxies (the velocity dispersions and absolute K-band magnitudes) or by the properties of the host cluster environment (the X-ray temperatures, luminosities, offsets and the presence of CFs)? More specifically, to determine whether any correlation can be found between the recent star formation epochs of the BCGs and the presence of CFs.

In this project the stellar populations of the central regions of the clusters are analysed and discussed. This dissertation will be structured as follows: Chapter 2 contains a brief description of galaxy evolution and formation. It should be noted here that I started with a rather broad approach to describe the background of galaxy formation and evolution without going in too much detail. This is due to the fact that the project focuses on the SFHs of BCGs and hence, special attention will be paid to the formation and evolution theories of BCGs. Chapter 3 contains the details of the sample selection, observations and the methods used in the data analysis. In Chapter 4, the derived parameters of the single and composite stellar populations will be derived and compared with the single stellar population equivalent parameters derived with the LICK indices. The correlations of the derived parameters with that of the internal galaxy kinematics (the velocity dispersions and absolute K-band magnitudes) and the properties of the host clusters (the X-ray temperatures, luminosities, offsets and the presence of CFs) will also be studied and discussed. In Chapter 5 a short summary of the analysis, the conclusions, recommendations and future work will be given. Appendix A contains the graphs referred to in Chapter 4.

CHAPTER 2

THEORETICAL BACKGROUND ON GALAXY FORMATION AND EVOLUTION

So amazing
You have named the stars
of the deepest night
and stilll You love me.
You have called my name
and I will follow You."

Taken from Emmanuel
PREFORMED BY HILLSONG

2.1 Introduction

In the southern hemisphere, particular during the cold winter months, the disk of our galaxy — the Milky Way, is clearly visible as a broad band stretching across the night sky. We are able to observe this spectacular structure because of the light emitted by the stars located in the Milky Way and also indirectly by the star light scattered by the dust grains located in the interstellar medium (ISM) between the galaxies and stars (Kraan-Korteweg & Lahav, 1998). Even viewed from behind a simple pair of binoculars, one can clearly discern the thousands and thousands of stars out of which these galaxies consist.

Gazing up at the night sky, and focusing on another part of the dark sky, you can easily pick out two different smaller, hazier patches — the Large and Small Magellanic Clouds (Vaisanen, 2009). With the help of a small telescope, hundreds, more smaller and much fainter patches can be discovered in the night sky. Fig. (2.1) illustrates the notion that galaxies can be described as fainter patches in the night sky but over the last few decades astronomers have discovered that these

patches are galaxies — massive systems of stars. In Fig. (2.1) the Small and Large Magellanic Clouds are shown as the hazy pathes with the Milky Way stretched across the photograph.

Figure 2.1: From the southern hemisphere, this photograph of the Milky Way (on the left–hand side) and the Large and Small Magellanic Clouds (upper and lower right–hand side) was taken in the Atacama Desert along the northwest coast of Chile. Charles Messier observed these patches in the night sky and found them to be stationary. With the help of Pierre Mechain, he later identified these patches as galaxies. Photograph taken by STEPHANE GUISARD.

In astronomy, almost all objects are classified, be it galaxies or stars. Classification schemes are used to better our understanding of the objects being studied. In the following two sections, the spectral classification of stars and galaxy classifications will be discussed.

2.2 Spectra Classification of Stars

Stars are usually divided into seven spectral classes/types: O, B, A, F, G, K and M — going from hotter (blue stars) to cooler (red stars) effective temperature (T_{eff}[1]). This classical scheme is mainly based on the strength of Hydrogen (H) Balmer lines. Stars, classified as A-type stars have the strongest observable H lines. The spectral features and T_{eff} of the different spectral classes are given in Table (2.1).

Table 2.1: The temperatures and spectral characteristics of the various spectral types of stars (adapted from Smith (1995) and Leblanc (2010)). The hot stars are referred to as early type stars while the cold stars are referred to as late type stars.

Spectral class	$\mathbf{T}_{eff}$	**Spectral characteristics**	**Colour**	**Example**
O (Hot)	$>$ 30 000 K	Strong HeII, faint H and strong multiply ionised metals	Blue	λ Ori
B	10 000-30 000 K	Strong HeI and moderate H	Blue-white	Rigel
A	7500-10 000 K	Maximum H lines	White	Vega
F	6000-7500 K	Strong ionised metals and moderate H	White-yellow	Procyon
G	5000-6000 K	Strong ionised metals and faint H	Yellow	Sun
K	3500-5000 K	Strong neutral, ionised metals and faint H	Orange	Arcturus
M (Cold)	$<$ 3500 K	Strong molecule bands (i.e. TiO), strong neutral metals and very faint H	Red	Betelgeuse

The stellar spectrum of a particular star is characterised by a continuum that can roughly be described by a black body spectrum (Smith, 1995). Superimposed on this continuum is a large number of absorption and emission lines. Although stars are not black bodies, their continua are very close to black body spectra and hence, an effective temperature can be defined. From the Stefan-Boltzmann law:

$$L = 4\pi R^2 \sigma T_{eff}^4 \tag{2.1}$$

it follows that the surface emissivity of a black body is given by σT^4, where σ is the Stefan-Boltzmann constant, i.e. 5.67×10^{-8} $\mathrm{Wm^{-2}K^{-4}}$. If it is assumed that stars are spherical, then Eq. (2.1) states the relation between the luminosity, L and T_{eff}, if the star has a radius of R.

[1] T_{eff} is the temperature of a black body that has the same size of the star and will radiate the same total power as the star.

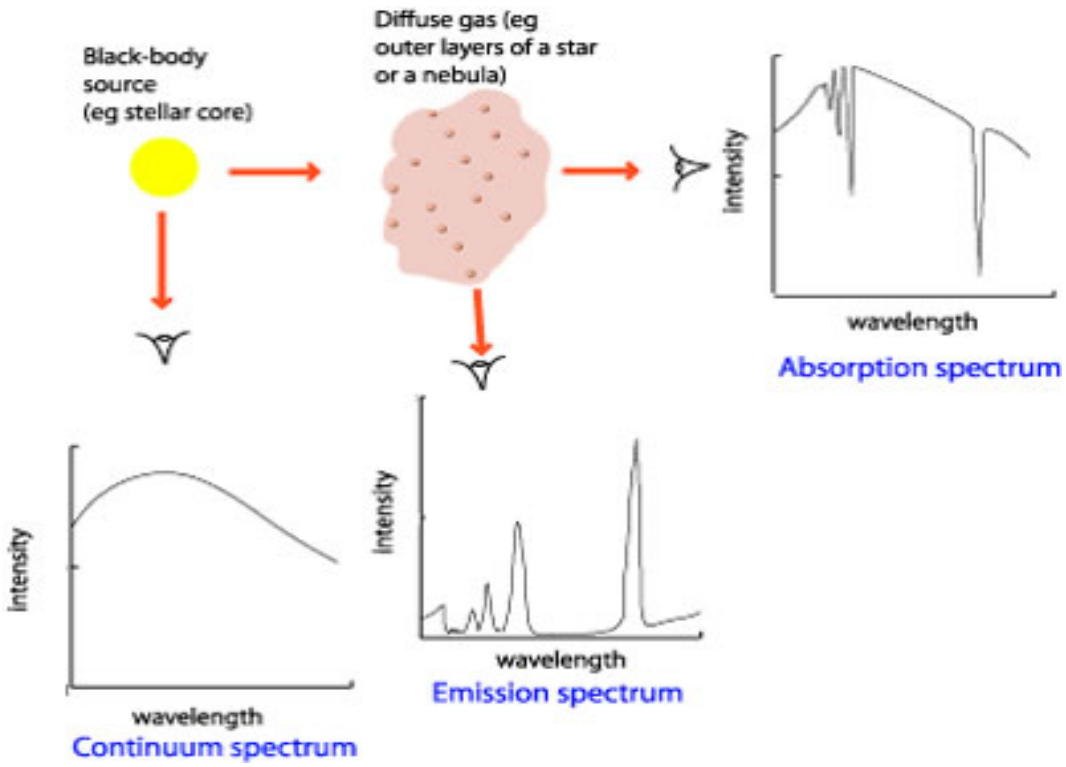

Figure 2.2: Schematic stellar spectrum of a star in an astronomical context. Figure adapted from Kaler (1989).

Fig. (2.2) gives a schematic illustration of the stellar spectrum of a star. As already stated the continuum of a star is very close to that of a black body and can be represented by the 'hill-shaped' graph of the electromagnetic radiation emitted by a black body that is the same size as the star. The spectra of a star that is not obscured by any gas or dust clouds will have a continuum spectrum radiated by a black body when observed by a person. An absorption spectrum in turn is produced when the flux of the continuum spectrum is reduced at certain frequencies, for example due to a gas cloud that is between the star and the Earth or the absorption of the wavelengths could also have taken place in the photosphere[2] of the star that emitted the light. Lastly, the emission spectrum of a star is produced when the light of a star passes through a gas cloud and the light is emitted rather than absorbed by the cloud. This is because the cloud can only emit the same wavelengths it absorbs and the particular wavelengths are depended on the chemical composition of the gas cloud.

As already stated, the spectral classification scheme is based on the strength of the H Balmer line (Leblanc, 2010). The Balmer continuum and absorption takes place in the photosphere of a star. The photosphere is cooler than the star's hot interior and this interior can be seen as a source that emits the black body radiation. The atoms in the photosphere absorb this continuum

[2]The thin surface layer of a star.

spectrum, re-radiate it in every direction and hence, produce the observed spectrum. Another way to describe it follows from the fact that continuum emission originates from the photosphere layers with temperatures that are the same as T_{eff} while absorption will take place in the cooler layers that are located higher up in the atmosphere of the star. Emission lines, in contrast are found in the layers where the temperatures are higher than T_{eff} (Smith, 1995). Line spectra can be used to determine the chemical compositions of a star's atmosphere due to the fact that each absorbing atom or ion has their own characteristic line pattern. The strength of the lines can in turn be used to determine element abundances, while the element abundances are used to determine to which population the stars belong, i.e. determine the stellar populations of the stars. There are three populations: Population III stars are the oldest stars and have a hypothetical metallicity ([Fe/H]) of zero (although these stars have never directly been observed), Population II stars are old stars with a small metallicity value while Population I stars are young stars with large metallicity values, for example the Sun.

2.3 Galaxy Classification

Galaxies present us with an interesting and fascinating view on the building blocks and the physical nature of the cosmos. Through only a few photons (which crossed the ISM for millions of years), passing through powerful telescopes, we are able to study the interactions that form galaxies as well as the various forms in which these structures develop.

In 1888, John Dreyer cataloged numerous nebulous objects in a catalogue called the *New General Catalogue of Nebulae and Clusters of Stars*. Since then two revised and supplementary *Index Catalogues* have appeared but it was not until Edwin Hubble discovered the Cepheid variable stars (located in the Andromeda Galaxy) in the 1920s, by using the newly opened 100" telescope on Mount Wilson, that many astronomers became convinced that many of these nebulous objects were indeed galaxies (Sparke & Gallagher, 2007).

Mo, van den Bosch & White (2010) state that extragalactic astronomy is still a relatively new science but great progress has been made towards the development and expansion of this research area. Examples of this can be seen in the numerous detailed surveys conducted on the galaxies contained in the Local Group, which covers the entire electromagnetic spectrum. From these surveys it is possible to construct redshift surveys of order 10^3 of galaxies to study the large-scale structures of the Universe. This in turn makes it possible for astronomers to study and reconstruct the stellar populations of high redshift galaxies contained in the Universe when it was only a small fraction of its current age.

2.3.1 Hubble's classification scheme

Galaxies are found in a myriad of different shapes and forms. In 1926, it was Edwin Hubble who first proposed some order for this bewildering diversity by introducing a classification scheme that

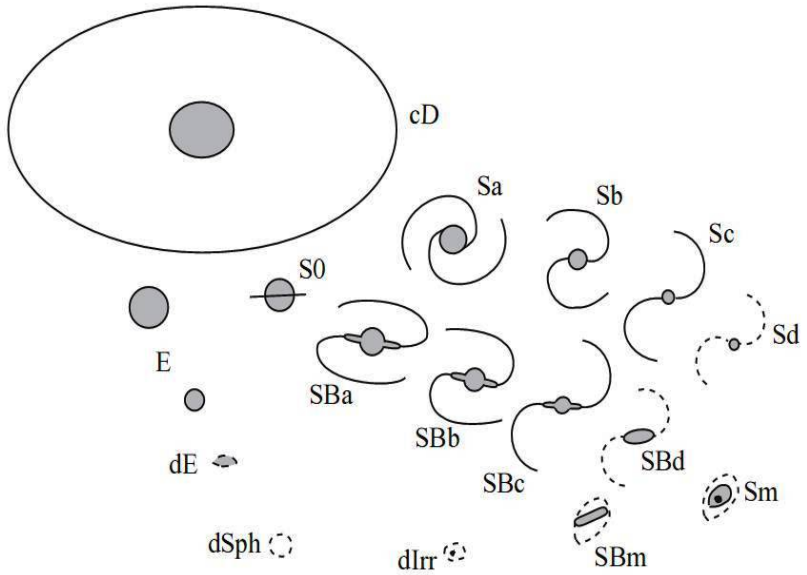

Figure 2.3: Galaxy classifications: a modified form of Hubble's identifications. Figure taken from Sparke & Gallagher (2007).

was formulated on the basis of galaxy morphology. This was called *Hubble's tuning fork* and an example of this classification scheme is given in Fig. (2.3).

The tuning fork is characterised by four major classes of galaxies: ellipticals, lenticulars, spirals and irregulars. Each class is also further described by a Hubble type, indicated by a combination of letters and numbers. The elliptical galaxies are located at the lower left–hand and spirals at the lower and upper right–hand side of Fig. (2.3). The spiral galaxies are divided into two types, called "normal" and "barred" spirals. Elliptical and lenticular galaxies are referred to as ETGs while the spiral and irregular galaxies are called late–type galaxies (Longair, 2008).

Cappellari et al. (2011) proposed a new revised scheme of the Hubble tuning fork — in this version the ETGs are more closely related to the spiral galaxies and consequently form a parallel sequence to these galaxies. The new version suggests a much closer connection between the ETGs and spiral galaxies than first assumed and will have to be considered in the future development of galaxy formation models. The original Hubble tuning fork was used in the further description of the galaxy classifications.

1. **Elliptical (E) galaxies**: These galaxies are characterised by smooth and round surface brightness profiles. These galaxies do not have the characteristic spiral arms or prominent dust lanes found in spiral galaxies. Hence, E galaxies are described as being almost featureless (Sparke & Gallagher, 2007). These galaxies contain small amounts of cool gas and

consequently have a red photometric colour, which implies that E galaxies contain old stellar populations (Mo et al. 2010). A study conducted by Bildfell et al. (2008) indicated that galaxies with blue cores and ultraviolet (UV) excess have signatures of ongoing star formation.

E galaxies are the most prominent galaxies found in rich clusters[3] of galaxies. The largest of the E galaxies are called cD galaxies (see §2.8 for more detail), which can be found in the densest part of the rich clusters. BCGs can also be described by these cD galaxies, which form a special sub-class of BCGs. Following from Dressler (1980a), E galaxies are often found in galaxy clusters and in compact groups of galaxies.

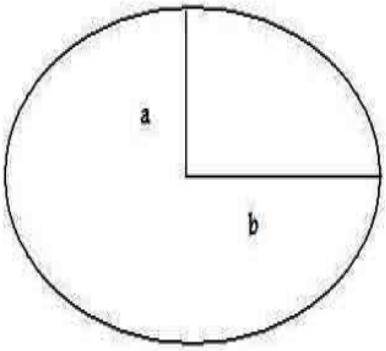

Figure 2.4: Semimajor axis, a, and the semiminor axis, b of an observed ellipse. This is used in Hubble's notation when the observed ellipticity of a galaxy is determined.

As found by Sparke & Gallagher (2007), the stars in low surface brightness E galaxies have a more structured rotational movement and less random motions. Some of these E galaxies might have a disk that is embedded within the elliptical body. The very faintest of these galaxies, usually with luminosities of $\sim$(1/10) of the Milky Way's luminosity, can be divided into two groups:

- The rare and compact elliptical galaxies.
- The faint diffuse dwarf elliptical (dE) galaxies and also the less luminous dwarf spheroidal (dSph) galaxies.

E galaxies can be divided into Hubble types ranging from E0, appearing circular, to E7 for the most elongated (Jones & Lambourne, 2003). The number, which follows the letter E in

[3]Inglis (2007) defined rich clusters as clusters consisting of more than a 1000 galaxies, many of which are E galaxies and stretches over an area of three Mpc in diameter. The galaxies are more concentrated towards the cluster's centre. The centre itself might contain one or two giant E galaxies. An example is the Virgo cluster, with the giant elliptical M87 located at its centre.

each type is an indication of the relative size of the semimajor *(a)* and semiminor *(b)* axes of an observed ellipse (see Fig. (2.4)). This number is obtained by multiplying the flattening factor, $f = (a-b)/a$ by ten and rounding the answer to the nearest whole number. As an example, the ratio of the semiminor to semimajor axes, (b/a), of E7 type galaxies give an answer of $(b/a) = 0.3$ (Longair, 2008).

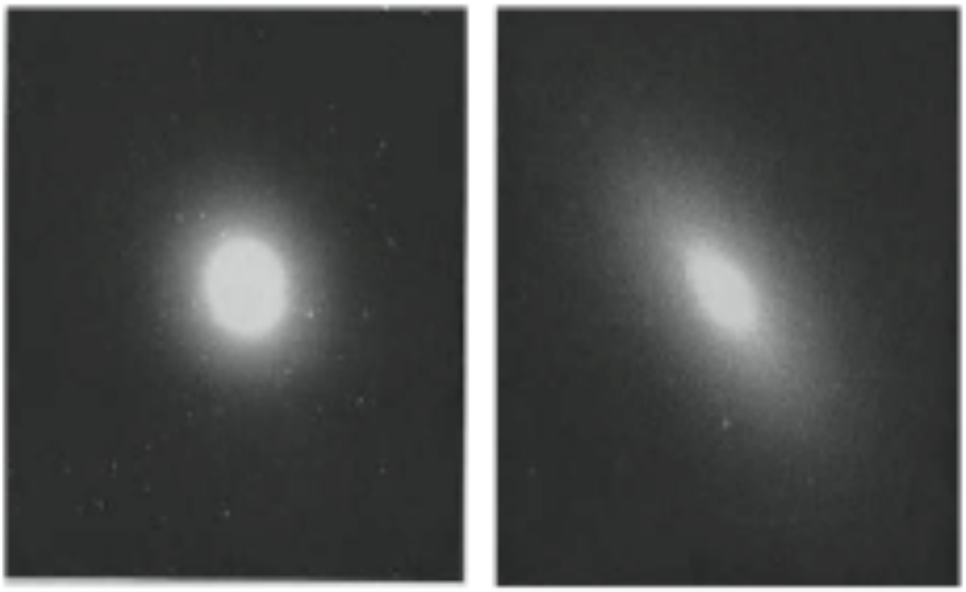

Figure 2.5: Examples of elliptical galaxies. From left to right: NGC 4278 (E1) and NGC 3377 (E6). Figure taken from Mo et al. (2010).

2. **Spiral (S) galaxies**: These galaxies have prominent bright spiral arms and a thin stellar disk. The spiral arms are outlined by clusters of bright, hot O and B stars and metal–rich gas, out of which stars form. Dressler (1980a) showed that the fraction of S galaxies decreased with increasing galaxy density while the opposite were true for E and irregular galaxies. This followed out of the morphology–density relation. S galaxies are therefore found in low-density regions[4]. Following from Longair (2008), the spiral arms come in pairs and the arms are remarkable symmetric with respect to the centre of the galaxy. These structures are not always that simple to describe and many more complicated configurations of these particular galaxies are known.

   S galaxies can be divided into subclasses according to whether or not the galaxy contains a central bar. Each of these subclasses is then divided into Hubble types: Sa, Sb, Sc (when no bar is detected) or SBa, SBb, SBc (when a central bar is detected). Three conditions are

[4]Regions with low galaxy densities typically refer to one galaxy for a spherical volume of the order of 20 Mpc^3 with a radius of $\sim$ 10 million light years (Dressler, 1980b). Rich clusters are contained in high galaxy density regions that are 100 – 1000 times as dense as the low-density regions.

used when dividing S galaxies into their Hubble types, and these criteria, as given by Mo et al. (2010) are the:

(i) Relative size of the central bulge;

(ii) Openness of the winding of the spiral arms and;

(iii) Proportions of the stars, dust lanes and the HII regions into which the arms are resolved.

Sparke & Gallagher (2007) indicated that in the progression of the spirals from Sa to Sc and Sd, the central bulge became less important in comparison to the fast rotating disk, whilst the spiral arms became more open and the fraction of gas and young stars in the disk increased. Thus, the HII regions became brighter and brighter during the transition from the Sa to Sc type.

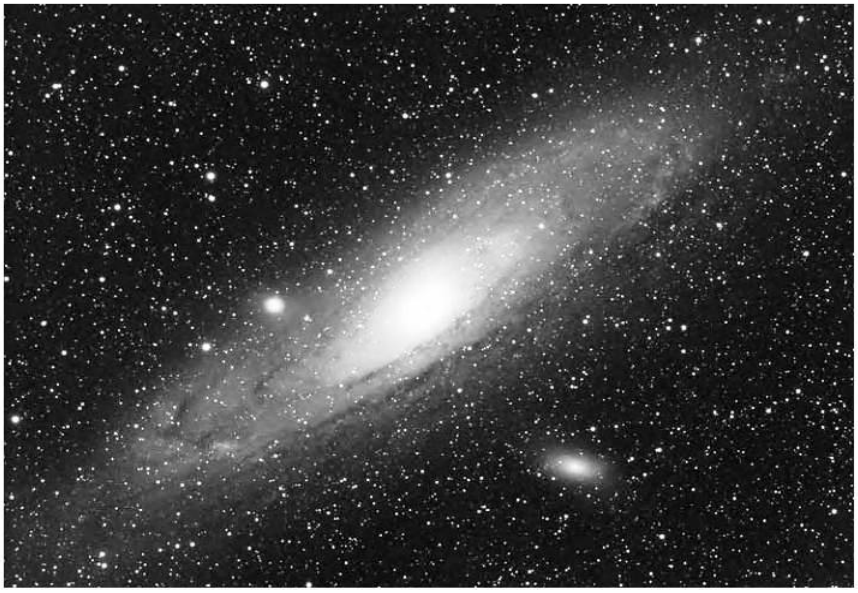

Figure 2.6: Our nearest large neighbor, the barred spiral galaxy (Sb) — the Andromeda Galaxy (M31). Note the large central bulge and dusty spiral arms in the disk. Two satellites galaxies are visible: M32 is round and closer to the centre while NGC 205 is the elongated object to the west. Figure taken from Sparke & Gallagher (2007).

On average, the Sa and Sb systems are brighter than the Sc and Sd types but some of the Sc galaxies are still brighter than a classical Sa spiral. At the end of the sequence, for the Sd system, the spiral arms become more frayed and less organised.

3. **Lenticular (L) galaxies**: They are called S0 (pronounced "ess–zero") galaxies because these galaxies form the intermediate class between E and S galaxies (Sparke & Gallagher, 2007) but the L galaxies share some similarities with E and S galaxies, for example the lenticulars galaxies:

- Have smooth surface brightness profiles (Longair, 2008);
- Do not contain the characteristic spiral arms, HII regions or dust lanes;
- Contain thin, fast-rotating stellar disks with central linear bars. These galaxies are then referred to as SB0 (Mo et al. 2010) and;
- Contain central bulges which are more dominant than the bulges found in S galaxies (Mo et al. 2010).

These L galaxies can be found in the regions of space where the number of galaxies are numerous (Dressler, 1980a).

Figure 2.7: An example of a lenticular galaxy — NGC 2787. Credit: NASA, ESA AND THE HUBBLE HERITAGE TEAM (STSCI/AURA).

4. **Irregular (Irr) galaxies**: These galaxies show little or no sign of disk symmetry or regularity and lack the dominating nuclei (Longair, 2008). Hubble did not include this type in his original classification scheme because he was uncertain whether or not it could be considered as an extension of any of the mentioned above classes. It is now generally accepted that they are extensions of S galaxies (Mo et al. 2010).

2.4 Galaxy Formation and Evolution

Research, regarding the formation and evolution of galaxies, is far more complex than similar research conducted on the evolution and formation of stars. This is because the structures of galaxies are far more complex than that of stars. Galaxies are not easy to observe and these observations

are even harder to interpret. The research of these structures is further complicated by the fact that little is known about the conditions regarding the formation processes in the early Universe. And finally, a galaxy may experienced several collisions, i.e. mergers and galaxy interactions during its existence, thus making it difficult to interpret the SFHs of these structures.

2.4.1 The signatures of galaxy evolution

The evolution of galaxies take place when galaxies gradually evolve as new stars are formed out of the gas and dust located in the ISM. The evolutionary tracks of main-sequence (MS) stars evolve into giants and finally into white dwarfs, neutron stars or black holes. It was from these evolutionary tracks that astronomers found that stellar evolution played an important role in the development of a galaxy's colour and chemical composition. From numerous studies and surveys it became apparent that galaxies evolved in different ways — internally (spectra and chemical compositions) and externally (dynamics). This was evident, especially for optical astronomers from the presence of the SFHs of the various galaxies.

The SFH can be deduced from the galaxy's luminosity function over the whole wavelength range of the electromagnetic spectrum, more specifically the superposition of the light contributions of all the stars (contained in the galaxies) as affected by the scattering and absorption of the starlight by the dust located in the ISM (Keel, 2007). Thus, astronomers can deduce the SFH of a galaxy by using high signal–to–noise (S/N) ratio *spectra* that covers a wide enough wavelength range. Out of these spectra, astronomers could deduce an approximated timeline for when galaxy formation was thought to have taken place, i.e. young galaxies could not contain old stars. This method could not only be applied to high redshift galaxies but also to surveys used to search for delayed galaxy formation which was proven to still take place today.

The presence of stellar evolution and the SFHs indicated that the *chemical composition* of the Universe had to undergo some kind of evolution (Keel, 2007). The elements, H, helium (He) and traces of deuterium, primarily made up the entire chemical composition of the early Universe and thus, the very first stars formed in the galaxies were composed out of these elements. Through nuclear fusion that took place in these stars, H was converted into He. In stars more massive than the Sun, further reactions converted He to carbon and oxygen in successive stages of stellar evolution. In the more heavier stars, the reaction continued to form silicon and iron (Fe). As these stars got older and eventually reached the end of their lives, the stars expelled their interior compounds into the ISM through processes like supernovae. Longair (2008) explained that as the process of star formation continue, the heavier elements will be included in future generations of stars formed. Astronomers can observe the amount of heavy elements in the Universe today and it is clear that the elements were formed through numerous processes. These processes are necessary for researchers to study and understand galactic evolution. These processes include the (1) SFR; (2) rate at which the elements are produced and ultimately the return of the elements to the ISM as a function of stellar mass and; (3) the initial mass function (IMF) (Rudolph et al. 2006).

Finally, galaxies will evolve *dynamically*, more specifically the galaxy components will exchange energy and angular momentum with each other and the environment. This may be the origin for the different types of galaxies because these interactions might cause the distribution of stars and characteristic structures to change, i.e. cause the disks, bars and rings to form or fade, from galaxy to galaxy.

The formation of galaxies in the early Universe took place at a much higher rate than at present times because stellar material were more diffuse and found in smaller groups (Keel, 2007). High redshift galaxies are studied in order to find tracers of the initial dynamical conditions of the galaxies, which have not changed because the probabilities are expected too be small for these galaxies to have experienced any mergers or collisions.

The *relaxation time* of gravitationally interacting bodies (stars in galaxies) are a measure of the time it takes for one star to be notably perturbed by the other stars in the galaxy (Sparke & Gallagher, 2007). This process originates when the orbits of two stars or objects are so close that they approach one another. The end result will be that a significant amount of the gravitational energy will be transferred from the galactic orbits over a characteristic period of 10^6 years. Keel (2007) found that these timescales were too long to account for the regular galaxy structures because the galaxies were far to young for star–star collisions to have had any influence on the structure of the galaxies. Observations have shown that some galaxies contain structural symmetry, which implies that the initial indicators of galaxy formation are no longer visible and the energy has been dispersed amongst the stars. These interactions took place at a particularly high rate for high redshift galaxies and hence, this process is referred to as *violent relaxation*.

A brief description of the internal evolution signs

The internal evolution will be described under the headings (a) *the luminosity function* and; (b) *stellar nucleosynthesis* or *chemical composition*. The internal evolution of a galaxy is further complicated by the fact that most of the galaxies are found in small groups or clusters where they interact with each other over extended time periods. These interactions may change the inner-structure of a galaxy, compress the interstellar gas and consequently trigger a sudden starburst. Some of these encounters can also lead to a central black hole that might be behind the violent activities in some of the galactic nuclei. The presence of starbursts and nuclear activities are taken as indications of interactions or mergers between galaxies.

(a) The luminosity function of galaxies

The luminosity of a galaxy is roughly speaking proportional to the number of stars contained in the galaxy and therefore also a measure of the stellar mass. The luminosity function of galaxies $(\phi(L)\,dL)$ is described as the number densities of galaxies per Mpc^{-3} with intrinsic luminosities in the range L to (L + dL) (Longair, 2008; Keel, 2007). The observed luminosity function of a galaxy is usually fitted against a more practical form known as the Schechter

luminosity function that is given by Schechter (1976) as:

$$\phi(L)\,dL = \phi_\star\,(L/L_\star)^\alpha exp\,(-L/L_\star)(dL/L_\star) \tag{2.2}$$

where $\phi_\star$ denotes the number of galaxies per unit volume, $L_\star$ is the characteristic luminosity and α is the asymptotic slope at low luminosities.

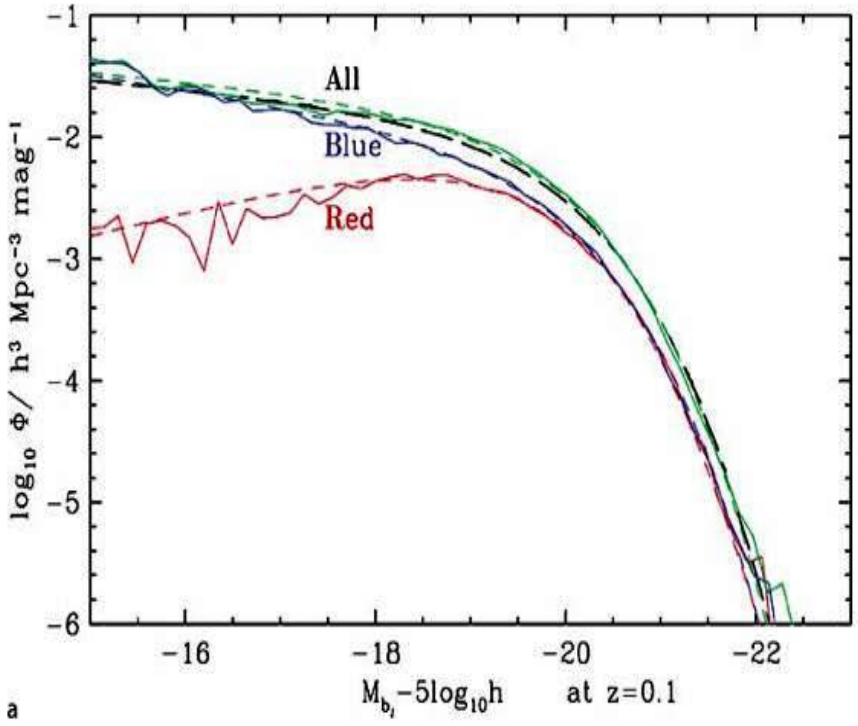

Figure 2.8: Schechter luminosity function for 221 414 galaxies observed in the 2–degree Field (2dF) Galaxy Redshift Survey. The overall luminosity function and those of the red and blue galaxies in the sample have been fitted by the Schechter luminosity function. Figure taken from Longair (2008).

Fig. (2.8) shows the Schechter luminosity function for 221 414 galaxies which have been observed in the 2dF galaxy survey — all the galaxies for which the spectroscopic redshifts and colours were available. The dashed line represents the overall Schechter luminosity function, while the luminosity functions for red and blue galaxies are indicated with the blue and red lines. Mo et al. (2010) state that at the faint end, the luminosity function, $\phi(L)$ follows the power law and reduces at high magnitudes while the number density of galaxies fall exponentially to a good approximation.

The luminosity functions of galaxies depend on the wavelength bands, redshifts, colours, environments and the morphologies of the galaxies. Currently, one of the most challenging problems in galaxy formation is to explain the general shape of the luminosity function.

(b) Stellar nucleosynthesis or chemical composition

In astronomy, heavy elements or metals are defined as all the elements heavier than H and He (Salaris & Cassisi, 2005). Following Mo et al. (2010), during the first three minutes of the BB (also called the epoch of primordial nucleosynthesis) nuclear reactions, involving neutrons and protons, were responsible for the production of $\sim 75\%$ H, $\sim 25\%$ He and traces of lithium. It is from this description of the chemical composition of the BB that astronomers know that the very first stars in the Universe consisted almost entirely of He and H.

A star is born when a cloud of interstellar gas, mainly consisting of H and He collapses under the influence of gravity. This happens when the cloud is cooler, denser and has lower kinetic energy than the surrounding regions. The temperature of the core is raised through compression and when the temperature is high enough, thermonuclear reactions are triggered to burn H into He, while releasing energy. A star will then reach a state where the energy, lost due to radiation, will be balanced by that produced by thermonuclear reactions (Mo et al. 2010). Eventually, the H in the core will also be depleted and there will not be enough fuel to supply energy being lost through radiation. The core contracts under gravity and the temperature in the core will rise again to trigger the reactions to turn He into other elements. This process continues until Fe-56 is reached — here the evolution ends because this element has the highest binding energy per nucleon (Keel, 2007). When this stage is reached, the fusion of Fe no longer produces energy and the stellar layers of the core will collapse and the envelope is expelled — giving birth to a supernova. After this explosion, the iron core is left behind to form a neutron star or a black hole, depending on the mass of the remnant. If the initial stellar mass of the remnant is below the Chandrasekhar limit (M$= 1.44 M_{\odot}$), the beginning of electron degeneracy at the end of the He burning phase prevents the temperature of the core to rise, which in turn would have led to the onset of the next burning phase. The energy of the non-degenerate ions is radiated away, causing the temperature and luminosity of the star to decrease, forming a white dwarf. When the initial stellar mass of the remnant is above the Chandrasekhar limit, the remnant will experience an ongoing gravitational collapse that will lead to the formation of neutron stars or black holes. From this description, it follows that the higher the mass of the star, the shorter the lifetime will be.

The stars that exploded as supernovae expelled their stellar content into the surrounding ISM. The newly enriched ISM then contributed to the formation of new generations of stars (Burbidge et al. 1975). Each of these new star generations increased the concentration of the elements in the interstellar clouds from which a next generation of stars were formed (Chaisson & McMillan, 2008) and hence, the spectra of the youngest stars contained more heavier elements than the older stars. Astronomers can study the ages of stars through stellar evolution, more specifically, purely from spectroscopic studies.

[Fe/H][5] is defined by Mo et al. (2010) as the mass fraction of the baryonic component[6] in metals. The formation of stars out of the metal–enriched ISM means that the younger stars will have a higher [Fe/H] than the older generation stars. From this process it is clear that the progression of stars is an ongoing process.

The research area of stellar nucleosynthesis, also described as the evolution of the chemical composition of the gas and stars in galaxies, is a very important tool used by astronomers to study the stellar evolution of galaxies. This is important because the (i) luminosities and colours of particular stellar populations depend on the ages, the IMF and [Fe/H] of the stars; (ii) cooling ability of the gas depends strongly on the [Fe/H] of the gas (the higher the [Fe/H], the faster the cooling efficiency of the gas) and; (iii) small dust grains mixed with the gas, located in the ISM absorb significant amounts of starlight and re-emit it in the infrared (IR) wavelength range. The brightness of a galaxy can significantly be reduced by the interstellar extinction caused by the dust in the ISM.

2.4.2 The star formation histories of the Universe

It was only after numerous high redshift surveys of galaxies have been undertaken that astronomers could begin to answer the questions related to galaxy evolution. One of the most intriguing questions, even asked today is about the cosmic SFH. Keel (2007) defined this SFH as the "*spatial averaged rate of star formation in solar masses per unit volume, as a function of the redshift*". Assuming that the different mechanisms of star formation can be neglected, Mo et al. (2010) write that the cosmic SFH can be approximated by the quantity $\dot{\rho}_\star(z)$, which is the total mass of gas turned into stars per unit time per unit volume at redshift z. To estimate $\dot{\rho}_\star(z)$, the number of galaxies as a function of luminosity have to be observed in some wavelength,

$$\dot{\rho}_\star(z) = \int (\dot{M}_\star)\, d\dot{M}_\star \int P(\dot{M}_\star|L,z)\,\phi(L,z)\,dL = \int \langle \dot{M}_\star \rangle (L,z)\,\phi(L,z)\,dL \tag{2.3}$$

where $P(\dot{M}_\star|L,z)\,d\dot{M}_\star$ is the probability for a galaxy with a luminosity L, in a given wavelength, at a redshift z, to have a SFR in the range $(\dot{M}_\star, \dot{M}_\star + \dot{M}_\star)$, while $\langle \dot{M}_\star \rangle (L,z)$ is the average SFR of galaxies with luminosities of L at redshift z and $\phi(L,z)$ is the luminosity function (which can be deduced from the high redshift surveys of galaxies). The method used to transform the observed luminosities to SFRs depends on the rest wavelength used to derive the luminosity function.

Fig. (2.9a) is the graphical representation of the cosmic SFH and is called the Madau diagram — named after Piero Madau who extensively researched the SFH of the Universe by studying the

[5]The standard notation of $[X/Y] = log(X/Y) - log(X_\odot/Y_\odot)$ is used when the [Fe/H] is described. The logarithm describes of the ratio of the stellar object's Fe abundance compared to that of the Sun (Howell et al. 2009). From this it can be seen that stars with a higher [Fe/H] than the Sun will have a positive logarithmic value, while those with a lower [Fe/H] than the Sun will have a negative value.

[6]Hot and cold gas as well as stars consisting of protons and neutrons.

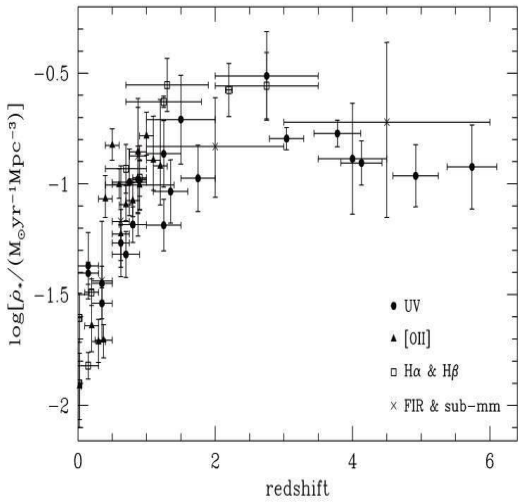

(a) Cosmic star formation history as a function of redshift, z. The different symbols indicate the different wavelength ranges used in the analysis. Figure taken from Mo et al. (2010).

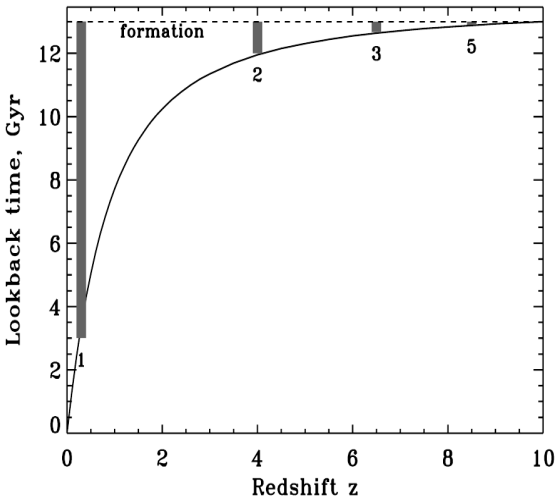

(b) Timescales of stellar evolution as a function of redshift, z. Figure taken from Keel (2007).

Figure 2.9

star formation of high redshift galaxies with Hubble Deep Field (HDF) data which contained photometric redshifts and UV luminosities. What Madau et al. (1996) found was that the SFR rapidly increased as the redshift increased from the current epoch ($z = 0$) to about $z \approx 1$. A wide peak was found around redshifts of $z \approx 2$ and from here the SFR decreased as the redshift increased. Fig. (2.9b) shows the timescales of stellar evolution. The dashed line at the top of the graph indicates galaxy formation. The shade areas show the stellar evolution timescales of stars with various masses. At $z = 0.3$, stars with masses of $1M_{\odot}$ will be visible from the initial burst, while more massive stars will have shorter lifespans and for this reason stars with $M = 5M_{\odot}$ will have to be observed at $z = 8$ from the initial star formation burst.

Keel (2007) stated that the average value of the cosmic SFR over time, as derived by Madau et al. (1996), was close to the expected average value of the SFR, derived from the [Fe/H] of the bright galaxies found today. Cowie (1988) indicated in her book that a link could be found between the UV light (emitted by these galaxies) and the production of heavy elements, as these elements are present in the stars, which provide an important contribution to the UV radiation emitted by the bright galaxies. The typical metal content of the Universe (determined from the bright galaxies) implied that the total surface brightness of the Universe is in the UV wavelength (Keel, 2007). When the average value of the SFR, as derived by Cowie (1988), was compared to that of Madau et al. (1996), some inconsistencies became evident. It was proposed that the inconsistencies were due to the internal dust absorption or because the star formation activities took place in weak, obscured regions that could not be detected by the HDF survey.

Brief description of star formation

Protostars form when interstellar matter condensates. These protostars are in hydrostatic equilibrium and have low temperatures. Stars can be modelled as gravitating gas spheres in hydrostatic equilibrium. These stars are fuelled by nuclear reactions and release gravitational energy but before stars can reach the hydrostatic equilibrium stage, the stars have to form out of the matter contained in the ISM. The vast space between the stars in galaxies and even between two other galaxies is filled with the interstellar matter (primarily made up of H, He and traces of heavier elements), which is heated and ionized by the photons emitted the stars. Another mechanism responsible for the ionization of the immediate region is the mechanical energy released during a supernova explosion. Following from Salaris & Cassisi (2005), large molecular clouds, consisting of molecular H and dust, can be found throughout the ISM and this is known as star formation regions. These clouds have a mass range of $10^5 - 10^6\ M_\odot$ and temperatures ranging between $10 - 100$ K, with average densities of $10^2 - 10^3$ particles/cm^3. For energy to be produced through nuclear reactions, the stars have to be much hotter and denser than the typical densities of molecular clouds. This in turn indicated that a process of gravitational contraction had to be present during star formation epochs.

The next section will discuss the source of this gravitational attraction but as an introduction — It was found that galaxy clusters contained dark matter (see §2.5 for more detail) and the presence of dark matter holoes in these clusters were confirmed by Ostriker & Peebles (1973). The missing gravitational attraction (needed for star formation) was found to be among the characteristics of dark matter. The gas in the holoes cooled down and flowed inwards, which in turn implied that the gravity (caused by the gas), would eventually dominate the dark matter gravity and hence, it would eventually collapse under its own weight. The cooling time of the gravitational collapse will rapidly decrease with comparison to the collapse time itself (Mo et al. 2010). This is due to the fact that the collapsing process increases the density and temperature of the gas in the centre of the gravitational collapse. It is only when these "runaway" collapses happen that the gas cloud eventually breaks into smaller pieces, each with a high density core and hence, a galaxy will be formed. See Fig. (2.10) for an illustration of galaxy formation in the presence of dark matter.

2.5 Dark Matter

Henry, Briel & Böhringer (1998) wrote that William Herschel and his sister, Caroline conducted their own separate study of the Messier objects just a few short years after Messier's initial observations in Paris. Due to the sensitive telescopes at their disposal they were able to find more than 2000 of these static objects — including 300 located in the Virgo cluster. But it was William and his son, John, who first noticed the chunky arrangements of these objects. These arrangements would later be called galaxies. Naturally the next undertaking would be to understand what influenced the galaxy structures. Two questions arose, the first of which was:

1. *What organised the galaxies into the particular patterns observed?*

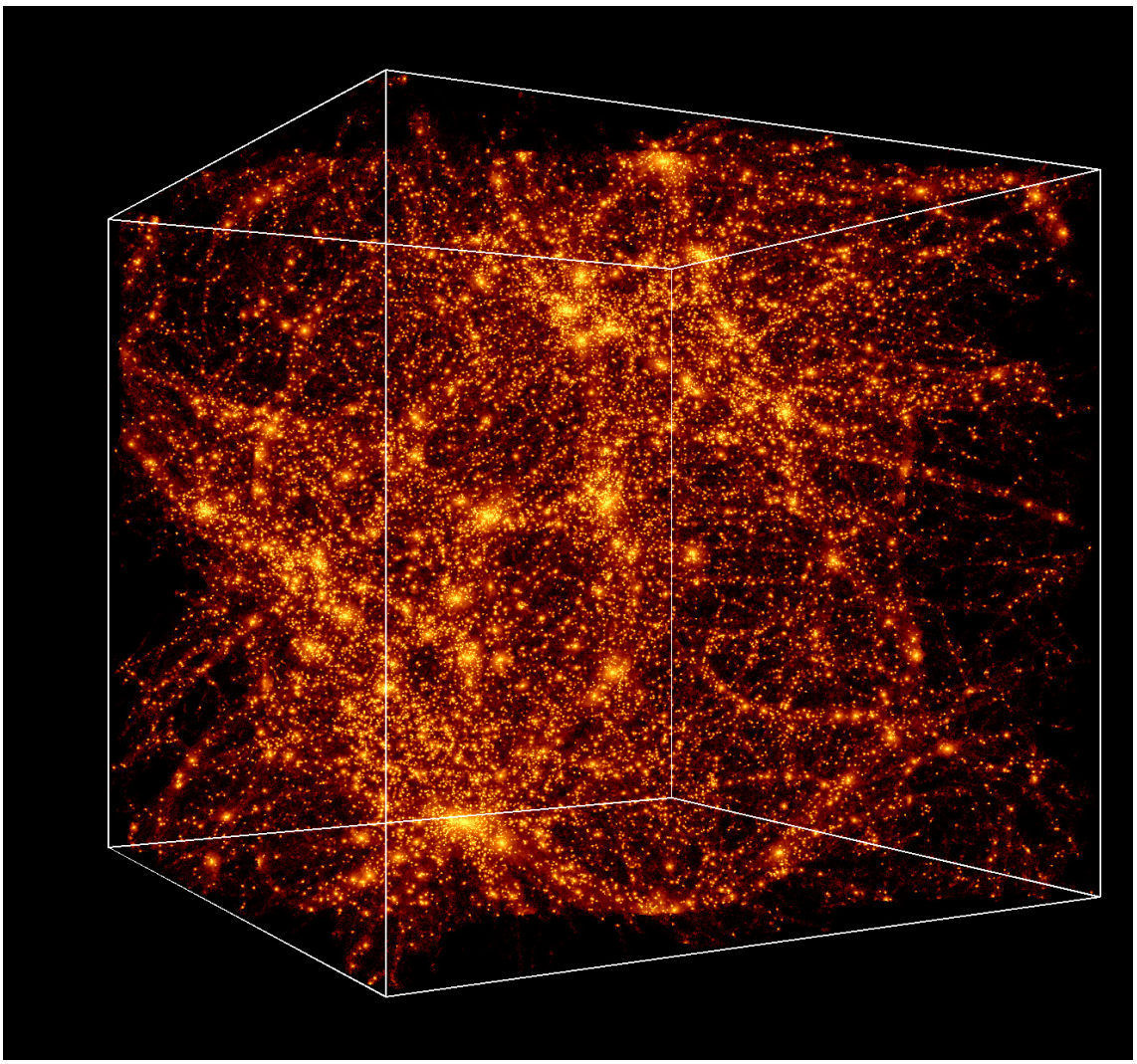

Figure 2.10: This simulation (simulated with GADGET) shows the Universe 13.4 billion years after the BB. The bright spots represent high concentrations of dark matter which are associated with sites of galaxy formation. The simulation shows how dark matter, an invisible material of unknown composition, gather luminous matter in the Universe from its initial smooth state into the cosmic web of galaxies and galaxy clusters that populate the Universe today. Image courtesy of ANDREY KRAVTSOV.

The astronomers Fritz Zwicky and Sinclair Smith measured the speed of the galaxies in both the Virgo and Coma clusters during the 1930's. They discovered that these galaxies orbited to fast for their combined mass to provide enough gravity to hold these galaxies together and that these galaxies roughly had to be a 100 times more massive than the visible matter contained within the galaxies or else these galaxies would have been thrown out of the clusters a long time ago. This led to the conclusion that these clusters consisted mostly of a dark, unseen matter and hence, a second question arose.

2. *What was the nature of this dark matter?*

To date, it is almost 87 years since Edwin Hubble found that the Universe expanded uniformly by using the kinematics of galaxies. Galaxies are also used to trace the evolution of the Universe and when the galaxies were studied, astronomers found that these large structures were made up of stars of various chemical compositions, ages and a unique mixture of gas, plasma and dust (Avila-Reese, 2006). But the most surprising aspect regarding galaxies was that the luminous matter (the stars, gas, active galactic nuclei (AGN), etc.) accounted for only $\sim$1 to 5% of the total mass measured in the galaxies and the giant holoes. It is the uneven distribution of the galaxies in the Universe and the unknown nature of dark matter that continues to baffle astronomers even today.

An indication of dark matter: the galactic rotational curve

Mo et al. (2010) stated that the kinematics of the disk of a galaxy can be represented by the rotational curve (V_{rot}) by graphically representing the rotational velocity of the stars or gas in the galaxy on the $y-$axis as a function of the galactocentic distance[7] indicated on the $x-$axis.

A study, undertaken by Bosma (1981) illustrated that a few galaxies reached a well-defined maximum in the rotational curve, while the rotational velocity decreased linearly with increasing distance from the centre of the galaxy while the luminosity in the disks, bulges and holoes of spiral galaxies exponentially decreased with increasing galactocentic distance. In the book *Galaxy Formation*, Longair (2008) wrote that the total mass of a galaxy would converge if the rotational velocity decreased to infinite distances. This result was similar to the mass derived from the rotational curve in the central regions of the disk of various galaxies. Astronomers discovered that the rotational curves of some galaxies presented a contradiction — the rotational velocities in the external regions of the galaxies remained approximately constant with increasing galactocentic distance. An example of this contradiction is given by the rotational curve of the Andromeda Galaxy (M31) shown in Fig. (2.11).

From Fig. (2.11) and other similar figures, the discrepancies concerning the observed mass–to–light ratio of matter between the disk regions and central parts of the galaxies can be derived. This is called the *galaxy rotational problem*. The source of these discrepancies is believed to be due to the dark matter spreading through the galaxy itself and extending into the halo of the galaxy.

Mo et al. (2010) wrote that *"the rotational curve is a direct measurement of the gravitational force within the disk"* of a galaxy. If it is assumed that the mass distribution (M) in a galaxy is spherical symmetrical and enclosed within a radius r, the mass distribution can be given by $M(\leqslant r)$. The rotational curve can be determined from a straightforward application of Gauss's theorem on

[7]Distance from the centre of the galaxy.

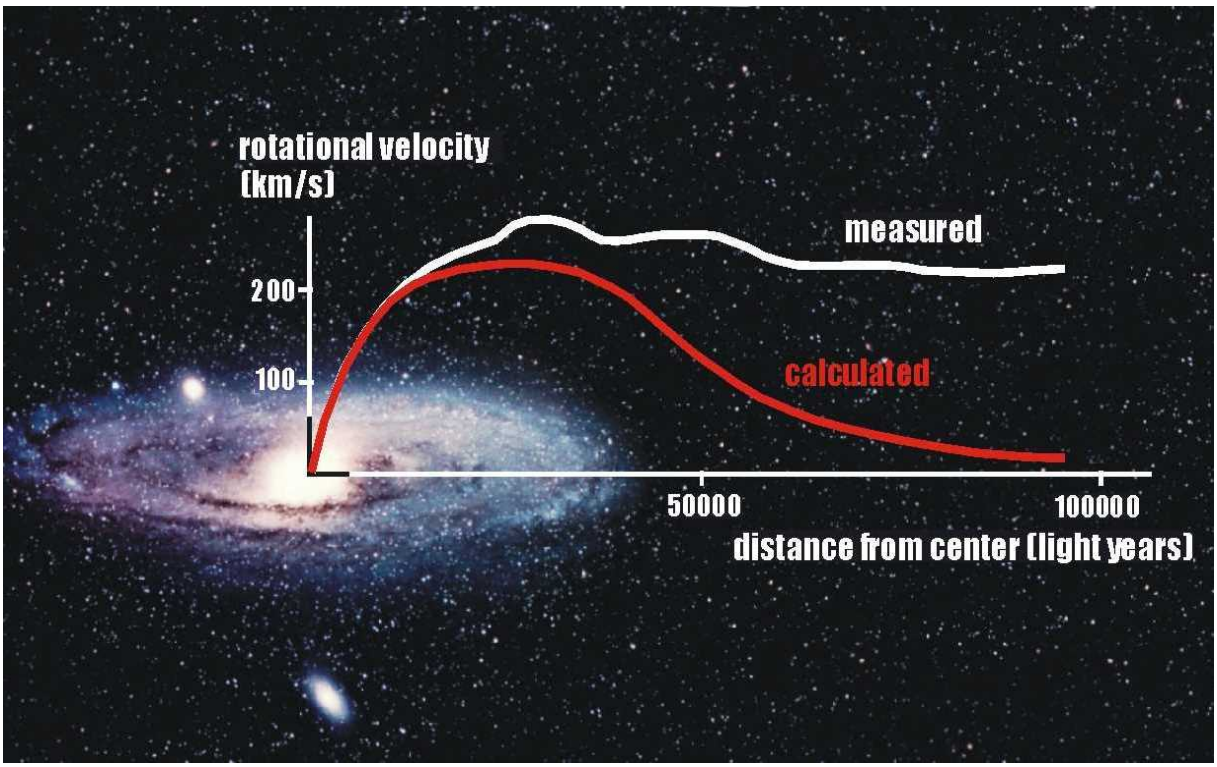

Figure 2.11: Rotational curve of the Andromeda Galaxy. The red line illustrates the velocities expected from the estimated mass of the visible matter contained in the galaxy while the actual rotational velocities of the outer stars are indicated by the white line. It is from these rotational curves that astronomers estimated that more than 80% of the mass of the galaxy is in the form of dark matter. Credit: QUEENS UNIV.

Newton's law of gravity (Longair, 2008):

$$\frac{GM(\leqslant r)}{r^2} = \frac{V_{rot}^2(r)}{r} \tag{2.4}$$

$$M(\leqslant r) = \frac{rV_{rot}^2(r)}{G} \tag{2.5}$$

where G is Newton's Universal Gravitational constant. For a point mass, i.e. the Sun, $M(\leqslant r) = M_{\odot}$, it follows that $V_{rot}(r) \propto r^{-1/2}$. Thus, if the majority of a galaxy's mass is concentrated in the centre, then the rotational velocity will vary. In the external regions, $V_{rot}(r)$ is approximately constant and this in turn implies that $M(r) \propto r$, meaning that the enclosed mass increases with the radius but the opposite is true for the enclosed luminosity, which decreases as the radius increases.

2.6 Galaxy Formation Theories

Astronomers now agree that galaxies began as small density fluctuations in the early Universe and evolved through the formation of stars and hierarchical mergers (Springel et al. 2005). From

Collins et al. (2009) it followed that stars form relatively quickly in the sub-galactic building blocks called dark matter holoes.

The density fluctuations of the cosmic microwave background suggested that the early Universe was homogenous after the BB. Dark and primordial matter were more evenly spread out in the early history of the Universe and mixed with baryons obtainable in the form of hot gas. The average density of the gas reduced as the Universe expanded but in slightly denser regions, clumps of matter were pulled together under their own gravity. The larger clumps attracted smaller ones and collided which compressed the gas and heated up as these clumps collided. Jones & Lambourne (2003) called this process *gravitational instability*. If the gas was dense enough to cool, the gas lost energy and started to fall inwards. The particles out of which the dark matter consists cannot lose energy, so the central part of a galaxy consists mainly of cool gas and luminous stars. Where the heated gas did not cool down, it was too diffuse, and the pressure prevented it from flowing inwards (Sparke & Gallagher, 2007).

Due to the difficulties in understanding galaxy evolution, astronomers are forced to use the fossil evidence of nearby galaxies, together with general theoretical principles to find plausible mechanisms responsible for galaxy evolution (Smith, 1995). Various theories and principles have been proposed and developed over the years, but the following formation theories had more merit:

1. Monolithic formation proposed by Eggen, Lynden-Bell & Sandage (1962).

2. Hierarchical merging proposed by White & Rees (1978) and;

2.6.1 Monolithic formation

This theory was first proposed by Eggen et al. (1962) in which they developed a model in which galaxies were formed through the gravitational collapse of primordial gas clouds. As gravity pulled the gas inward, the cloud fragmented into smaller clouds and due to the fact that the gas was turbulent, the stars had random velocities (Seeds & Backman, 2007). They proposed this theory as an explanation for the different morphological types of galaxies found in the Universe and hence, this theory is also referred to as the nature argument. On the other hand the model showed that if a cloud remained gaseous during collapse, gravitational energy would be released through radiative cooling and shocks and then the cloud would shrink until it is supported by angular momentum, leading to the formation of a rotationally supported disk.

As telescopes develop and become more sophisticated, astronomers are able to make more detailed observations, which in turn leads to a huge quantity of available data. This allows astronomers to test and develop more accurate hypotheses. From these observations astronomers found that the monolithic collapse theory were not always adequate enough to describe the formation of all the galaxies observed which led to the development of the hierarchical merging theory.

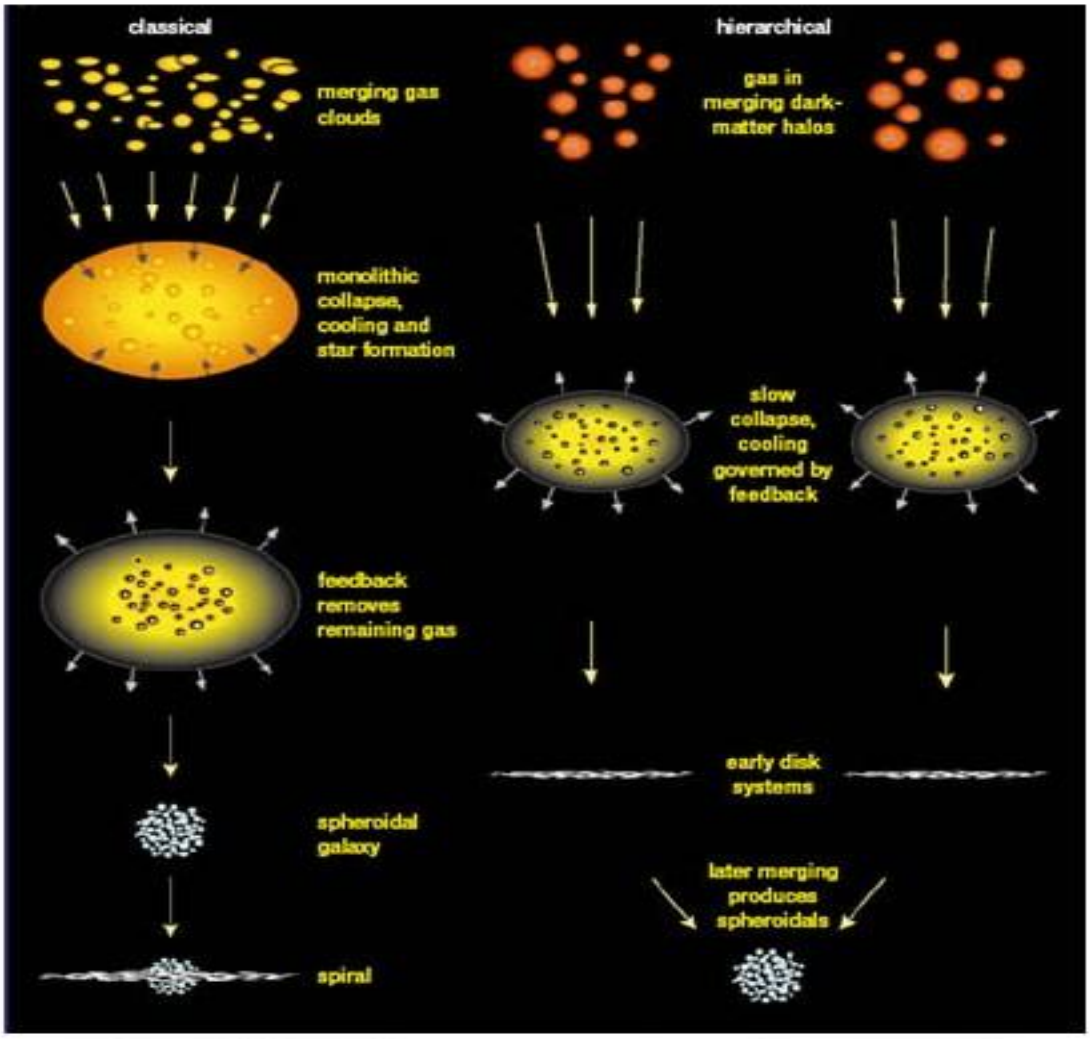

Figure 2.12: Model simulating the monolithic collapse and the hierarchical merger of a galaxy. Image courtesy of JEFF STANGER.

2.6.2 Hierarchical merging

This theory proposes that a galaxy is formed through the continuous coalescence or mergers of smaller progenitors of galaxies (Mo et al. 2010). In the paradigm of the Lambda Cold Dark Matter (ΛCDM), astronomers believe that the merging process still continues to the present epoch. This is also called the nurture argument, meaning that the morphology of a galaxy will be changed depending on the merger history (Loubser, 2009a).

Cold Dark Matter (CDM) was described by Jones & Lambourne (2003) as dark matter consisting of massive, slow moving particles. These hypothetical particles have random speeds that are small when compared to the speed of light. Computer-based simulations of this process revealed

that the first structures that formed had masses of order $10^6 M_\odot$ which was lower than the masses of galaxies found today (usually of the order $10^{11} M_\odot$). Larger structures developed with further collapses and mergers of smaller structures. The process is also called the "bottom–up" scenario.

As indicated in the research conducted by Trager et al. (2008), the bottom–up model predicted the following trends in the ages of ETGs:

1. The ages of the stellar populations in the larger ETGs should be older than those of smaller ETGs located in the dense and less dense environments. Mo et al. (2010) called this downsizing.

2. The ETGs, of a given mass form stars early on in the densest environments, hence these galaxies should have older stellar populations than those in the lower–density environments.

3. The massive ETGs in the high–density environments should have a small spread in the stellar population age compared with lower mass ETGs and also with those located in the lower density environments.

The hierarchical merging or the bottom–up scenario (under the influence of CDM) is presently the most widely accepted formation theory. This is supported in the research conducted by Trager et al. (2008) and Niederste-Ostholt et al. (2010).

Spinrad (2005) gives a contrast between the two models: a single, monolithic collapse falls in from the immediate environment, with little star formation beyond the initial burst while another "dormant" stage would likely be observable over $0 \leqslant z \leqslant 2$. *The other model, more relevant to the structure of giant elliptical systems and other galaxies, is the hierarchical merging "tree". Here the mergers are accompanied by star formation bursts and will eventually build up a galaxy with baryonic mass, meaning stars and gas. These two theories seem to oppose each other, but gathering observational evidence has made the models less distinct in recent years (Loubser et al. 2008).*

2.7 Stellar Populations

The history of any celestial object is characterised through changes that have taken place during the life span of these objects. In the case of galaxies, the formation histories are changed through any processes that influence the stellar evolution of the stars.

Elliptical galaxies were found to contain massive, low mass stars with a mass of $0.5 M_\odot$, were already evolved and star formation epochs have ended. These galaxies have a red photometric colour, while irregular galaxies on the other hand have a bluer colour than spiral galaxies (which in turn is bluer than elliptical galaxies). This follows because spiral and irregular galaxies still contain gas used for star formation and hence, young stars are still present in these galaxies. Elliptical

Figure 2.13: An example of galaxy interactions. The interacting pair of galaxies is called Arp 273 and is located 300 million light years away in the northern constellation of the Andromeda Galaxy. Despite the fact that these interacting galaxies look like a rose, this tranquil appearance is shattered by the fact that the larger S galaxy at the top of this image is in the process of being gravitationally ripped apart by the smaller galaxy. Connecting these two galaxies is a thin thread of stars stretching over tens of thousands of light years. Photograph courtesy of NASA, ESA, AND THE HUBBLE HERITAGE TEAM (STSCI/AURA).

galaxies are therefore found to contain population II stars (relatively old stars), while irregular and spiral galaxies contain both population I and II stars (young and old stars) (Leblanc, 2010).

As already discussed, the two competing galaxy formation scenarios accepted by astronomers today are the hierarchical formation scenario (galaxies assemble through the mergers of less massive galaxies) and the monolithic collapse (galaxies form through gravitational collapse). The majority of astronomers now agree that galaxies form hierarchically in a CDM dominated Universe (Schaivon, 2010). This was the reason behind the numerous studies undertaken to determine the ages and [Fe/H] compositions of the stellar population of massive ETGs.

The developers of software packages which is used in galaxy formation simulations, use the analysis of unresolved stellar populations to put constraints on these models, with the primary aim of making these models more accurate and sophisticated. Earlier versions of stellar population synthesis models used low resolution spectrophotometric observations and high resolution

photographic spectroscopy to determine the ages of stellar populations in galaxies. These models delivered some promising, yet unreliable conclusions as a result of the age-metallicity degeneracy (Worthey, 1994).

The evolution of a star with a given mass depends on its chemical composition. Stars with higher [Fe/H] evolve much faster than those with lower [Fe/H] (Mo et al. 2012). Studies conducted on stellar populations, consisting of young stars and therefore high [Fe/H], have shown that the spectral energy distributions (SEDs) of these young stars are the same for stellar populations containing old stars with low [Fe/H]. Hence, the two stellar populations have the same colour. *Shortly described, this age-metallicity degeneracy is a manifestation of the dependence of the temperatures of MS and giant stars, contained in a particular stellar population, on the age and [Fe/H]. This causes the colour of the stellar populations (especially in the optical and near UV) to change with variations in the ages and [Fe/H] of the stellar populations.*

The importance of spectral indices in breaking the age-metallicity degeneracy

Stellar populations are studied in order to understand how galaxies were formed and evolved, more specifically, the derived ages and [Fe/H] are key parameters that are used in the interpretation of the observational properties of galaxies. The problem becomes apparent in the degeneracy of the effects caused when one varies the ages or [Fe/H]. Even in the most simplest, unresolved stellar populations, these effects can be hard to separate and therefore, cause the age and [Fe/H] determinations to be uncertain. This led astronomers to focus on specific spectral features that are more sensitive to ages or [Fe/H] (Kong & Cheng, 2008). An example of such an approach was developed by Worthey (1994) where the effects of the ages and [Fe/H] on the integrated light of stellar populations were investigated. Suppose that an index changes with an amount ΔI, which can either be described as purely an age or [Fe/H] variation. Crudely stated, the parameter sensitive to changes in [Fe/H] is described by the ratio of the percentage changes in the age to the percentage changes in the [Fe/H], where larger numbers indicate that the parameter has a greater metallicity sensitivity.

One of the most extensive libraries of spectral indices, the LICK indices was developed by Faber and co-workers at the Lick Observatory (Faber et al. 1985; Worthey et al. 1994). An adapted version of the LICK indices are given in Table (2.2) which gives the spectral indices which are used to determine the ages and [Fe/H] of unresolved stellar populations and also shows how the metal indices are affected by the various elements. In the LICK system, the strengths of absorption lines are characterised by indices where each central feature band is bounded by a red and blue continuum band. A graphical representation of the LICK indices can be found in Fig. (2.14) where the Balmer indices are illustrated as an example. Here the central absorption features i.e. H_δ and H_γ are indicated with the filled gray boxes, while the blue and red pseudo-continuum sidebands are indicated by the bold horizontal strokes. The pseudo-continuum used for index measurement is represented by the dashed line between the flanking sidebands and the blue sidebands for the $H_{\gamma F}$ and $H_{\gamma A}$ are the same. For a more detailed analysis of the LICK indices, refer to Worthey et al. (1994) and Trager et al. (1998).

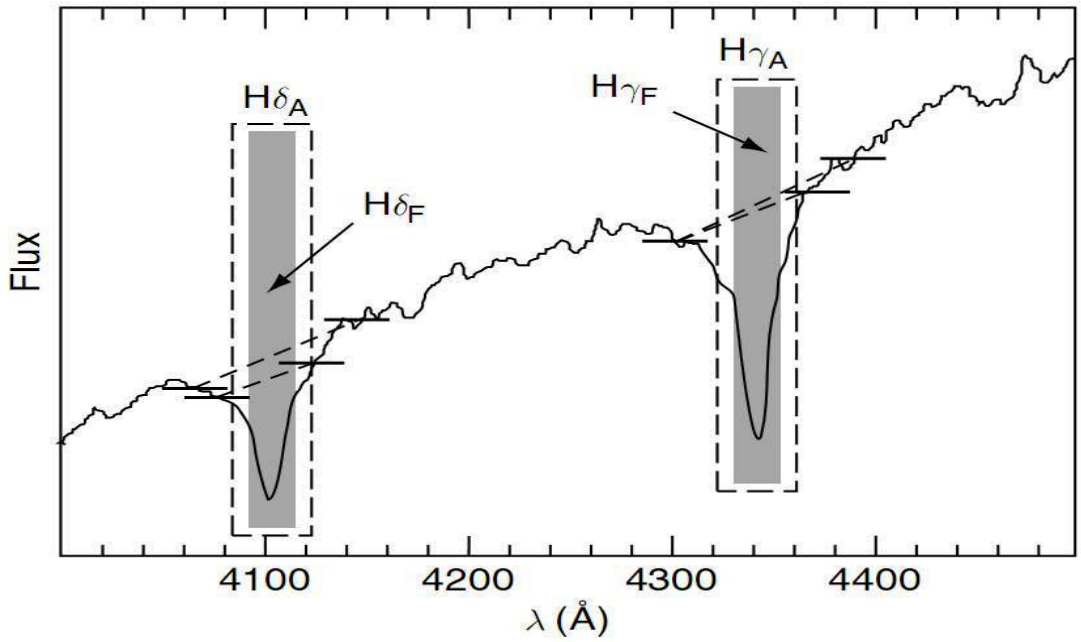

Figure 2.14: Representative stellar spectra, plotted with the definitions of the Balmer lines. The flux scale is arbitrary and the spectra have not been flattened or fluxed, for the spectra to still contain the instrumental response of the image dissecting scanner. The central bands are indicated with the filled gray boxes, while the blue and red pseudo-continuum sidebands are indicated by the bold horizontal strokes. The dashed line between the flanking sidebands represents the pseudo-continuum used for index measurement. Figure taken from Salaris & Cassisi (2005).

Many of the spectral indices are affected by the abundance of the heavy elements. These spectral indices are therefore very sensitive to the metal content of single stellar populations (SSPs). Although the Balmer lines (strength of these lines are determined through the H_β, H_γ and H_δ indices) are not completely unaffected by metallicity effects in the integrated light, they are relative immune to metals due to the fact that Balmer lines are very depended on the behavior of the MS turnoff (TO) temperatures with ages and [Fe/H] (Worthey & Ottaviani, 1997) rather than due to the behavior of the temperature of the red giant branch (RGB). In principle, strong Balmer lines are produced at a given age with decreasing [Fe/H] due to the hot TO stars. The young, more massive MS stars have very high temperatures and strong H absorption lines. The difference in sensitivity of the Balmer lines and metallic absorption features in the RGB are measured through the ratio of changes in age to changes in [Fe/H]. Following this process, the mean age and [Fe/H] values can simultaneously be derived assuming that a proper stellar population model is used (Worthey et al. 1994). On the other hand, spectral indices affected by metal abundances are primarily influenced by the temperature of cool stars (i.e. the RGB and asymptotic giant branch (AGB) stars).

Table 2.2: Example of the LICK indices, which is used in the age and [Fe/H] determinations of stellar populations. Column 1 gives the name of the spectral index, Column 2 gives the central index band, Columns 3 & 4 give the index in the red and blue pseudo-continuum. Table is adapted from Salaris & Cassisi (2005).

Name	**Index band (Å)**	**Blue continuum (Å)**	**Red continuum (Å)**	**Measures**
$H_{\delta A}$	(4084, 4122)	(4042, 4080)	(4129, 4161)	
$H_{\delta F}$	(4091, 4112)	(4057, 4089)	(4115, 4137)	
Ca4227	(4222, 4235)	(4211, 4220)	(4241, 4251)	Ca, (C)
G4300	(4281, 4316)	(4266, 4283)	(4319, 4335)	C, (O)
$H_{\gamma A}$	(4320, 4364)	(4284, 4320)	(4367, 4420)	
$H_{\gamma F}$	(4331, 4352)	(4284, 4320)	(4355, 4385)	
Fe4383	(4369, 4420)	(4359, 4370)	(4443, 4455)	Fe, C, (Mg)
Ca4455	(4452, 4475)	(4446, 4455)	(4477, 4492)	(Fe), (C), Cr
Fe4531	(4514, 4559)	(4504, 4514)	(4561, 4579)	Ti, (Si)
$C_2$4668	(4634, 4720)	(4612, 4630)	(4743, 4757)	C, (O), (Si)
H_β	(4848, 4877)	(4828, 4848)	(4877, 4892)	
Fe5015	(4978, 5054)	(4947, 4978)	(5054, 5065)	(Mg), Ti, Fe
Mg_b	(5160, 5193)	(5143, 5161)	(5191, 5206)	Mg, (C), (Cr)
Fe5270	(5246, 5286)	(5233, 5248)	(5286, 5318)	Fe, C, (Mg)
Fe5335	(5312, 5352)	(5305, 5316)	(5353, 5363)	Fe, (C), (Mg), Cr
Fe5406	(5388, 5415)	(5376, 5388)	(5415, 5425)	Fe
Fe5709	(5697, 5720)	(5673, 5697)	(5723, 5737)	(C), Fe
Fe5782	(5777, 5797)	(5765, 5775)	(5798, 5812)	Cr
Na_D	(5877, 5909)	(5861, 5876)	(5922, 5948)	Na, C, (Mg)

A problem arose when astronomers studied the integrated light of stellar populations; more specifically they found that the light suffered from an effect called the age-metallicity degeneracy. This effect was found by Worthey et al. (1994), where he quantified the degeneracy as the ratio $\Delta\,\text{age}\,/\,\Delta\,[\text{Fe/H}] \approx 3/2$, that is when one generates the spectrum of an object with age $\sim$ 15 Gyr and [Fe/H] = -0.1, then this spectrum will look similar to the spectrum of an object with an age a factor three times younger (in this example $\sim$ 5 Gyr) but double the [Fe/H] (in this example [Fe/H] = $+0.2$). *Hence, the age-metallicity degeneracy can be described as an effect where a metal-rich stellar population can be simulated by decreasing the mean temperature (that is, increasing the age) of a more metal-poor stellar population.* Worthey et al. (1994) concluded that a few indices will break the age-metallicity degeneracy by either being more abundance sensitive (i.e. the Fe4668, Fe5015, Fe5709 and Fe5782 indices) or more age sensitive (i.e the G4300, H_δ indices). Some indices, i.e. the Ca4227 and Mg_b are degenerate, meaning that there cannot be distinguished between the effects of age or metallicity abundances (Loubser, 2009a).

Fig. (2.15) illustrates the age-metallicity degeneracy as described in the previous paragraph. The observed values of the H_β and Fe5270 indices are compared for a sample of Galactic and extragalactic globular clusters, with theoretical calibrations for different ages and [Fe/H]. From the figure it follows that H_β is not sensitive to the [Fe/H] of ages $\gtrsim 1$ Gyr while the Fe5270 index is not affected by the age at all. From this figure, one can independently determine the ages and [Fe/H] of observed SSPs.

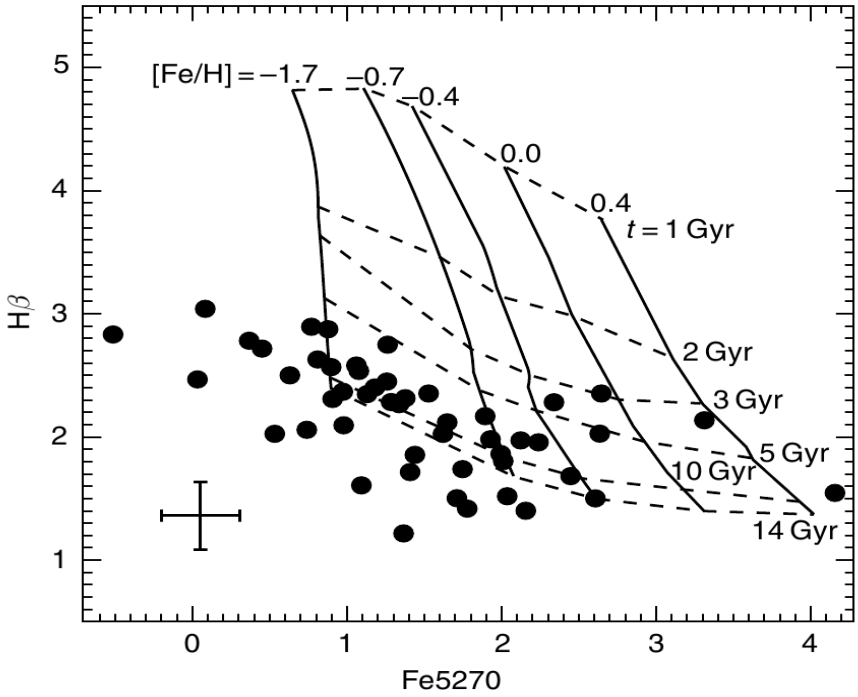

Figure 2.15: Calibration of the $H_\beta - Fe5270$ indices diagram for the labelled values of age and [Fe/H] that is compared against the observed data of a sample of Galactic and extragalactic globular clusters (data taken from Trager et al. (1998)). The typical observational error bars are also shown. Figure taken from Salaris & Cassisi (2005).

2.7.1 Single stellar populations

The term SSP refers to the most elementary populations of stars consisting of stars born at the same time in a star formation epoch, where the objects all have the same initial chemical composition (Salaris & Cassisi, 2005).

The stellar populations of high redshift galaxies cannot be resolved into individual stars. Photometric and spectroscopic observations only provide integrated magnitudes, colours and spectra

that include the contribution of all the stars out of which the stellar populations are comprised. An example is shown in Fig. (2.16) where the contribution of different stellar evolutionary phases to the total bolometric luminosity of an SSP is illustrated. The monochromatic integrated flux, F_λ^I received from an unresolved SSP of age t, and metallicity Z, can be written as:

$$F_\lambda^I(t,Z) = \int_{M_1}^{M_u} f_\lambda(M,t,Z)\,\phi(M)\,dM \tag{2.6}$$

where $f_\lambda(M,t,Z)$ is the monochromatic flux emitted by a star of mass M, metallicity Z and age t. $\phi(M)\,dM$ is the IMF, M_1 is the mass of the lowest mass star and M_u is the mass of the highest mass star still present in the SSP (Salaris & Cassisi, 2005). M_u is the initial mass of the object evolving towards the white dwarf sequence at the SSP age. The contribution of white dwarfs to the integrated flux is usually negligible.

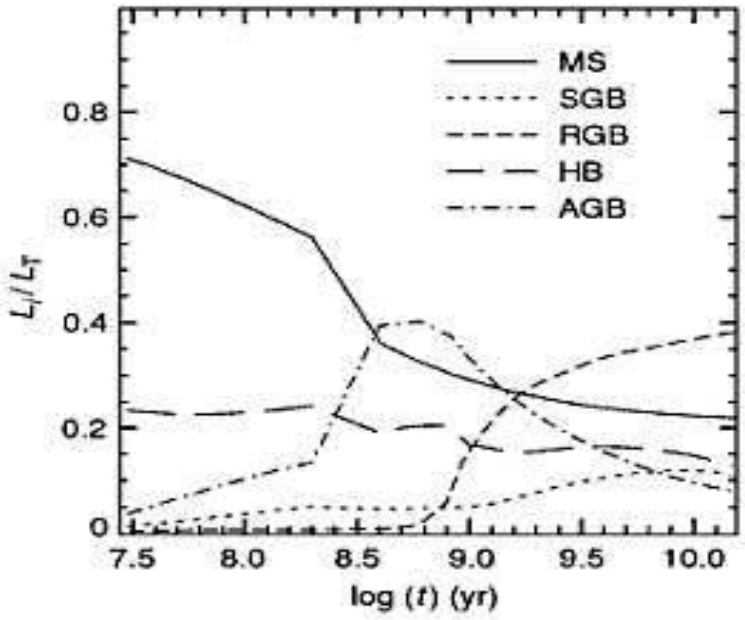

Figure 2.16: Contribution of different evolutionary phases to the total bolometric luminosity of an SSP. The abbreviations in the legend stand for the MS stars, the super giant branch (SGB), the RGB, horizontal branch (HB) and the AGB. Figure taken from Salaris & Cassisi (2005).

Eq. (2.6) states that the integrated flux is the sum of the individual fluxes of the stars belonging to the SSP, represented by the term $f_\lambda(M,t,Z)$; the IMF gives the number of stars formed with a given mass M. Theoretically, the proposal of an universal IMF and the effect of age and chemical compositions are included in $f_\lambda(M,t,Z)$ — since the energy output of a star of mass M and its wavelength distribution depends on both t and Z — also in M_u.

2.7.2 Composite stellar populations

A composite stellar population (CSP) is defined by Salaris & Cassisi (2005), as a group of stars formed at different times and with different chemical compositions. This theoretical concept can be used to describe galaxy evolution, since galaxies are comprised of multiple generations of stars and often show signs of recent star formation.

When astronomers analyse the unknown SFH of a galaxy, they use CSPs during the analysing process. A disadvantage of using this method is that researchers could only determine an average value for the age and [Fe/H] when the observed colours were compared to the calibrations for SSPs.

Li & Han (2007) found that IF galaxies experienced a more complex SFH, i.e. more than one star formation epoch, then the ages of the stellar populations would be strongly biased towards the age of the younger population instead of, as would be expected, towards the dominant population by mass fraction. This was also confirmed by Salaris & Cassisi (2005), which stated that if the unknown SFH of a galaxy can be presented with a CSP, then only a mean age and [Fe/H] can be determined from comparing the observed integrated colours with the corresponding SSP-equivalent calibrations. The mean age will be biased towards the age of any young population that might be present. This is due to the young MS stars that have larger luminosities in the blue part of the observed spectrum and also stronger Balmer lines than the older stellar populations. As an example, if the CSP had an uniform [Fe/H], then approximately $1-2\%$ of a young stellar population would be enough dominate the (B – K) colours of a CSP. When the Balmer lines are studied, the same trend is observed, i.e. when a CSP consists of various ages and [Fe/H], the dominant stellar population will be younger *or* metal-poorer, since lower [Fe/H] produce hotter stars at a given age.

When Serra & Trager (2007) studied the [Fe/H] of the galaxies that experienced a more complex SFH, they found that the SSP equivalent [Fe/H] will be more biased towards the [Fe/H] of the old stellar populations, depending on the mass fraction. This follows because the line indices that contain metals are dominated by the cooler and more metal-rich stars (these stars produce stronger metal lines). Hence, the mean [Fe/H] of an unresolved CSP will be biased towards the older stellar *or* metal-rich population. This referred metal-rich population refers to another stellar component as the population that determines the strength of the age-sensitive colours and indices.

Astronomers are currently not able to resolve the stars located in galaxies further than the local Universe. Following this, the studies of unresolved stellar populations are important because it contains the insights necessary to understand galaxy formation. One way to provide an empirical foundation, upon which a complete galaxy formation theory can be based, is to determine the SFR from the stellar populations by using the whole observed spectra of galaxies. Even with the continuous improvements made to telescopes, resolving the individual stars in the galaxies will be hard if not impossible.

2.8 Brightest Cluster Galaxies

The BCGs are called such because these galaxies are the brightest, most luminous and massive galaxies (De Lucia & Blaizot, 2007) to be found at or very near the centre of dense galaxy clusters (Liu et al. 2012). Katayama et al. (2003) stated that these galaxies have a mass of $\sim 10^{13} M_{\odot}$. These BCGs can also be described by a special sub-class, called cD galaxies (where 'cD' refers to centrally dominant), meaning that these galaxies have a rather diffuse and very large outer envelope (Dressler, 1984). An example of a cD galaxy can be found in Fig. (2.17).

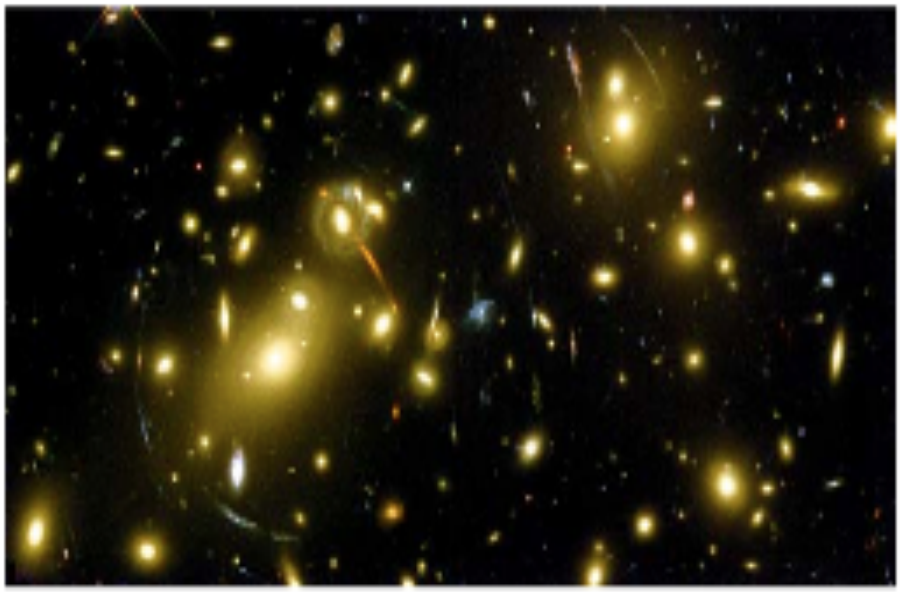

Figure 2.17: An example of a cD galaxy. The central galaxy in this cluster is called a supergiant cD galaxy, which is much brighter than all the other galaxies in the cluster. The image also shows a number of arcs which are the gravitationally lensed images of very distant background galaxies. Image courtesy of NASA, ESA AND THE SPACE TELESCOPE SCIENCE INSTITUTE.

The light distributions of BCGs can be described by the empirical Sèrsic formula (Sparke & Gallagher, 2007):

$$I(R) = I(0)\, exp\left[-(R/R_0)^{1/n}\right] \tag{2.7}$$

where $I(R)$ is the surface brightness, $I(0)$ the central surface brightness, R_0 the central radius and R the radius. When the parameter $n = 4$, the equation is called the *de Vaucouleurs surface brightness law ($R^{1/4}$)* and shown in Fig. (2.18). This law was first proposed in 1948 by Gèrard de Vaucouleurs to describe the light distribution of massive E galaxies. By rewriting Eq. (2.7) as

$$I(R) = I(Re)\, exp\left[-b\,(R/Re)^{1/n}\right] \tag{2.8}$$

where the constant b is chosen in such a way that the effective radius (Re) of the circle includes half of the light of the galaxy image.

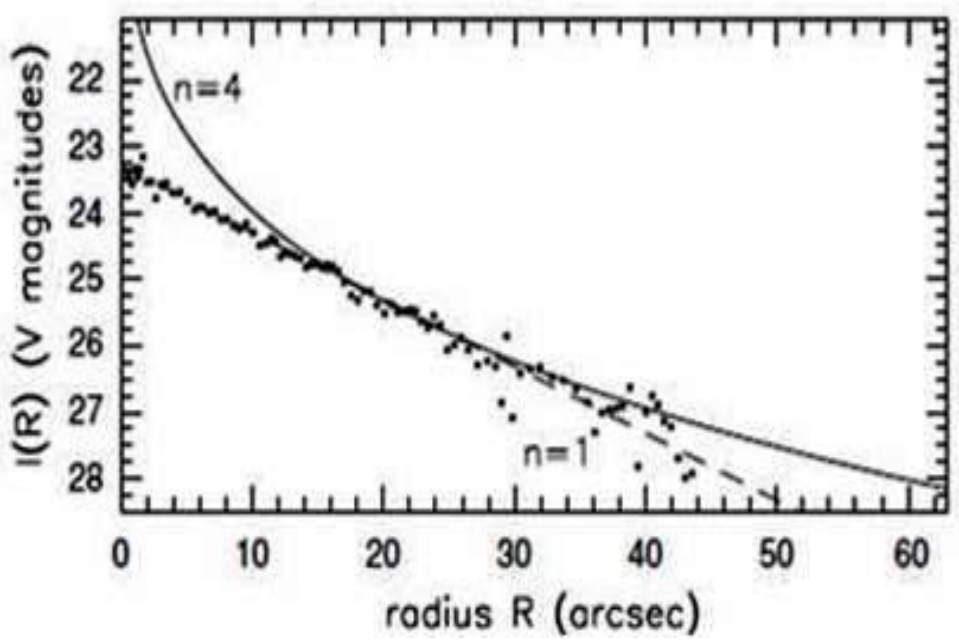

Figure 2.18: Shown here is From Eq. (2.7) where the dashed line represents $n = 1$ and $n = 4$ is represented by the solid line. When comparing the $R^{1/4}$ profile with the exponential it can be seen that $R^{1/4}$ has a higher luminosity at large radii. Figure taken from Sparke & Gallagher (2007).

Dubinski (1998) stated that BCGs have luminosities of $L \sim 10L_\star$ where $L_\star = 1.0 \times 10^{10} h^2 L_\odot$ (Schombert, 1986). In Kormendy (1989) it was stated that the de Vaucouleurs law provided a good approximation for the surface brightness of the centre of the galaxies, but at larger radii this law was no longer applicable to cD galaxies because the brightness was much higher than calculated with Eq. (2.7), meaning that this region is the extended envelope of light of the cD galaxies.

The unique properties of BCGs are influenced by the high mass of these galaxies and also by the cluster environments (Barrena et al. 2012). From Von der Linden et al. (2007) it followed that the special positions of BCGs in the cluster environments should be the cause for any of the properties that would make the distinguishing, between the BCGs and other galaxies easier. However, these distinctions are complicated due to the fact that BCGs form the dominant population at the high luminosity end of the galaxy luminosity function.

Fabian (1994) states that BCGs are located at the bottom of the gravitational potential well and are therefore, well aligned with the cluster galaxy distribution. The unique position of these galaxies points to the fact that the origin of BCGs are closely related to the formation of the host cluster because the stars have settled to the bottom of this well. Hence, these distinct properties of BCGs indicate that the formation and evolution of these galaxies are closely linked to the environments in which they are found (Brough et al. 2002). However, the mechanisms behind their formations are still not fully understood.

2.8.1 The BCG formation theories

One of the challenging problems faced in the research area of galaxy formation is the formation of massive BCGs at the centre of their host clusters. When standard galaxy formation models were viewed in the context of the Λ CDM cosmology, researchers found that the models were affected by the 'over-cooling problem' — massive galaxies are predicted to be brighter and bluer than the massive galaxies in the nearby Universe (Martizzi, Teyssier & Moore, 2012). A solution to this problem has been proposed and involves feedback processes from AGNs. Through theoretical analyses it was found that the accumulation of gas in the central regions of the clusters are prevented because these feedback processes provide enough energy to prevent gas accumulation and will therefore hinder any further star formation activities (Ciotti & Ostriker, 1997).

Currently, the most widely accepted galaxy formation theory among astronomers can be found in the Λ CDM cosmology (De Lucia & Blaizot, 2007). In a CDM dominated universe, the large-scale structures of the Universe will form hierarchically from the bottom–up through filamentary structure formations and the tidal forces may cause alignments between (a) galaxies and their host clusters; (b) clusters and super-clusters and; (c) clusters (Niederste-Ostholt et al. 2010).

In the next few subsections the proposed formation theories of BCGs, as given by Dubinski (1998) will be given and discussed in detail. These proposed formation theories are as follows:

Theory 1: Star formation, due to the *CFs* expected to be found in the dense, cool centres of X-ray clusters (Fabian, 1994).

Theory 2: Through a process called *galactic cannibalism* which is the accretion of existing galaxies through dynamical friction and tidal stripping (Ostriker & Tremaine, 1975; Ostriker & Hausman, 1977).

Theory 3: Merritt (1985) proposed another theory — primordial origin, also known as *galaxy merging*. This process took place in the early history of cluster formations (as predicted by the hierarchical cosmological models).

Theory 1: Cooling flows

The large structures, more specifically the clusters and galaxies observed in the Universe today were formed out of gas clouds, heated by the energy released during the initial gravitational collapse (Fabian, 1994). These gas clouds cooled through the emission of X-rays through the process of thermal bremsstrahlung (Peres et al. 1998). The density of the gas rises towards the centre of the clusters, which in turn increases the cooling rate of the gas, and therefore the cooling time (t_{cool}) of the gas decreases. Hence, an inward flow has to be established to support the weight of the overlying gas and to maintain the energy balance (Edge, Stewart & Fabian, 1992). This inward flow of gas is called a CF (Mo et al. 2010). Inward decreasing temperature gradients and shorter t_{cool} have been confirmed by observations done with the Chandra X-ray Observatory on clusters

containing CFs. These are features of CFs (Bîrzan et al. 2004). See Fig. (2.19) for an example of a CF observed with the Chandra X-ray Observatory.

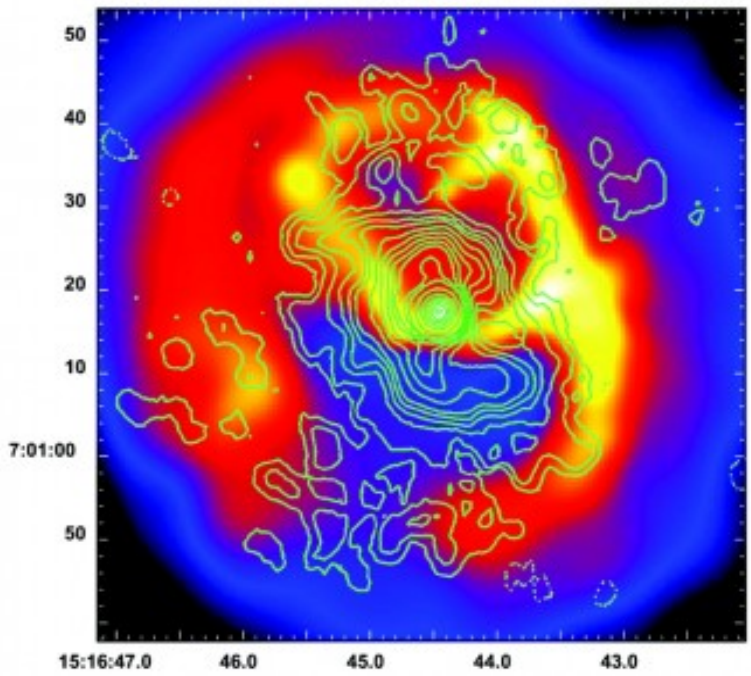

Figure 2.19: An example of a CF. The Chandra X-ray image of the core of the cluster Abell 2052 which contains a CF on which the contours of the radio emissions are superimposed. In the CF model, large amounts of gas in the intracluster medium are expected to cool radiatively and flow to the core of the cluster. But, the expected quantities of cool gas and the gas associated with the formation of stars are not seen and therefore called the CF problem. Image courtesy of PROF. ELIZABETH BLANTON, BOSTON UNIV.

These CFs present astronomers with a plausible formation theory since CF clusters have extremely high luminosities and large central galaxies, but the connection between the cooling of the X-ray emitting gas and the formation of the BCGs are still not clear. It was stated by Edwards et al. (2007) that BCGs are more frequently found in the centre of CF clusters. This implies that if the density in the cores of the clusters are high enough, then stars will form at the bottom of the gravitational well. The presence of blue cores and UV excess in some BCGs are taken as an indication of recent star formation (Liu et al. 2012). The tendency for BCGs to align with their host clusters, implies an origin coinciding with the collapse of the clusters and for that reason the evolution of BCGs follow that of their host clusters (Katayama et al. 2003).

The bottom of the gravitation well is also referred to as the bottom of the cluster's dark matter halo. Martizzi et al. (2012) state that stars will form at the bottom of dark matter haloes because (1) some of the stars formed when the first density clumps (at high redshifts) collapsed, which in turn indicated that these galaxies and therefore, also the dark matter haloes quickly virialized through rapid and violent mergers and eventually ended up in the centre of the clusters; (2) after

the formation of the clusters, stars may have accumulated through dynamical friction and mergers with other BCGs and; (3) cold gas is expected to collect at the bottom of the potential well, causing stars to form in situ.

From studies, for example conducted by Burns (1990), it was found that BCGs were most likely to host radio–loud AGNs than other galaxies with the same stellar mass (De Lucia & Borgani, 2012). AGN activities have been proposed as a solution for the CF problem (Best et al. 2007), more specifically causing only a moderate amount of the gas to cool down that will produce stars at the centre of the galaxy clusters despite the short cooling times derived from X-ray emissions. The radiative cooling times of gas found in the central regions of clusters are very shorter than the Hubble time and in the absence of a heat source, a CF is expected to form, causing the temperature in the central regions to decrease and this in turn triggers the gas to flow inwards at rates of $\sim 1000 M_{\odot}$ yr^{-1}. Best et al. (2007) indicated that some heating source has to be present to counteract the radiative cooling timescales of the gas (Von der Linden et al. 2007). Recent X-ray observations of CF clusters, done with the XMM-Newton and Chandra observatories indicated that the temperature at the cluster's centre does not fall below $\sim 30\%$ of the temperatures expected to be found in the outer regions at large radii and the amount of cooling gas are $\sim 10\%$ lower than that expected from classical CFs (this is also known as the CF problem). From this it is clear that some heating source has to be present to prevent the gas from cooling down further. Best et al. (2006) found that for elliptical galaxies, the time averaged heating was almost balanced by the radiative cooling losses from the hot haloes of these ellipticals. Thus, heating from a central AGN was found to play an important role in galaxy formation in order to reproduce the observed exponential cut-off at the high luminosity end of the galaxy luminosity function and to reproduce the old stellar populations of the most massive galaxies, i.e. ellipticals (De Lucia & Borgani, 2012).

For BCGs this picture is quite different: unless BCGs show a different mode of radio activity to that of ordinary ellipticals, then these activities cannot provide enough heating to balance the cooling of the gas in clusters and may therefore undergo more than one star formation epoch due to the presence of the cool gas. It clearly follows from this paragraph that both CFs and AGNs plays an important role in regulating the cooling rate of the gas in the centre of galaxy clusters (Loubser et al. 2008).

Theory 2: Galactic cannibalism

This theory was first proposed by Ostriker & Tremaine (1975) and further developed by Ostriker & Hausman (1977). The process called galactic cannibalism is the process through which a central galaxy is formed through the mergers/capturing of less massive objects (Loubser et al. 2008). This process was confirmed by Dubinski (1998) who found that by using a N–body simulation of galaxy clusters, that mergers would naturally produce a central galaxy resembling the surface brightness profile and velocity dispersion of a BCG. An example of galactic cannibalism is shown in Fig. (2.20).

Figure 2.20: An example of galactic cannibalism. A pair of interacting galaxies, called Arp 147, contain the remnants of a spiral galaxy (right) that is being merged with the elliptical galaxy (left). This produces an expanding wave of star formation that can clearly be seen in the blue ring that contains the new young stars. Image courtesy of NASA, ESA, M. LIVIO.

In a study conducted by De Lucia & Blaizot (2007) by using the Millennium simulations, they found that the stars in BCGs formed very early on in the formation of these galaxies (at $z \sim 5$ about 50% of the stars were already formed). By using numerical simulations, Gao et al. (2004) found that BCGs which were contained in clusters with redshifts higher than ~ 1, experienced a significant number of mergers. The nature of these mergers was dissipationless. Therefore, no new stars were formed during these mergers and the BCGs were expected to consist of only old stellar populations. This in turn implied that the monolithic approach failed to completely describe the SFHs of BCGs.

A disadvantage of this theory is that the luminosity expected from the matter accreted through mergers, does not match the luminosities of the BCGs given in the literature. This is due to the fact that the duration of the dynamical friction timescales are generally too long (Dubinski, 1998).

Theory 3: Galaxy merging

This theory is also called the primordial origin and was first proposed by Merritt (1983). An example of galaxy merging is shown in Fig. (2.21). Merritt (1983) found that there are three periods in the evolution of rich clusters when the merging of galaxies are the most significant:

(a) Very early on in the lifetime of galaxies, pairs of galaxies on the same trajectory or near–bound orbits will come together after just a few orbits.

(b) In the later stages of cluster formations, the slow moving galaxies will move to the centre of the clusters due to dynamical friction. Repeated mergers of galaxies in the core (due to the dense environment) will lead to the formation of supermassive objects in the centres of these clusters.

(c) In between these two periods, the velocities of the galaxies are too high for mergers to take place too frequently.

The failures of galactic cannibalism theory pointed to the fact that BCGs must have had an earlier origin than that determined through the dynamical friction timescales. A merger could therefore have taken place during the collapse of a cosmological hierarchy and will consequently present another formation theory (Dubinski, 1998). The hierarchical cosmological models specify that galaxies are formed through the mergers of smaller objects that are dragged into the centre of the clusters by dynamical frictions (De Lucia & Blaizot, 2007).

Figure 2.21: An example of galaxies in the process of merging. Two galaxies in the early stages of a cosmic collision form a stellar exclamation mark in a newly released picture that combines data from two NASA telescopes. Image courtesy of CXC/IFA/STScI/NRAO/NASA.

These different formation theories are a subject of debatability amongst astronomers due to the various advantages and disadvantages of the theories. What follows is a short summary of

each theory described in the order in which the theories were devised to describe the formation of BCGs:

1. *Firstly, it was thought that BCGs might have formed when the galaxies in the host cluster sank to the bottom of the potential well and then merged. This is referred to as galactic cannibalism. A few years after Ostriker & Tremaine (1975) developed this theory, Merritt (1985) found that tidal stripping reduced the mass of the clusters to such a degree that the timescales over which the dynamical friction took place were to long to be considered a viable formation theory.*

2. *The next theory: cooling flows, were developed parallel to the cannibalism theory. The gas at the centre of the clusters reached high densities and then cooled considerably to form an inward flow of gas and therefore form a CF. This theory implies that the stellar populations of BCGs should be young and blue, which is inconsistent with the red photometric colour of the BCGs, which in turn implies that the stellar populations are old.*

3. *The two theories previously described did not take any of the processes into account when clusters form through mergers. According to the hierarchical formation models, the BCGs are formed through the mergers of smaller galaxies dragged into the centre of the clusters through dynamical friction (Coccato et al. 2011). Dubinski (1998) found, by using N–body simulations, that a central, dominant galaxy form naturally through the mergers of massive galaxies when the clusters collapse along the filaments. The study conducted by De Lucia & Blaizot (2007) found that most of the stars contained in BCGs formed very early on in the SFHs of the BCGs and that mergers took place in the final stages of the BCG evolution where nearly all the gas was converted into stars. Hence, these mergers are dissipationless and no significant star formation is expected to take place in these BCGs.*

In the numerous studies referred to in this project, for example Dubinski (1998), Katayama et al. (2003), Von der Linden et al. (2007), Coccato et al. (2011), etc. it was found that the evolution of BCGs follow that of their host clusters. Niederste-Ostholt et al. (2010) concluded that a reason for the alignments between the BCGs and the host clusters could be due to the fact that the galaxies in the clusters are collapsing along the primordial filaments and merging during the formation of the clusters.

The formation histories of the massive ETGs, more specifically the BCGs located in host clusters and the role these cluster environments play in galaxy formation, are important but still not fully understood. It is difficult to find progenitors of these ETGs by means of direct observations and astronomers had to find alternative approaches to studying the SFHs of the large samples of nearby galaxies in terms of the ages and [Fe/H] of the stellar populations of BCGs.

CHAPTER 3

DATA ANALYSIS

"When in doubt, press *q*. And if all else fails, nuke it from space."

Remarked during a practical IRAF session - ISYA 2012
DR. STEVE CRAWFORD

3.1 Introduction

Astronomers found that they could decipher and analyse the physical conditions, composition and the motion of the remote Universe by enlisting the help of spectroscopic data from various astronomical bodies and sources (Koleva et al. 2009). In the past, a researcher needed to be an expert when trying to extract any useful information out of spectroscopic data, more specifically the identification and analysis of spectral signatures. This was because researchers were required to have an adequate understanding of the physical processes responsible for these signatures. With advancements made, for example in the sensitivity of telescopes and technology, it also required the various models used in the analysis of the vast amounts of data to become more automated and in certain cases more efficient.

The approach followed by some of these models is based on the idea that the observed spectroscopic data is compared with a collection of empirical libraries or models with known characteristics on a pixel-by-pixel basis (Koleva et al. 2009). These models are commonly used (1) for determining stellar population histories and; (2) in the analysis of stellar atmospheres. These approaches have been used in several automated spectral fitting routines analysing the (1) stellar population histories, for example Ocvirk et al. (2006, STECKMAP) and Tojeiro et al. (2007, VESPA) and; (2) stellar atmospheres, for example Katz et al. (1998, TGMET) and Recio-Blanco,

Bijaoui & de Laverny (2006, MATISSE). These models have both advantages and disadvantages, more specifically the main advantage is that the whole observed spectrum is used instead of picking specific features, while a disadvantage is that researchers lose the ability to find a direct link between the strength of a specific spectral feature and a physical characteristic.

3.2 Comparing models that implements indices and full spectral fitting

Before discussing the BCG sample as well as the methods used in the data analysis of the sample, it is useful to compare models that use spectrophotometric indices, i.e. the LICK indices that concentrates on the strengths of specific features against models that implement full spectral fitting, using all the information by fitting all the pixels.

Spectra classified as low or mid resolutions are used to measure spectrophotometric indices, i.e. the LICK indices (Worthey et al. 1994) and compare it against model predictions. The LICK indices measure the strength of certain spectral indices that is expected to trace the abundances of certain elements (Koleva et al. 2008) or correlate with the average age of the stellar populations. However, this approach should be handled with some care due to the fact that the spectrum of a galaxy is broadened by internal kinematics and therefore, the indices are defined at low resolutions and will be the results of the blending of many spectral lines and this causes the indices' response to the ages and [Fe/H] to be quite complex.

A few disadvantages of the LICK indices are that

- Only a few small passbands out of the whole observed spectrum is used;
- The indices are influenced by missing or bad pixels which are caused by detector defects or cosmic rays and;
- These indices are also affected by weak emission lines.

Full spectrum fitting models on the other hand use all the information present by using all the pixels, is insensitive to extinction or flux calibrations and it is not limited by the broadening of the galaxy spectrum. The full spectrum fitting method is three times more sensitive than the LICK indices, but still consistent when compared (Koleva et al. 2008).

Full spectrum fitting models use high resolution spectra because at low resolutions the spectral features will be weak and the models will rely on strong spectral features and therefore, use the same approach adopted by models that uses the LICK indices. At even lower resolutions, only the Balmer lines will be strong enough to provide sufficient information on the stellar populations. A disadvantage of the full spectrum fitting method, when compared to the LICK indices is that it is sensitive to the wavelength range and spectral resolution.

3.3 Description of the BCG Sample

The sample of galaxies analysed in this study is based on the sample of BCGs analysed by Loubser et al. (2008) (hereafter Paper 1). In this paper, they initially analysed galaxies classified as a subclass of BCGs, called cD galaxies, by using astronomical databases, for example, the NASA/IPAC Extragalactic Database (NED)[1] and literature. For a more detailed description of the methods used in identifying these cD galaxies, see Paper 1. Here, I note that I adopted the notation of Paper 1 by calling the sample of galaxies analysed in this project the BCG sample.

Due to discrepancies in the literature regarding the classification of cD galaxies, the galaxies analysed in this sample may not all be classified as cD galaxies. However, as described by Loubser et al. (2009b) (hereafter Paper 2) all the galaxies in this sample are the dominant galaxies which were located closest to the X-ray peaks in the centres of the respective clusters and thus for a small fraction, these galaxies might not strictly be the brightest galaxy in the cluster. I called these central cluster galaxies BCGs to concur with the recent definitions given in the literature, for example, De Lucia & Blaizot (2007).

Both Paper 1 & 2 contain a more detailed description of the BCG sample identification but in summary:

(i) *Paper 1* contained 41 BCGs, as classified by either NED (classified as cD galaxies in the morphological notes or in notes from previous observations) and/or have surface brightness profiles breaking the de Vaucouleurs $r^{\frac{1}{4}}$ law. In addition, two ordinary E galaxies, NGC 4946 and NGC 6047 were also included and observed with the same instrumental setup as the BCGs.

(ii) *Paper 2* contained eight additional BCGs observed on the Gemini South Telescope (GST) during July 2007 to January 2008.

Hence, this BCG sample contains a total of 51 galaxies as described in Papers 1 & 2. A complete list of the galaxies contained within the BCG sample with their host clusters are given in Table (3.1). This table also notes the telescopes used to observe these galaxies: the Gemini North Telescope (GNT), Gemini South Telescope and the William Herschel Telescope (WHT).

[1] `http://www.ipac.caltech.edu/`.

Table 3.1: The host clusters of all the 49 BCGs contained within the BCG sample and the two ordinary elliptical galaxies (indicated with a ✶). Columns 1 & 2 contain the galaxies and the host cluster in which they are located. Column 3 & 4 give the right ascension (RA) and the declination (DEC) of the galaxies. Column 5 gives the redshift (z) and Column 6 indicates whether the galaxy contained emission lines – a ✔ indicated yes and a ✘ no. Column 7 gives the velocity dispersion of the galaxy (σ_{BCG}) as given by Loubser et al. (2009b). Column 8 gives the names of the stars used in the line spread function and Column 9 gives the telescopes with which these galaxies were observed.

Object Name	**Cluster**	**RA** (hrs min sec)	**DEC** (deg min sec)	**Redshift** (z)	**Emission Lines**	σ_{BCG} (km s^{-1})	**Star**	**Telescope**
ESO146-028	RXCJ2228.8-6053	22 28 51.1	– 60 52 55	0.04119	✘	299	HD 004307	GST
ESO202-043	AS0479	04 37 47.6	– 51 25 23	0.03709	✘	256	HD 004307	GST
ESO303-005	RBS521	04 13 58.8	– 38 05 50	0.04981	✘	276	HD 004307	GST
ESO346-003	A S1065	22 49 22.0	– 37 28 20	0.02867	✘	226	HD 004307	GST
ESO349-010	A4059	23 57 00.7	– 34 45 33	0.04905	✔	282	HD 004307	GST
ESO444-046	A3558	13 27 56.9	– 31 29 44	0.04690	✘	292	HD 004307	GST
ESO488-027	A0548	05 48 38.5	– 25 28 44	0.03709	✘	248	HD 004307	GST
ESO541-013	A0133	01 02 41.8	– 21 52 55	0.05695	✘	295	HD 004307	GST
ESO552-020	CID 28	04 54 52.3	– 18 06 53	0.03140	✘	229	HD 004307	GST
GSC555700266	A1837	14 01 36.4	– 11 07 43	0.06912	✘	312	HD 004307	GST
IC1101	A2029	15 10 56.1	+ 05 44 41	0.07795	✘	378	HD 004307	GST
IC1633	A2877	01 09 55.6	– 45 55 52	0.02425	✘	400	HD 004307	GST
IC4765	AS0805	18 47 18.5	– 63 19 50	0.01503	✘	286	HD 004307	GST
IC5358	A4038	23 47 45.0	– 28 08 26	0.02884	✘	243	HD 004307	GST
Leda094683	A1809	13 53 06.4	+ 05 08 59	0.07883	✘	332	HD 004307	GST
MCG-02-12-039	A0496	04 33 37.8	– 13 15 40	0.03281	✔	271	HD 004307	GST
NGC 0533	A0189B	01 25 31.5	+ 01 45 33	0.00475	✘	299	HD 004307	GST
NGC 0541	A0194	01 25 44.3	– 01 22 46	0.01809	✔	246	HD 004307	GST
NGC 1399	FORNAX-A	03 38 29.0	– 35 26 58	0.00475	✘	371	HD 004307	GST
NGC 1713	CID 27	04 58 54.6	+ 00 29 20	0.01478	✔	251	HD 004307	GNT
NGC 2832	A0779	09 19 46.9	+ 33 44 59	0.02318	✘	364	HD 004307	GNT
NGC 3311	A1060	10 36 42.9	– 27 31 37	0.01198	✔	196	HD 004307	GST
NGC 3842	A1367	11 44 02.2	+ 19 56 59	0.02107	✘	287	HD 004307	WHT

Continued on Next Page . . .

Table 3.1 – Continued

Object Name	Cluster	RA (hrs min sec)	DEC (deg min sec)	Redshift (z)	Emission Lines	σ_{BCG} (km s^{-1})	Star	Telescope
NGC 4839	A1656	12 57 24.2	+ 27 29 54	0.02456	✘	278	HD 004307	GNT
NGC 4874	A1656	12 59 35.5	+ 27 57 36	0.02394	✔	267	HD 004307	WHT
NGC 4889	A1656	13 00 07.9	+ 27 58 41	0.02166	✘	380	HD 004307	WHT
NGC 4946 (✶)	A3526	13 05 29.4	– 43 35 28	0.01027	✔	201	HD 140283	GST
NGC 6034	A2151	16 03 32.1	+ 17 11 55	0.03388	✘	325	HD 004307	WHT
NGC 6047 (✶)	A2151	16 05 09.1	+ 17 43 48	0.03126	✘	230	HD 004307	WHT
NGC 6086	A2162	16 12 35.6	+ 29 29 06	0.03185	✘	318	HD 004307	GNT
NGC 6160	A2197	16 27 41.1	+ 40 55 37	0.03176	✘	266	HD 004307	GNT
NGC 6166	A2199	16 28 38.5	+ 39 33 04	0.03035	✔	310	HD 004307	WHT
NGC 6173	A2197	16 29 44.9	+ 40 48 42	0.02930	✔	304	HD 140283	GNT
NGC 6269	AWM5	16 57 58.1	+ 27 51 16	0.03480	✘	343	HD 140283	GNT
NGC 7012	AS0921	21 06 45.8	– 44 48 49	0.02935	✔	240	HD 140283	GST
NGC 7597	A2572	23 18 30.3	+ 18 41 20	0.03757	✘	264	HD 140283	GNT
NGC 7647	A2589	23 23 57.4	+ 16 46 38	0.04112	✘	271	HD 004307	WHT
NGC 7649	A2593	23 24 20.1	+ 14 38 49	0.04166	✔	250	HD 140283	GNT
NGC 7720	A2634	23 38 29.5	+ 27 01 51	0.03022	✔	409	HD 004307	WHT
NGC 7768	A2666	23 50 58.3	+ 27 08 51	0.02732	✘	272	HD 004307	WHT
PGC004072	A0151	01 08 50.8	– 15 24 31	0.05307	✘	313	HD 140283	GST
PGC025714	A0754	09 08 32.4	– 09 37 47	0.05480	✘	274	HD 140283	GST
PGC026269	A0780	09 18 05.7	– 12 05 44	0.05488	✘	222	HD 184406	GST
PGC030223	A0978	10 20 26.6	– 06 31 35	0.05425	✘	337	HD 184406	GST
PGC044257	A1644	12 57 11.4	– 17 24 36	0.04748	✔	247	HD 140283	GST
PGC071807	A2622	23 35 01.5	+ 27 22 20	0.06147	✘	315	HD 184406	GNT
PGC072804	A2670	23 54 13.7	– 10 25 09	0.07769	✘	311	HD 184406	GST
UGC00579	A0119	00 56 16.2	– 01 15 22	0.04446	✘	246	HD 069267	GST
UGC02232	A0376	02 46 03.9	+ 36 54 19	0.04858	✘	314	HD 069267	GNT
UGC05515	A0957	10 13 38.3	+ 00 55 32	0.04434	✘	362	HD 069267	GST
UGC10143	A2147	16 02 17.3	+ 15 58 28	0.03551	✘	262	HD 004307	WHT

3.4 Observations

Because the BCG sample studied in this project is based on the sample of galaxies compiled and analysed in both Papers 1 & 2, I shortly describe the instrumental setup used to obtain the high S/N ratio, long-slit spectra for the sample for completeness in §3.4.1 & 3.4.2. For a detailed description of the observational setup for the WHT and the GTs please refer to Paper 1.

3.4.1 Gemini observations

The GTs consists of two individual telescopes — the Northern and Southern telescopes which are two 8.1 m telescopes respectively located in Hawaii and Chile. These telescopes are shown in Fig. (3.1).

(a) The Northern Telescope. (b) The Southern Telescope.

Figure 3.1: Gemini Telescopes located in Hawaii and Chile. Credit: SCIENCE PHOTO LIBRARY.

During an extensive observational campaign, 15 of the galaxies were observed during August 2006 to January 2007, 18 galaxies were observed during February 2007 to August 2007 and the last eight galaxies were observed during July 2007 to January 2008, a total of 41 galaxies were observed out of the BCG sample (listed in Table (3.1)). The observations took place over the space of more than a year because the Gemini Multi-Object Spectrograph (GMOS) operates on queue scheduling, spans the whole night sky and was used to carry out these observations.

The dispersion was taken as 0.914 Å pixel^{-1} with a spatial scale of 0.146 arcsec pixel^{-1} (2 $\times$ 2 binning). The B600 grating was used with a resolution of 2.7 Å with a slit width of 0.5 arcsec. A full spectrum with a wavelength range of $(3700, 6500)$ Å was obtained by using three CCDs, which were mosaicked together and the spectral dithering was carried out for wavelengths at 5080 and 5120 Å (Loubser et al. 2009b). The spectra were centered at these wavelengths to avoid the loss of any important spectral features in the gaps left between the CCDs.

3.4.2 WHT observations

The 4.2 m WHT is located at the Observatoria del Roque de los Muchachos on the La Palma Island (part of the Canary Island chain) in Spain. This telescope is part of the Isaac Newton Group of Telescopes and is used for optical and near-infrared observations. This telescope is shown in Fig. (3.2).

Figure 3.2: William Hershel Telescope located on the La Palma Island in Spain. Credit: SCIENCE PHOTO LIBRARY.

During the observational period of 23 to 26 June 2006, the spectroscopic data of ten of the 51 galaxies were observed on this telescope. The WHT is equipped with the Intermediate dispersion Spectrograph and Imaging System (ISIS) double spectrograph mounted at the f/11 Cassegrain focus. This Cassegrain system is formed by a hyperboloidal secondary mirror, which is 1.0 m in diameter, made of Zerodur and has a 15 arcmin field of view (Boksenberg, 1985). Loubser et al. (2008) specified that the CCDs used on the WHT during these observations were the Marconi2 (mounted on the red arm) and the EEV12 (mounted on the blue arm). Each of these CCDs had a spatial range of 0.4 arcsec pixel^{-1} (2×2 binning) and a slit width of 1 arcsec was used.

During the four nights of observations, two different dichroics were used:

1. For the first three nights, the 5300 Å dichroic was used which gave a spectral range of $(3900, 5460)$ Å in the blue arm and $(5730, 6960)$ Å in the red arm.

2. For the last night, the 6100 Å dichroic was used which gave a spectral range of $(4500, 6120)$ Å in the blue arm and $(7950, 9600)$ Å in the red arm.

The dispersion of the blue arm was 0.90 Å pixel^{-1} with a grating of R600B, while the dispersion for the red arm was 0.88 Å pixel^{-1} with a grating of R600R. The resolution of the observed spectra depends on the dichroic and the arm used.

3.5 *ULySS* — A Short Overview

As already discussed in §3.1, some of these new spectral fitting packages enables researchers to fit the entire observed spectrum against a model. An example of such a package is called the *ULySS*[2] (Université de Lyon Spectroscopic analysis Software) package which is a stellar population synthesis code which can be used to determine (i) the stellar atmospheric parameters and; (ii) the star formation and metal enrichment history of galaxies.

ULySS was written in the Interactive Data Language (IDL) software because many of the required routines were already available as public libraries (Koleva et al. 2009). A future version of *ULySS* will most likely be written in Python. *ULySS* includes various algorithms and procedures, which enables the user to:

- Read data from FITS files;
- Define the number of components to fit against the observed spectra;
- Perform the fit and;
- Assess the relevance and reliability of solutions by constructing χ^2-maps and Monte–Carlo (MC) simulations.

This software has the advantage of (a) using all the pixels (weighted against their inverse squared estimated errors) and; (b) to minimize all the parameters at the same time which in turn provides the most significant solution despite the degeneracies that might exist between the parameters. An example of such a degeneracy is the well known age–metallicity degeneracy.

This software enables a full-spectrum fit for the study of stellar populations of galaxies and star clusters (Du et al. 2010). The entire observed spectrum of an object is fitted against a model that is expressed in the form of a linear combination of non-linear components. These components are given in the form of non-linear functions of age, [Fe/H], wavelengths and other parameters. Bouchard et al. (2010) explains that the models are combined with a line–of–sight velocity distribution (LOSVD) and multiplied with a polynomial to absorb the effects of flux calibrations errors and the Galactic extinction which may influence the shape of the spectra. By defining additional parameters, for example, the velocity dispersions, redshifts, the error spectra, and the wavelength ranges of the galaxies a more complex model could then be created to be used in the analysis of the BCG sample. A line spread function (LSF) is then injected into the models to match the resolutions of the observed spectrum with that of the models used (see §3.7.5 for more detail). The observed spectrum of an object is then compared to the model in the pixel space (Koleva et al. 2009) through a method of minimizing the χ^2-value, which is based on a grid of initial guesses.

[2] `http://ulyss.univ-lyon1.fr/`.

Koleva et al. (2008) compared the STECKMAP and *ULySS* software packages with each other and found that the STECKMAP code had a difficulty in providing a degree of confidence for a solution. This lead to the development of a parametric minimization method which in turn would simplify the understanding of the structure of the parametric space by constructing χ^2-maps and performing MC simulations which determines the influences, degeneracies and the errors of the parameters.

For the purpose of this study, the BCG sample was analysed by using the software package *ULySS*, which fitted SSP and CSP models against the observed spectra of the BCG sample.

3.6 Models incorporated in *ULySS*

The *ULySS* software contains a number of models with different stellar libraries. These models are described in detail on the official website of this software package — see §3.5 for more detail. Koleva et al. (2008) studied the various models included in the *ULySS* software and found that the Pegase.HR (P.HR) and Vazdekis/MILES (V/M) models were the most trustworthy and consistent of the models. What follows is a short description of the two independent models used in the analysis: the (1) P.HR and; (2) V/M models.

Before discussing the two stellar population models, it is worth mentioning a study conducted by Maraston & Strömbäck (2011), where they studied various high resolution stellar population models, which incorporated the MILES, STELIB, MARCS and ELODIE v3.1 stellar libraries. For the purpose of this dissertation I will only concentrate on the results they obtained with the MILES and ELODIE v3.1 stellar libraries. The methods applied during their study and comparisons will not be discussed in this dissertation, but a few remarks will be made in reference to their findings and conclusions of the flux calibrations and the temperature scales of the two libraries as well the influences the libraries had on the ages and [Fe/H] obtained through the SSP models.

3.6.1 Pegase.HR model

This model computes the synthetic evolutive optical spectra of galaxies with a very high resolution and incorporates the use of the stellar library ELODIE v3.1 (Prugniel et al. 2007b), which is based on the spectra of 1388 stars catalogued in the spectroscopic archive of the Observatoire de Haute–Provence (Moultaka et al. 2004). This library covers a wavelength range of about $(3892, 6800)$ Å. An updated version of this stellar library, called ELODIE v4.0 is being developed and will contain the spectra of about 5000 stars (Prugniel et al. 2007a).

Prugniel & Soubiran (2001) gave a detailed discussion of the ELODIE stellar library, more specifically the methods used in the flux calibration and data reduction. Le Borgne et al. (2004) state that the ELODIE v3.1 stellar library is incorporated into the P.HR model, which is then used

in the analysis of stellar populations of galaxies and stars.

This stellar library allows the components of the model to be expanded by defining the type of IMF, evolutionary track and SFR. Du et al. (2010) defined these isochrones as being solar scaled at various values of the total metallicity, Z. This stellar library is generated by the evolutionary tracks of 1994 Padova isochrones (Bertelli et al. 1994). This version of the stellar library computes the SSPs with the Salpeter IMF (Salpeter, 1955) with a mass of $0.1 \leqslant M_{\odot} \leqslant 120$ and a slope of -1.35. This model covers an age range of $(0.01, 20.000)$ Gyr and a [Fe/H] of $(-2.30, 0.69)$ dex.

Since the ELODIE library is wholly comprised out of archive spectra, rather than being part of a specific observational campaign, there were no standard stars observed. For the flux calibrations, Maraston & Strömbäck (2011) had to use the instrumental responses which were compared against other low and high resolution stellar libraries after which the spectra were then corrected accordingly. They found that at ~ 3900 Å (also called the blue limit of the ELODIE spectrograph), the efficiency of the instrument dropped by a factor of 50 and this in turn might compromise any attempted flux calibrations at the blue end of the spectra.

SSP models as function of the ELODIE v3.1 stellar library:

1. **The ages and [Fe/H] coverage:** Since the ELODIE library contains very hot O-type stars, the SSP models should generate very young stellar populations (around ~ 1 Myr) but the spectra of these young stars are reddened due to the influence of close-by dust and/or have the presence of several emission lines and hence, had to be excluded in the analysis of Maraston & Strömbäck (2011). This caused the age limit (at solar [Fe/H]) to be set at ~ 3 Myr and at half-solar [Fe/H] it is the shortage of hotter supergiants (with temperatures > 6000 K) that cause the age limit of the models to be very young.

   Maraston & Strömbäck (2011) found that even after the worst spectra were removed, that the youngest stellar population models were still influenced by the turn-off stars' dust reddening. At $\sim 1/100\,Z_{\odot}$, the sampling of the atmospheric parameters, i.e. the T_{eff} and log(g) gave a rather crude estimate and therefore, a caustic approach was needed when this library was incorporated into the stellar population models, more specifically a few ages could be modeled but a complete evolutionary coverage was lacking.

3.6.2 Vazdekis/MILES model

The V/M model contains the Medium-resolution Isaac Newton Telescope Library of Empirical Spectra (MILES) stellar library which is build up out of the spectra of 985 stars (Sánchez–Blázquez et al. 2006). This stellar library covers a wavelength range of $(3525, 7409)$ Å, an age range of $(0.063, 17.780)$ Gyr and a [Fe/H] range of $(-2.30, 0.20)$ dex.

This stellar library is generated by the evolutionary tracks of 2000 Padova isochrones (Girardi et al. 2000) and contains hot red giant branch stars (Du et al. 2010) but also covers a wide temperature range. The MILES stellar library also uses the Salpeter IMF (Salpeter, 1955) to determine the SSPs with a mass of $0.1 \leqslant M_{\odot} \leqslant 100$ and have a slope of -1.35.

Maraston & Strömbäck (2011) found that when several observations of the same stars were compared, that random root mean square errors affected the flux calibrations around ~ 0.013 mag for the (B-V) colour. When these results were compared against the Lausanne photometric database, they found a mean offset of ~ 0.015 mag for the (B-V) colour. Thus, for any combination of filters allowed by the wavelength range which the libraries have in common, the statistical significant offsets show the MILES stars to exhibit bluer colours. The flux calibrations $\sim$6500 Å is also complicated since this part of the spectra is left out of the quality check.

Another shortcoming of the MILES library, highlighted by the analysis of Maraston & Strömbäck (2011), is the chosen temperature scale of the library. The temperature scales, used in the different stellar population models, are different and hence, these scales may cause differences in the integrated stellar population spectra (generated with the different models) which will be hard to describe/explain, i.e. the near-IR flux drop of the MILES library around ~ 6000 Å is due to the adopted temperature scale of the RGB stars of the Padova tracks that is used in the model.

SSP models as function of the MILES stellar library:

1. **The ages and [Fe/H] coverage:** Maraston & Strömbäck (2011) state that the MILES library had a difficulty to model SSPs with young ages and low [Fe/H] (they used these SSPs to model the chemical evolution of the Milky Way). This is due to the fact that none of the libraries, used in their analysis contained any hot stars with low [Fe/H] and this in turn is because the star formation of the Milky Way takes place in the metal-rich disc. They also found that the atmospheric parameters at these low [Fe/H] are rather rough and the model should be used with some caution.

3.6.3 Shortcoming of the models: the $\alpha-$enhancement ratios

The tracers of SFHs of galaxies and stars can be established from the patterns of the chemical abundances contained within the spectra of these objects. The signatures of star formation are very sensitive to changes in the relative amounts of metals produced by Type II supernovae on short time-scale $(\sim 10^7 \text{yrs})$ and also on longer time-scales $(\text{a few} \times 10^9 \text{yrs})$ produced by Type Ia supernovae (Coelho et al. 2007). The ratio of these star formation time-scales is more commonly known as the $\alpha-$enhancement ([α/Fe]). The time-scales of the different types of supernovae in turn gives researchers more information about the duration of the star formation process. For example, any populations of stars that were formed before a Type Ia supernova explosion will be lacking in Fe but will have an abundance of $\alpha-$elements, i.e. oxygen and magnesium and will therefore have a

high [α/Fe] value.

Von der Linden et al. (2007) studied a group of BCGs (together with their host clusters) extracted from the Sloan Digital Sky Survey (SDSS). They found that the stellar populations of the galaxies (classified as BCGs and non-BCGs) were the same but that BCGs, on average had a higher $\alpha-$enhancement. This high $\alpha-$enhancement value indicates that star formation time-scales are shorter for BCGs than in elliptical galaxies. However, this cannot be taken as the only indicator of the star formation time-scales of these galaxies. The other aspects to be take into consideration are the cluster environments and the position of the BCGs in these clusters. The position of the BCG in the cluster is likely to influence the chemical abundance ratios (Loubser et al. 2009a).

High resolution spectroscopic data is needed to study the stellar contents of galaxies. For this purpose high resolution stellar population synthesis models, i.e. the P.HR and V/M models, have been developed to study SFHs, atmospheric parameters and the SEDs of galaxies. With the P.HR and V/M models the physical parameters, for example the ages and [Fe/H] of the stellar populations can be determined but these models have a disadvantage: the [α/Fe] have not yet been included in the algorithms used by these models. It is expected, that even if the [α/Fe] were determined together with the ages and [Fe/H] values, that the age and [Fe/H] values would slightly be changed by the [α/Fe] and it will not influence the number of SSP components which provide the most probable representation of the galaxies' SFHs.

Different methods have been taken by many authors, for example Thomas, Maraston & Bender (2003), to model the [α/Fe] and these values can be influenced by different choices of parameters (i.e. the IMF) included in the algorithms of the models. The detail of these methods are outside the scope of this project and therefore not discussed. It was only recently, more specifically November of 2011, that the models in the *ULySS* software were modified to take the $\alpha-$enhancements into account and so far only the P.HR model with the Elodie stellar library can be used to determine the [α/Fe]. This model is still in the preliminary testing phase and due to the time constraints of this project, I did not determine the $\alpha-$enhancements of the BCG sample but I will give a short summary of the methods employed by the developers.

The [α/Fe] was measured by comparing the Elodie spectra to the grid determined by Coelho et al. (2007) and then the χ^2-values were minimised to determine the best fit. The fits were only performed for $3500 < T_{eff} < 7000$ because of the limitations set by the grid. Prugniel & Koleva (2011) assumed that the remaining stars followed the abundance patterns of the nearby solar neighborhood. The Elodie stellar library was then taken as a reference point to determine the $\alpha-$enhancements in the other libraries by using the same full-spectrum fitting method employed by the *ULySS* software.

3.7 Method used in the Data Analysis

In the following section, I will describe the method followed in analysing the spectra of the BCG sample. First I will describe how the galaxies, which had a presence of weak emission lines, were reduced to separate the emission line contribution to the spectra of the galaxies. The subsections to follow will then be used to describe the additional parameters with which the models were elaborated on. The galaxy ESO146-028 will be used as an example throughout this section.

3.7.1 GANDALF

Absorption lines are used to study the chemical composition of galaxies or more specifically the chemical compositions of stellar populations, but emission lines create problems when studying these absorption lines. This is because the main absorption indices studied in stellar populations, i.e. Mg_b is affected by the $[N_I]\,\lambda\,5199$ emission line. Balmer lines on the other hand are weakened by emission lines and will therefore lead to older derived ages.

In the BCG sample there were 31 galaxies, which had no emission lines while the remaining ten galaxies showed the presence of weak emission lines (hereafter called emission galaxies).

The spectra of these emission galaxies were analysed with the Gas AND Absorption Line Fitting (GANDALF) routine (Sarzi et al. 2006) to accurately separate the stellar and emission line contributions to the observed spectra. The basic idea behind the routine is to treat the emission lines as additional Gaussian templates which linearly solves the amplitudes and finds the best combination of stellar templates at each step of the iteration. Each of these templates is then convolved by the most effective stellar LOSVD (for more details refer to Paper 2).

3.7.2 Wavelength range

The initial approach followed in determining the best wavelength range representation of all the galaxies in the sample, was to analyse each galaxy independently by comparing the two stellar population models (P.HR and V/M models) against the observed spectra of the galaxies without specifying the wavelength range. This approach is illustrated in Fig. (3.3) where the ESO146-028 galaxy is shown as an example. In this figure the spectrum of ESO146-028 was generated with both the P.HR and V/M models without restricting the wavelength range. This was done to investigate how the models and the observed spectra of the galaxies compared with each other, i.e. at which wavelength did the respective models deviate from the galaxy spectrum? By just looking at both Figs. (3.3a) and (3.3b), one can easily see that both the models deviated from the observed spectrum at ~ 5600 Å.

For the next analysis, a wavelength range of $(3800, 5600)$ Å was then enforced on the two models to test the sensitivity of the age and [Fe/H] results. For the results to be consistent, these values had to be comparable within the determined error margins. The results derived with the

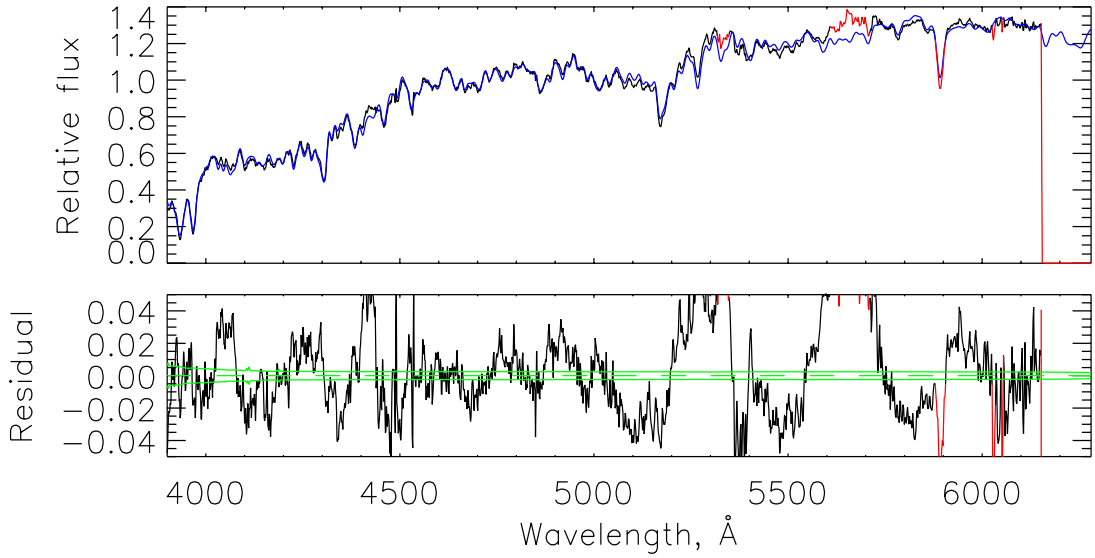

(a) P.HR model.

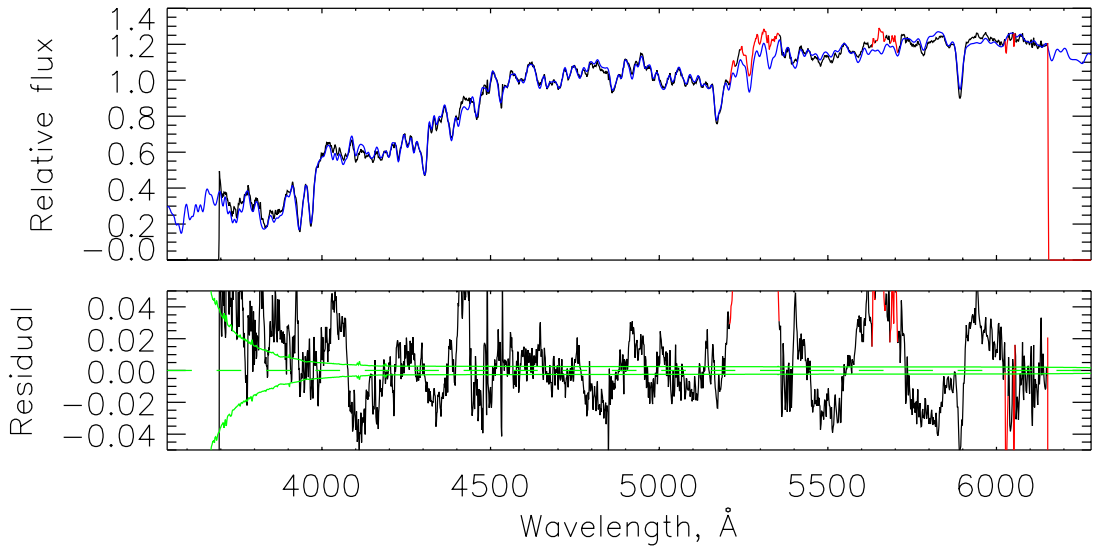

(b) V/M model.

Figure 3.3: Represented here is the spectrum of ESO146-028 as generated by the (a) P.HR and (b) V/M models without restricting the wavelength of the galaxy. The *top panel* of each figure shows the spectrum in black and the best fit is indicated in blue. The regions in red are the parts of the spectrum rejected by the model. The *bottom panels* indicate the residuals from the best fit. The continuous green lines mark the $\pm 1\sigma$ deviation, and the dashed green line is the mean residual value (zero–axis).

models with the wavelength range of $(3800, 5600)$ Å is shown in Table (3.2). On closer inspection of the table, one finds that the age and [Fe/H] values of the first components are not consistent (even with the errors taken into consideration) while the second components show more consistent and comparable results. Clearly this approach has shortcomings, i.e. the age and [Fe/H] values are not consistent and comparable. Apart from this, there is another shortcoming, that is the wavelength is too short to include the most important spectral indices (i.e. Fe5709 and Fe5782) used to accurately determine the age and [Fe/H] of SSPs (for more detail refer to §2.7). Therefore, a better wavelength range had to be found.

Table 3.2: Age and [Fe/H] values of ESO146-028, determined with the P.HR and V/M models with the wavelength range $(3800, 5600)$ Å.

	P.HR model		**V/M model**	
# SSP	**Age (Gyr)**	**[Fe/H] (dex)**	**Age (Gyr)**	**[Fe/H] (dex)**
1	0.572 ± 0.096	-1.458 ± 0.110	4.950 ± 1.978	-1.884 ± 0.218
2	16.411 ± 0.650	0.276 ± 0.008	16.259 ± 0.558	0.233 ± 0.021

A final factor that had to be taken into the wavelength consideration was the behavior of the models with the wavelength choice. As already discussed in §3.6, Maraston & Strömbäck (2011) found that the flux of the MILES stellar library dropped around ~ 6000 Å, due to the adopted temperature scale of the RGB stars of the Padova tracks that is used in this model. Due to the fact that both the P.HR and V/M models are used in the data analysis, it is important to choose a wavelength range that both these models have in common (see listed reason two below for more detail).

Taking all of the shortcomings of the different wavelength approaches into consideration, it follows that the best choice for the wavelength range is $(3800, 6000)$ *Å and the reasons for this are listed below:*

1. *This wavelength range includes the important spectral indices which are used to determine the ages and [Fe/H] of the SSPs. The spectral indices are listed in Table (2.2) and the implementation of the spectral indices is discussed in §2.7.*

2. *The P.HR model covers a wavelength range of around* $(3892, 6800)$ *Å, while the V/M model covers (3525, 7409) Å. Due to the fact that the flux of the V/M model drops* ~ 6000 *Å, the wavelength range (which will be used in the data analysis) had to be restricted to 6000 Å to avoid the drop to influence the reliability of the age and [Fe/H] values.*

3.7.3 Signal–to–noise ratio vs. error spectra

Incorporated into the *ULySS* software is the ULYSS algorithm that is used to analyse the observed spectra of galaxies. One of the important parameters that has to be specified for this algorithm is the S/N ratio. In this section I will firstly discuss the average S/N ratio, followed by the weighted averages in the S/N ratio (hereafter called the weighted S/N ratio) and then the error spectra will be discussed. Finally the S/N ratio of the galaxies will be compared against their error spectra and I will discuss which approach will be used in the further analysis.

Average S/N ratio

For the initial approach the average S/N ratio was used. This average S/N ratio was determined over the whole observed spectra of the respective galaxies. These S/N values (used in this initial approach) are given in Table (4.3) of Loubser (2009a), where the values were determined for the central aperture of each galaxy as measured in the H_β region.

Illustrated in Fig. (3.4) is the average S/N ratio of the ESO146-028 galaxy. The S/N value in the H_β region (indicated with the red lines) is 93 (follows from Loubser (2009a)). It can clearly be seen that the average S/N ratio change significantly over the extent of the wavelength range.

Setting the S/N value of the ULYSS algorithm to 93 (for this galaxy), it followed that the $\chi^2 = 6.103$. The χ^2-values are used to determine the most probable representation of the SFH of a galaxy, that is the most probable representation will have a χ^2-value close to one (see §3.9 for more information). By changing the S/N values of the galaxies, in order to get the χ^2-value as close to one as possible (therefore also obtaining the most probable representations of the SFHs), it followed that the χ^2-values were very sensitive to any changes in the S/N ratio. This approach was not valid since the S/N ratio of the respective galaxies could not be changed because it had to remain constant. Therefore a more precise method had to be devised to be used in the further analysis.

Weighted S/N ratio

The next step taken to devise a more precise method, was to determine whether the use of the weighted S/N ratio in the ULYSS algorithm would give a more probable SFH representation than when the average S/N value was implemented, that is whether the χ^2-value of the weighted S/N ratio was closer to one.

Listed below is the method that was followed to determine the weighted S/N ratio:

1. The weighted averages of the number of counts, present in the respective galaxies were determined.

2. Then the wavelength, where this weighted average occurred was determined.

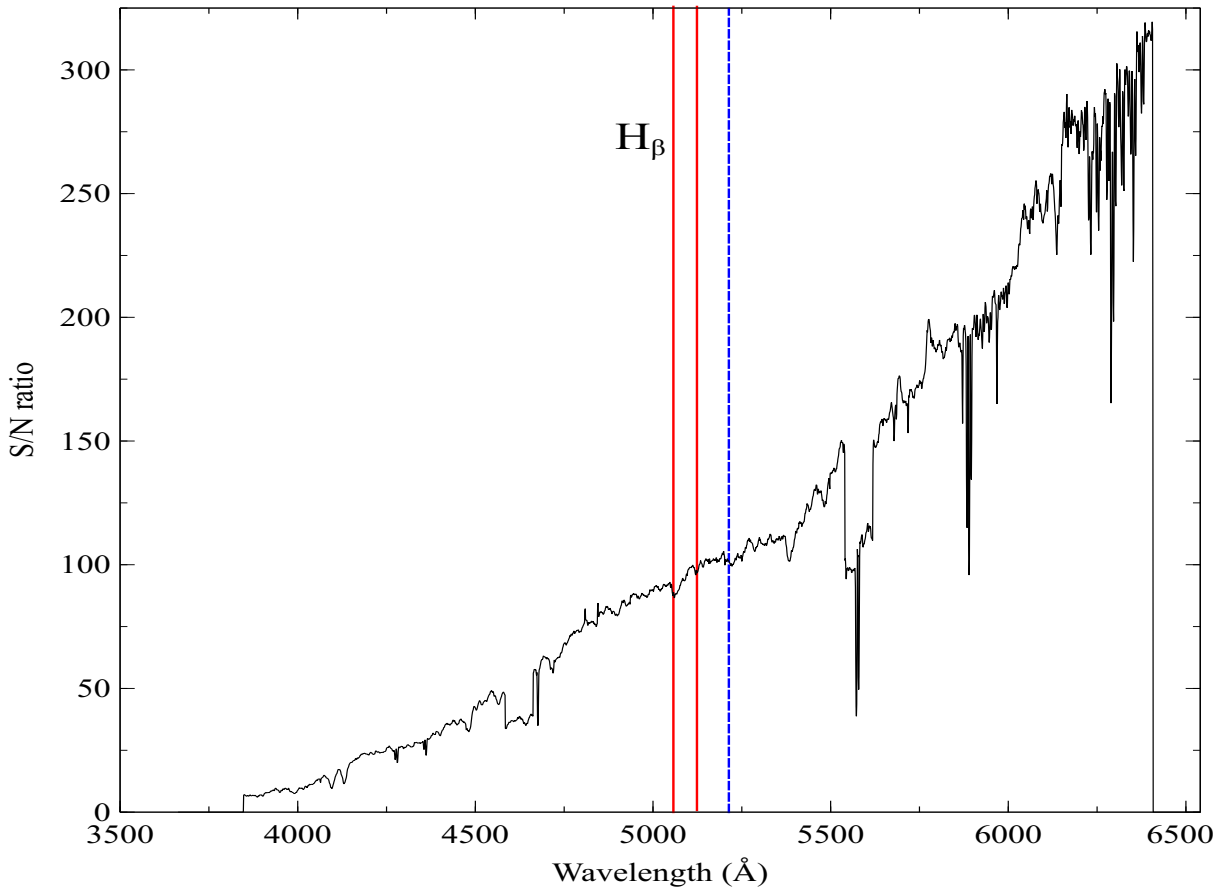

Figure 3.4: Illustrating the S/N ratio of the ESO146-028 galaxy. The average S/N value, determined in the H_β region is indicated with the red solid lines. The weighted S/N value is indicated with the blue dashed line.

3. Lastly the weighted S/N value at this wavelength was determined.

The galaxies were then analysed with both the average and weighted S/N ratios by using the ULYSS algorithm. The χ^2-values obtained through each of these analyses were then compared with each other to determine which S/N ratio provided the best fit, that is the S/N value which have an χ^2-value closest to one, will be used in the further data analysis. However, if the obtained χ^2-values did not differ too much from each other then the average S/N ratio (values given in Table (4.3) of Loubser (2009a)), could still be used.

The weighted average of ESO146-028 counts was found to be 3.50 and the wavelength where this average occurred was around $\sim$ 5399 Å (represented by the blue line in Fig. (3.4)). The weighted S/N value at this wavelength was 105. Lastly, the χ^2-values of the average and weighted S/N ratios are $\chi^2 = 6.103$ and 7.779 respectively. By comparing these χ^2-values, one can see that they are comparable but the use of the average S/N ratio (in the ULYSS algorithm) provided a better

representation of the SFHs because its χ^2-value was closest to one. From this it follows that the average S/N ratio, instead of the weighted S/N ratio would be used in the further data analysis. But as already stated, this approach has shortcomings and therefore, the error spectra of the galaxies were analysed as an alternative method.

More precise method: the error spectra

The last step taken to derive a more precise method to determine the SFHs of the galaxies was to determine whether the error spectrum or the average S/N ratio of the respective galaxies provided a more probable representation of the SFHs.

Fig. (3.5) illustrates the spectrum of the ESO146-028 galaxy, generated with the ULYSS algorithm (incorporated into the P.HR model) by using the (a) average S/N ratio and (b) error spectrum of the galaxy. Upon closer inspection of both the figures, it can be seen that the best fit model (blue line), generated by using the error spectrum, deviated less from the observed spectrum (black line) than best fit model generated with the average S/N ratio. This follows because when one looks at the wavelength range $(3800, 5050)$ Å, it can clearly be seen that the best fit model (generated by using both the average S/N ratio and the error spectrum) closely correlated with the observed spectrum. However, when looking at Fig. (3.5a) it can be seen that from $(5050, 6000)$ Å, the best fit model deviated from the observed spectrum, while the opposite was true for the same wavelength range in Fig. (3.5b), that is the best fit model correlated closely with the observed spectrum.

Therefore, the error spectra of the galaxies provided a better representation of the SFHs of the galaxies than when the average S/N ratio was used. Hence, the error spectra will be used in the further data analysis.

3.7.4 Velocity scale

The keyword *VELSCALE* is defined by *ULySS* to conserve the number of pixels. This number is related to the instrumental broadening (σ_{int}) of the telescopes used during the observations.

The σ_{int} of the telescopes were determined by the measuring the emission lines of the Copper-Argon (CuAr) arc spectrum and these lines were fitted against Gaussian functions from which the Full Width at Half Height (FWHF) were determined for the (a) GTs and; (b) WHT.

(a) The σ_{int} for the GTs, which used the GMOS CCD was determined to be 1.09 Å and this value was the same for both the North and South GTs.

(b) The σ_{int} for the WHT, which used the ISIS CCD was determined for the two different dichroics used during the observations.

- For the 5300 Å dichroic the values for the σ_{int} was 1.62 Å for the blue arm and 1.73 Å for the red arm.

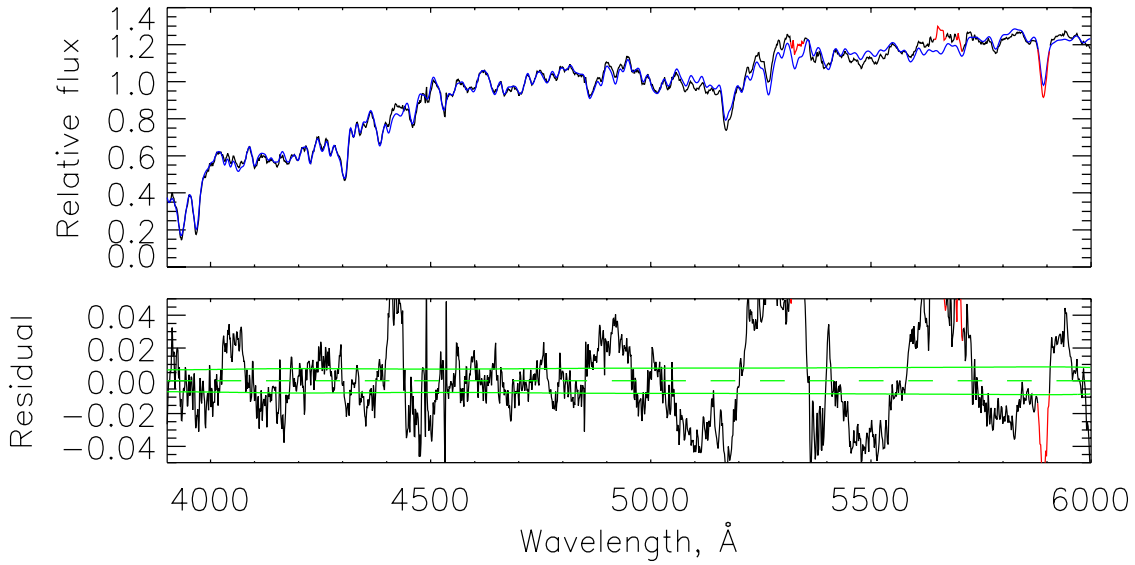

(a) Average S/N ratio.

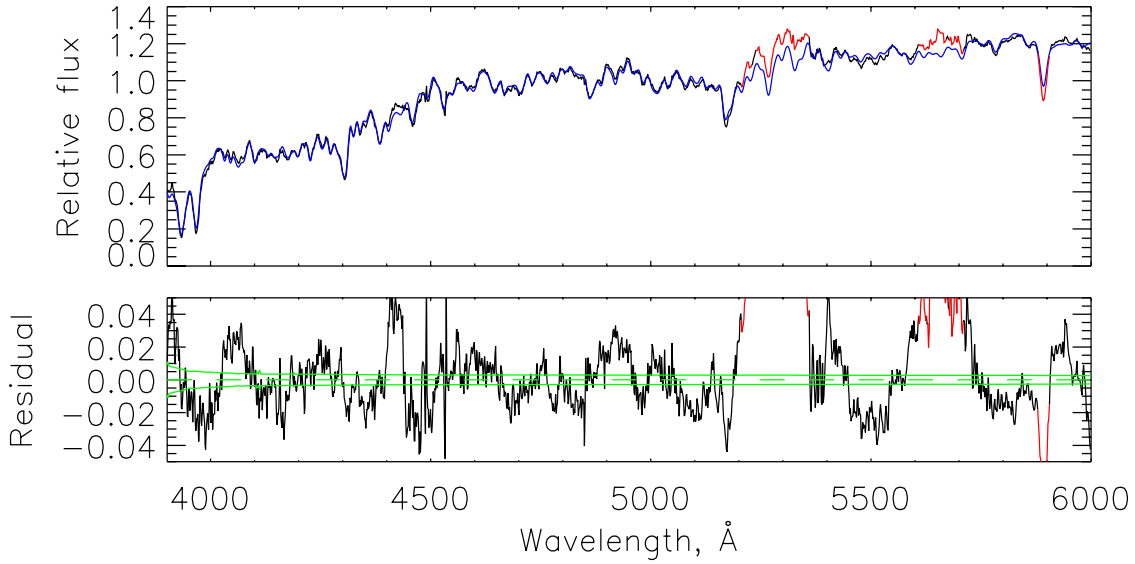

(b) Error spectrum.

Figure 3.5: Shown here is the spectrum of ESO146-028 generated by the P.HR model with the (a) average S/N ratio and (b) error spectrum. The spectrum is indicated in black and the best fit in blue. The regions in red are the parts of the spectrum rejected by the model.

- For the 6100 Å dichroic the values for the σ_{int} was 1.56 Å for the blue arm and 1.39 Å for the red arm.

For the WHT observations, I only considered the observations done with the 5300 Å dichroic because I was only interested in the red continuum of the observed spectrum.

The broadening of the galaxy spectra can be determined with the equation

$$VELSCALE \quad = (\Delta\lambda/\lambda) \times c \tag{3.1}$$

where λ is the observed wavelength in Å, $\Delta\lambda$ is the difference of the wavelengths in Å and c is the speed of light in km s^{-1}.

By using Eq. (3.1) the *VELSCALE* for the GTs was determined as follow:

$$\begin{aligned} VELSCALE &= (\Delta\lambda/\lambda) \times c \\ &= (1.09/3847) \times \left(3.00 \times 10^5 \text{ km s}^{-1}\right) \\ &= 85.00 \text{ km s}^{-1} \end{aligned} \tag{3.2}$$

And the *VELSCALE* for WHT was

$$\begin{aligned} VELSCALE &= (\Delta\lambda/\lambda) \times c \\ &= (1.73/5300) \times \left(3.00 \times 10^5 \text{ km s}^{-1}\right) \\ &= 97.92 \text{ km s}^{-1} \end{aligned} \tag{3.3}$$

3.7.5 Line spread function

For a model to be compared against the observed spectrum of a galaxy, the spectral resolutions of both have to match. This is accomplished by using the line spread function (LSF) which transforms either the resolution of the model to match that of the observed spectrum or the other way around. The LSF or the instrumental broadening (Du et al. 2010) is regarded by Koleva et al. (2009) as the spectral analog of the point spread function (PSF) for when images are considered. It is necessary to know the LSF to determine the additional broadening of the spectral features due to the velocity dispersion of the galaxy itself.

In practice, the LSF is responsible for the description of the flux wavelength distribution when an unresolved spectral line is analysed. It can therefore not always be described as being Gaussian but will vary with the wavelength and position in the long-slit spectroscopy (Du et al. 2010). Typically, the model has to have a higher resolution than that of the observed spectrum otherwise the high resolution characteristic contained within the internal kinematics of the spectra will not be analysed.

When comparing the spectral resolutions of the models against that of the observed spectra, one has to

1. Determine the relative LSF and;
2. Inject this relative LSF into the model.

Determining the LSF

The relative LSF will be determined between the observation spectrum and the model and can be considered to be a given constant for a certain observational setup or instruments. Koleva et al. (2009) state that it should be determined by using calibration observations. There are different ways in which the LSF can be determined, i.e. by using (i) arc spectra, (ii) twilight spectra and; (iii) spectra of standard stars.

(i) When using an **arc spectrum** for wavelength calibrations, the profiles of the lines can be determined at varying wavelengths and positions in the field. This option is currently not supported by *ULySS* but can be determined by using data reduction software, for example the Image Reduction and Analysis Facility (IRAF) package.

(ii) The method that uses **twilight spectra** is the preferred method when determining a LSF. In this method the twilight spectrum is compared against that of the solar spectrum that has the same LSF as the model used in the analysis.

(iii) When using the **spectra of standard stars**, the user has to make sure that these spectra have the same resolution as that of the model used. Here, either stars with known or unknown atmospheric parameters can be used. In the case of unknown parameters, *ULySS* can be used to determine these parameters.

For the data analysis of the BCG sample, the spectra of standard stars have been used to determine the relative LSF and Table (3.3) summarises the atmospheric parameters of the standard stars used in this determination. These stars were observed with the same instrumental configuration as the galaxies in the sample (see §3.4 for more detail) and were used as templates for the kinematic measurements of the galaxies for the LSF determination. The values for the T_{eff}, gravity (g) and [Fe/H], used in the expansion of the LSF, were taken from Worthey et al. (1994).

Table 3.3: The stars used in the determination of the LSF. Columns 1 & 2 respectively give the names of the stars and the effective temperature (T_{eff}) (measured in Kelvin (K)). Columns 3 & 4 give the gravity (Log g) and metallicity ([Fe/H]) of the stars. In the 2nd last column of Table (3.1), the stars are given with which the various LSFs were determined and also indicated with which stars the respective galaxies were analysed.

Star Name	**T_{eff} (K)**	**Log (g)**	**[Fe/H] (dex)**
HD 004307	5650	3.93	–0.52
HD 069267	4032	1.60	–0.36
HD 140283	5650	4.24	–2.45
HD 184406	4428	2.45	0.22

Injecting the LSF into a model

The relative LSFs were determined by comparing the composite spectra of the standard stars against that extracted from the P.HR and V/M models. The LSF was then injected into the P.HR model, for example, to create the resolution-matched P.HR model by using the LSF convulsion procedure included in the *ULySS* software. The resolution-matched P.HR model was then used in the further analysis of the spectra and I still called it the P.HR model. The same procedure was followed to generate the resolution–matched V/M model.

An example of a LSF analysis

As an example of the LSF analysis, I analysed the star HD 004307 with the method described under the two preceding headings. In Fig. (3.6) the relative LSF between the star and the ELODIE v3.1 stellar library is shown. It was determined by using the ULY_LSF procedure where the relative gaussian broadening and the velocity offset was determined by wavelength intervals of 600 Å and spaced by 300 Å. The change of the σ_{int} with wavelength is significant: from 50 to 86 km s^{-1} and this is due to the characteristics of the spectrograph and grating. The relative velocity (v) changes from 52.8 to 58 km s^{-1} due to the uncertainty in the wavelength calibration (Bouchard et al. 2010).

To determine the velocity dispersion, the observations and the stellar templates (observed with the same instrumental setup) had to be compared. Koleva et al. (2009) stated that the LSF underwent changes but the redshift of the nearby galaxies didn't have a large influence on the velocity dispersion while the shift in the LSF, due to the redshift, had a significant effect on the distant galaxies.

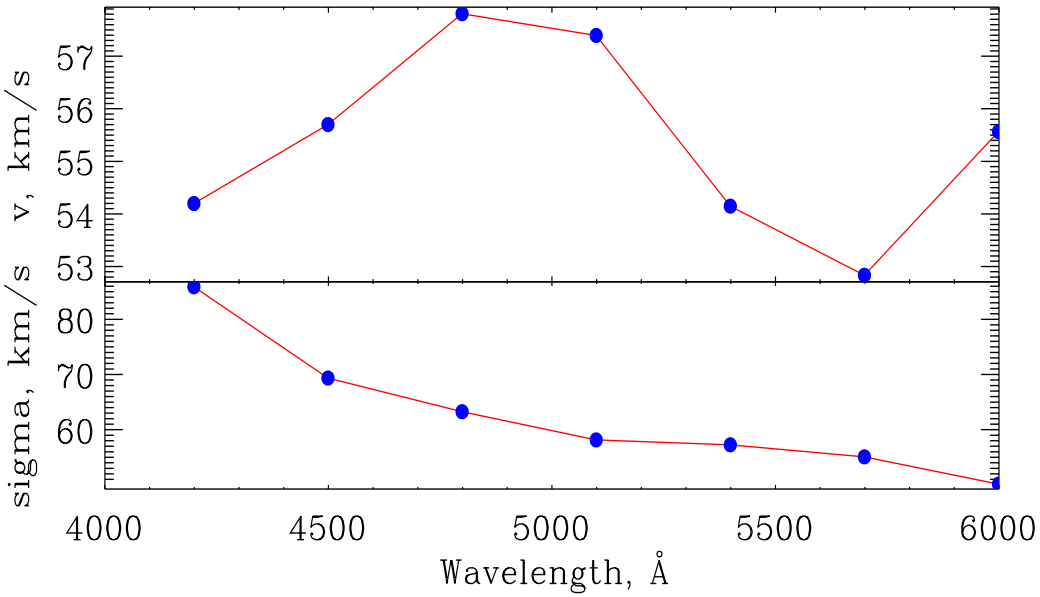

Figure 3.6: Relative LSF between HD 004307 and the stellar library ELODIE v3.1. The *top and bottom panels* illustrates the relative (v) and instrumental (σ_{int}) velocity dispersions. The blue dots indicates the measured LSF, while the red line represents the smoothed LSF used in the further analysis.

3.8 Construction of the Stellar Populations

In general, galaxies have rather complex SFHs and understanding the physics of the SFRs, as these galaxies evolve, form an important part of galaxy evolution research.

In this section the SFHs of the galaxies in the BCG sample will be reconstructed by using both the P.HR and V/M models as independent stellar population models. The SFHs will be determined through SSP–equivalent characteristics by using the full-spectrum fitting abilities of *ULySS*. This is accomplished by fitting the observed spectrum against a number of SSP components which is represented by the 'luminosity–weighted' period of the star formation (Du et al. 2010). Each of these SSP components are characterised by age and [Fe/H]. Future versions of the *ULySS* software package will include α–enhancements ([α/Fe]) while Prugniel et al. (2007a) stated that this parameter is currently only included in the semi–empirical models (see §3.6.3 for more detail).

3.8.1 Single Stellar Populations

The first step followed to determine the SFHs of individual galaxies, was to fit an SSP model against the observed spectrum of each galaxy. This is illustrated in Fig. (3.7) where the spectrum of the ESO146-028 galaxy was simulated with the P.HR model with a single star formation epoch.

The obtained SSPs characterises the stellar populations of these galaxies and therefore provides a general view of the SFHs of the galaxies.

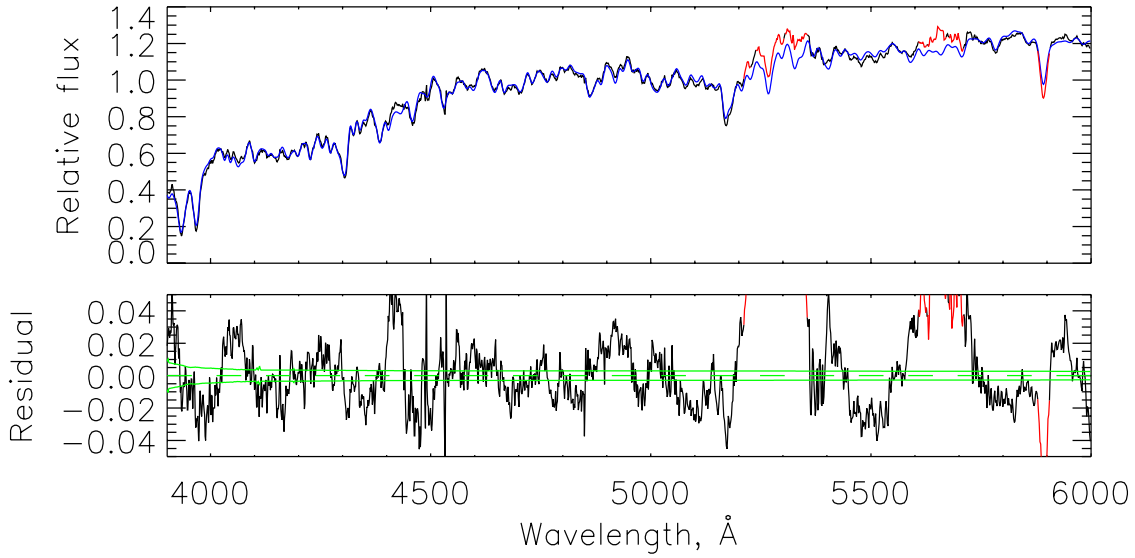

Figure 3.7: An example of an SSP of the ESO146-028 spectrum performed by *ULySS*. This fit was generated by the P.HR model with the ELODIE v3.1 stellar library. The *top panel* shows the spectrum in black and the best fit in blue. The regions in red are the parts of the spectrum rejected by the model. The *bottom panel* indicates the residuals from the best fit. The continuous green lines mark the $\pm 1\sigma$ deviation, and the dashed green line is the mean residual value (zero–axis).

The SSP fit illustrated in Fig. (3.7) indicated that the age and [Fe/H] are respectively given by (6.396 ± 0.018) Gyr and (0.190 ± 0.003) dex. The SSP components can be seen as the fitting boundaries imposed on the observed data to create the general SSP spectra to be fit against the whole observed spectra. This is done by using a single CSP that interpolates a grid of SSPs in terms of the ages and [Fe/H] (Koleva et al. 2009). The SSP method used is compatible with the 'luminosity–weighted' average over the whole distributions and from this the SFHs can then be deduced. The SSP is characterised by the age and [Fe/H] together with the errors on these values. The errors given are the standard deviation (1σ) on the average values of the age and [Fe/H]. These errors are determined by the MPFIT algorithm[3] which uses a covariance matrix to determine the best fit and the 1σ errors on the parameters (Koleva et al. 2009).

3.8.2 Composite Stellar Populations

It is sometimes found that for a given galaxy, an SSP cannot provide a satisfactory fit to the observed spectrum of the galaxy. This suggests that the SFH of the galaxy is more complex, that

[3] `http://cow.physics.wisc.edu/~craigm/idl/idl.html`

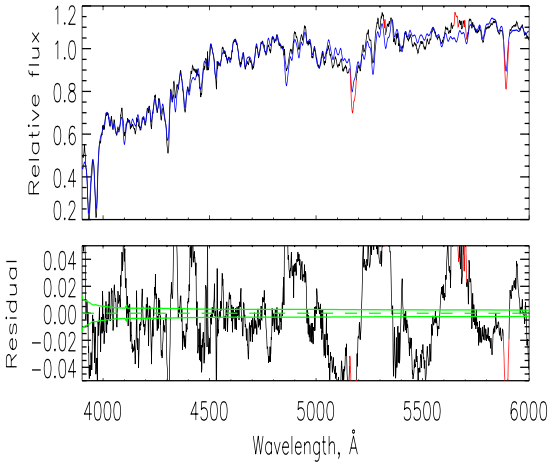

(a) First component.

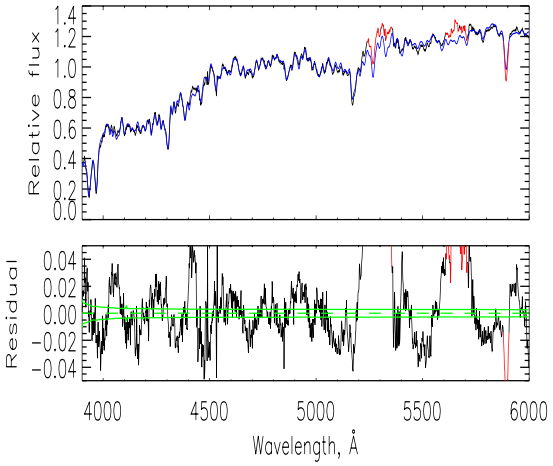

(b) Second component.

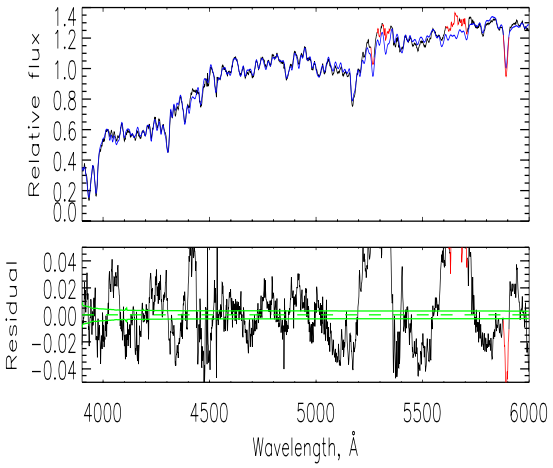

(c) Third component.

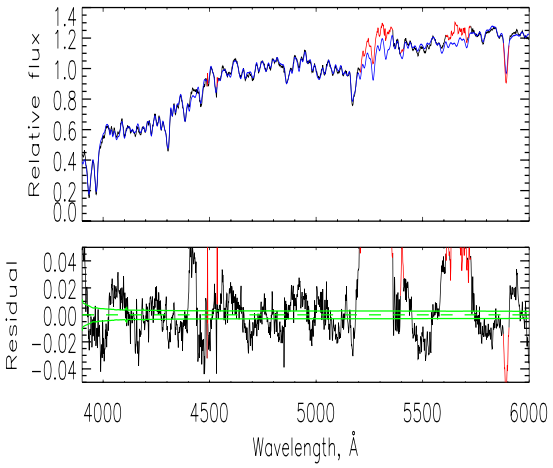

(d) An example of a CSP fit.

Figure 3.8: Shown here is an example of a CSP fit of the ESO146-028 spectrum performed by *ULySS*. This fit was generated by the P.HR model with the ELODIE v3.1 stellar library. Illustrated in (a) is the first component of the CSP fit, (b) is the second component, (c) is the third component and (d) is the composite fit of all three components. The *top panel* shows the spectrum in black and the best fit in blue. The regions in red are the parts of the spectrum rejected by the model. The *bottom panel* indicates the residuals from the best fit. The continuous green lines mark the $\pm 1\sigma$ deviation, and the dashed green line is the mean residual value (zero–axis).

is, the galaxy experienced more than one star formation epoch and hence, CSPs are used to represent the SFHs. CSPs can be described as a positive linear combination of many SSPs (Du et al. 2010). An example of a CSP fit is given in Fig. (3.8). This figure illustrates how the CSP fit is

constructed. For example, the first component (Fig. (3.8a)) have an age value of 0.5 Gyr, while the second component have an age value of 10 Gyr and is illustrated in Fig. (3.8b) and the third component is given in Fig. (3.8c) with an age value of 15 Gyr. The three components are combined by the ULYSS algorithm to form the CSP fit which is shown in Fig. (3.8d). It is these combined CSP fits that *ULySS* use in the SFH analysis of the respective galaxies if SSPs does not provide a satisfactory representation of the SFHs.

With the *ULySS* software package, the complex SFHs of galaxies can be reconstructed by using the CSP method but *ULySS* confines the star formation periods to two or four epochs (Koleva et al. 2009) because this technique creates instabilities due to the (i) degeneracies between the SSP components and; (ii) the finite resolution between the models and observations.

These degeneracies were overcome by starting with a simple physical assumption — the presence of an old stellar population (OSP) and then the time axis was divided into intervals by setting limits on two or more intervals. Therefore, the CSPs in this dissertation were studied in terms of three epochs: an OSP, an intermediate–age stellar population (ISP) and a young stellar population (YSP). The three epochs were chosen from the following three different boxes, which were generated by setting limits on the ages (Du et al. 2010) while no limits were imposed on the [Fe/H].

When using the P.HR model, the three boxes were chosen as follows: (i) For the OSP box: the age boundaries were fixed to $(12, 20)$ Gyr. (ii) For the ISP box: the age boundaries were fixed to $(4, 12)$ Gyr. (iii) For the YSP box: the age boundaries were fixed to $(0.01, 1.00)$ Gyr.

When using the V/M model, the three boxes were chosen as follows: (i) For the OSP box: the age boundaries were fixed to $(12.00, 17.78)$ Gyr. (ii) For the ISP box: the age boundaries were fixed to $(4, 12)$ Gyr. (iii) For the YSP box: the age boundaries were fixed to $(0.1, 1.0)$ Gyr. This was necessary because the upper and lower limits of the respective models are different.

Each of the galaxies in the sample were fitted against the three components and the optimal solutions were given in terms of the age, [Fe/H], light fraction (LF), mass fraction (MF) and the errors on these respective values. During the fits, the three boxes were suitable for the BCG sample, except for some galaxies that had results reaching to the boundaries of at least one of the three boxes. For these cases, the upper or lower age boundaries of the boxes were changed until the final results converged. This method is also justified by the fact that whenever four or more components were fitted the weights of the additional components were zero.

3.9 Checking the Reliability of the Solutions

The last step will be to check the reliability of the solutions determined by the respective models. This is necessary because of the degeneracies that might exist between the SSP components. The *ULySS* software includes techniques to determine the significance and reliability of the results, for

example convergence maps, MC simulations and χ^2-maps. In this section I will discuss how the MC simulations and the χ^2-maps have been used to check the reliability of the solutions.

3.9.1 The Monte–Carlo simulations

The MC simulations are used to (1) visualize the degeneracies for the solutions (Du et al. 2010) and; (2) to estimate the errors of the dependent parameters (Koleva et al. 2009).

The simulations are generated by a sequence of spectrum analyses, while random noise (equivalent to that of the observation noise) is added each time in order to determine the reliability of the results (Bouchard et al. 2010). The observation noise is different for each telescope because the noise is determined through the characteristics of the respective detectors used. Koleva et al. (2009) state that the noise have a Gaussian distribution that takes the correlations between the pixels into account. These correlations arise from the data reduction where the signal is resampled when the spectra are extracted and wavelength calibrated. The MC simulations use these ratios to determine a reliable estimation for the error.

Before I discuss the implemented method to generate the MC simulations, it has to be mentioned here that the error spectra of the galaxies were included into the MC simulations through the use of the ULYSS algorithm. This algorithm is discussed in §3.7.3 and this algorithm is used to analyse the spectrum of a galaxy by fitting stellar population models against the observed spectrum and incorporated the error spectra to select the most probable SFH of the galaxies.

During the study of the BCG sample, a series of 500 MC simulations were preformed to asses the reliability of the solutions and afterwards the number of MC simulations were increased to 2000 simulations as a means to test the sensitivity of the results. These simulations are shown in Fig. (3.9), while the mean age and [Fe/H] values (obtained from these simulations) indicated that the sensitivity of the results did no change when the number of simulations were increased. This follows from the fact that the obtained mean age and [Fe/H] values of the

- **500 MC** are (6.601 ± 0.034) Gyr and (0.209 ± 0.006) dex respectively.
- **2000 MC** are (6.601 ± 0.035) Gyr and (0.209 ± 0.006) dex respectively.

The errors on these mean values are the standard deviations. The reader may ask why the sensitivity of the results did not change, even though the number of MC simulations were increased? The answer lies in the *central limit theorem of statistics*. In layman's term, *this theorem states that given a sufficient large sample population with a finite level of variance, the mean of any sample from the same population will approximately be the same as the mean of the population.* Applied to the MC simulations, it follows that by increasing the number of MC simulations, the sample/population was increased and through the central limit theorem we know that the mean age and [Fe/H] values of the 500 and 2000 MC simulations have to be the same.

Therefore, although the simulations were increased from 500 to 2000, the sensitivity of the results did not change and it also followed that the 2000 MC simulations were too time consuming in terms of computing resources. Hence, 500 MC simulations were used during the analysis of the BCG sample to check the residual of the fits and assess the relevance of the solutions, aiding the selection of the most probable SFHs of the BCGs.

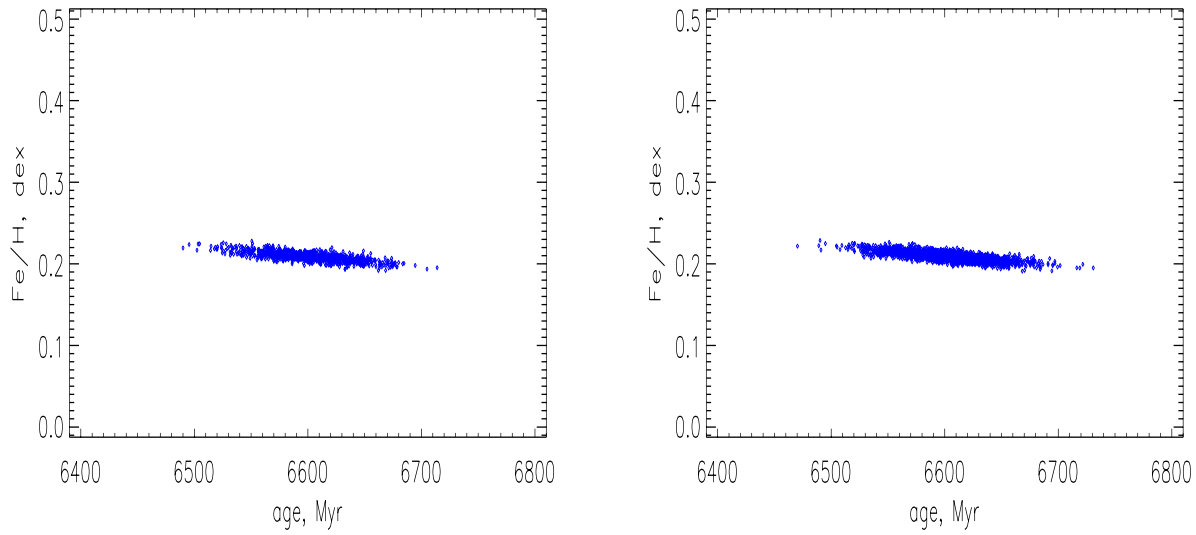

(a) 500 MC simulations.

(b) 2000 MC simulations.

Figure 3.9: Blue dots represent the result of the 500 and 2000 MC simulations, constructed during the analysis of ESO146-028.

3.9.2 The χ^2-maps

Pearson (1900) was the first to put emphasis on the χ^2-test as a fundamental cornerstone of modern statistical analysis, more specifically in astronomy. Consider observational data that can be binned and a hypothetical model, which is used to predict the behavior of the population in each bin. The χ^2-statistic is then used as a measure to describe the goodness of the fit of the hypothetical model against the data (Wall & Jenkins, 2003).

In the *ULySS* software package, the χ^2-maps are the end result of the MC simulations – these maps are used to visualize the degeneracies between the parameters and to reveal the presence of the local minima (Koleva et al. 2009). Koleva et al. (2009) state that these χ^2-maps are based on a grid of initial guesses and then a global minimization is performed. The convergence maps are then used to evaluate the region where the parameter space converges to the absolute minimum of the χ^2. The χ^2-maps are then constructed by choosing a grid of intersecting lines in a two dimensional projection of the parameter space (for example the [Fe/H] and age), while each intersecting

point is minimized. The local minima will be shown on the map, provided that the grid is fine enough. These maps were constructed using the ULY_CHIMAP algorithm.

The topology of the χ^2-maps will differ for when the SFHs are represented by SSPs or CSPs:

1. For the SSPs, the topology of the maps will indicate the dependencies between the parameters and indicate the local minimum. An example of a χ^2-map for an SSP fit is shown in Fig. (3.10a) where NGC 7597 was analysed. From the figure it can be seen that the map is regular, with weak dependences (indicated with the blue lines) between the parameters and a single minimum.

2. When galaxies have more complex SFHs, the CSP fits are used. Fig. (3.10b) shows an example of the χ^2-map of the CSP fit of the ESO146-028 galaxy. For CSPs, the maps will only show the local minima.

Hence, the χ^2-statistical test was used to select the most probable fit for the SFHs, more specifically whether the SFHs of the galaxies could better be presented by an SSP or a CSP fit. This was accomplished by comparing the χ^2-values of each fit, i.e. the fit with a χ^2-value closest to one gave the most probable representation of the galaxy's SFH. After this, the χ^2-maps were drawn to assist in understanding the structure of the parameter space.

3.10 Gemini vs. WHT galaxies

As already described in §3.4, the wavelength ranges of the telescopes, i.e. the WHT and GTs, used during the observations were very different.

A test was conducted on a small subsample of galaxies in the BCG sample that were observed with the different telescopes and therefore, the wavelengths used during the observations were different. The aim of this comparison was to determine whether the age and [Fe/H] values gave any indication of consistency if the wavelengths varied during the observations. The subsample used is shown in Table (3.4) and it contains a few non-emission galaxies which have an SSP representation of the SFHs. Initially these galaxies were analysed with the varying wavelengths as shown in Table (3.4). These wavelengths were chosen to include the best fit between the models and the observed spectra (see §3.7.2 for an explanation on what is meant with the best fit). When the galaxies in the subsample were analysed with these varying wavelengths, it was found that the results (shown in Columns 2 & 3 of Tables (3.5a) & (3.5b) varied due to the fact that some of these wavelengths did not include the most important spectral indices used for the determination of the SSP's age and [Fe/H] (see §2.7 for a more detailed discussion on these indices). All the galaxies in the subsample were then analysed with a wavelength range of $(3800, 5100)$ Å because this was the wavelength range used in the analysis of the WHT galaxies. The analysis with $(3800, 5100)$ Å was done to determine whether the values of the derived parameters of the GTs and WHT galaxies showed any consistency when compared.

Table 3.4: The wavelength range of a subsample of the BCG sample used in the comparison test between the galaxies observed with the GTs & WHT. Column 1 gives the names of the galaxies and Column 2 gives the wavelength ranges which included the best fit.

Object Name	**Wavelength range (Å)**
ESO303-005	(3800, 5500)
ESO488-027	(3800, 5700)
IC1633	(3800, 5500)
NGC 2832	(3800, 6000)
NGC 4839	(3800, 6000)
PGC004072	(3800, 5300)
PGC026269	(3800, 5300)

The age and [Fe/H] values, determined with the $(3800, 5100)$ Å wavelength range are shown in Columns 4 & 5 of Tables (3.5a) & (3.5b). The values, determined with the old and new wavelengths were then subtracted from each other to determine whether the differences were larger than the errors. If this was the case then there were no noticeable difference between the ages and [Fe/H] of the galaxies observed with the GTs and WHT. When looking at Columns 6 & 7 it can be seen that this was not the case for the subsample analysis. When analysing the tables in detail, it followed from Table (3.5a) that the ages, determined with the modified wavelength, were not a precise representation of the age range of the BCG sample because all the galaxies were almost the same age and in terms of galaxy evolution, very young. This was also due to the fact that the $(3800, 5100)$ Å wavelength did not include the important spectral indices (used to determine the ages and [Fe/H] of an SSP), i.e. Mg_b and Fe5270 in the red continuum of the spectrum. From Table (2.2) it follows that if the red continuum of the spectrum were analysed, then the important Balmer lines would not be included within this wavelength range. Refer to §2.7 for a more detailed discussion on how these spectral indices are used in the determination of the ages and [Fe/H]. Hence, from this test and with good motivation, only the galaxies observed with the GTs will be used in any future analysis. The new BCG sample now consisted of 41 galaxies, that is 40 BCGs and one elliptical galaxy.

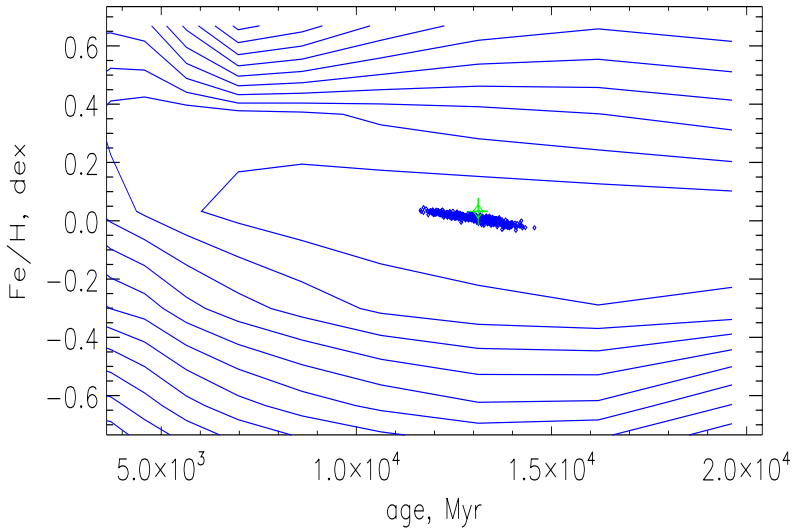

(a) Example of a χ^2-map for an SSP fit. The galaxy analysed is NGC 7597 and the degeneracies between the parameters are indicated with the blue lines and the local minimum with the green cross.

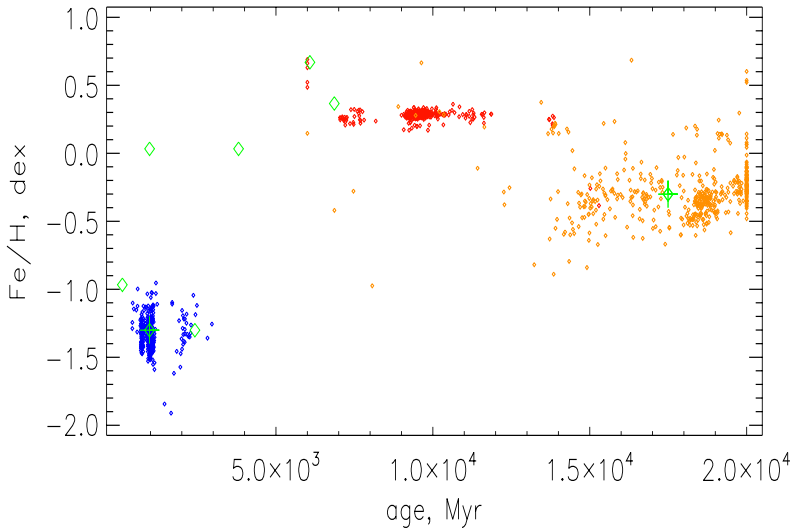

(b) Example of a χ^2-map for a CSP fit. The galaxy analysed is ESO146-028, which has a complex SFH that can be represented by three SSPs. The YSP, ISP and OSP are respectively indicated by the blue, red and orange dots while the local minima are indicated by the green crosses. The diamond symbols indicate other possible solutions for the local minima but the optimal value for the local minimum is indicated by the cross.

Figure 3.10: Example of χ^2-maps, drawn for an SSP and a CSP fit.

Table 3.5a: The ages of the subsample determined by the P.HR and V/M models in Gyr. Column 1 gives the names of the galaxies, Columns 2 & 3 give the ages of the galaxies determined with the original wavelength while Columns 4 & 5 give the ages of the galaxies determined with the modified wavelength. Columns 6 & 7 give the deviation in the age values between the original and modified wavelengths.

Object Name	**Original P.HR value**	**Original V/M value**	**Modified P.HR value**	**Modified V/M value**	**Age deviation P.HR value**	**Age deviation V/M value**
ESO303-005	14.746 ± 0.540	6.557 ± 0.037	6.395 ± 0.041	6.530 ± 0.053	8.352 ± 0.542	0.027 ± 0.065
ESO488-027	9.582 ± 0.158	10.994 ± 0.037	4.910 ± 0.127	5.795 ± 0.436	4.672 ± 0.203	5.199 ± 0.437
IC1633	6.078 ± 0.054	10.000 ± 0.000	6.088 ± 0.056	6.501 ± 0.031	0.010 ± 0.078	3.499 ± 0.031
NGC 2832	12.969 ± 0.294	15.789 ± 1.090	6.129 ± 0.044	6.540 ± 0.032	6.840 ± 0.297	9.249 ± 1.090
NGC 4839	16.152 ± 0.120	16.403 ± 0.305	6.294 ± 0.045	6.513 ± 0.049	9.858 ± 0.129	9.890 ± 0.309
PGC004072	6.401 ± 0.041	6.587 ± 0.036	6.405 ± 0.040	6.567 ± 0.046	0.004 ± 0.057	0.020 ± 0.058
PGC026269	2.768 ± 0.028	2.351 ± 0.020	2.440 ± 0.019	2.573 ± 0.020	0.328 ± 0.034	0.222 ± 0.028

Table 3.5b: The [Fe/H] of the subsample determined by the P.HR and V/M models in dex. Column 1 gives the names of the galaxies, Columns 2 & 3 give the [Fe/H] of the galaxies determined with the original wavelength while Columns 4 & 5 give the [Fe/H] of the galaxies determined with the modified wavelength. Columns 6 & 7 give the deviation in the [Fe/H] values between the original and modified wavelengths.

Object Name	**Original P.HR value**	**Original V/M value**	**Modified P.HR value**	**Modified V/M value**	**[Fe/H] deviation P.HR value**	**[Fe/H] deviation V/M value**
ESO303-005	0.006 ± 0.007	0.197 ± 0.006	0.176 ± 0.006	0.172 ± 0.009	0.169 ± 0.009	0.027 ± 0.011
ESO488-027	0.423 ± 0.003	0.135 ± 0.003	0.214 ± 0.008	0.175 ± 0.018	0.209 ± 0.009	0.039 ± 0.018
IC1633	0.350 ± 0.007	0.128 ± 0.003	0.361 ± 0.007	0.206 ± 0.006	0.010 ± 0.009	0.078 ± 0.006
NGC 2832	0.436 ± 0.003	0.166 ± 0.005	0.348 ± 0.006	0.217 ± 0.006	0.088 ± 0.006	0.051 ± 0.008
NGC 4839	0.258 ± 0.006	0.177 ± 0.005	0.150 ± 0.006	0.156 ± 0.006	0.108 ± 0.008	0.021 ± 0.008
PGC004072	0.195 ± 0.008	0.200 ± 0.006	0.200 ± 0.007	0.166 ± 0.006	0.005 ± 0.011	0.033 ± 0.008
PGC026269	-0.073 ± 0.012	-0.001 ± 0.008	-0.014 ± 0.010	-0.026 ± 0.013	-0.059 ± 0.016	0.025 ± 0.015

CHAPTER 4

RESULTS AND DISCUSSION

"The more we kill, the better we feel."

Referring to another data reduction session successfully finished - ISYA 2012
PATRICIA SKELTON

4.1 Introduction

In this chapter the results obtained during the data analysis of the BCG sample will be given and discussed. In §4.2, the galaxy excluded from the analysis will be discussed as well as the reason why it was excluded. In §4.3 the SFHs of the galaxies in the BCG sample, determined with both the P.HR and V/M models will be given and discussed. In §4.4 a short test was conducted to determine which stellar population model gave the most probable representation of the galaxies' SFHs. In §4.5, the SSP equivalent derived ages and [Fe/H] are given and analysed in detail. The comparisons with the Lick indices will be discussed in §4.6. The CFs and possible connections of theses flows to star formation will be discussed in §4.7. Lastly, the comparison with the environment properties will be discussed in §4.8.

The graphs referred to in this chapter can be found in Appendix A.

4.2 Exclusions from Analysis

The galaxy NGC 6173 was excluded from any future analysis because both the P.HR and V/M models provided a visibly poor fit to the observed spectrum. This was concluded from Fig. (4.1)

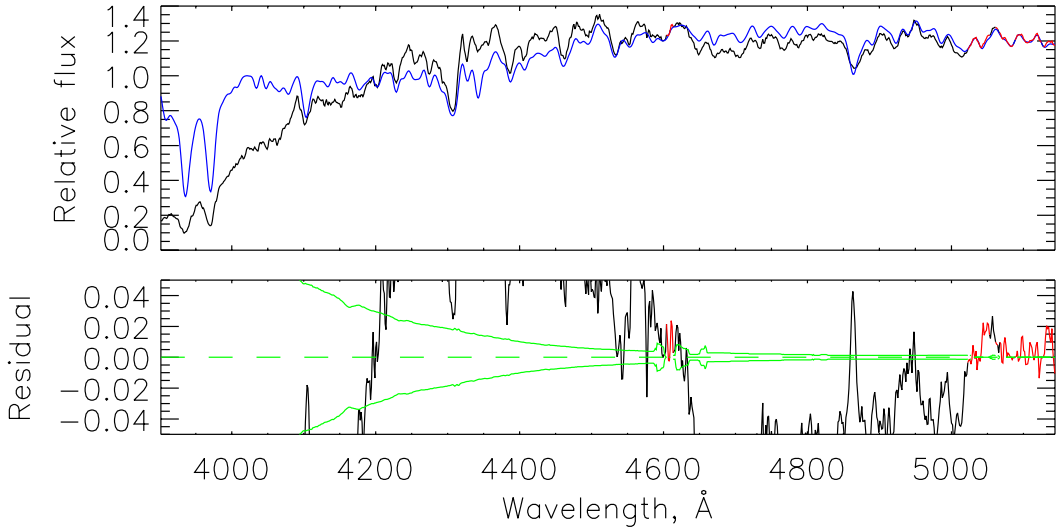

(a) P.HR model.

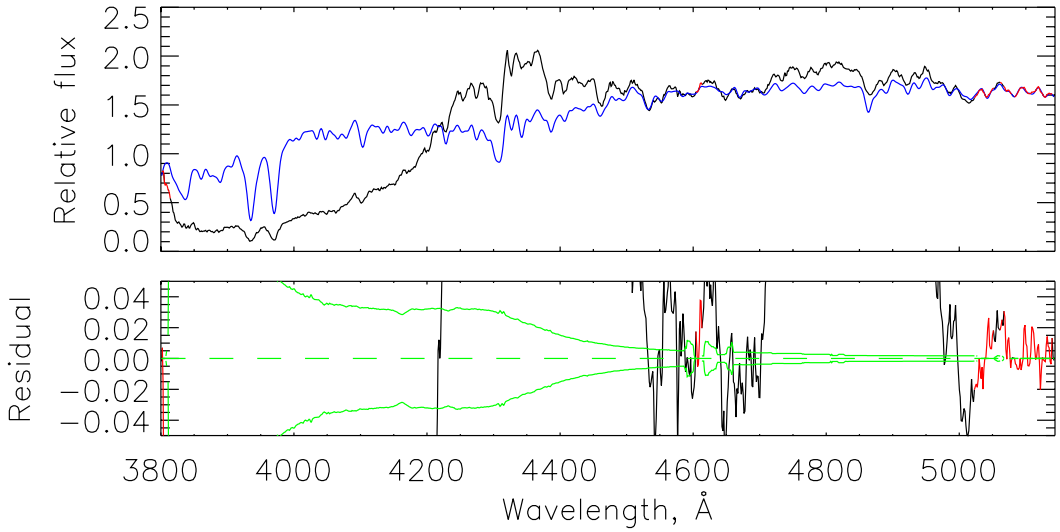

(b) V/M model.

Figure 4.1: The P.HR and V/M models respectively generated these spectrum fits of the NGC 6173 galaxy. The *top panel* of both figures shows the spectrum in black and the best fit is indicated in blue. The regions in red are the parts of the spectrum excluded from the fit. The *bottom panel* of each figure indicates the residuals from the best fit. The continuous green lines mark the $\pm 1\sigma$ deviation, and the dashed green line is the mean residual value (zero–axis).

because the best fit (indicated in blue), as determined with both the models deviated from the observed spectrum of this galaxy (indicated in black). The reason for this was that the choice of the star, more specifically HD140283 used in the LSF procedure was a poor choice because this star did not match the resolutions of the models with that of the galaxy's observed spectrum.

4.3 Simple or Composite Stellar Components?

The BCG sample, now consisting of 40 galaxies were analysed with the methods described in Chapter 3. In this section, each galaxy was respectively fitted against the P.HR and V/M models to determine the number of SSPs which gave the most probable representation of the SFH of each galaxy and the results are given in Table (4.1).

It should be mentioned here that the galaxies were divided into the groups; *emission* and *non-emission* (depending on the presence of emission lines), for the analysis to determine the SFHs of the galaxies contained within the sample. Readers should not take this as an indication that any special attention should be paid into which group the respective galaxies were divided. This distinction was only made to determine whether the SFHs of the two groups could be compared or showed any significant difference.

From Table (4.1), it followed that both models determined that the majority of the galaxies in the sample could be represented by an SSP fit. In the case of the P.HR model, 22 of the 40 galaxies could be represented by 1 SSP, while the V/M , in turn indicated that 26 of the 40 galaxies could be represented by 1 SSP.

Table 4.1: The fractions of simple and composite stellar components of the BCG sample as determined by both the P.HR and V/M models. The term *non-emission* refers to the galaxies that lack emission lines, while *emission* refers to galaxies with the presence of weak emission lines.

Component		**P.HR**	**V/M**
1 SSP	Non-emission	15/40	19/40
	Emission	7/40	7/40
	Total	22/40	26/40
2 SSPs	Non-emission	14/40	12/40
	Emission	2/40	1/40
	Total	16/40	13/40
3 SSPs	Non-emission	2/40	—
	Emission	—	1/40
	Total	2/40	1/40

In the case of the P.HR model, this model indicated that the remaining 18 galaxies could be represented by 2 and 3 SSPs, more specifically, 16 of the 40 galaxies could be represented by 2 SSPs and the two remaining galaxies by 3 SSPs.

In the case of the V/M model, this model indicated that the remaining 14 galaxies could be represented by 2 and 3 SSPs, more specifically, 13 of the 40 galaxies could be represented by 2 SSPs and the remaining galaxy by 3 SSPs.

When analysing Table (4.1) in more detail to determine whether the SFHs of the two groups were different, it was found that for the

1. P.HR model, the results indicated that the *non-emission* galaxies which had a combined CSP fit (the 2 and 3 SSPs combined) had a slightly higher fraction of 16/40 when compared to the *non-emission* galaxies which had an SSP fit with a fraction of 15/40.

2. P.HR model, the results indicated that the *emission* galaxies which had a combined CSP fit (the 2 and 3 SSPs combined) had a smaller fraction of 2/40 when compared to the *emission* galaxies which had an SSP fit with a fraction of 7/40.

   ➔ In summary, when comparing (1) and (2), the P.HR model indicated that the majority of the *non-emission* galaxies in the sample could be represented by a CSP, though there were still *non-emission* galaxies which could be represented by an SSP. On the other hand, the majority of the *emission* galaxies were represented by an SSP and a very small fraction of these *emission* galaxies could be represented by CSPs.

3. V/M model, the results indicated that the *non-emission* galaxies which had a combined CSP fit (the 2 and 3 SSPs combined) had a smaller fraction of 12/40 when compared to the *non-emission* galaxies which had an SSP fit with a fraction of 19/40.

4. V/M model, the results indicated that the *emission* galaxies which had a combined CSP fit (the 2 and 3 SSPs combined) had a smaller fraction of 2/40 when compared to the *emission* galaxies which had an SSP fit with a fraction of 7/40.

   ➔ In summary, when comparing (3) and (4), the V/M model indicated that the majority of the *non-emission* galaxies in the sample could be represented by an SSP but some of these *non-emission* galaxies could also be represented by CSPs. This trend was also found in the *emission* galaxies.

4.4 The P.HR vs. V/M model

The P.HR and V/M models were described in detail in §3.6. Koleva et al. (2008) found a relative consistency between the results obtained with the P.HR and V/M models. An example of the age values, derived with the stellar populations are shown in the second and third columns of Table (3.5a). However, these values were obtained with varying wavelength ranges and as already stated in Chapter 3, this approach was not a valid choice and hence, these values could be discarded. Therefore, the analysis of the sample was repeated with the (3800, 6000) Å wavelength range and the age values are shown in the fourth and fifth columns of Table (3.5a). When these values are compared, one can easily see that the values are very consistent with respect to each other, except in the case of ESO488-027 where the values differed quite significantly. Du et al. (2010) conducted a similar study on a sample of E+A galaxies that were retrieved from the SDSS Data Release Five and they found that the derived parameter values were different and showed little consistency.

The differences in the values might emerge from the differences between the models. These differences become more apparent when one considers the stellar populations used in the different models. This is because these stellar populations are generated with different population synthesis codes which use different stellar libraries and the choices of the physical conditions of the models are also different, for example the atmospheric parameters. Refer to §3.6 for a more complete discussion.

In this section a separate test was conducted to compare the two stellar population models with each other in order to determine which model gave the most probable representation of the SFHs of the galaxies in the BCG sample and the results are summarised in Table (4.2). *The most probable SFH representation was chosen on the principle that the local minimum (indicated with the green cross and determined through the* χ^2-*maps) of each component and the component had to coincide for the case of a CSP*. Figs. (A.1) & (A.2) illustrate the best model criterium for the CSP case. *For the SSP case, the local minimum had to be located within* (2000 ± 500) *Myr from the component and were located in the same contour plane. The contour lines are indicated with the blue lines and these lines represent the degeneracies between the parameters.* Figs. (A.3) & (A.4) illustrate the best model criterium for the SSP case. Figs. (A.1) to (A.4) will be discussed after Table (4.2).

Table 4.2: The comparison test between the P.HR and V/M models. Column 1 gives the names of the galaxies. Columns 2 & 3 respectively give the models which provided the most probable representation of the SFHs of the various galaxies. Column 4 specifies that both models provided the most probable representation of the SFHs while Column 5 specifies that none of the models provided a good representation.

Object Name	**P.HR**	**V/M**	**Both**	**None**
ESO146-028				✔
ESO202-043			✔	
ESO303-005				✔
ESO346-003	✔			
ESO349-010				✔
ESO444-046		✔		
ESO488-027				✔
ESO541-013				✔
ESO552-020				✔
GSC555700266	✔			
IC1101				✔
IC1633			✔	
IC4765				✔
IC5358				✔
Leda094683		✔		
MCG-02-12-039				✔
NGC 0533			✔	
NGC 0541				✔
NGC 1399	✔			
NGC 1713				✔
NGC 2832		✔		
NGC 3311			✔	
NGC 4839		✔		
NGC 4946	✔			
NGC 6086	✔			
NGC 6160	✔			
NGC 6269			✔	
NGC 7012	✔			
NGC 7597	✔			
NGC 7649		✔		
PGC004072	✔			
PGC025714	✔			
PGC026269				✔

Continued on Next Page . . .

Table 4.2 – Continued

Object Name	**P.HR**	**V/M**	**Both**	**None**
PGC030223				✔
PGC044257			✔	
PGC071807				✔
PGC072804				✔
UGC00579		✔		
UGC02232		✔		
UGC05515	✔			
Total	11/40	7/40	6/40	16/40

In the next six figures, the most probable representation of the SFHs will be discussed and explained as well as the best model criteria:

- Figs. (A.1), (A.2), (A.3) & (A.4) give a few examples of galaxies where the P.HR model provided the most probable representation of the respective galaxies' SFHs. This was due to the fact that for the CSP case, i.e. Figs. (A.1) & (A.2) the local minima of the respective components coincided with the components. For the SSP case, i.e. Figs. (A.3) & (A.4) the P.HR model was the model that gave the best fit because the local minima of the components were located within (2000 ± 500) Myr from the respective components and also in the same contour plane. The diamond symbols indicate other possible solutions for the local minima but the cross indicates the optimal value for the local minimum.

- Figs. (A.5) & (A.6) give two examples of galaxies where both the P.HR and V/M models provided the most probable representation of the SFHs of the galaxies in the BCG sample. Once again this was because the local minimum of the component coincided with the spread of the component and both the minima and components were located in the same contour line.

From Table (4.2), it follows that the P.HR model was the model that gave the most probable representation of the SFHs of the galaxies in the sample. This follows because for 17 of the 40 galaxies in the sample, the P.HR model gave the most probable representation of the SFHs while the V/M model could represent only 13 of the 40 galaxies. Hence, only the P.HR model will be used in the further analysis of the BCG sample.

4.5 Ages and [Fe/H] of the BCG Sample

Now that it has been determined that the P.HR model is the model that gave the most probable representation of the SFHs, the results obtained through this model for the SFH analysis will be

discussed in this section.

It is worth mentioning here that when the reader analyses Table (4.3) in detail, it will be found that some of the SSP components of the galaxies have ages that are larger than the age of the Universe, that is Log(Age) > Log(13.7 Gyr) = 1.1 Gyr. This is because the main aim of this analysis was to determine whether BCGs experienced more than one star formation epoch, i.e. if the SFHs could be represented by CSPs. Therefore, no limits were imposed on the ages of the components.

Another strange trend will become apparent, more specifically the [Fe/H] values of the SSP components will not be as expected, i.e. OSPs have high [Fe/H] values and YSPs have low [Fe/H] values. This is due to the fact that the model does not include $\alpha-$enhancements (see §3.6.3 for more detail) and some spectral indices might force the model to take on a certain [Fe/H] value. Koleva et al. (2008) found that the isochrones implemented in the P.HR model are solar-scaled at various values of Z and therefore, the non-solar abundances of α-elements are responsible for the miss-fit of strong spectral features, i.e. the MgH band that is used in the determination of the age and [Fe/H] of stellar populations. For this reason the [Fe/H] values have to be interpreted with caution.

The analysis was conducted by fitting each of the galaxies against the P.HR model and with the help of the χ^2-maps the most probable representation of the SFH was chosen, more specifically whether an SSP or a CSP gave the most probable representation of the SFH (refer to Chapter 3 for more detail). The values given in Table (4.3) are the SSP-equivalent derived ages and [Fe/H].

From here on the young aged stellar populations are characterised by the ages $-2.0 <$ Log(Age) $<$ 0.0, the intermediate aged stellar populations by $0.0 \leqslant$ Log(Age) < 0.8 and the old aged stellar populations by the ages $0.8 \leqslant$ Log(Age) < 1.3.

Table 4.3: The ages and [Fe/H] of the BCG sample as obtained by the P.HR model. Column 1 gives the names of the galaxies while Column 2 gives the number of SSP components which gave the most probable representation of the SFHs. The notation adopted for the # SSP is as follows: 1/1 is an SSP fit, the 1/2 and 2/2 are a 2 SSP fit, etc. Columns 3 & 4 give the age and [Fe/H] of the components. Columns 5 & 6 give the light fraction and mass fraction of each component.

Object Name	**# SSP**	**Log(Age) (Gyr)**	**[Fe/H] (dex)**	**MF (%)**	**LF (%)**
ESO146-028	1/3	0.001 ± 0.144	1.326 ± 0.101	0.740 ± 0.011	11.537 ± 0.127
	2/3	0.980 ± 0.044	0.283 ± 0.056	69.464 ± 0.991	63.991 ± 0.593
	3/3	1.252 ± 0.057	-0.276 ± 0.213	29.795 ± 0.930	24.473 ± 0.717
ESO202-043	1/2	0.339 ± 0.359	-1.175 ± 0.164	2.368 ± 0.010	20.881 ± 0.087
	2/2	1.161 ± 0.020	0.378 ± 0.009	97.632 ± 0.140	79.118 ± 0.081
ESO303-005	1/1	0.989 ± 0.144	0.153 ± 0.078		

Continued on Next Page ...

Table 4.3 – Continued

Object Name	**# SSP**	**Log(Age) (Gyr)**	**[Fe/H] (dex)**	**MF (%)**	**LF (%)**
ESO346-003	1/2	-1.010 ± 0.546	-0.200 ± 0.372	0.025 ± 0.001	2.560 ± 0.036
	2/2	1.100 ± 0.012	0.424 ± 0.008	99.975 ± 0.05	97.440 ± 0.033
ESO349-010	1/1	0.785 ± 0.004	0.157 ± 0.006		
ESO444-046	1/2	-0.716 ± 0.230	-0.731 ± 0.388	0.098 ± 0.004	4.181 ± 0.131
	2/2	1.234 ± 0.093	0.353 ± 0.427	99.902 ± 3.648	95.819 ± 1.865
ESO488-027	1/1	0.902 ± 0.006	0.434 ± 0.002		
ESO541-013	1/2	1.041 ± 0.043	-2.120 ± 0.079	1.837 ± 0.017	9.252 ± 0.083
	2/2	1.273 ± 0.012	0.113 ± 0.010	98.163 ± 0.122	90.748 ± 0.080
ESO552-020	1/1	0.803 ± 0.002	0.344 ± 0.005		
GSC555700266	1/2	0.950 ± 0.022	0.279 ± 0.010	93.327 ± 0.063	88.004 ± 0.041
	2/2	1.292 ± 0.070	-1.787 ± 0.116	6.673 ± 0.024	11.996 ± 0.043
IC1101	1/1	0.985 ± 0.012	0.078 ± 0.005		
IC1633	1/3	-0.926 ± 0.109	-0.151 ± 0.173	0.114 ± 0.123	5.481 ± 5.497
	2/3	0.745 ± 0.006	0.566 ± 0.011	68.924 ± 35.538	69.798 ± 22.182
	3/3	1.258 ± 0.059	-0.498 ± 0.090	30.962 ± 36.426	24.720 ± 27.296
IC4765	1/2	-0.032 ± 0.435	-1.367 ± 0.308	0.029 ± 0.009	1.567 ± 0.047
	2/2	1.248 ± 0.005	0.343 ± 0.010	99.971 ± 0.060	98.433 ± 0.042
IC5358	1/1	0.788 ± 0.002	0.475 ± 0.005		
Leda094683	1/1	0.798 ± 0.002	0.246 ± 0.006		
MCG-02-12-039	1/1	0.781 ± 0.003	0.256 ± 0.006		
NGC 0533	1/2	-0.200 ± 0.209	-1.116 ± 0.261	0.038 ± 0.005	2.215 ± 0.028
	2/2	1.261 ± 0.007	0.429 ± 0.007	99.961 ± 0.037	97.785 ± 0.026
NGC 0541	1/2	0.491 ± 0.058	0.698 ± 0.005	32.692 ± 1.685	41.268 ± 1.834
	2/2	1.185 ± 0.045	-0.378 ± 0.016	67.308 ± 2.791	58.732 ± 1.892
NGC 1399	1/2	0.622 ± 0.029	0.096 ± 0.045	81.656 ± 43.370	90.704 ± 21.857
	2/2	1.247 ± 0.057	-0.793 ± 0.409	18.344 ± 43.916	9.296 ± 21.815
NGC 1713	1/1	0.701 ± 0.016	0.151 ± 0.010		
NGC 2832	1/1	1.113 ± 0.010	0.436 ± 0.003		
NGC 3311	1/1	0.730 ± 0.038	0.045 ± 0.028		
NGC 4839	1/1	1.208 ± 0.003	0.258 ± 0.006		
NGC 4946	1/1	0.723 ± 0.030	0.312 ± 0.034		
NGC 6086	1/2	-0.223 ± 0.481	-0.816 ± 0.683	0.010 ± 0.001	0.899 ± 0.027
	2/2	1.211 ± 0.015	0.392 ± 0.009	99.990 ± 0.030	99.100 ± 0.021
NGC 6160	1/2	-0.062 ± 0.105	-1.415 ± 0.117	0.846 ± 0.034	6.373 ± 0.155
	2/2	1.180 ± 0.016	-0.009 ± 0.009	99.154 ± 4.596	93.626 ± 0.903
NGC 6269	1/2	-1.637 ± 0.132	0.086 ± 0.184	0.0213 ± 0.001	2.933 ± 0.020
	2/2	1.2634 ± 0.006	0.275 ± 0.007	99.979 ± 0.022	97.067 ± 0.015
NGC 7012	1/1	0.773 ± 0.008	0.235 ± 0.011		
NGC 7597	1/1	1.113 ± 0.020	0.009 ± 0.014		
NGC 7649	1/2	0.846 ± 0.016	0.385 ± 0.013	90.579 ± 60.183	76.881 ± 36.794

Continued on Next Page ...

Table 4.3 – Continued

Object Name	# SSP	Log(Age) (Gyr)	[Fe/H] (dex)	MF (%)	LF (%)
	2/2	1.048 ± 0.035	-2.024 ± 0.050	9.241 ± 16.242	23.119 ± 38.408
PGC004072	1/1	1.103 ± 0.215	0.125 ± 0.071		
PGC025714	1/1	1.257 ± 0.016	0.053 ± 0.007		
PGC026269	1/1	0.488 ± 0.032	-0.119 ± 0.034		
PGC030223	1/1	0.897 ± 0.013	0.115 ± 0.005		
PGC044257	1/1	0.914 ± 0.014	-0.047 ± 0.015		
PGC071807	1/2	-0.643 ± 0.128	-2.111 ± 0.580	0.057 ± 0.001	7.283 ± 0.027
	2/2	1.271 ± 0.019	0.169 ± 0.009	99.943 ± 0.036	92.717 ± 0.023
PGC072804	1/1	0.804 ± 0.002	0.271 ± 0.005		
UGC00579	1/2	0.544 ± 0.125	-1.760 ± 0.538	1.608 ± 0.010	16.010 ± 0.096
	2/2	1.294 ± 0.022	0.015 ± 0.085	98.392 ± 0.149	83.900 ± 0.090
UGC02232	1/2	0.191 ± 0.530	0.442 ± 0.391	6.013 ± 0.001	18.914 ± 0.001
	2/2	1.244 ± 0.072	-0.055 ± 0.045	93.987 ± 0.006	81.086 ± 0.001
UGC05515	1/1	0.923 ± 0.018	-0.011 ± 0.022		

From Table (4.1) it can be seen that 18 of the galaxies in the sample could be represented by 2 & 3 SSPs, indicating that at least 48% of the galaxies in the sample underwent more than one star formation period. By analysing Table (4.3) in greater detail it followed that for the 2 SSP case, there were 16 galaxies which had a YSP as a first component while the remaining 8 galaxies had a ISP as a first component. All these galaxies had a OSP as a second component. For 13 of these 16 galaxies, the LFs and MFs of the OSPs dominated over the LFs and MFs of the YSPs or ISPs. The contrast was true for GSC555700266, NGC 1399 and NGC 7649 because here the LFs and MFs of the ISPs dominated over that of the OSPs. For the 3 SSP case there were two galaxies which could be represented by this fit and were comprised out of a YSP, ISP and OSP. In both these galaxies the LF and MF of the ISP dominated over that of the LFs and MFs of the YSP and OSP. All the galaxies with an SSP fit are comprised out of ISPs. For the galaxies with a 2 & 3 SSP fit, the LF of the first component is always higher than the MF, except for GSC555700266 and NGC 7649 where the MF is higher than the LF. Serra & Trager (2007) confirmed these results except in the case where the YSP was very young and had a significant MF.

To summarise, 55% of the galaxies in the sample are comprised out of galaxies which could be represented by a single intermediate aged stellar population. The galaxies represented by 2 & 3 SSP fits were dominated by OSPs because the LFs and MFs of the OSPs dominated over that of the YSP and ISP. The OSPs were the dominant contributors to the light and mass of the galaxy.

The results of Table (4.3) is illustrated in Fig. (A.7) as the age and [Fe/H] distributions of the BCG sample. Referring to Fig. (A.7a), which shows the age distribution, it was found that for the

- **1 SSP** there were three significant peaks located at $\sim$ (0.70), (0.90) and (1.25) Gyr.
- **2 SSPs** the *first component* had two significant peaks located at $\sim$ (– 0.25) and (0.85) Gyr while the *second component* had a significant peak located at $\sim$ (1.27) Gyr.
- **3 SSPs** had no significant peaks for any of the three components.

Referring to Fig. (A.7b), which shows the [Fe/H] distribution, it was found that for the

- **1 SSP** there were four significant peaks located at $\sim$ (0.025), (0.15), (0.27) and (0.45) dex.
- **2 SSPs** the *first component* had no significant peaks while the *second component* had two significant peaks located at $\sim$ (0.05) and (0.3) dex.
- **3 SSPs** had no significant peaks for any of the three components.

When representing the distribution of the ages and [Fe/H] with a histogram, one has to bin the data. A reason why no significant peaks could be detected in the age and [Fe/H] distribution of the 3 SSP galaxies is because there were only two galaxies which indicated that a 3 SSP fit could be used to represent the SFHs of these galaxies. Hence, no significant peaks could be deduced from just using these two galaxies.

4.5.1 Mass-to-Light fraction

Stellar population models predict that stars will spend a significant fraction of their lifetimes on the zero-age main sequence where most of the hydrogen in the core of the stars have been burned up to fuel the evolution of the stars (Salaris & Cassisi, 2005). These stars will display a close connection between the total mass and the luminosity, called the mass-to-light (M/L) ratio.

The most efficient way to determine the M/L fraction is by gathering two dimensional photometric and kinematic data over a large range of radii and compare this against a variety of dynamical models (Bacon, Monnet & Simen, 1985). The methods used to derive the M/L ratio is not discussed in this section as it is outside the scope of this project, but I will mention the three methods given by Faber & Gallagher (1979) to determine the ratio:

1. The global virial theorem is discussed in detail by Podeva (1958) and after some assumptions and a few steps of mathematics it follows that it can be written as:

$$\frac{M}{L} = \frac{9\sigma^2 R_e}{GL} \tag{4.1}$$

where R_e is the effective half light radius, G is the universal gravitational constant and L the total luminosity.

2. A method devised by King & Minkowski (1972) which is based on the stellar hydrodynamic equations applied to the core of the galaxies. To determine the value at the core, the velocity dispersion, radius (R_C) and the surface brightness (I_0) at the core are required. This ratio will be determined by the equation given by Tonry & Davis (1981):

$$\frac{M}{L} = \frac{9\sigma^2}{2\pi G I_0 R_C} \tag{4.2}$$

3. To find a test particle in circular motion around a spheroid component.

Burbidge & Burbidge (1975) conducted a study on the M/L ratio of ETGs and found the average ratio to be 19.7 while King & Minkowski (1972) found the ratio for the luminous E galaxies to be between seven and 20. This was achieved by applying the method devised by these two authors.

4.5.2 Average age and [Fe/H] values

Table (4.4) gives the average values of the ages and [Fe/H] of the 1, 2 & 3 SSP fits given in Table (4.3). The errors derived here are the standard errors on the average values.

Table 4.4: The average values for the ages and [Fe/H] of each stellar population as determined by the P.HR model for the BCG sample. The term *non-emission* refers to galaxies which lacked emission lines, while *emission* refers to galaxies with the presence of weak emission lines. The errors derived here are the standard errors on the average values.

	# SSP		**Log(Age) (Gyr)**	**[Fe/H] (dex)**
1 SSP		Non-emission	0.956 ± 0.047	0.071 ± 0.117
		Emission	0.850 ± 0.091	0.312 ± 0.007
2 SSP	1/2	Non-emission	-0.060 ± 0.759	-0.851 ± 0.875
		Emission	0.669 ± 0.251	0.542 ± 0.221
	2/2	Non-emission	1.234 ± 0.054	0.018 ± 0.610
		Emission	1.117 ± 0.097	-1.201 ± 1.164
3 SSP	1/3	Non-emission	-0.463 ± 0.655	-0.738 ± 0.831
		Emission	—	—
	2/3	Non-emission	0.862 ± 0.166	0.425 ± 0.200
		Emission	—	—
	3/3	Non-emission	1.255 ± 0.004	-0.387 ± 0.157
		Emission	—	—

When analysing Table (4.4) in detail it follows that:

- When the age values of the 1 SSP fit (for both the *non-emission* and *emission* galaxies) were compared, it was found that these values were almost the same and indicated that both groups, on average had an intermediate aged stellar population. The [Fe/H] values for these two groups showed no consistency when compared.
- For the case of the 2 SSP fit, the age values for both the *non-emission* and *emission* galaxies were different when they were compared. The *non-emission* galaxies on average were comprised out of a young and old aged stellar population while the *emission* galaxies on average were made up of intermediate and old aged stellar populations. The [Fe/H] values for these two groups showed no consistency when they were compared.
- There were no *emission* galaxies for which a 3 SSP fit could be used to represent the SFHs but for the *non-emission* galaxies the opposite were true and were comprised out of a young, intermediate and old aged stellar population.

4.6 Comparison with the LICK indices

In this section, the derived ages and [Fe/H] of the BCG sample (as given in §4.5) were compared against the ages and [Fe/H] derived by Loubser et al. (2009b), who used the LICK indices and is given in Table 3 of Paper 2. For this comparison, each of the galaxies in the BCG sample was fitted against a single component P.HR model and the results are given in Table (4.5).

Before the [Fe/H] comparison could be done, the total metallicity ([Z/H]) of the galaxies given in Paper 2 had to be changed to [Fe/H]. This was done by taking the [α/H] of each galaxy into account. From Thomas et al. (2003), the relation between [Z/H] and [Fe/H] can be written as:

$$[Z/H] = [Fe/H] + A[\alpha/H] \tag{4.3}$$

with

$$A = -\frac{\Delta[Fe/H]}{\Delta[\alpha/Fe]} \tag{4.4}$$

where the constant A depends on the ratio between the enhanced and suppressed elements in the spectrum of the galaxy. Thomas et al. (2003) followed the approach taken by Tantalo, Chiosi & Bressan (1998) and determined that $A = 0.94$ for their adopted mixtures.

By substituting Eq. (4.4) into Eq. (4.3) and rewriting it, follows that:

$$[Fe/H] = [Z/H] - 0.94[\alpha/H] \tag{4.5}$$

and it is from this equation that the [Fe/H] of the LICK indices were computed.

Table 4.5: The comparison between the derived SSP parameters obtained through the P.HR model and the LICK indices. Column 1 gives the names of the galaxies while Columns 2 & 3 give the ages and [Fe/H] derived with the SSP model. Columns 4 & 5 give the ages and [Fe/H] derived with the LICK indices. The values for the [Fe/H] were derived by using Eq. (4.5). Column 6 indicates whether the P.HR model determined that an SSP fit was the most probable representation of the galaxy's SFH (follows from §4.3).

Object Name	**P.HR Log(Age) (Gyr)**	**P.HR [Fe/H] (dex)**	**LICK Log(Age) (Gyr)**	**LICK [Fe/H] (dex)**	**Indicate whether 1 SSP was best fit**
ESO146-028	0.799 ± 0.003	0.196 ± 0.006	0.970 ± 0.180	-0.684 ± 0.066	
ESO202-043	0.800 ± 0.002	0.340 ± 0.006	0.580 ± 0.180	0.157 ± 0.066	
ESO303-005	0.989 ± 0.144	0.154 ± 0.078	0.810 ± 0.230	-0.045 ± 0.057	✔
ESO346-003	1.173 ± 0.002	0.499 ± 0.003	0.630 ± 0.043	0.148 ± 0.094	
ESO349-010	0.785 ± 0.004	0.157 ± 0.149	0.890 ± 0.220	-0.072 ± 0.093	✔
ESO444-046	1.195 ± 0.021	0.065 ± 0.007	1.250 ± 0.200	-0.735 ± 0.129	
ESO488-027	0.902 ± 0.006	0.434 ± 0.002	0.850 ± 0.130	0.119 ± 0.085	✔
ESO541-013	1.148 ± 0.015	0.009 ± 0.007	0.750 ± 0.380	-0.161 ± 0.098	
ESO552-020	0.803 ± 0.002	0.344 ± 0.005	1.120 ± 0.190	-0.431 ± 0.075	✔
GSC555700266	0.821 ± 0.003	0.189 ± 0.005	0.660 ± 0.370	0.015 ± 0.057	
IC1101	0.986 ± 0.012	0.078 ± 0.005	0.700 ± 0.150	0.156 ± 0.089	✔
IC1633	0.767 ± 0.001	0.595 ± 0.003	0.940 ± 0.190	-0.034 ± 0.071	
IC4765	1.254 ± 0.008	0.299 ± 0.009	1.010 ± 0.230	0.078 ± 0.079	
IC5358	0.788 ± 0.002	0.475 ± 0.005	0.920 ± 0.320	-0.105 ± 0.110	✔
Leda094683	0.798 ± 0.002	0.246 ± 0.006	—	—	✔
MCG-02-12-039	0.781 ± 0.003	0.256 ± 0.006	1.050 ± 0.210	-0.339 ± 0.075	✔
NGC 0533	1.255 ± 0.007	0.427 ± 0.006	1.250 ± 0.100	-0.217 ± 0.110	
NGC 0541	0.669 ± 0.015	0.139 ± 0.008	0.660 ± 0.550	0.013 ± 0.088	
NGC 1399	0.777 ± 0.002	0.495 ± 0.004	0.930 ± 0.100	-0.003 ± 0.102	
NGC 1713	0.701 ± 0.016	0.151 ± 0.010	1.030 ± 0.340	-0.177 ± 0.128	✔
NGC 2832	1.113 ± 0.010	0.436 ± 0.003	0.930 ± 0.020	0.123 ± 0.071	✔
NGC 3311	0.730 ± 0.039	0.045 ± 0.028	0.940 ± 0.270	-0.256 ± 0.075	✔
NGC 4839	1.208 ± 0.003	0.258 ± 0.006	1.070 ± 0.120	-0.199 ± 0.057	✔
NGC 4946	0.723 ± 0.030	0.312 ± 0.034	—	—	✔
NGC 6086	1.169 ± 0.007	0.406 ± 0.004	1.000 ± 0.140	0.280 ± 0.070	
NGC 6160	0.861 ± 0.013	0.348 ± 0.005	1.050 ± 0.060	-0.111 ± 0.044	
NGC 6269	1.261 ± 0.012	0.254 ± 0.009	0.950 ± 0.080	0.022 ± 0.049	
NGC 7012	0.773 ± 0.008	0.235 ± 0.011	0.690 ± 0.190	0.143 ± 0.085	✔
NGC 7597	1.113 ± 0.020	0.009 ± 0.014	0.670 ± 0.290	0.024 ± 0.053	✔
NGC 7649	0.583 ± 0.010	0.304 ± 0.011	—	—	
PGC004072	1.103 ± 0.215	0.125 ± 0.071	0.900 ± 0.200	-0.113 ± 0.079	✔
PGC025714	1.257 ± 0.016	0.053 ± 0.007	—	—	✔

Continued on Next Page . . .

Table 4.5 – Continued

Object Name	**P.HR Log(Age) (Gyr)**	**P.HR [Fe/H] (dex)**	**LICK Log(Age) (Gyr)**	**LICK [Fe/H] (dex)**	**Indicate whether 1 SSP was best fit**
PGC026269	0.488 ± 0.032	-0.119 ± 0.034	—	—	✔
PGC030223	0.897 ± 0.013	0.115 ± 0.005	—	—	✔
PGC044257	0.914 ± 0.011	-0.048 ± 0.015	0.630 ± 0.190	0.209 ± 0.107	✔
PGC071807	0.821 ± 0.002	0.291 ± 0.005	0.630 ± 0.400	-0.012 ± 0.102	
PGC072804	0.804 ± 0.002	0.271 ± 0.005	0.690 ± 0.370	0.123 ± 0.057	✔
UGC00579	1.278 ± 0.002	-0.153 ± 0.007	0.910 ± 0.270	-0.266 ± 0.107	
UGC022329	0.891 ± 0.013	0.128 ± 0.007	0.990 ± 0.170	-0.378 ± 0.066	
UGC05515	0.923 ± 0.018	-0.011 ± 0.022	0.880 ± 0.340	-0.220 ± 0.128	✔

It has to be emphasized that the parameters derived by the LICK indices are SSP equivalent parameters and can therefore be seen as galaxies which have an SSP fit as a representation of their SFHs. For this reason, the ages derived with the P.HR model and LICK indices show a great consistency.

Table 4.6: The $\alpha-$enhancements of the BCG sample as determined by Loubser et al. (2009) used in the age and [Fe/H] residual comparisons. Column 1 gives the names of the galaxies while Columns 2 gives the $\alpha-$enhancements.

Object Name	**[α/Fe]**
ESO146-028	0.60 ± 0.03
ESO202-043	0.45 ± 0.03
ESO303-005	0.41 ± 0.03
ESO346-003	0.30 ± 0.03
ESO349-010	0.30 ± 0.05
ESO444-046	0.59 ± 0.05
ESO488-027	0.32 ± 0.03
ESO541-013	0.49 ± 0.04
ESO552-020	0.48 ± 0.03
GSC555700266	0.41 ± 0.03
IC1101	0.27 ± 0.04
IC1633	0.44 ± 0.04
IC4765	0.30 ± 0.04
IC5358	0.41 ± 0.05

Continued on Next Page ...

Table 4.6 – Continued

Object Name	**[α/Fe]**
Leda094683	—
MCG-02-12-039	0.51 ± 0.03
NGC 0533	0.38 ± 0.05
NGC 0541	0.38 ± 0.04
NGC 1399	0.45 ± 0.05
NGC 1713	0.39 ± 0.07
NGC 2832	0.38 ± 0.04
NGC 3311	0.40 ± 0.03
NGC 4839	0.35 ± 0.03
NGC 4946	—
NGC 6086	0.39 ± 0.04
NGC 6160	0.32 ± 0.02
NGC 6269	0.36 ± 0.03
NGC 7012	0.39 ± 0.03
NGC 7597	0.40 ± 0.02
NGC 7649	—
PGC004072	0.45 ± 0.04
PGC025714	—
PGC026269	—
PGC030223	—
PGC044257	0.31 ± 0.04
PGC071807	0.46 ± 0.05
PGC072804	0.38 ± 0.03
UGC00579	0.56 ± 0.04
UGC022329	0.54 ± 0.03
UGC05515	0.50 ± 0.07

4.6.1 Age comparison

Comparison of BCGs where an SSP was the best fit

The first comparison done was to compare the SSP derived parameters (as determined by both the P.HR model and LICK indices) of the galaxies for which the P.HR model determined that an SSP fit was the most probable representation of the SFHs and these galaxies are indicated in Column 6 of Table (4.5) with a tick.

The ages, derived by both these methods were compared and found that the values showed a considerable consistency except in the cases of the following galaxies: ESO552-020, IC1101, MCG-02-12-039, NGC 1713, NGC 7597 and PGC044257 where the differences between the values were quite significant. Figs. (A.8a) & (A.8c) illustrates the residual effect ($\mathrm{Log(P.HR_{age})} - \mathrm{Log(LICK_{age})}$) between the ages as determined by the two different methods. Fig. (A.8a) illustrates the age residual compared against the P.HR age values and from this figure it is apparent that the values are systematically off. This trend is also observed in Fig. (A.8c) where the age residuals are compared against the ages determined with the LICK indices. It is difficult to explain the origin of these systematic differences from these figures alone and additional analyses will have to be preformed to determine the cause of these systematic differences. These tests are outside the scope of this dissertation but it has been suggested that these systematic offsets might be an artifact caused by the different methods implemented in the models that were used for the analysis. Refer to §3.2 for a comparison between models that implement spectrophotometric indices, i.e. the LICK indices and full spectrum fitting models, i.e. the P.HR model. Another possible reason for these offsets might emerge due to the exclusion of the [α/Fe] in the P.HR model. In Fig (A.9a), the $\alpha-$enhancements (found in Table (4.6)) are plotted against the age residuals and from this figure it is still unclear to what extend the $\alpha-$enhancements influence the age values and therefore, additional analyses would be required.

In Fig. (A.10a), the ages of the galaxies, that could be fitted against a single P.HR component model, are compared against that of the LICK indices. A least-square fitting routine was applied to the data and a mean slope of (-0.122 ± 0.178) was determined, where the error is the standard error. When comparing this to the slope of the 1:1 relation (indicated with the solid line), it can be concluded that the age values are systematically off when compared because the slope of the least-square fitting routine is not close to one. If the slope of the least-square fitting routine was close to one, then the age values of the P.HR model and LICK would have been the same and no systematic differences could have been detected.

Comparison of all BCGs fitted against an SSP

For the next comparison, each galaxy in the BCG sample was fitted against a single stellar population by using the P.HR model. The SSP derived parameters of all the galaxies in the sample were then compared to those derived with the LICK indices. When comparing the rest of the galaxies, which did not have a ✔ sign in Column 6, it was found that the ages differed significantly in both the cases, except for the following galaxies: ESO444-046, IC4765, NGC 0533, NGC 6086 and UGC022329 where the ages agreed within the errors.

This comparison is shown in Fig. (A.11a) and by preforming a least-square fitting routine to the data, a mean slope of (0.225 ± 0.132) was found, where the error is the standard error. By comparing this to the slope of the 1:1 relation (indicated with the solid line), it can be concluded that the age values of the two models are systematically off when compared.

Age distribution

Illustrated in Fig. (A.12a) is the age distribution (as summarised in Table (4.5)) of the BCG sample as determined with the P.HR model (black bars) and LICK indices (blue bars). The Kolmogorov-Smirnov (KS) test was preformed to check whether the age values of the different methods differed significantly. This was accomplished by determining the critical value of the KS test at the 95% confidence level, i.e. $D = \sqrt{\frac{a+b}{a\times b}}$ with a and b the number of galaxies in the BCG sample respective analysed in this project and in Loubser et al. (2009b). The critical value was found to be 0.315 while the KS test value was found to be 0.128. If the KS test value is less than the critical value, then the samples are significantly compatible to each other at the 95% confidence level. As the results from the test show, these two samples are significantly compatible.

When the age distributions were compared against each other, it was found that the age distribution represented by the black bars showed a significant peak at $\sim (0.70)$ Gyr, a secondary peak at $\sim (0.90)$ Gyr and a third peak located at $\sim (1.25)$ Gyr. Loubser et al. (2009b) found two peaks in their analysis (blue bars) of the same BCG sample that were located at $\sim (0.65)$ and (0.90) Gyr. However, they found that the first peak was not statistically significant according to the KS test when the BCG sample were compared to normal E galaxies. The first two peaks found in the BCG sample by both these methods showed significant consistency when compared. This comparison and the KS test showed yet again that the 1 SSP equivalent ages, derived with the P.HR model showed a significant consistency with that derived with the LICK indices.

4.6.2 [Fe/H] comparison

Comparison of BCGs where an SSP was the best fit

Here the [Fe/H] comparison, between the galaxies where the P.HR model determined that an SSP was the most probable SFH representation and the LICK indices indicated that all the galaxies, with PGC026269, PGC044257, UGC00579 and UGC05515 as exceptions were presumed to be young, but the age values indicated a different story. The age values indicated that these galaxies were made up of ISPs or OSPs. The galaxies that were the exception, were comprised out of YSPs. The LICK indices, in turn indicated that 48% of the galaxies were made up of OSPs and 33% of the galaxies were comprised out of YSPs or ISPs.

By visually comparing the [Fe/H] values (determined with the two methods), shown in Columns 2 & 5 of Table (4.5), it can clearly be seen that these values show no consistency. A reason for this is because the P.HR model does not take $\alpha-$enhancements into account and might also be an affect of the methods implemented in the models which were used in the analysis. The comparison of the [Fe/H] residuals against the [Fe/H] values of the P.HR model and LICK indices are respectively shown in Figs. (A.8b) & (A.8d). By inspecting these figures in detail, it can be seen that the [Fe/H] values were systematically off. By following the same approach as taken in the previous section, the [Fe/H] residuals were compared against the $\alpha-$enhancements (found in Table (4.6))

in Fig. (A.9b) to determine to what extend the [α/Fe] influenced the [Fe/H] values. By comparing Fig. (A.9b) with Fig. (A.9a), one can clearly see that the [α/Fe] have a stronger influence on the [Fe/H] residual than on the age residual due to the fact that the $\alpha-$enhancements in Fig. (A.9b) increases with [Fe/H]. The $\alpha-$enhancements in Fig. (A.9a) are more scattered, that is the influence of [α/Fe] on the derived ages are more difficult to discern.

In Fig. (A.10b), the [Fe/H] of the galaxies, that could be fitted against a single P.HR component model, are compared against that of the LICK indices. A least-square fitting routine was applied to the data and a mean slope of (-0.047 ± 0.266) was determined, where the error is the standard error. When comparing this to the slope of the 1:1 relation (indicated with the solid line), it can be concluded that the [Fe/H] values are systematically off when compared because the slope of the least-square fitting routine is not close to one. If the slope of the least-square fitting routine was close to one, then the [Fe/H] values of the P.HR model and LICK would have been the same and no systematic differences could have been detected.

Comparison of all BCGs fitted against an SSP

For the [Fe/H] comparison where all the galaxies in the sample were fitted against a single P.HR component model, the comparison between the [Fe/H], determined by the P.HR model and LCK indices is shown in Fig. (A.11b). A least-square fitting routine was applied to the data and a mean slope of (0.0302 ± 0.202) was determined, where the error is the standard error. When comparing this to the slope of the 1:1 relation (indicated with the solid line), it can be concluded that the [Fe/H] values are systematically off when compared because the slope of the least-square fitting routine is not close to one. If the slope of the least-square fitting routine was close to one, then the [Fe/H] values of the P.HR model and LICK would have been the same and no systematic differences could have been detected.

[Fe/H] distribution

Illustrated in Fig. (A.12b), the [Fe/H] distributions of the BCG sample as determined by the P.HR model (black bars) and LICK indices (blue bars). The KS test was also preformed on these two [Fe/H] samples and the critical value was found to be 0.315, while the KS test value was found to be 0.138. Once again the KS test value was smaller than the critical value and therefore, the two samples are significantly compatible to each other at the 95% confidence level.

By inspecting Fig. (A.12b) in more detail, it followed that the black bars indicated two significant peaks at $\sim$ (0.25) and (0.33) dex while the blue bars had two significant peaks at $\sim$ ($-$ 0.05) and (0.17) dex. The [Fe/H] values derived by the two methods showed no consistency because the P.HR model did not take $\alpha-$enhancements into account when determining the metallicity of the stellar populations.

4.7 Cooling Flows

One of the hot topics in the research area of galaxy evolution is CFs and the effects that these flows have on the evolution of galaxies. Studies regarding BCGs are particularly challenging. This is because BCGs are usually located close to the centres of the clusters which are densely populated and it is expected that these galaxies are made up of old stars and does not experience any significant star formation epochs (Liu et al. 2012). But several authors, for example Edwards et al. (2007) and Bildfell et al. (2008) found evidence of recent and ongoing star formation in BCGs located in CF clusters.

In this section the host clusters of the BCG sample were studied to see whether or not these clusters had a CF by collecting information regarding CFs from the literature and is summarised in Table (4.7).

The cosmological model of $H_0 = 70$ km s^{-1} Mpc^{-1}, $\Omega_m = 0.3$ and $\Omega_\Lambda = 0.7$ have been assumed when deriving the cooling times and determining the X-ray properties (Rafferty, McNamara & Nulsen, 2008; Martizzi et al. 2012). For this cosmological model the age of the Universe is ≈ 13.7 Gyr.

Before going into the detail of discussing the classification of clusters as CF or non-CF clusters, it should be mentioned that this is a rather subjective classification complicated by the fact that the mass-deposition rates and cooling times of the clusters are depended on the assumptions made during the analysis of the various studies referred to in this section.

4.7.1 Cooling times

Classifying clusters as non-CF or CF clusters can be a rather difficult task. For this classification, researchers use the X-ray cooling time (t_{cool}) which can be used as a fundamental indicator of cool gas in the centres of the clusters (Rawle et al. 2012). The t_{cool} of the cluster is usually taken to be less than the age of the cluster (Edge et al. 1992), which in turn is assumed to be roughly equal to the age of the Universe ($t_H \approx 13.7$ Gyr). The t_{cool} of the gas in a cluster is the measurement of the ratio between the radiation of the thermal bremsstrahlung and the rate of energy lost through radiative or conductive cooling processes. Within the cooling radius the t_{cool} becomes smaller and under gravity and thermal pressure (Peres et al. 1998), the cooling gas causes an inward flow that is required to maintain the energy balance, and therefore a *CF* is formed (Edge et al. 1992). Hence, by using the estimated central cooling times of the clusters, it can be used to determine whether a cluster contains a CF or not, more specifically, indicating if $t_{cool} < t_H$, then the cluster contained a CF.

I used the relation, as described by Donahue et al. (2005):

$$t_{cool}(K_0) \sim 10^9\,\mathrm{yrs}\left(\frac{K_0}{10\,\mathrm{keV\ cm^2}}\right)^{3/2}\left(\frac{\mathrm{kT}_x}{5\,\mathrm{keV}}\right)^{-1} \tag{4.6}$$

to determine the cooling time. K_0 is the central entropy derived from a simple power law profile and kT_x is the average X-ray temperature of the gas. Both these values have been obtained from the Archive of Chandra Cluster Entropy Profile Tables survey (Cavagnolo et al. 2009) which presented the values for ten of the 40 clusters in the BCG sample. I found that six of these ten galaxies had a $\mathrm{t}_{cool} \lesssim 13$ Gyr and thus these galaxies had a CF. The cooling times of these galaxies are indicated in Table (4.7) in Column 5. All ten galaxies, with the exception of NGC 3311, corresponded to what was found in the literature, more specifically indicating whether the cluster contained a CF or not.

4.7.2 Mass-deposition rate

Large amounts of cooled material are deposited throughout the centres of the clusters by CFs (Peres et al. 1998). The mass-deposition rate ($\dot{M}$) of a cluster is defined as the rate at which the gas in the CF cools down and this can be inferred from the X-ray image of the respective clusters (Mo et al. 2010). As already stated in the Chapter 2, the surface brightness profiles of clusters with CFs are sharply peaked within the cooling radius and this implies that $\dot{M} \propto r$. Hence, if other effects are ignored, the cooling gas will be deposited over a relative large region of the cluster core while the remaining hot gas continues to flow inwards.

Mo et al. (2010) indicated that the deduced $\dot{M}$ implies that more than $10^{11} M_\odot$ of the cold gas was deposited within < 1 Gyr and within a cooling radius of > 0.1 Mpc but the true deduced $\dot{M}$ of BCGs are still debatable. It was indicated by White, Jones & Forman (1997) that the literal interpretation of the $\dot{M}$ is different for each study because the assumptions made during each analysis is different. They proposed that any $\dot{M}$ value should only be considered to be probable within a factor of two. Therefore, the values given in Table (4.8) were given as an indication for the values available in the literature but not for the purpose of comparison.

Table 4.7: The CFs contained in the BCG sample. Column 1 & 2 give the names of the galaxies and host clusters while Column 3 indicates whether or not the galaxy contains a CF and Column 4 gives the references to the literature from which this conclusion was derived. Column 5 gives the cooling time (t_{cool}) as determined with Eq. (4.6).

The references given are e = Edwards et al. (2007), ch = Chen et al. (2007), g= Giovannini, Liuzzo & Giroletti (2008), mc = McCarthy et al. (2004), r = Rafferty et al. (2006) and w = White et al. (1997).

Object name	**Cluster**	**CF**	**Ref.**	**t_{cool} (Gyr)**
ESO146-028	RXCJ2228.8-6053	—	—	
ESO202-043	AS0479	—	—	
ESO303-005	RBS521	—	—	
ESO346-003	A S1065	—	—	
ESO349-010	A4059	✓	ch, e, r	0.638 ± 0.211
ESO444-046	A3558	✗	ch, e	33.964 ± 0.140
ESO488-027	A0548	✓	w	
ESO541-013	A0133	✓	ch, mc, r, w	2.640 ± 0.043
ESO552-020	CID 28	—	—	
GSC555700266	A1837	✓	w	
IC1101	A2029	✓	ch, mc, r, w	0.729 ± 0.1000
IC1633	A2877	✗	w	
IC4765	AS0805	—	—	
IC5358	A4038	✓	ch	11.862 ± 0.047
Leda094683	A1809	✗	w	
MCG-02-12-039	A0496	✓	e, mc, w	0.835 ± 0.118
NGC 0533	A0189B	—	—	
NGC 0541	A0194	✗	w	
NGC 1399	FORNAX-A	✓	w	
NGC 1713	CID 27	—	—	
NGC 2832	A0779	✓	w	
NGC 3311	A1060	✓	ch, w	29.361 ± 0.118
NGC 4839	A1656	✗	e, g	
NGC 4946	A3526	—	—	
NGC 6086	A2162	✗	g	
NGC 6160	A2197	✓	g, w	
NGC 6269	AWM5	—	—	
NGC 7012	AS0921	—	—	
NGC 7597	A2572	—	—	
NGC 7649	A2593	✗	w	
PGC004072	A0151	—	—	

Continued on Next Page . . .

Table 4.7 – Continued

Object name	**Cluster**	**CF**	**Ref.**	**t_{cool} (Gyr)**
PGC025714	A0754	✗	ch, e	70.738 ± 0.132
PGC026269	A0780	✓	e	
PGC030223	A0978	—	—	
PGC044257	A1644	✓	w	2.847 ± 0.095
PGC071807	A2622	—	—	
PGC072804	A2670	✓	w	
UGC00579	A0119	✗	ch, e, w	96.520 ± 0.562
UGC02232	A0376	✗	e	
UGC05515	A0957	✗	w	

The next step was to search for references in the literature to find previously determined t_{cool} and $\dot{M}$ values for the clusters contained in the BCG sample. These values are given in Table (4.8). Before going into a detailed analysis of Table (4.8), it should be mentioned that the central cooling times are very sensitive to the resolution of the data used (Edge et al. 1992) and consequently it is not always possible to assign a specific cooling time to the respective clusters. White et al. (1997) found that the cooling times depend on the size of the bin used in the analysis of the innermost central region of the cluster image which in turn is depended on the S/N ratio of the spectra, the distance to the cluster and therefore on the resolution of the data.

From analysing Table (4.8), it was found that 14 of the galaxies in the sample contained CFs. Out of these 14 galaxies:

- Ten galaxies, which could be represented by an SSP fit, contained CFs and were made up of ISPs.
- Four galaxies, which could be represented by 2 SSPs, contained CFs and were all made up of ISPs and OSPs but NGC 6160 was the exception, being made up of a YSP and OSP.
- For both galaxies, which could be represented by 3 SSPs, no values were found in the literature to indicate whether a CF was present or not.

The fact that the 1 SSP galaxies were comprised out of intermediate aged stellar populations and could be found in clusters which housed CFs were in agreement with the results found by Loubser et al. (2009b) in Paper 2 and were also confirmed by the photometric studies conducted by Bildfell et al. (2008).

Upon further investigation it could be seen that of the nine emission galaxies, four of these galaxies (which had an SSP fit) were contained in CF clusters while the remaining five galaxies

were located in non-CF clusters. The analysis done by Loubser et al. (2009b) also verified these results but they found that five of the nine emission galaxies were contained in CF clusters. The reason for this was due to the fact that the emission galaxy NGC 6173 was included in their analysis and excluded from this analysis. Edwards et al. (2007) found that emission galaxies tended to be found more frequently in CF clusters than in non-CF clusters. When applying this to the BCG sample, a similar trend was found, however not as pronounced as in Edwards et al. (2007). In this sample, 35% contained CFs (compared to 70% as found by Edwards et al. (2007)), 28% contained no CFs (compared to 10% as found by Edwards et al. (2007)) and for the remaining 38% no information could be found in the literature. Edge et al. (1992) found that the percentage of CFs in a cluster can be anything from 50 – 60%. However this percentage might be regarded as a lower limit because the detection can be biased towards the detection of more distant CFs located at higher redshifts and the fraction can be as high as 90%.

The fact that the majority of the CFs were housed by clusters containing intermediate or young BCGs, indicated that a possible connection existed between the presence of the CFs and recent star formation periods. This analysis have shown that CFs are responsible for some of the star formation activities, but could not account for all the star formation. However, it is difficult to pinpoint what exactly might be the cause of the star formation epochs in these galaxies. Other proposed sources for the gas fuelling the recent star formation in BCGs are the accretion of satellites and recycling of stellar ejecta. The recycling of stellar ejecta was originally proposed by Menanteau, Abraham & Ellis (2001). They found that this process leads to the blue cores of BCGs due to the increased potential well in the centre (Loubser, 2009a) which causes the star formation epoch to last longer.

Table 4.8: The cooling times and mass-deposition rate of the CFs contained in the BCG sample. Column 1 gives the names of the galaxies while Column 2 indicates whether or not the galaxy contains a CF. Columns 3 – 6 indicate the average values of the cooling time (t_{cool}) while Columns 7 – 10 give the mass-deposition rates ($\dot{M}$). These numbers are the 50th percentiles with 10th and 90th percentile limits. Column 11 gives the references to the literature from which these times and rates were derived. The values given in the 3rd and 7th columns, were derived from the 1st reference given in Column 11, the values given in the 4th and 8th columns, were derived from the 2nd reference, etc.

The references given are e = Edwards et al. (2007), f = Edge et al. (1992), ch = Chen et al. (2007), g= Giovannini et al. (2008), r = Rafferty et al. (2006) and w = White et al. (1997).

Object name	Cooling Flow	t_{cool} (Gyr)				$\dot{M}$ ($M_\odot$ / yr)				Ref.
(1)	(2)	(3)	(4)	(5)	(6)	(7)	(8)	(9)	(10)	(11)
ESO146-028	—	—	—	—	—	—	—	—	—	—
ESO202-043	—	—	—	—	—	—	—	—	—	—
ESO303-005	—	—	—	—	—	—	—	—	—	—
ESO346-003	—	—	—	—	—	—	—	—	—	—
ESO349-010	✓	$0.27^{+0.65}_{-0.65}$	0.02	$0.58^{+0.05}_{-0.05}$	—	124^{+42}_{-38}	3^{+2}_{-2}	69^{+20}_{-15}	—	f, r, ch, e
ESO444-046	✗	—	—	—	—	—	—	—	—	ch, e
ESO488-027	✓	$0.71^{+0.74}_{-0.25}$	—	—	—	10^{+32}_{-10}	—	—	—	w
ESO541-013	✓	—	$0.50^{+0.18}_{-0.11}$	0.14	$0.23^{+0.09}_{-0.04}$	—	110^{+71}_{-67}	5^{+3}_{-3}	108^{+55}_{-51}	f, w, r, c
ESO552-020	—	—	—	—	—	—	—	—	—	—
GSC555700266	✓	$0.77^{+0.48}_{-0.30}$	—	—	—	12^{+29}_{-12}	—	—	—	w
IC1101	✓	$0.29^{+0.05}_{-0.05}$	$0.53^{+0.22}_{-0.10}$	0.02	$0.26^{+0.01}_{-0.01}$	402^{+50}_{-40}	431^{+236}_{-288}	< 1.90	514^{+93}_{-78}	f, w, r, ch
IC1633	✗	—	—	—	—	—	—	—	—	w
IC4765	—	—	—	—	—	—	—	—	—	—
IC5358	✓	$0.40^{+0.02}_{-0.02}$	—	—	—	68^{+14}_{-12}	—	—	—	ch
LEDA094683	✗	—	—	—	—	—	—	—	—	w
MGC-02-12-039	✓	$0.16^{+0.02}_{-0.02}$	$0.36^{+0.10}_{-0.06}$	—	—	112^{+20}_{-16}	134^{+58}_{-85}	—	—	f, w, e
NGC0533	—	—	—	—	—	—	—	—	—	—
NGC0541	✗	—	—	—	—	—	—	—	—	w
NGC1399	✓	$0.25^{+0.09}_{-0.06}$	$2.50^{+0.20}_{-0.18}$	—	—	$> 19^{+0}_{->6}$	0^{+0}_{-0}	—	—	w, ch

Continued on Next Page . . .

Table 4.8 – Continued

Object name (1)	Cooling Flow (2)	t_{cool} (Gyr) (3)	(4)	(5)	(6)	$\dot{M}$ ($M_\odot$ / yr) (7)	(8)	(9)	(10)	Ref. (11)
NGC1713	—	—	—	—	—	—	—	—	—	—
NGC2832	✓	$0.16^{+0.77}_{-0.05}$	—	—	—	$3.10^{+1.10}_{-1.10}$	—	—	—	w
NGC3311	✓	$0.17^{+0.25}_{-0.25}$	$0.74^{+1.73}_{-0.62}$	$1.29^{+0.11}_{-0.11}$	—	9^{+9}_{-6}	$8.0^{+14.9}_{-8.0}$	0^{+0}_{-0}	—	f, w, ch
NGC4839	✗	—	—	—	—	—	—	—	—	f, e
NGC4946	—	—	—	—	—	—	—	—	—	—
NGC6086	✗	—	—	—	—	—	—	—	—	g
NGC6160	✓	$0.72^{+0.71}_{-0.19}$	—	—	—	$2.40^{+3.00}_{-2.40}$	—	—	—	w
NGC6269	—	—	—	—	—	—	—	—	—	—
NGC7012	—	—	—	—	—	—	—	—	—	—
NGC7597	—	—	—	—	—	—	—	—	—	—
NGC7649	✗	—	—	—	—	—	—	—	—	w
PGC004072	—	—	—	—	—	—	—	—	—	—
PGC025714	✗	—	—	—	—	—	—	—	—	ch, e
PGC026269	✓	—	—	—	—	—	—	—	—	e
PGC030223	—	—	—	—	—	—	—	—	—	—
PGC044257	✓	$0.31^{+0.08}_{-0.08}$	$0.96^{+0.09}_{-0.10}$	—	—	19^{+3}_{-3}	12^{+19}_{-12}	—	—	f, w
PGC071807	—	—	—	—	—	—	—	—	—	—
PGC072804	✓	$0.16^{+0.04}_{-0.04}$	$0.91^{+0.42}_{-0.24}$	—	—	—	41^{+71}_{-41}	—	—	f, w
UGC00579	✗	—	—	—	—	—	—	—	—	f, w, ch, e
UGC02232	✗	—	—	—	—	—	—	—	—	e
UGC05515	✗	—	—	—	—	—	—	—	—	w

4.8 Correlations

Researchers predict that the formation of a galaxy is closely related to the evolution of the host cluster but these tracers are not always visible in the formation of the stars because some of the stars in a galaxy could have been acquired through merging processes and could therefore have been formed before the formation of the galaxy in which they are presently found (Mo et al. 2010).

The main idea behind this analysis was to determine whether the stellar populations of the BCGs were either more influenced by their own internal properties or by the characteristic of the host cluster in which these galaxies are housed.

In the this section, any possible correlation that might exist between the derived parameters (ages and [Fe/H]) and the internal properties (the velocity dispersions and absolute K-band magnitudes) of the galaxies were analysed. This was also done for the properties of the host cluster (the X-ray temperatures, luminosities, X-ray offset and the presence of CFs) in which the respective galaxies were located.

The values for the X-ray luminosity, temperatures and the host clusters velocity dispersions were found in the literature. The X-ray offsets, indicated by Loubser et al. (2009b) were determined by finding the projected angular separations between the X-ray emission peak and the location of the BCG in the literature. For the clusters, where these offsets were not given, they calculated it from BCG and published X-ray peak coordinates. This approach could not be taken for all the clusters (indicated with the ✶ sign) because the BCGs were not located in the centre of the clusters but rather located closer to the local minimum X-ray density. The same cosmological model, used in §4.7 have been used when the X-ray properties of the clusters have been determined. All these properties, except the presence of CFs are summarised in Table (4.9).

The absolute K-magnitudes were determined from the equation given by Tayler (1994)

$$M = m - 5\,log\,(d/10) \tag{4.7}$$

where M is the absolute magnitude, m is the 2MASS K-band 20th apparent magnitude and d is taken as the galactocentic distance in parsec. Both the values for m and d have been taken from the NED database.

In the next few sections the correlations of the derived ages and [Fe/H] with the properties of the galaxies and the host clusters will be given and discussed under separate headings. The properties are analysed in the following order: (1) X-ray luminosity (L_X); (2) X-ray temperature (T_X); (3) velocity dispersions of the BCGs (σ_{BCG}); (4) host clusters velocity dispersions ($\sigma_{cluster}$); (5) absolute K-band magnitudes (M_K); (6) distance from the BCG to the X-ray peak (R_{off}) and; (7) presence of CFs.

In order to test for the presence of any correlations between the properties of the galaxies and the host clusters and the derived parameters, the data was fitted against a linear relation, y = a + b $\times$ log(x), where y is the derived parameter tested and x is the property against which the parameter is tested. A t-test was then preformed to test the null hypothesis (b=0). If the value of the t-test was larger than 1.96, then a true correlation could be found between the variables (b $\neq$ 0) at the 95% confidence level. P is the probability of being wrong in concluding that a true correlation exists between the variables. The values for the t-test and the probabilities of being wrong will be discussed under the respective headings.

It is worth noting here that because there were only two BCGs in the sample which their SFHs could be represented by 3 SSPs, the correlation with L_X, T_X, the velocity dispersions of the BCG and the host cluster as well as R_{off} were not described under these headings. The reason for this is that no correlation can be deduced with just these two BCGs.

Table 4.9: The X-ray properties and velocity dispersions of the host clusters of the galaxies in the BCG sample. Column 1 gives the names of the galaxies while Columns 2 & 3 give the X-ray luminosity (L_X) and the references to the articles where it was taken from. Column 4 gives the X-ray temperature (T_X) of the host clusters. Columns 5 & 6 give the velocity dispersion of the host cluster ($\sigma_{cluster}$) and the references where it was gotten from. Column 7 gives the projected distance between the galaxy and the X-ray peak (R_{off}). The ✶ indicates that these galaxies are not located at the centre of the clusters, but closer to the local minimum X-ray density (which is located at different coordinates as given in the literature). Column 8 gives the absolute K-band magnitude calculated from Eq. (4.7). This table was adapted from Table 7 of Paper 2.

The references are b = Böhringer et al. (2004), b_a = Böhringer et al. (2000), e = Edwards et al. (2007), ch = Chen et al. (2007), cr = Cruddace et al. (2002), l = Ledlow et al. (2003), m = Mahdavi & Geller (2001), p = Patel et al. (2006), pe = Peres et al. (1998), r = Rafferty et al. (2006), st = Struble & Rood (1991), st_a = Struble & Rood (1999) and w = White et al. (1997). If the reference has the word *cal* in front of it, it means that the value was calculated from that article.

Object Name	$L_X \times 10^{44}$ (erg s^{-1})	Ref.	T_X (keV)	$\sigma_{cluster}$ (km s^{-1})	Ref.	R_{off} (Mpc)	Ref.	M_K (mag)
ESO146-028	0.17	b	—	—	—	0.051	cal b	– 26.10
ESO202-043	—	—	—	—	—	—	—	– 25.65
ESO303-005	0.79	b	—	—	—	0.010	cal b	—
ESO346-003	0.096	cr	—	—	—	0.032	cal cr	– 25.26
ESO349-010	2.80 $\pm$ 0.06	ch	3.5	845	w	0.019	e	– 26.47
ESO444-046	6.56 $\pm$ 0.04	ch	3.8	986	w	0.019	e	– 26.60
ESO488-027	0.21	b	2.4	853	w	✶	cal b	– 25.56
ESO541-013	2.85 $\pm$ 0.04	ch	3.8	767	w	0.017	e	– 26.33
ESO552-020	0.16	b	—	—	—	0.013	cal b	– 26.06

Continued on Next Page ...

Table 4.9 – Continued

Object Name	$L_X \times 10^{44}$ (erg s^{-1})	Ref.	T_X (keV)	$\sigma_{cluster}$ (km s^{-1})	Ref.	R_{off} (Mpc)	Ref.	M_K (mag)
GSC555700266	1.28	b	2.4	596	w	0.020	cal b	– 26.58
IC1101	17.07 ± 0.18	ch	7.8	786	w	0.131	p	– 26.81
IC1633	0.20	b	3.5	738	w	0.015	cal b	– 26.46
IC4765	0.03	b	—	—	—	0.007	cal b	– 25.30
IC5358	1.92 ± 0.04	ch	—	891	m	0.002	cal b	– 25.41
Leda094683	—	—	3.7	249	w	0.044	p	—
MCG-02-12-039	3.77 ± 0.05	ch	4.7	705	w	0.031	e	– 25.89
NGC 0533	0.04	b	—	—	—	0.004	cal b	– 25.82
NGC 0541	0.14	b	1.9	480	w	0.037	cal b	– 24.89
NGC 1399	0.08 ± 0.01	ch	—	240	w	< 0.001	cal b	– 24.81
NGC 1713	—	—	—	—	—	—	cal b	– 24.60
NGC 2832	0.07	b	1.5	503	w	0.038	cal l	– 26.06
NGC 3311	0.56 ± 0.03	ch	3.3	608	w	0.015	pe	– 24.93
NGC 4839	—	—	—	—	—	✶	—	– 25.66
NGC 4946	1.19 ± 0.04	ch	—	—	—	elliptical		– 24.01
NGC 6086	—	—	—	323	st	0.053	cal l	– 25.52
NGC 6160	0.13	b_a	1.6	564	w	0.017	cal b_a	– 25.61
NGC 6269	0.36	b_a	—	—	—	0.002	cal b_a	– 26.27
NGC 7012	—	—	—	—	—	—	—	– 25.59
NGC 7597	0.58	b_a	—	676	st_a	0.048	cal b_a	– 25.43
NGC 7649	—	—	3.1	690	w	0.020	cal l	– 25.83
PGC004072	0.99	b	—	715	st	0.006	cal b	—
PGC025714	3.97 ± 0.11	ch	8.7	747	w	0.328	e	– 26.15
PGC026269	5.61	b	—	641	e. r	0.015	e	– 25.66
PGC030223	0.50	b	—	498	st_a	0.027	cal b	– 25.81
PGC044257	3.92 ± 0.34	ch	4.7	933	w	0.009	pe	– 26.46
PGC071807	—	—	—	942	st	0.249	cal b_a	– 25.63
PGC072804	2.70	b	3.9	1038	w	0.035	cal b	– 26.40
UGC00579	3.34 ± 0.05	ch	5.1	863	w	0.054	e	– 25.85
UGC022329	1.36	b_a	5.1	903	w	0.136	cal b_a	– 25.73
UGC05515	0.81	b	2.9	669	w	0.037	cal b	– 26.16

X-ray luminosity (L_X)

4.8.1 Age – Log(L_X)

Figs. (A.13a) & (A.14a) show the ages against the L_X of the BCGs which SFHs could be represented by 1 & 2 SSPs respectively, while Figs. (A.25a) & (A.26a) refer to the CF analysis.

For both the 1 & 2 SSP cases, no evidence was found to support any correlation between the derived ages and the X-ray luminosity. This was concluded from the t-test in which the t-test values for the 1 SSP case was 0.81 with a probability of 0.43. The 1 SSP case is illustrated in Fig. (A.13a) and with visual inspection no correlation could be deduced.

When analysing the 2 SSP case, shown in Fig. (A.14a) in greater detail, it was found that the ages > 0.75 Gyr changed little with increasing luminosity while the contrast was true for the younger ages of the 2 SSP fit. These ages varied significantly with increasing luminosity but no clear correlation could be derived between both the old and young derived ages and the L_X. No correlation for the two components could be deduced from the t-test, where the t-test values for the first and second components respectively were 1.41 and 0.64 with probabilities of 0.19 and 0.54.

By referring to Figs. (A.25a) it can be seen that the the majority of the CF clusters are located at higher luminosities than the non-CF clusters while Fig. (A.26a) does not show this trend. Peres et al. (1998) also found evidence to support the notion that CF clusters are located at higher X-ray luminosities due to Eq. (4.8)

$$L_{cool} = \dot{M} \times T \tag{4.8}$$

where L_{cool} is the cooling luminosity.

Once again, no correlations for the CF and non-CF clusters could be deduced from the t-test, that is the CF clusters had a t value of 1.25 with a probability of 0.25, while the non-CF clusters had a t value of 1.75 with a probability of 0.13. By referring to Fig. (A.25a), it can be seen that the younger galaxies are located in CF clusters (indicated with the black dots). Bildfell et al. (2008) found in their study that the star forming BCGs in their sample were located in cool-core clusters. This implies that the origin of the cold gas that fuels the star formation in these clusters might be linked to the processes that give rise to the L_X excess, and points to the presence of CFs as the source of the cold gas in galaxies with YSPs.

Thus, for all the cases discussed above, no clear correlations could be deduced from the t-tests due to the fact that all the t values were smaller than 1.96.

4.8.2 [Fe/H] – Log(L_X)

Figs. (A.13b) & (A.14b) show the [Fe/H] against the L_X of the BCGs which SFHs could be represented by 1 & 2 SSPs respectively, while Figs. (A.25b) & (A.26b) refer to the CF analysis.

For both the 1 & 2 SSP cases, no correlations could be found between the derived [Fe/H] and the X-ray luminosity. This was concluded from the t-test in which the t-test values for the 1 SSP case was 1.74 with a probability of 0.10. However, by inspecting Fig. (A.13a) in more detail it can

be seen that the younger BCGs are mainly found in clusters with X-ray excess. The 1 & 2 SSP cases are illustrated in Figs. (A.13b) & (A.14b) and with visual inspection no correlation could be deduced. The fact that no correlations were found between the [Fe/H] and the density of the host cluster is consistent with the result found for normal elliptical galaxies in earlier studies, i.e. Thomas et al. (2005). For the 2 SSP case no correlation for the two components could be deduced from the t-test, where the t-test values for the first and second components respectively were 0.44 and 0.42 with probabilities of 0.67 and 0.68.

By referring to Figs. (A.25b) & (A.26b), no clear correlation could be derived between the [Fe/H] of the CF and non-CF clusters for the 1 & 2 SSP cases. This is supported by the t-tests in which the t value for the CF clusters is 0.09 with a probability of 0.07, while the non-CF clusters had a t value of 1.15 with a probability of 0.29.

The t-tests indicated that no correlations existed between the derived [Fe/H] and L_X because in all the cases discussed above the t-test values were smaller than 1.93. It was stated by Loubser (2009a) that even if a slight true correlation existed between the X-ray luminosity and derived parameters, the correlations can be masked by residual effects generated in the derivation of the parameters.

X-ray temperature (T_X)

4.8.3 Age – Log(T_X)

Figs. (A.15a) & (A.16a) show the ages against the T_X of the BCGs which SFHs could be represented by 1 & 2 SSPs respectively, while Figs. (A.27a) & (A.28a) refer to the CF analysis.

For the 1 SSP case, shown in Fig. (A.15a), no evidence was found to support any correlation between the derived ages and the X-ray temperature by visual inspection. This was concluded from the t-test in which the t-test values for the 1 SSP case was 0.61 with a probability of 0.56.

Upon closer investigation of the 2 SSP case, shown in Fig. (A.16a) it was found that most of the galaxies were located at higher T_X values, more specifically > 0.15 keV. The ages > 0.75 Gyr changed little with increasing T_X but the younger ages of the 2 SSP fit varied with increasing T_X values but no trend could be deduced from these figures. For the 2 SSP case no correlation for the two components could be deduced from the t-test, where the t-test values for the first and second components respectively were 0.67 and 0.11 with probabilities of 0.53 and 0.92.

By referring to Figs. (A.27a) & (A.28a), no clear correlation could be derived between the ages of the CF and non-CF clusters for the 1 & 2 SSP cases. This is supported by the t-tests in which the t value for the CF clusters is 0.82 with a probability of 0.45, while the non-CF clusters had a t value of 1.93 with a probability of 0.31.

Thus, for all the cases discussed above, no clear correlations could be deduced from the t-tests due to the fact that all the t values were smaller than 1.96.

4.8.4 [Fe/H] – Log(T_X)

Figs. (A.15b) & (A.16b) show the [Fe/H] against the T_X of the BCGs which SFHs could be represented by 1 & 2 SSPs respectively, while Figs. (A.27b) & (A.28b) refer to the CF analysis.

For both the 1 & 2 SSP cases, no evidence was found to support any correlation between the derived [Fe/H] and the X-ray temperature. This was concluded from the t-test in which the t-test values for the 1 SSP case was 1.75 with a probability of 0.12. The 1 & 2 SSP cases are illustrated in Figs. (A.15b) & (A.16b) and with visual inspection no correlation could be deduced. For the 2 SSP case no correlation for the two components could be deduced from the t-test, where the t-test values for the first and second components respectively were 0.18 and 1.12 with probabilities of 0.86 and 0.30.

By referring to Figs. (A.27b) & (A.28b), no clear correlation could be derived between the [Fe/H] of the CF and non-CF clusters for the 1 & 2 SSP cases. This is supported by the t-tests in which the t value for the CF clusters is 0.40 with a probability of 0.05, while the non-CF clusters had a t value of 0.07 with a probability of 0.10.

The t-test indicated that no correlation existed between the derived [Fe/H] and T_X because in both cases the t-test value was smaller than 1.93.

Velocity dispersion of the BCGs and host clusters

4.8.5 Age – Log(σ_{BCG})

Figs. (A.29) & (A.30) show the ages against the σ_{BCG} of the BCGs which SFHs could be represented by 1 & 2 SSPs respectively, while Figs. (A.29a) & (A.30a) refer to the CF analysis.

For the 1 SSP case (shown in Fig. (A.29)) no evidence was found to support any correlation between the derived ages and the σ_{BCG} through visual inspection. This was concluded from the t-test in which the t-test values for the 1 SSP case was 1.43 with a probability of 0.02.

When Fig. (A.18a), which represents the 2 SSP fit, was analysed, it was found that all the galaxies were grouped closely together in the range $2.34 < \mathrm{Log}(\sigma_{BCG}) < 2.60$ km s^{-1}. Upon closer investigation it was found that the ages > 0.75 Gyr changed little with increasing Log(σ_{BCG}) values but the younger ages of the 2 SSP fit varied significantly with increasing Log(σ_{BCG}) values. Once again no clear correlation could be deduced because the t-test values for the two components respectively were 1.87 and 0.44 with probabilities of 0.01 and 0.67.

By referring to Fig. (A.29a) no trend could be deduced. Once again, no correlations for the CF and non-CF clusters could be deduced from the t-test, that is the CF clusters had a t value of 1.82 with a probability of 0.02, while the non-CF clusters had a t value of 1.03 with a probability of 0.13. Fig. (A.30a) indicated that the ages of the second components of the CF clusters are almost consistent with the ages of the second components of the non-CF clusters while the ages of the first component of the CF clusters varied significantly from the ages of the first component of the non-CF clusters with increasing $\sigma_{\rm BCG}$ values.

Thus, for all the cases discussed above, no clear correlations could be deduced from the t-tests due to the fact that all the t values were smaller than 1.96.

4.8.6 [Fe/H] – Log($\sigma_{\rm BCG}$)

Figs. (A.17b) & (A.18b) show the [Fe/H] against the $\sigma_{\rm BCG}$ of the BCGs which SFHs could be represented by 1 and 2 SSPs respectively, while Figs. (A.29b) & (A.30b) refer to the CF analysis.

For both the 1 and 2 SSP cases, no evidence was found to support any correlation between the derived [Fe/H] and the BCGs internal velocity dispersions. This was concluded from the t-test in which the t-test values for the 1 SSP case was 0.06 with a probability of 0.95. The 1 & 2 SSP cases are illustrated in Figs. (A.17b) & (A.18b) and with visual inspection no correlation could be deduced. For the 2 SSP case no correlation for the two components could be deduced from the t-test, where the t-test values for the first and second components respectively were 0.08 and 0.23 with probabilities of 0.93 and 0.82. Loubser (2009a) also found that no statistically significant correlation could be found between the metallicity and velocity dispersion of BCGs.

By referring to Figs. (A.29b) & (A.30b), no clear correlation could be derived between the [Fe/H] of the CF and non-CF clusters for the 1 & 2 SSP cases. This is supported by the t-tests in which the t value for the CF clusters is 0.93 with a probability of 0.38, while the non-CF clusters had a t value of 1.27 with a probability of 0.46.

The t-tests indicated that no correlations existed between the derived [Fe/H] and Log($\sigma_{\rm BCG}$) because in all the cases discussed above the t-test values were smaller than 1.93.

4.8.7 Age – Log($\sigma_{\rm cluster}$)

Figs. (A.19a) & (A.20a) show the ages against the $\sigma_{\rm cluster}$ of the BCGs which SFHs could be represented by 1 & 2 SSPs respectively, while Figs. (A.31a) & (A.32a) refer to the CF analysis.

For both the 1 & 2 SSP cases, no evidence was found to support any correlation between the derived ages and the host cluster velocity dispersions. These results were also confirmed in Paper 2 for the 1 SSP case (shown in Fig. (A.19a)) where the authors fitted the linear equation

$P = a + b \times Log(\sigma_{\rm cluster})$ against their sample and then preformed the t-test to test the null hypothesis ($b = 0$). Although they only derived SSP equivalent ages and [Fe/H] they did not find a clear correlation between the host cluster velocity dispersion and the derived ages. This was concluded from the t-test in which the t-test values for the 1 SSP case was 0.16 with a probability of 0.88. For the 2 SSP case (Fig. (A.20a)), the ages of the 2 SSP fit, more specifically the ages > 0.75 Gyr changed little with increasing host cluster velocity dispersion but the younger ages of the 2 SSP fit changed significantly. No correlation for the two components could be deduced from the t-test, where the t-test values for the first and second components respectively were 0.41 and 0.67 with probabilities of 0.69 and 0.52.

By referring to Fig. (A.31a) it can be seen that the majority of the non-CF clusters are comprised out of OSP and are located at lower velocity dispersions while the majority of the CF clusters are comprised out of ISP and YSP and are located at higher velocity dispersions. Fig. (A.32a) indicated the contrast, more specifically the non-CF clusters are located at higher velocity dispersions than the CF clusters. However, no statistically significant correlations for the CF and non-CF clusters could be deduced from the t-test, that is the CF clusters had a t value of 0.18 with a probability of 0.86, while the non-CF clusters had a t value of 1.59 with a probability of 0.06.

Thus, for all the cases discussed above, no clear correlations could be deduced from the t-tests due to the fact that all the t values were smaller than 1.96.

4.8.8 [Fe/H] – Log($\sigma_{\rm cluster}$)

Figs. (A.19b) & (A.20b) show the [Fe/H] against the $\sigma_{\rm cluster}$ of the BCGs which SFHs could be represented by 1 & 2 SSPs respectively, while Figs. (A.31b) & (A.32b) refer to the CF analysis.

For both the 1 & 2 SSP cases, no evidence was found to support any correlation between the derived [Fe/H] and the host cluster velocity dispersions. This was concluded from the t-test in which the t-test values for the 1 SSP case was 0.37 with a probability of 0.72. The 1 & 2 SSP cases are illustrated in Figs. (A.13b) & (A.14b) and with visual inspection no correlation could be deduced. These results were also confirmed by Loubser et al. (2009b) in Paper 2 where they could not find a clear correlation between the host cluster velocity dispersion and the SSP derived [Fe/H]. For the 2 SSP case no correlation for the two components could be deduced from the t-test, where the t-test values for the first and second components respectively were 0.53 and 1.11 with probabilities of 0.61 and 0.30.

By referring to Figs. (A.31b) & (A.32b), no clear correlation could be derived between the [Fe/H] of the CF and non-CF clusters for the 1 & 2 SSP cases. This is supported by the t-tests in which the t value for the CF clusters is 0.14 with a probability of 0.89, while the non-CF clusters had a t value of 1.01 with a probability of 0.04.

The t-tests indicated that no correlations existed between the derived [Fe/H] and Log($\sigma_{\rm cluster}$) because in all the cases discussed above the t-test values were smaller than 1.93.

The K-band magnitude

4.8.9 Age – M_K

Figs. (A.21a) & (A.22a) show the ages against the K-band magnitudes of the BCGs which SFHs could be represented by 1 & 2 SSPs respectively, while Figs. (A.33a) & (A.34a) refer to the CF analysis.

For both the 1 & 2 SSP cases (shown in Figs. (A.21a) & (A.22a)), no evidence was found to support any correlation between the derived ages and the absolute K-band magnitudes. The 1 SSP correlation was also investigated by Loubser et al. (2009b) who found no correlation with the SSP derived ages. This was concluded from the t-test in which the t-test values for the 1 SSP case was 1.49 with a probability of 0.15. For the 2 SSP case, the ages > 0.75 Gyr changed little with increasing K-band magnitudes while the contrast was true for the younger ages. These ages were sensitive to the increasing K-band magnitudes. No correlation for the two components could be deduced from the t-test, where the t-test values for the first and second components respectively were 1.54 and 0.03 with probabilities of 0.15 and 0.98.

By referring to Figs. (A.33a) & (A.34a), no clear correlation could be derived between the ages of the CF and non-CF clusters for the 1 & 2 SSP cases. That follows because the CF clusters had a t value of 1.32 with a probability of 0.22, while the non-CF clusters had a t value of 1.66 with a probability of 0.14.

Thus, for all the cases discussed above, no clear correlations could be deduced from the t-tests due to the fact that all the t values were smaller than 1.96.

4.8.10 [Fe/H] – M_K

Figs. (A.21b) & (A.22b) show the [Fe/H] against the K-band magnitudes of the BCGs which SFHs could be represented by 1 and 2 SSPs respectively, while Figs. (A.33b) & (A.34b) refer to the CF analysis.

For both the 1 & 2 SSP cases, no evidence was found to support any correlation between the derived [Fe/H] and the absolute K-band magnitudes. The 1 SSP correlation was also investigated by Loubser et al. (2009b) who found no correlation with the SSP derived [Fe/H]. No correlation could be deduced from Fig. (A.21b) due to the fact that the test value for the 1 SSP case was 0.77 with a probability of 0.45. For the 2 SSP case, shown in Fig. (A.22b), no correlation for the two components could be deduced from the t-test, where the t-test values for the first and second

components respectively were 0.30 and 0.90 with probabilities of 0.77 and 0.38.

By referring to Figs. (A.33b) & (A.34b), no clear correlation could be derived between the [Fe/H] of the CF and non-CF clusters for the 1 & 2 SSP cases. That follows because the CF clusters had a t value of 0.50 with a probability of 0.63, while the non-CF clusters had a t value of 1.03 with a probability of 0.34.

The t-tests indicated that no correlations existed between the derived [Fe/H] and L_X because in all the cases discussed above the t-test values were smaller than 1.93.

The presence of old and red stellar populations in massive ETG influences the K-band magnitudes. These magnitudes are also a good measurement of the total stellar mass of ETGs and the absolute K-band magnitudes, used in these correlations were extracted from the 2MASS database. This database was the ideal choice since Lauer et al. (2007) found that the photometry used in the 2MASS survey had the smallest chance to be influenced by possible errors which will be caused by sky subtractions and crowding effects. These magnitudes were not corrected for passive evolution. During their study, Loubser et al. (2009b) found that it will not make any significant difference whether or not a correlation could be detected between the derived parameters (ages and [Fe/H]) and K-band magnitudes. This was concluded from an analysis conducted by Brough et al. (2007) who found by using the stellar population synthesis code of Bruzual & Charlot (2003) and assuming that the galaxies were formed in a single formation burst and are 10 Gyr old, that this correlation was only -0.2 *mag for a galaxy located at* $z \sim 0.054$.

Offset between the galaxy and the X-ray peak (R_{off})

4.8.11 Age – R_{off}

Figs. (A.23a) & (A.24a) show the ages against the R_{off} of the BCGs which SFHs could be represented by 1 & 2 SSPs respectively while, Figs. (A.35a) & (A.36a) refer to the CF analysis.

For both the 1 & 2 SSP cases, it was found that most of the BCGs were located with a X-ray offset of < 0.05 Mpc and some of the BCGs were located at an X-ray offset of > 0.10 Mpc. Most of the BCGs were located very close to the centres of the clusters. When analysing Figs. (A.23a) & (A.24a) it was found that there did not exist any significant difference between the R_{off} of the intermediate and old aged BCGs. This is in contrast to what was found by Bildfell et al. (2008). The t-test for the 1 SSP case indicated that a true correlation could be found between R_{off} and the ages due to the fact that the t value was determined to be 2.56 with a probability of 0.02. However, no correlation for the two components of the 2 SSP case could be deduced from the t-test, where the t-test values for the first and second components respectively were 0.62 and 0.52 with probabilities of 0.54 and 0.61.

When analysing Figs. (A.35a) & (A.36a) in detail, it followed that the BCGs made up of ISPs and contained in CF clusters were located closer to the centre of the respective CF clusters that contained BCGs with OSPs. More specifically, eight BCGs, comprised out of ISPs and OSPs and contained in CF clusters were located closer to the centre of the clusters while one BCGs, comprised out of OSPs and contained in CF clusters were located farther away from the centre of the clusters. In contrast, it was found that seven BCGs, comprised out of ISPs and OSPs and contained in non-CF clusters were located closer to the centre of the clusters while only one BCGs, comprised out of OSPs and contained in non-CF clusters were located farther away from the centre of the clusters. Loubser et al. (2009b) also found that intermediate aged BCGs were found in CFs and confirmed the results derived from both Fig. (A.35a) & (A.23a) but they found that that these intermediate aged BCGs were not necessary located closer to the centre of the clusters than the older BCGs.

Rafferty et al. (2008) found that a central galaxy will undergo a period of star formation when the (1) X-ray centre and galaxy's centre of mass are within $\sim$ 0.02 Mpc of each other and; (2) $t_{cool} < 0.8$ Gyr or similarly $K_0 = 30\,\mathrm{keV\ cm^2}$. Hence, for star formation to be a consequence of CFs, the younger stars have to be located very close to the centre of the clusters even if these stars are not located in a CF. From the results derived in the analysis of Fig. (A.35a), only five of the seven intermediate aged BCGs were located in CFs located at $\sim$ 0.02 Mpc and thus not all of the star formation activities can be due to the presence of CFs. However, the t-test did not indicate any significant correlations between the ages and the CF and non-CF clusters. This is because the t-tests gave the following values for the respective cases — the t value for the CF clusters is 1.34 with a probability of 0.22, while the non-CF clusters had a t value of 1.14 with a probability of 0.07.

For the 1 SSP case, a statistically significant correlation could be deduced between the ages and R_{off} due to the fact that the t value was larger than 1.96. This correlation implies that galaxies contained in CF clusters and comprised out of ISPs are located at or near the centres of their respective clusters than the older CF clusters. This in turn implies that at least some of the star formation activity (but not all of it) can be accounted for by the presence of the CFs in the clusters. The influence of CFs can be limited by either feedback processes or by the physical extent of the CFs (Loubser, 2009a).

4.8.12 [Fe/H] – $\mathbf{R_{off}}$

Figs. (A.23b) & (A.24b) show the [Fe/H] against the R_{off} of the BCGs which SFHs could be represented by 1 & 2 SSPs respectively, while Figs. (A.35b) & (A.36b) refer to the CF analysis.

For both the 1 & 2 SSP cases, no correlations could be found between the derived [Fe/H] and R_{off}. This was concluded from the t-test in which the t-test values for the 1 SSP case was 0.72 with a probability of 0.48. The 1 & 2 SSP cases are illustrated in Figs. (A.23b) & (A.24b) and with visual inspection no correlation could be deduced. For the 2 SSP case no correlation for the two components could be deduced from the t-test, where the t-test values for the first and second

components respectively were 0.53 and 0.96 with probabilities of 0.61 and 0.36.

By referring to Figs. (A.35b) & (A.36b), no clear correlation could be derived between the [Fe/H] of the CF and non-CF clusters for the 1 & 2 SSP cases. This is supported by the t-tests in which the t value for the CF clusters is 0.18 with a probability of 0.86, while the non-CF clusters had a t value of 0.80 with a probability of 0.45.

In summary: No trend, what so ever could be deduced between the derived [Fe/H] and any of the properties investigated. This could be because the exclusion of the $\alpha-$enhancements in the P.HR model. This would influenced the [Fe/H] values of the stellar populations derived with this model. When investigating the correlations between the derived ages and the properties I found that for the clusters which had complex SFHs, the ages of OSP components did not change significantly with increasing values of the properties inspected, while the contrast was true for the ages of the YSP and ISP components. The CF clusters are located at higher X-ray luminosities than the non-CF clusters. Galaxies, comprised out a single OSP and having no CF, are located at higher host cluster velocity dispersions than YSP/ISP clusters containing CFs. When studying galaxies with more complex SFHs the opposite was found: non-CF clusters are located at higher velocity dispersions than the CF clusters. The majority of the galaxies containing CFs and comprised out of ISPs are located at or near the centres of their respective clusters than the older CF clusters. This in turn implies that at least some of the star formation activity (but not all of it) can be accounted for by the presence of the CFs in the clusters.

CHAPTER 5

SUMMARY, CONCLUSIONS AND FUTURE WORK

"You stood before creation
eternity within Your hand.
You spoke all life into motion.
My soul now to stand in awe
of the One who gave it all."

Taken from The Stand
PREFORMED BY HILLSONG

5.1 Introduction

Central galaxies are often defined as the most massive ETGs. Dressler (1980a) found that these galaxies are found in the densest part of the host clusters and the SFRs of the ETGs located in these high density environments are lower than the galaxies located in less dense environments (Kauffmann et al. 2004). From this it followed that the most massive galaxies formed stars at a lower rate per unit mass (Liu et al. 2012) than the less massive ones. This was supported by the studies, for example, conducted by Thomas et al. (2005) who found that most of the stars in these massive ETGs formed at earlier periods than those stars found in less massive galaxies.

A special sub-class of these massive ETGs, namely BCGs were studied in this analysis. These galaxies are usually located close to or in the densely populated centres of the clusters and hence it was expected that these galaxies were made up of old stars and did not experience any significant star formation epochs. These BCGs present astronomers with a conundrum when they study the formation and evolution of these galaxies because BCGs have quite unique properties, i.e. the surface brightness profiles of BCGs are different from that of ordinary, massive ETGs.

A study conducted by Edwards et al. (2007) on the presence of emission lines in BCGs, found that the presence of emission lines increased in the presence of CFs. This and similar studies confirmed that some of the BCGs experienced periods of significant and recent star formation. This in turn provided astronomers with evidence to suggest that the evolution of these galaxies were not that straightforward and simple, as widely assumed.

This project tried to answer the question of whether the SFHs of the BCG sample could be represented by a single epoch of star formation or whether a more complex approach was needed, more specifically to determine whether CSPs were needed. Another aim was to determine whether the internal BCG properties or the properties of the host cluster environment formed any meaningful correlations with the derived ages and [Fe/H] which would help with the unraveling of the evolution and formation of BCGs.

5.2 Brief Summary of Analysis

High S/N ratio, long–slit spectra have been obtained for a BCG sample consisting of 49 BCGs and two elliptical galaxies which were observed on the GTs and the WHT.

The observed spectra of these galaxies were fitted against the stellar population models, more specifically the P.HR and V/M models, included in the *ULySS* software package. *ULySS* was used in the analysis of this project. These models were used to determine the SFHs of the galaxies, more specifically whether an SSP or a CSP provided the most probable representation of the SFHs. These models were broadened by defining additional input parameters, for example, the redshifts, velocity dispersions, error spectra and a wavelength range of (3800, 6000) Å for each of the respective galaxies. I also incorporated a LSF to match the resolutions of the models with that of the observed spectra of the galaxies. The observed spectrum of each galaxy was respectively fitted against an SSP and a CSP model and then the χ^2-statistical test were preformed to assist in choosing the most probable fit. A series of 500 MC simulations were then performed, checking the residual of the fits and assessing the relevance of the solutions, aiding the selection of the most probable SFH of the BCGs. After this, the χ^2-maps were drawn to assist in understanding the structure of the parameter space.

The SFHs of the galaxies, derived with the P.HR and V/M models were given in the form of stellar population components characterised by the derived ages and [Fe/H]. These ages and [Fe/H] were then compared to that derived with the LICK indices to determine whether these different approaches produced consistent results. Lastly the derived ages and [Fe/H] were tested against the internal BCG properties and the properties of the host cluster environment to see whether any correlations could be derived to shed light on the evolution and formation of BCGs.

5.3 Conclusions

(i) Although Koleva et al. (2008) found that the P.HR and V/M models produced consistent results when the deriving ages and [Fe/H] of these two models were compared, I found that the majority of my results in Columns 2 & 3 in Table (3.5a) showed consistencies except in the cases of ESO303-005, IC1633 and NGC 2832. When comparing the results derived by both these methods it was found that 17 of the 40 galaxies in the BCG sample could best be represented by the P.HR model and only 13 of the 40 galaxies could best be represented by the V/M model. Therefore the P.HR model was the model that gave the most probable representation of the SFHs of the largest part of the BCG sample and therefore only this model was used in the further analysis of the BCG sample.

(ii) Out of the BCG sample containing 40 galaxies, the P.HR model indicated that the SFHs of 22 of these galaxies could be represented by a single star formation epoch, more specifically with an SSP fit, while SFHs of 16 galaxies could be represented by 2 SSPs and the remaining two galaxies indicated that 3 SSPs provided the most probable representation of their SFHs.

A more detailed analysis showed that 55% of the galaxies in the sample experienced a single star formation epoch and were all comprised out of ISPs. 40% of galaxies in the sample could be represented by 2 SSPs for which half of these galaxies had first components containing YSPs and ISPs, while all the galaxies had OSPs as second components. The remaining 5% of the galaxies in the sample could be represented by 3 SSPs that both had a YSP as a first component, an ISP as a second component and an OSP as a third component.

Within the framework of the current model calculations, I conclude that although the majority of the sample experienced a single star formation epoch, the remaining 45% of the galaxies in the sample experienced a more recent star formation period as shown by the 2 & 3 SSPs which in turn indicated that at least some of the BCGs in the sample had a more complex SFH than first assumed by astronomers.

(iii) The ages of the galaxies which could be represented by an SSP fit, showed a significant consistency when the values as determined by both the P.HR model and the LICK indices were compared. This is because the ages and [Fe/H] derived by the LICK indices are SSP equivalent parameters and hence these two methods could be compared when looking at the ages of the galaxies with an SSP fit.

When comparing the [Fe/H] derived by these two methods, I found no consistency when the values were compared. The reason for this is because the current P.HR model does not include $\alpha-$enhancements.

(iv) The developers of *ULySS* have developed modified versions of the P.HR and V/M models to take the $\alpha-$enhancements into account but these models are still in the testing phase (Prugniel & Koleva, 2011). Due to the time constraints of this project I could not take the $\alpha-$enhancements into account. The enhancement will slightly change the values of the ages and [Fe/H] but it is expected that these enhancement will not change the number of components derived from the SFH analysis.

(v) Several studies, i.e. Edge et al. (1992), Liu et al. (2012) and Peres et al. (1998) have proposed possible sources for the gas fuelling the star formation in BCGs, for example: (i) CFs; (ii) the re-use of matter ejected in stellar ejections and; (iii) the accretion of other stellar matter i.e satellites. The presence of CFs has long since puzzled astronomers as to whether there existed a connection between the presence of these flows and the star formation epochs in these BCGs.

From this analysis it followed that 14 clusters in the sample contained CFs. Ten of these CFs were housed by galaxies which could be presented by an SSP and were comprised of ISPs. The remaining four CFs were housed by galaxies which were represented by 2 SSPs and comprised out of ISPs and OSPs. The fact that the majority of the CFs were housed by clusters containing intermediate or young BCGs, indicated that a possible connection existed between the presence of the CFs and recent star formation periods.

(vi) No clear correlations could be derived between the ages and [Fe/H] of the 1 & 2 SSP cases and the velocity dispersions of the BCGs and the host clusters and also for the absolute K-band magnitudes of the galaxies.

(vii) No clear correlations could be derived between the ages and [Fe/H] of the 1 & 2 SSP cases and the X-ray luminosities and the temperatures.

(viii) The galaxies containing in clusters with CFs were located at higher X-ray luminosities than the galaxies in clusters without CFs. Peres et al. (1998) found that very luminous systems harbors very massive CFs and can contribute more than 70% of the clusters bolometric luminosity.

(ix) A correlation between the ages of the SSP case and the offset between the BCG and the X-ray peak could be detected. The majority of the BCGs were located close to the centre of the clusters and it was found that the ISP galaxies, which housed CFs, were located closer to the centres than the OSP galaxies containing CFs. The fact that some of the galaxies (containing CFs) were located further away from the centre of the clusters indicates that at least in some of these galaxies, the CFs were not entirely responsible for the star formation activities. Loubser et al. (2009b) suggested that the gas fuelling the star formation activity in these galaxies had to originated from mergers because the merging/capturing of less massive galaxies are enhanced due to the unique location of the BCGs in the cluster potential well.

In summary: the P.HR model gave the most probable representation of the SFHs of the galaxies contained in the BCG sample. Although the majority of the galaxies experienced a single star formation epoch, some of the galaxies in the sample experience a period of more recent star formation activity. This indicates that at least some of these galaxies have a more complex SFH than first thought by researchers. When comparing the ages (derived with the P.HR model and the LICK indices) of the galaxies which had an SSP fit it was found that there were significant consistencies between these values. The contrast was true for the [Fe/H] values because the P.HR model does not include $\alpha-$enhancements in its algorithm. The sample contained 14 CFs, ten of which were housed in ISP galaxies and the remaining four housed in galaxies which were comprised out of YSPs/ISPs and OSPs. From this it follows that the majority of the CFs were housed in young/intermediate aged galaxies and therefore the star formation activities can be seen as a result from the presence of the CFs. No correlations could be derived between the ages and [Fe/H] of the galaxies with 1 & 2 SSP fits and the X-ray luminosity, X-ray temperature, the velocity dispersions of the BCG itself and the host clusters and the absolute K-band magnitudes of the galaxies. The galaxies containing CFs were located at higher X-ray luminosities than the non-CF galaxies and therefore contributes the majority of the clusters bolometric luminosities. A correlation could be derived between the ages of the 1 SSP galaxies and the X-ray offset, more specifically the intermediate aged galaxies (which contained CFs) are located closer to the centre of the clusters than the older galaxies containing CFs. This implies that not all the star formation activities in the BCGs can be accounted for due to the presence of CFs and hence, more than one process is responsible for the star formation in BCGs. It is proposed that the younger BCGs experience star formation due to mergers with less massive galaxies and the accretion of gas. This points to the fact that the processes in the centre of the clusters and the star formation activities are complex and not yet fully understood.

It should be noted that the derived properties discussed here were only determined for the stellar populations in the central regions of the clusters.

5.4 Future Work

There exists a lot of confusion surrounding the classification of the cD galaxies in the literature due to the lack of deep photometry which will aid researchers in distinguishing between BCGs and non-BCGs. The current method used to study the stellar populations of these BCGs is long–slit spectroscopy but this has its own limitations. For large, diffuse objects, i.e. the BCGs, the observations are limited to the centre of the galaxies and normally does not extend to the halos of the galaxies. Currently the analysis of the kinematics of the galaxies are made difficult by the constraints of the telescopes and the magnitudes of the objects being observed. In the future, deep photometric information will be used to distinguish between cD and non-cD galaxies by testing whether a halo is present or not. and by using this method, it can be guaranteed that all the galaxies in the sample are actual cD galaxies.

Using stellar population synthesis models to analyse the stellar populations of the galaxies are not that straightforward and complicated by the different assumptions made during the algorithms of the different models, for example the solar abundances of the elements and the age–metallicity degeneracy. It is these uncertainties that make the interpretation of the derived values especially difficult and subject to a number of assumptions.

The software package *ULySS* have been used to study the ages and [Fe/H] of the stellar populations of the BCGs but these derived parameters could be made more probable by using the new modified versions of the P.HR and V/M models which includes the $\alpha-$enhancements. These models are currently in the testing phase but it is expected that these models will be fully operational by the time that a follow up study will be undertaken.

Radio observations can be used to shed some light on the possible connection between the formation of the BCGs and the cluster environments. This is because BCGs are known to have different radio properties than that of ordinary galaxies, more specifically that BCGs house radio–loud AGNs which might help to solve the CF problem. Submillimeter observations can be used to observe the neutral and molecular gas contained within the BCGs and hence, determine whether there are a connection between the star formation, the presence of CFs and the mergers experienced by these young BCGs in the centres of the host clusters.

The questions posed in this project still remains largely unanswered but by using software packages to simulate the large–scale structures of the Universe, astronomers can determine and understand the evolution and formation of the galaxies and possibly identify the processes responsible for the formation of these structures. With the sensitivity of the telescopes increasing and therefore also the quality of the data, the uncertainties in the research regarding galaxy formation and evolution are expected to be diminished and hopefully eliminated.

APPENDIX A

GRAPHS PERTAINING TO THE RESULTS

The figures shown in this Appendix are the figures discussed in Chapter 4.

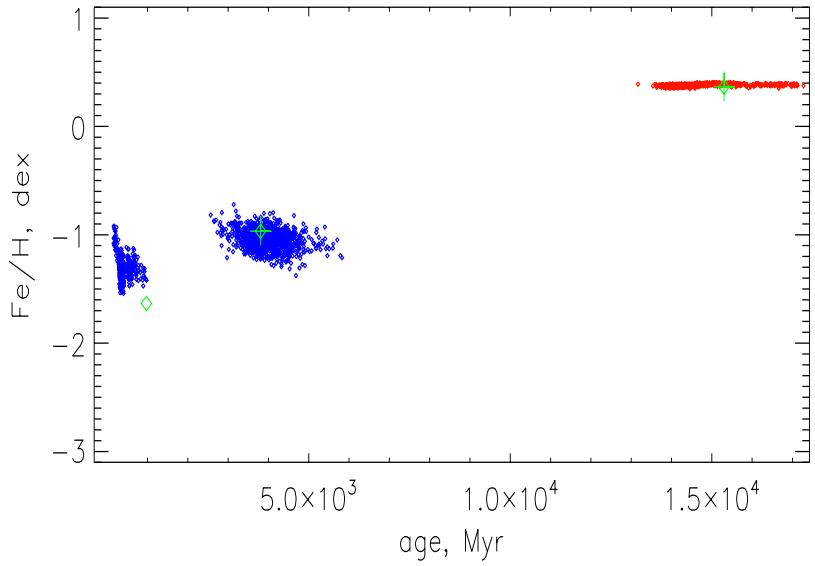

(a) Generated by the P.HR model.

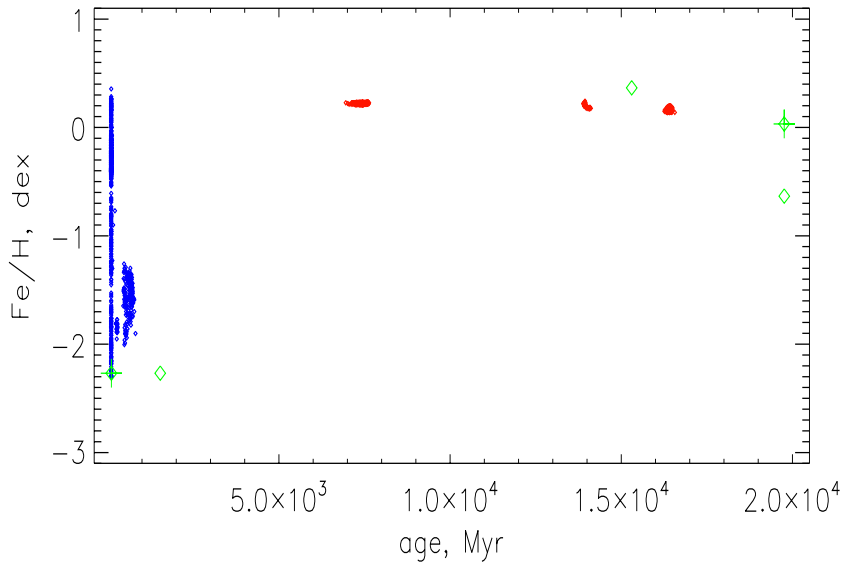

(b) Generated by the V/M model.

Figure A.1: Shown here is the SFH of ESO202-043 as determined by the models. Both models indicated that 2 SSPs gave the most probable representation of the SFH. The P.HR model gave the most probable representation because the local minima (indicated by green +) of both components coincided with the components. This was not the case for the V/M model.

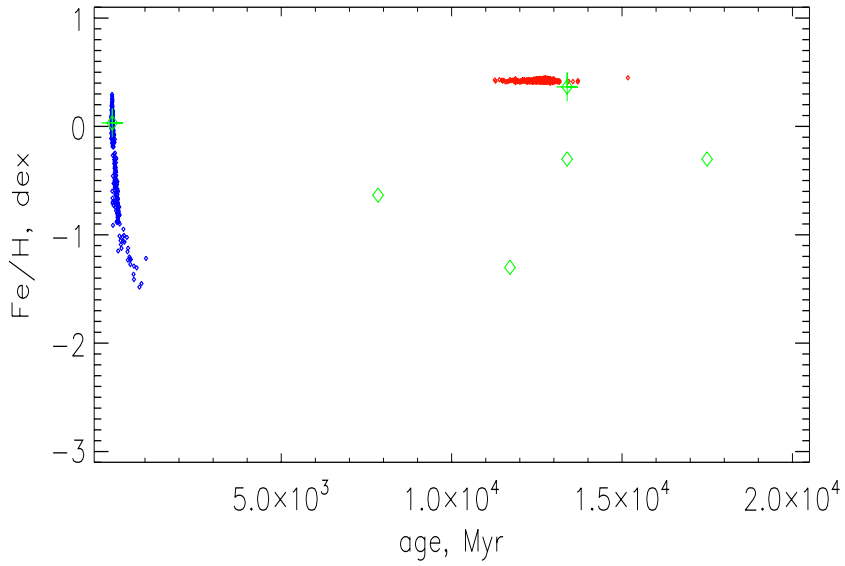

(a) Generated by the P.HR model.

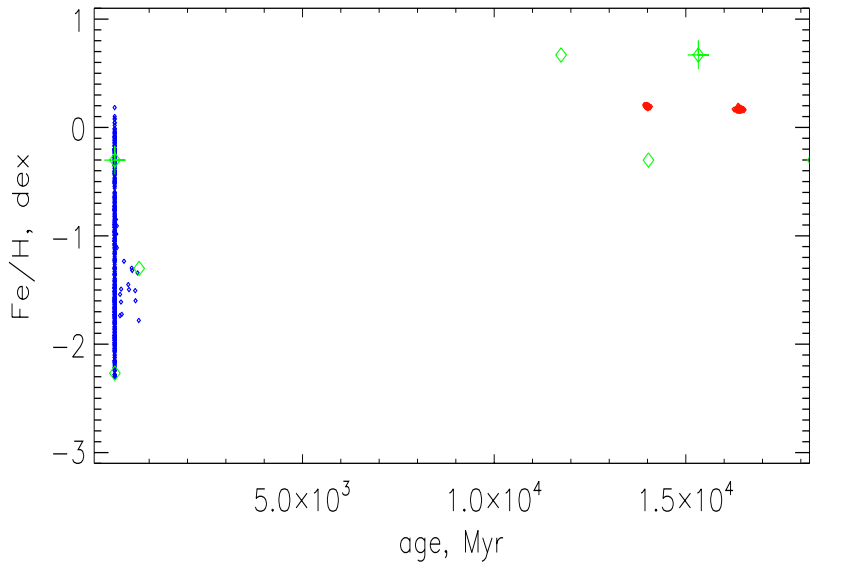

(b) Generated by the V/M model.

Figure A.2: Shown here is the SFH of ESO346-003 as determined by the models. Both models indicated that 2 SSPs gave the most probable representation of the SFH. The P.HR model gave the most probable representation because the local minimum (indicated by green +) coincided with the age spread of each component. This was not the case for the V/M model.

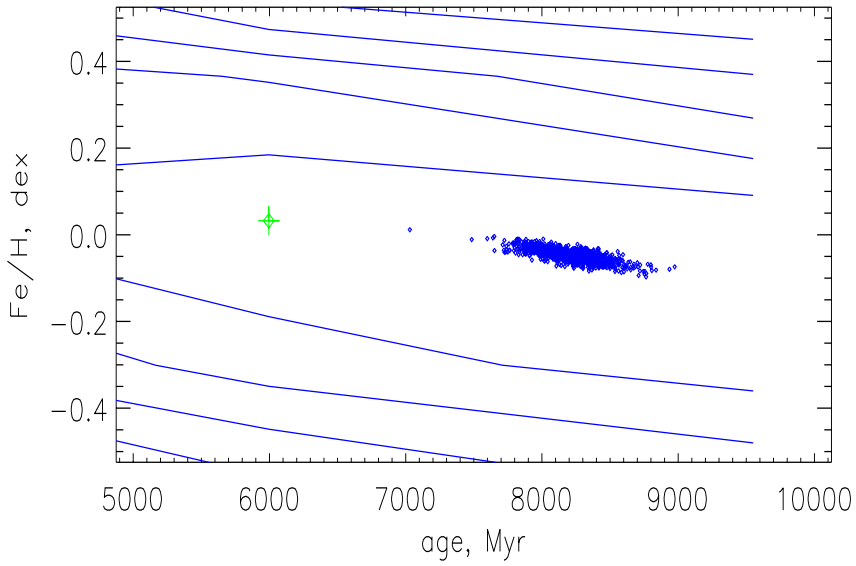

(a) Generated by the P.HR model.

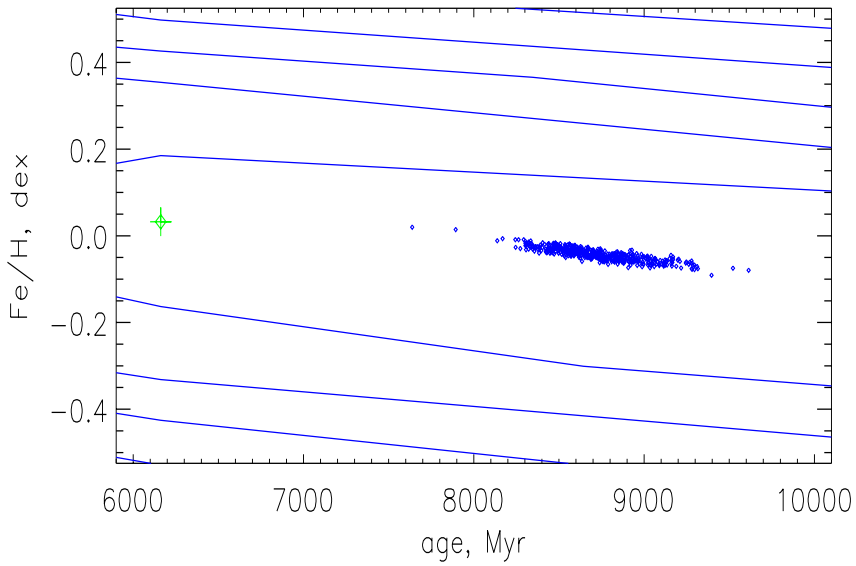

(b) Generated by the V/M model.

Figure A.3: Shown here is the SFH of PGC044257 as determined by the models. Both models indicated that an SSP gave the most probable representation of the SFH. The P.HR model gave the most probable representation because the local minimum (indicated by green $+$) was located within (2000 ± 500) Myr from the component and also in the same contour line. This was not the case for the V/M model.

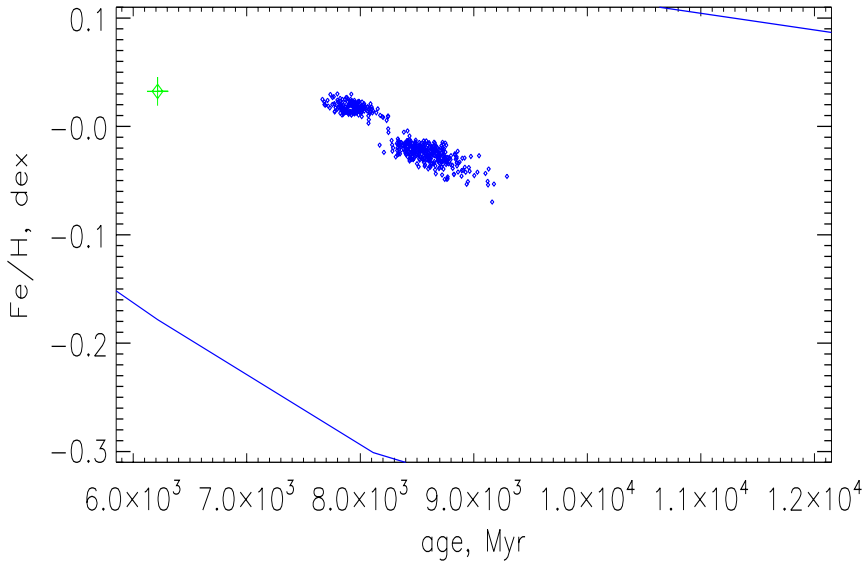

(a) Generated by the P.HR model.

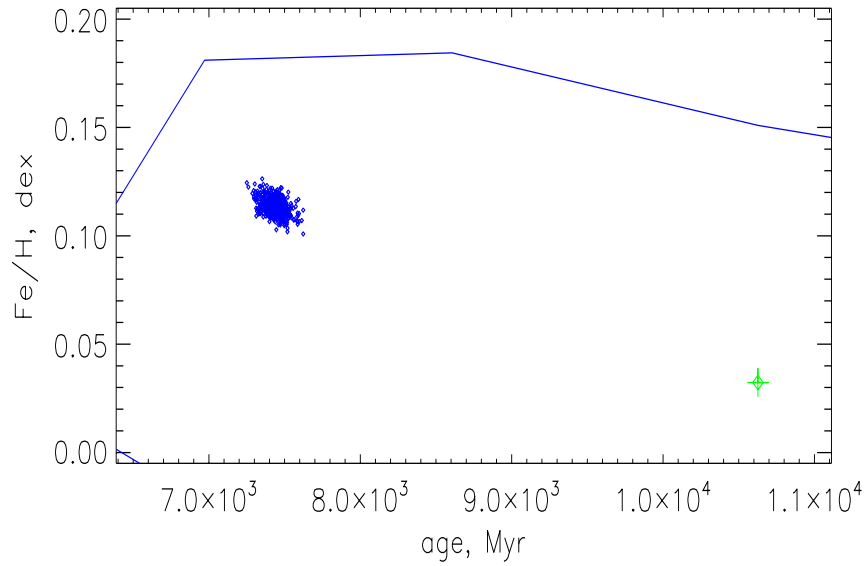

(b) Generated by the V/M model.

Figure A.4: Shown here is the SFH of UGC05515 as determined by the models. Both models indicated that an SSP gave the most probable representation of the SFH. The P.HR model gave the most probable representation because the local minimum (indicated by green $+$) was located within (2000 ± 500) Myr from the component and also in the same contour line. This was not the case for the V/M model.

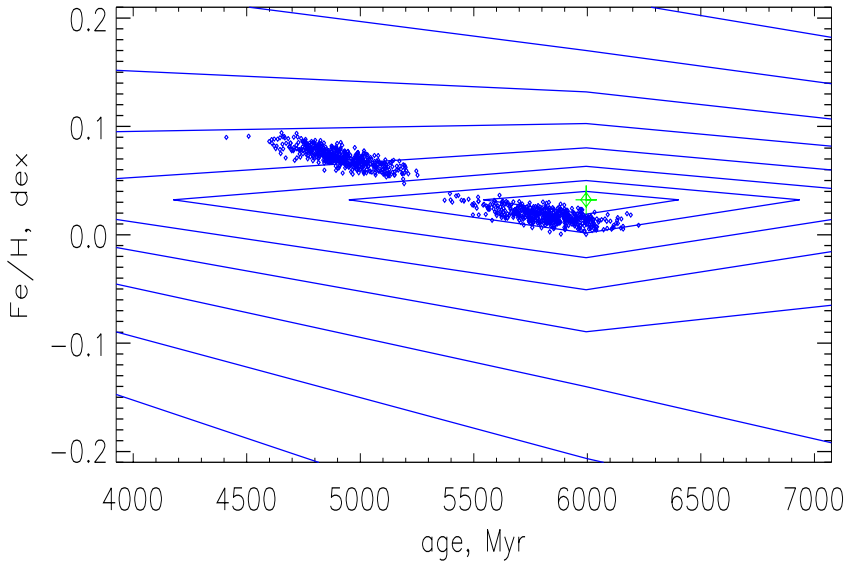

(a) Generated by the P.HR model.

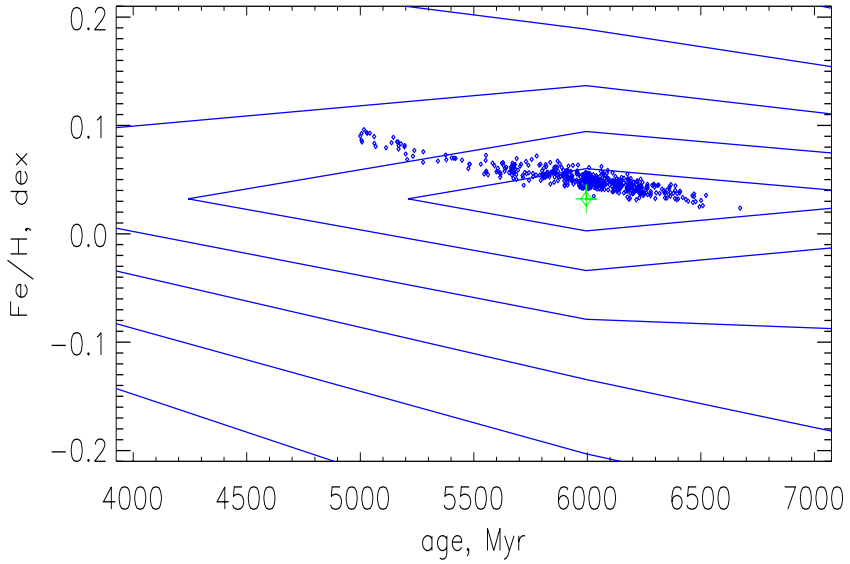

(b) Generated by the V/M model.

Figure A.5: Shown here is the SFH of NGC 3311 as determined by the models. Both the P.HR and V/M models gave the most probable representation of the SFH because the local minima (indicated by green +) and the components coincided while both the minima and components were located in the same contour line.

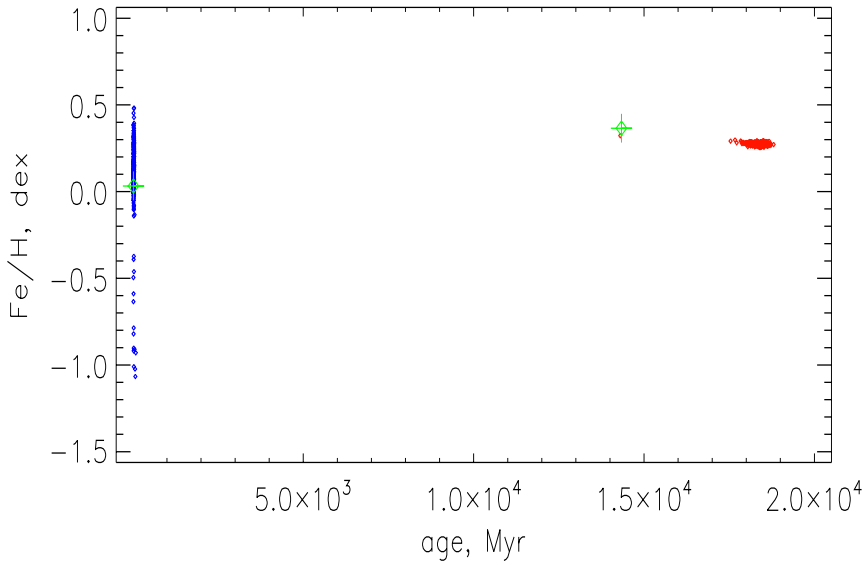

(a) Generated by the P.HR model which indicated that 2 SSPs were the most probable representation of the SFH.

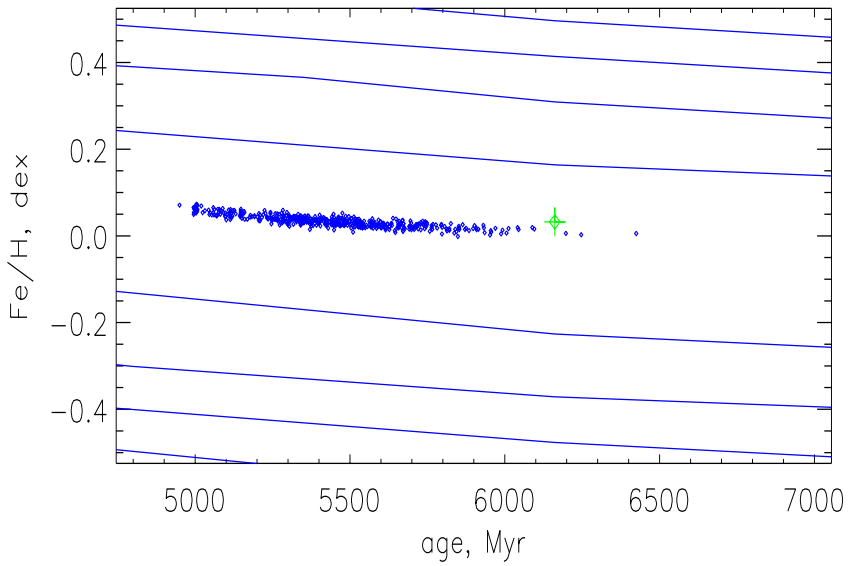

(b) Generated by the V/M model which indicated that 1 SSP was the most probable representation of the SFH.

Figure A.6: Shown here is the SFH of NGC 6269 as determined by the models. Both the P.HR and V/M models gave the most probable representation of the SFH because the local minima (indicated by green +) coincided with the components.

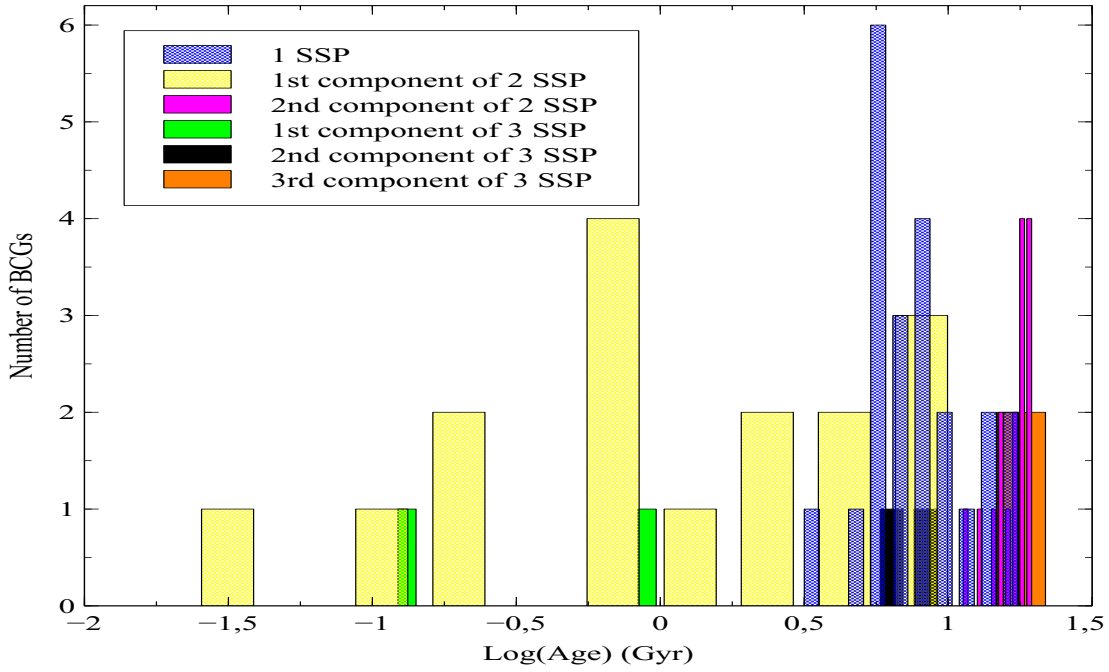

(a) Age distribution.

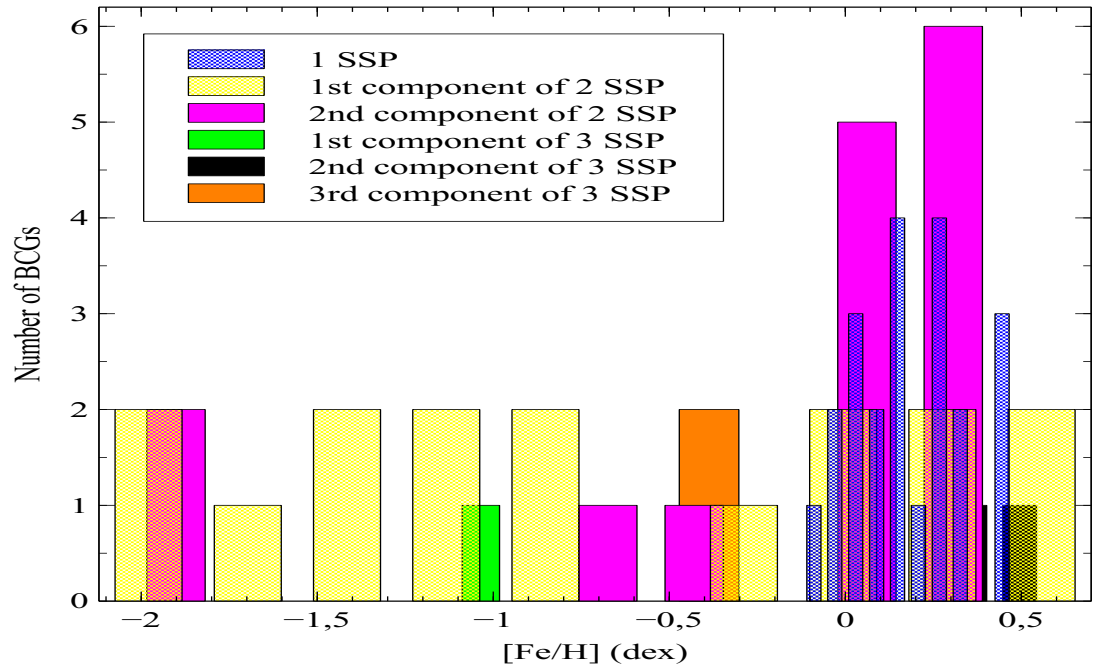

(b) [Fe/H] distribution.

Figure A.7: Age and [Fe/H] distribution of the BCG sample. The blue bars represents the 1 SSP, the yellow and purple bars the 2 SSPs while the green, black and orange bars represents the 3 SSPs.

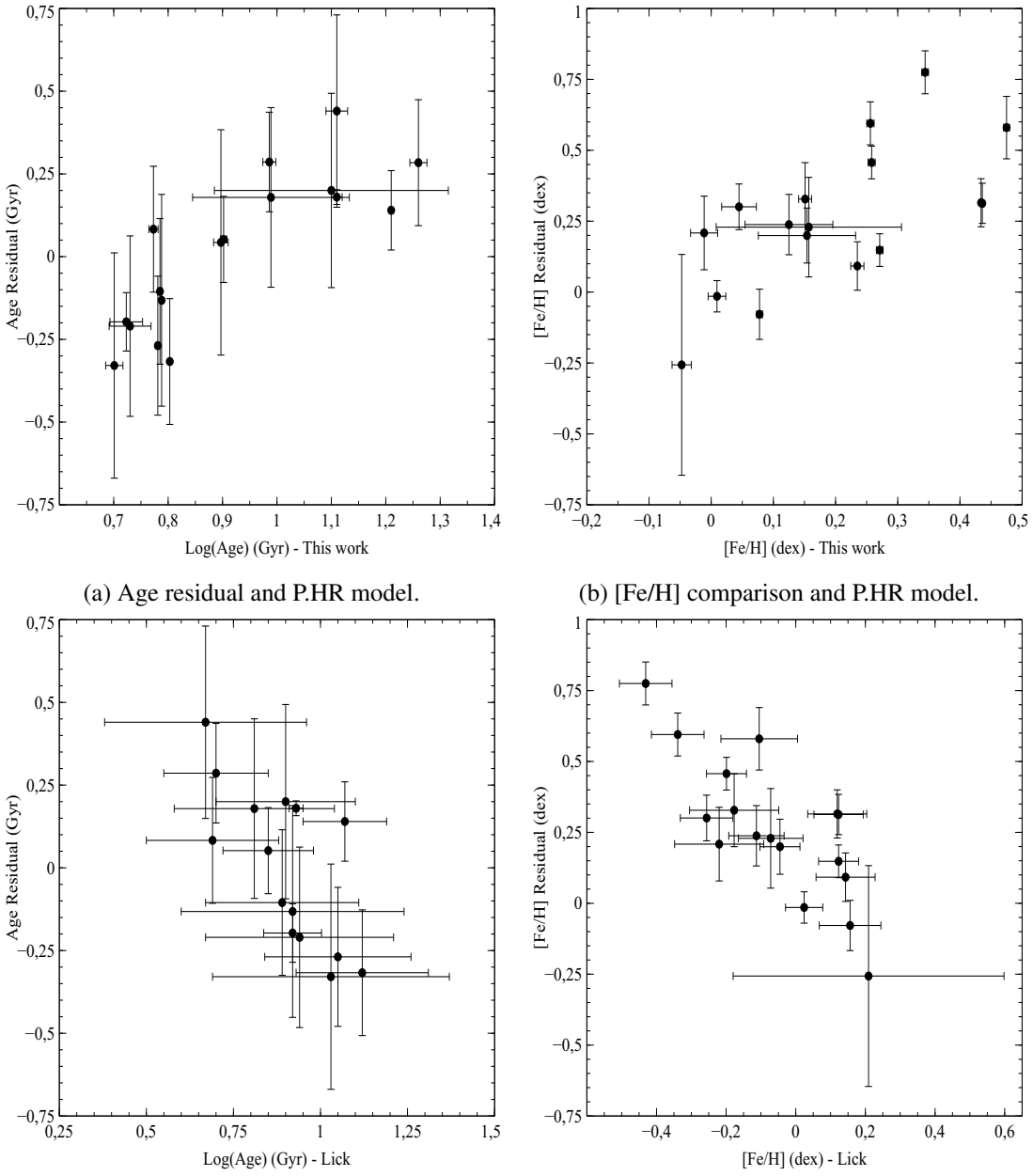

(a) Age residual and P.HR model.

(b) [Fe/H] comparison and P.HR model.

(c) Age residual and LICK indices.

(d) [Fe/H] comparison and LICK indices.

Figure A.8: Comparison of the age and [Fe/H] residuals between the P.HR model and LICK indices.

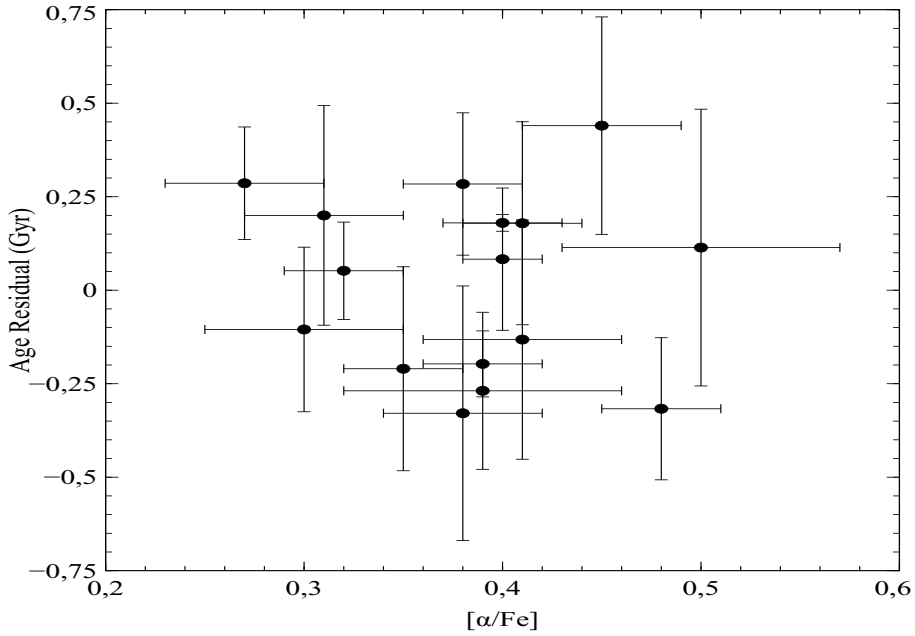

(a) Age residual.

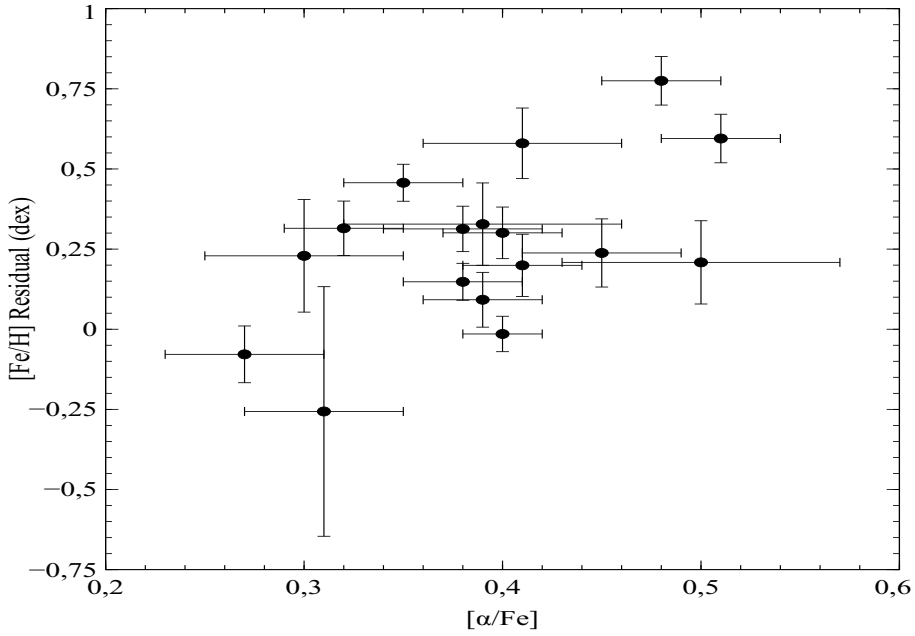

(b) [Fe/H] residual.

Figure A.9: Comparison of the age and [Fe/H] residuals with the $\alpha-$enhancements.

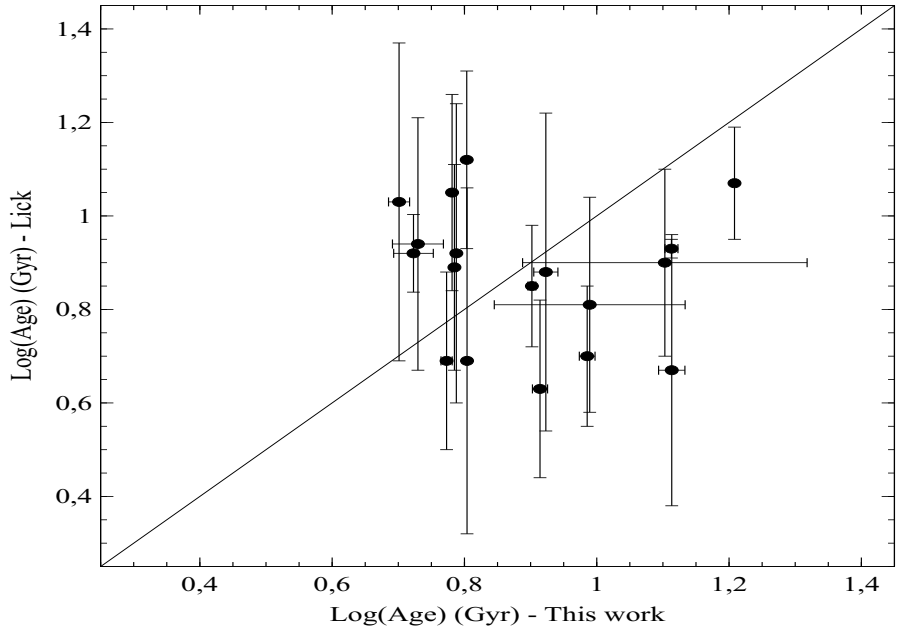

(a) Age comparison.

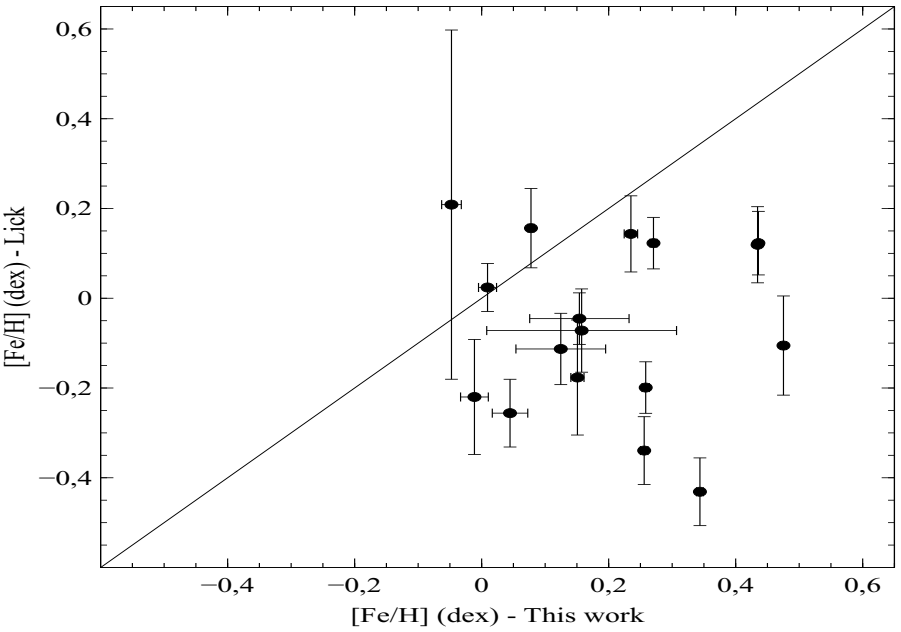

(b) [Fe/H] comparison.

Figure A.10: Comparison of the ages and [Fe/H] derived by the LICK indices and the P.HR model. For this comparison only the galaxies, for which the P.HR model determined that 1 SSP was the most probable representation of the SFHs, were used.

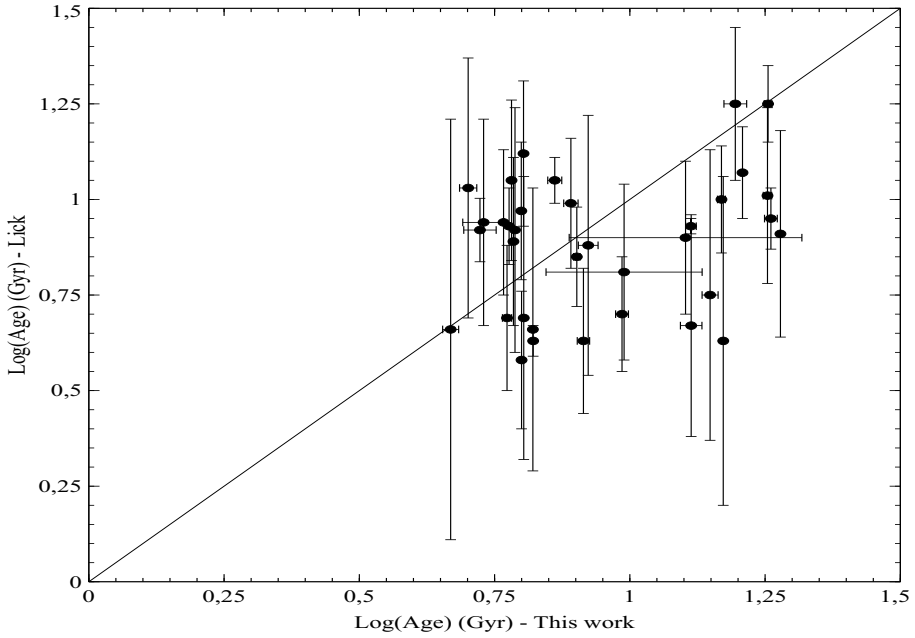

(a) Age comparison.

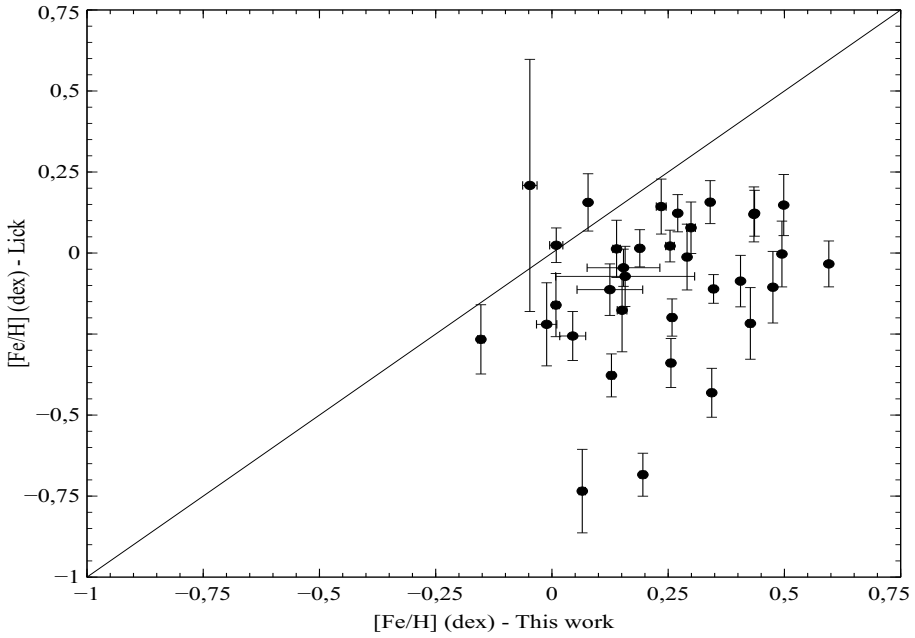

(b) [Fe/H] comparison.

Figure A.11: Comparison of the ages and [Fe/H] derived by the LICK indices and the P.HR model. For this comparison each galaxy in the BCG sample was fitted against a 1 SSP model.

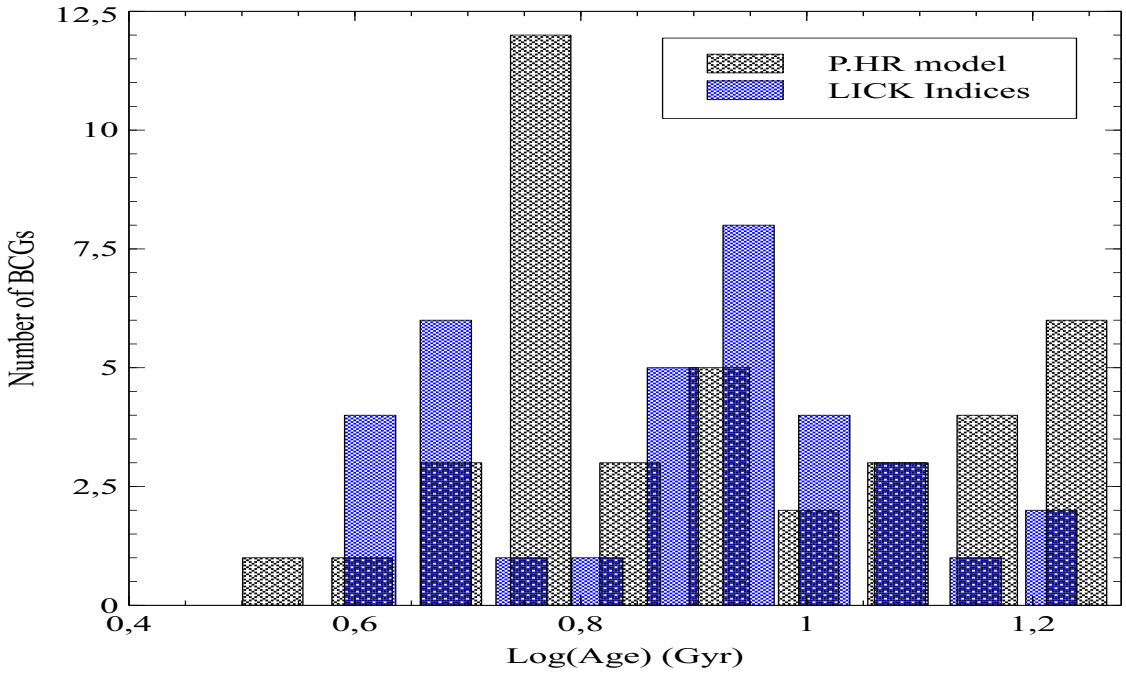

(a) Age distribution.

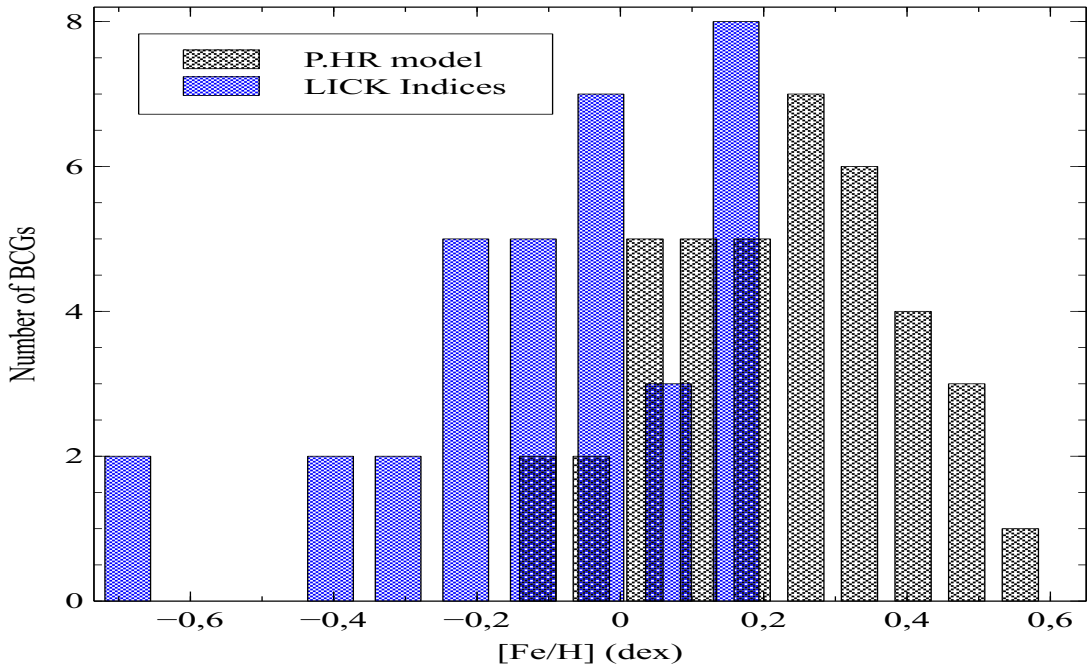

(b) [Fe/H] distribution.

Figure A.12: Age and [Fe/H] distribution of the BCG sample determined by the P.HR model and the LICK indices. The black bars represents the P.HR model while the blue bars represent the LICK indices.

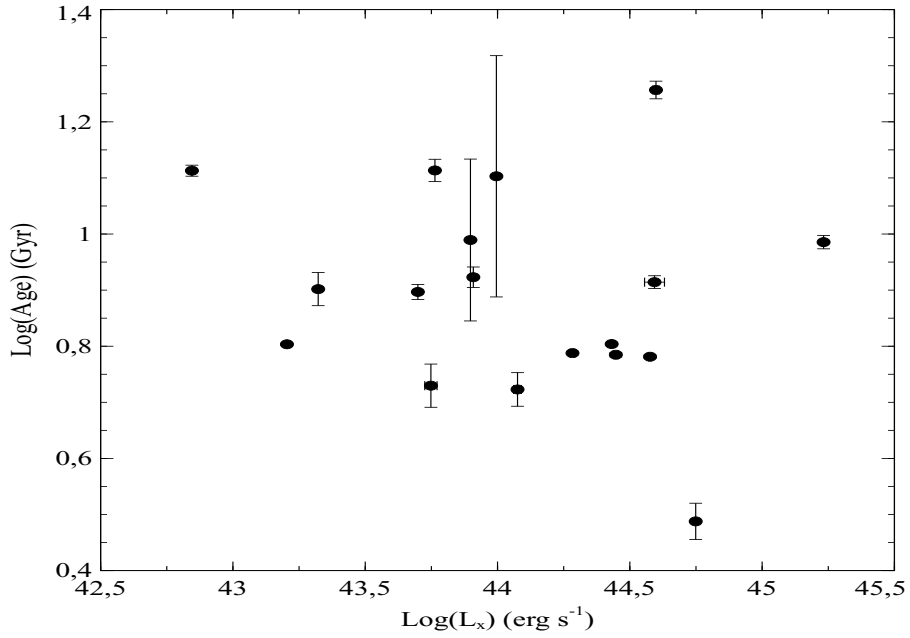

(a) Age – Log(L_X)

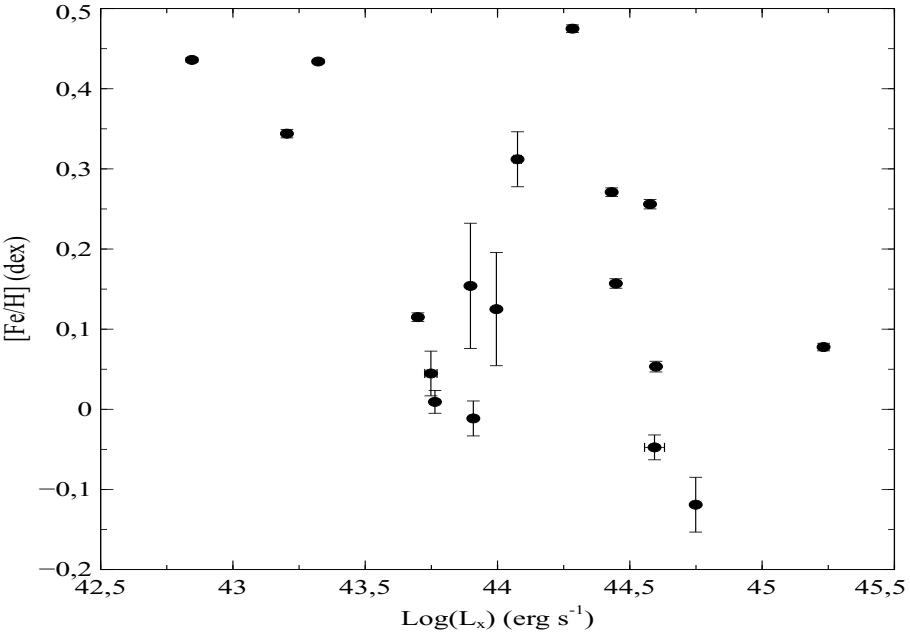

(b) [Fe/H] – Log(L_X)

Figure A.13: Shown here is the age and [Fe/H] against the Log(L_X) for the BCGs which had a SFH of 1 SSP.

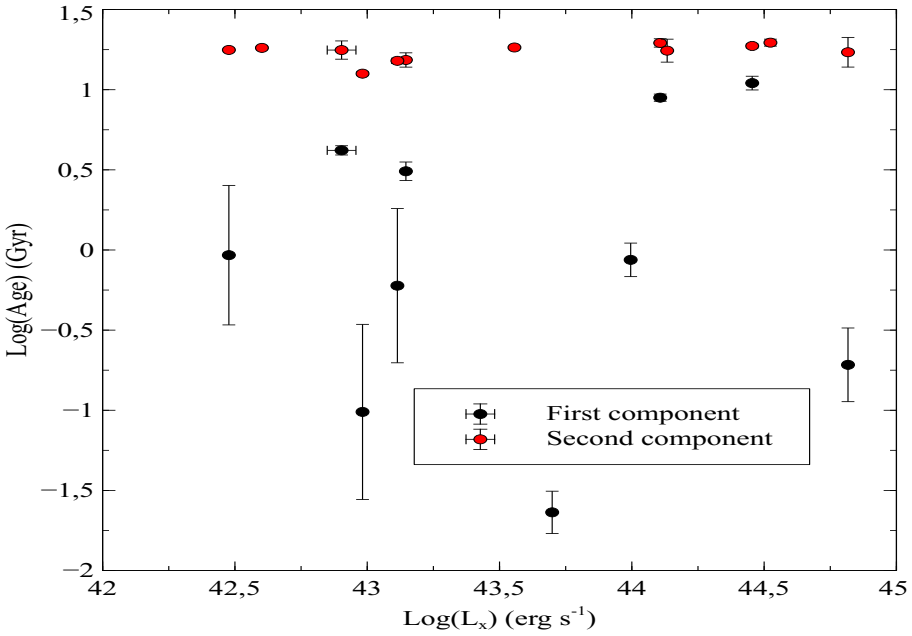

(a) Age – Log(L_X)

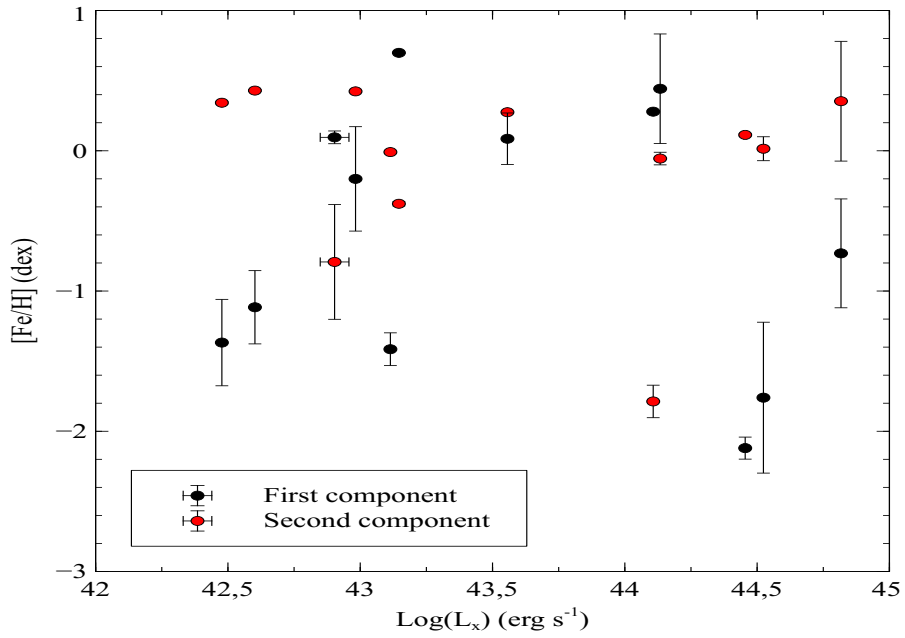

(b) [Fe/H] – Log(L_X)

Figure A.14: Shown here is the age and [Fe/H] against the Log(L_X) for the BCGs which had a SFH of 2 SSPs. The black dots represents the first component of the 2 SSPs while the red dots represents the second component.

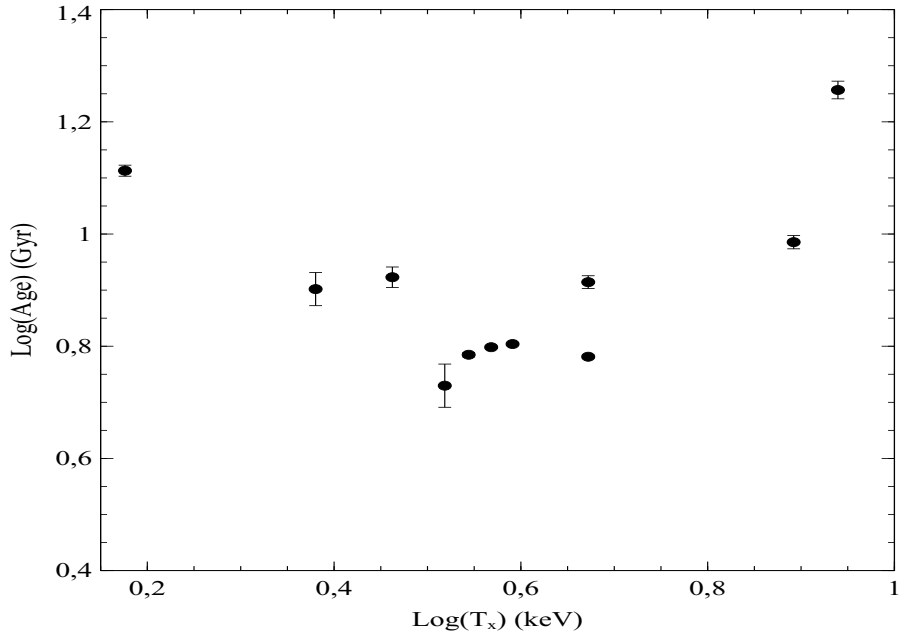

(a) Age – Log(T_X)

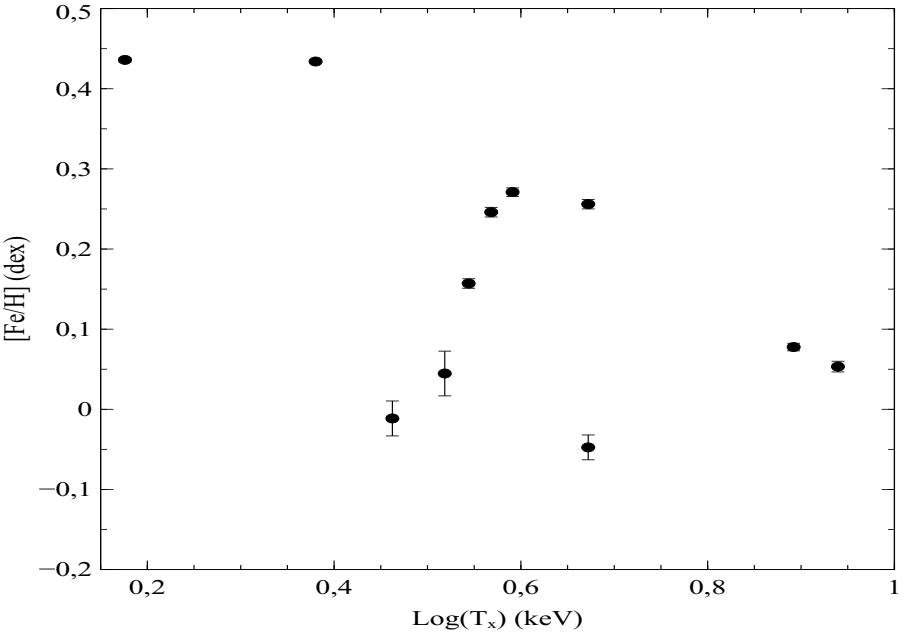

(b) [Fe/H] – Log(T_X)

Figure A.15: Shown here is the age and [Fe/H] against the Log(T_X) for the BCGs which had a SFH of 1 SSP.

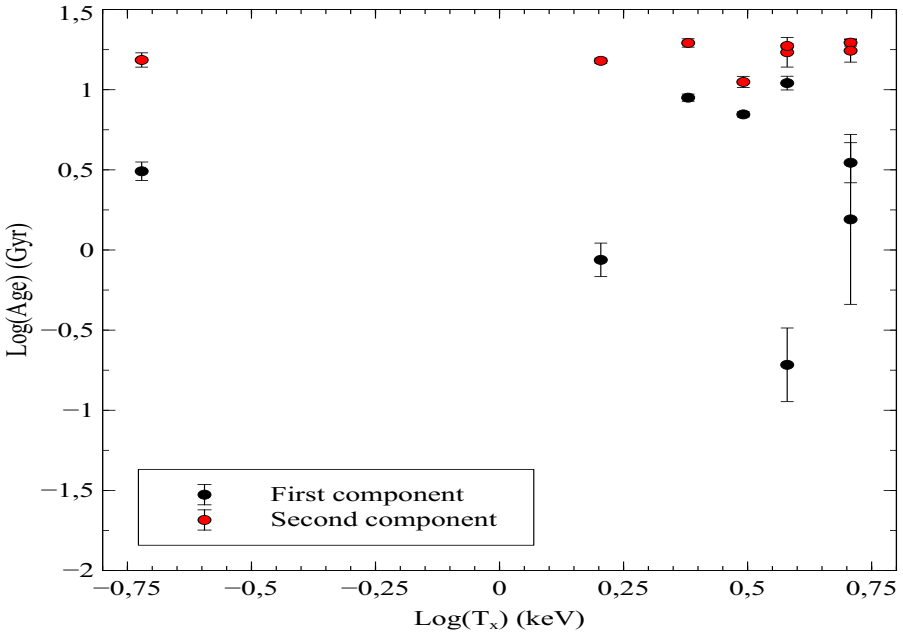

(a) Age – Log(T_X)

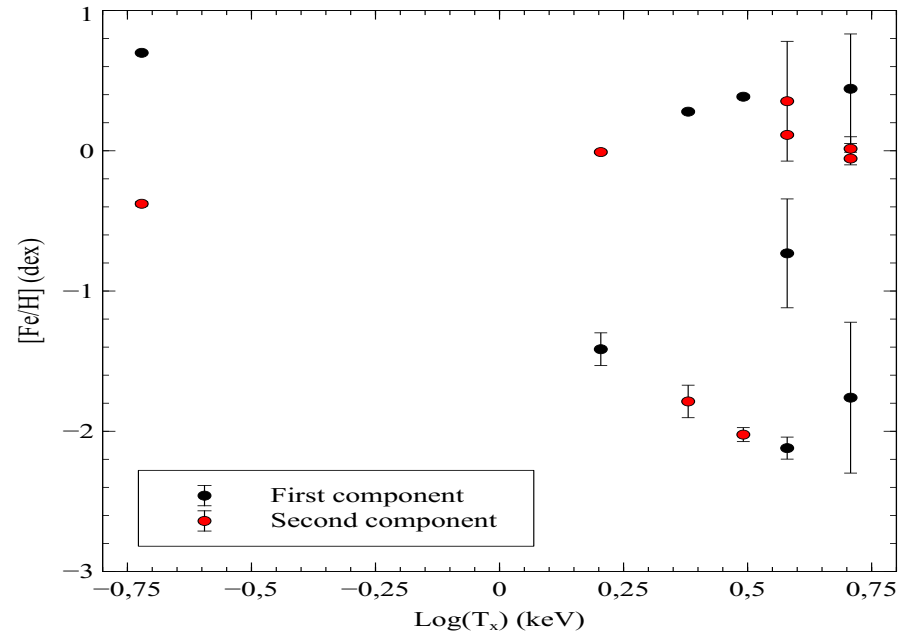

(b) [Fe/H] – Log(T_X)

Figure A.16: Shown here is the age and [Fe/H] against the Log(T_X) for the BCGs which had a SFH of 2 SSP. The black dots represents the first component of the 2 SSPs while the red dots represents the second component.

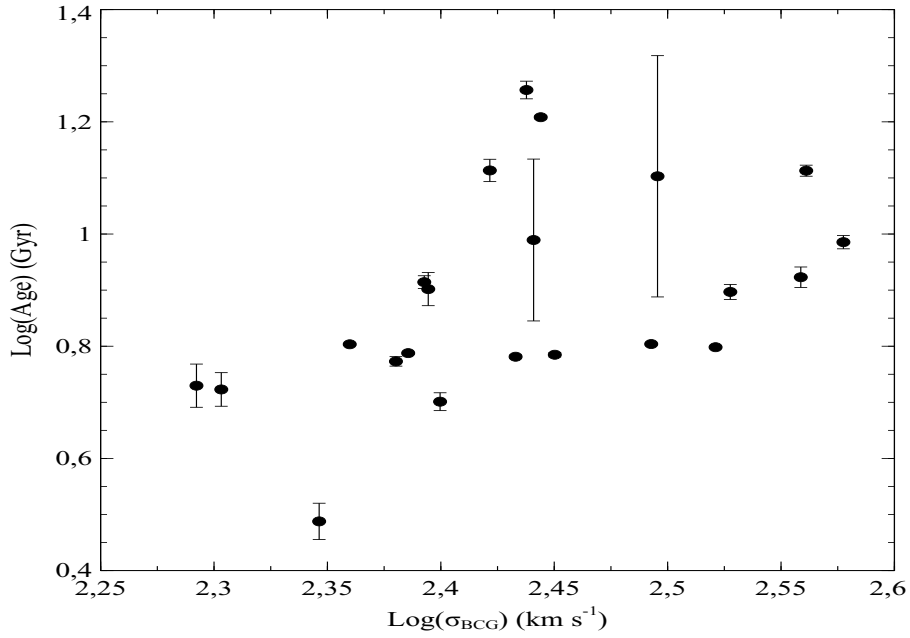

(a) Age – Log(σ_{BCG})

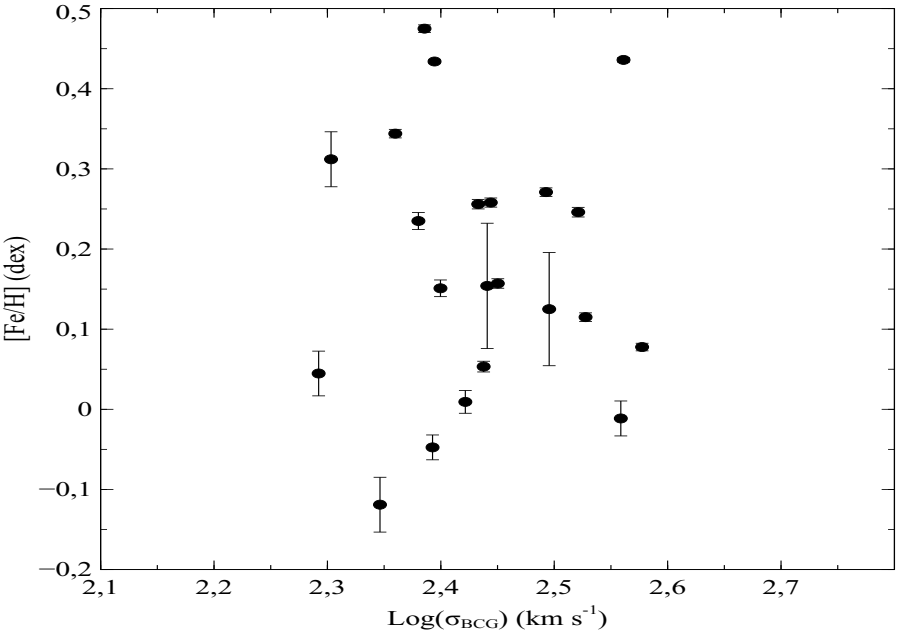

(b) [Fe/H] – Log(σ_{BCG})

Figure A.17: Shown here is the age and [Fe/H] against the Log(σ_{BCG}) for the BCGs which had a SFH of 1 SSP.

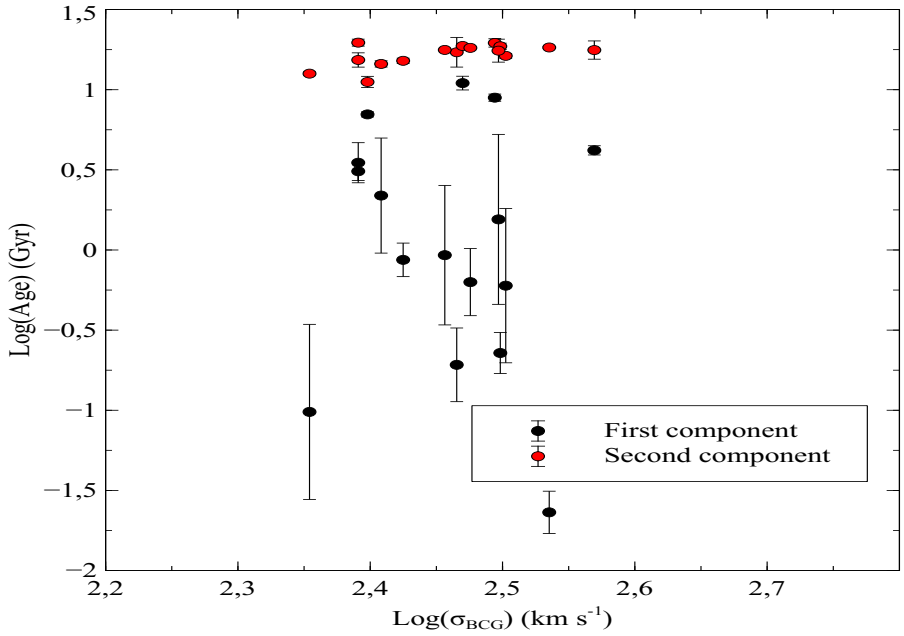

(a) Age – Log(σ_{BCG})

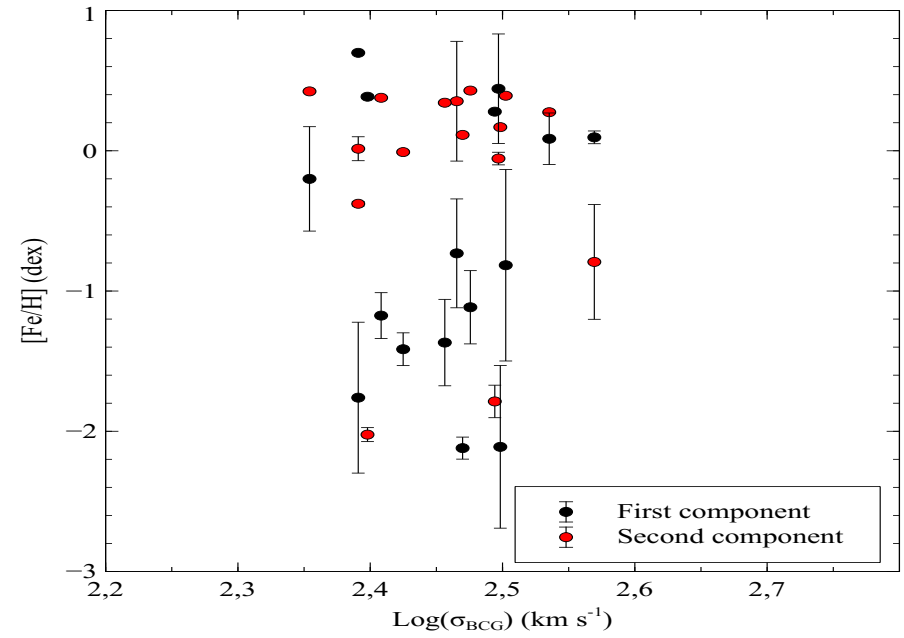

(b) [Fe/H] – Log(σ_{BCG})

Figure A.18: Shown here is the age and [Fe/H] against the Log(σ_{BCG}) for the BCGs which had a SFH of 2 SSP. The black dots represents the first component of the 2 SSPs while the red dots represents the second component.

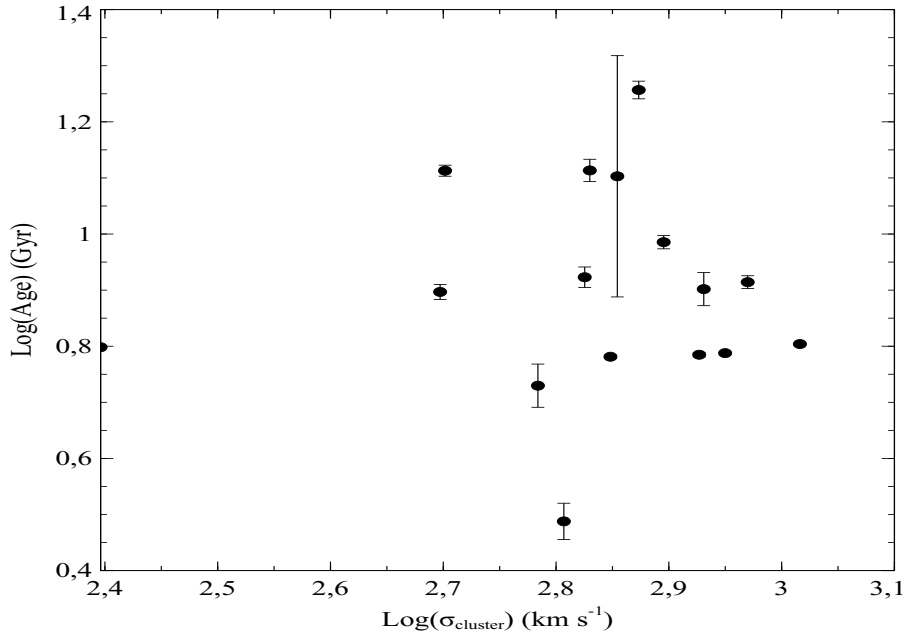

(a) Age – Log(σ_{cluster})

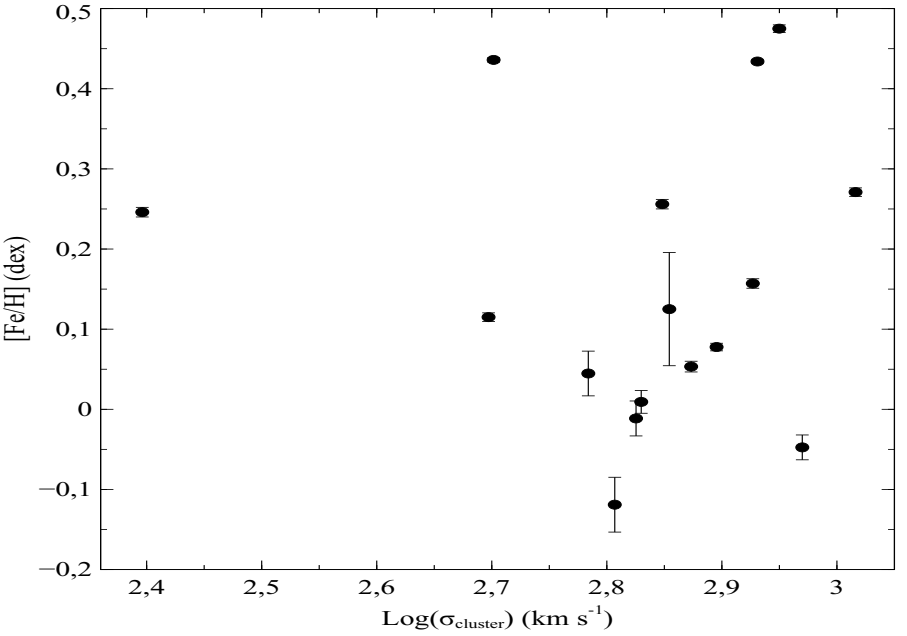

(b) [Fe/H] – Log(σ_{cluster})

Figure A.19: Shown here is the age and [Fe/H] against the Log(σ_{cluster}) for the BCGs which had a SFH of 1 SSP.

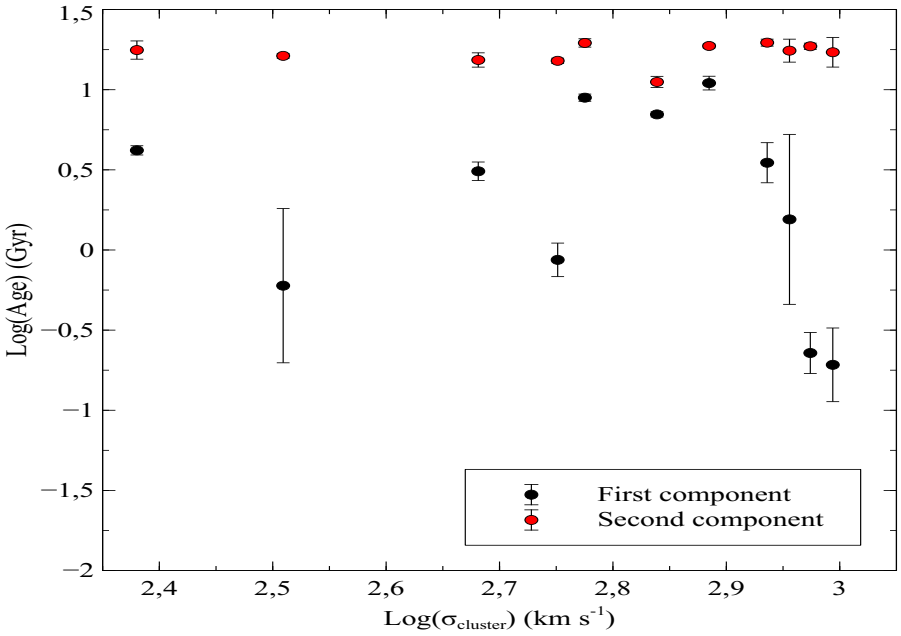

(a) Age – Log(σ_{cluster})

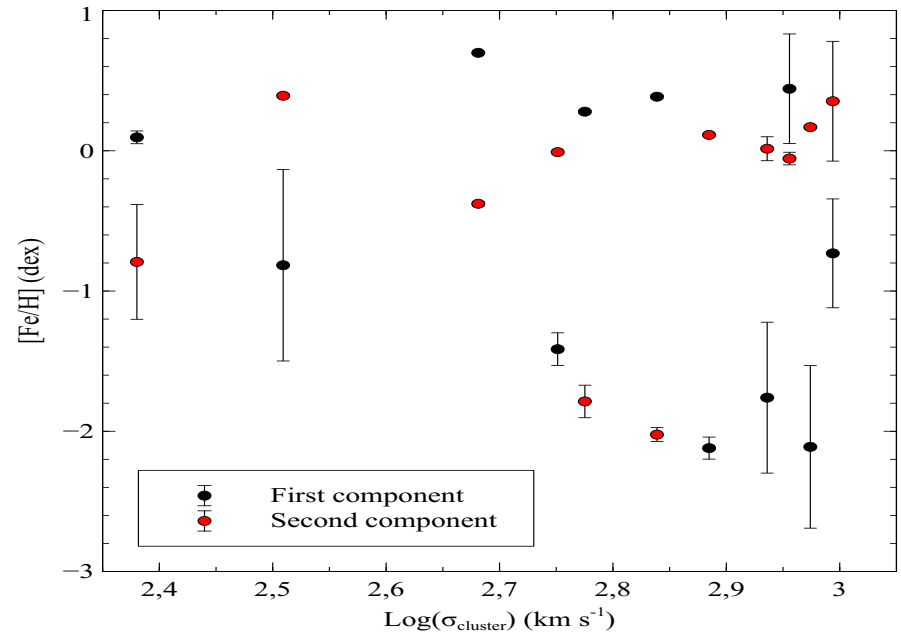

(b) [Fe/H] – Log(σ_{cluster})

Figure A.20: Shown here is the age and [Fe/H] against the Log(σ_{cluster}) for the BCGs which had a SFH of 2 SSP. The black dots represents the first component of the 2 SSPs while the red dots represents the second component.

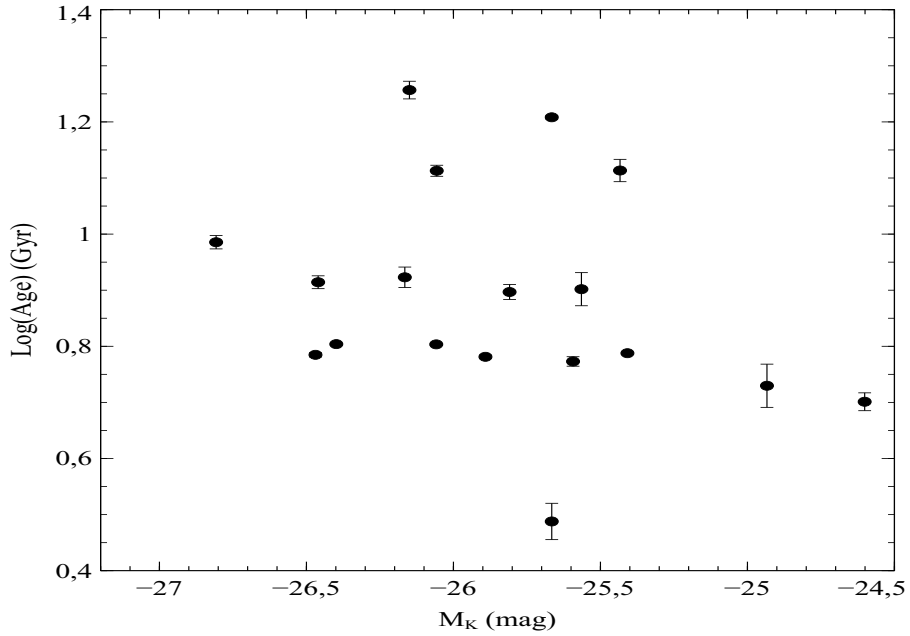

(a) Age – M_K

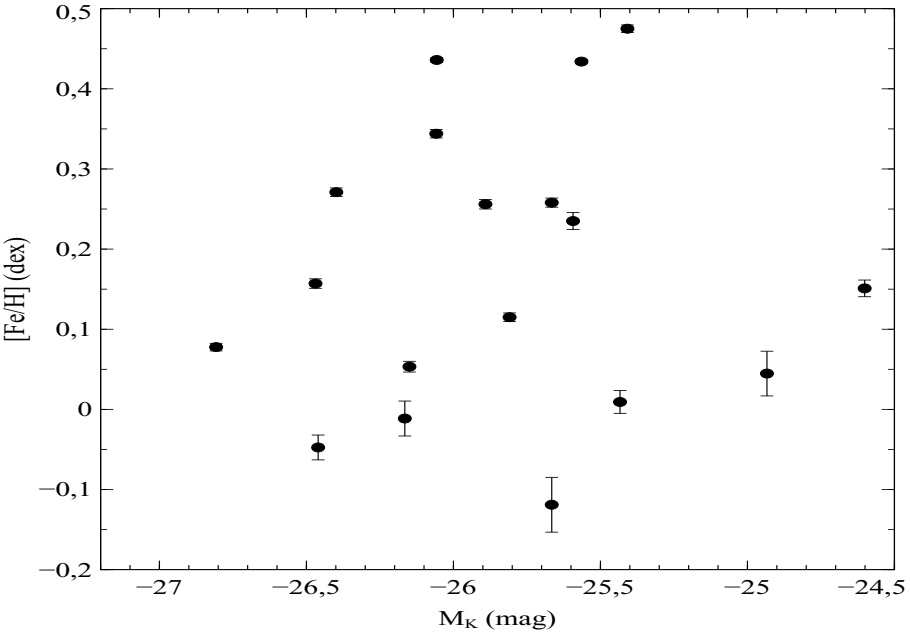

(b) [Fe/H] – M_K

Figure A.21: Shown here is the age and [Fe/H] against the M_K for the BCGs which had a SFH of 1 SSP.

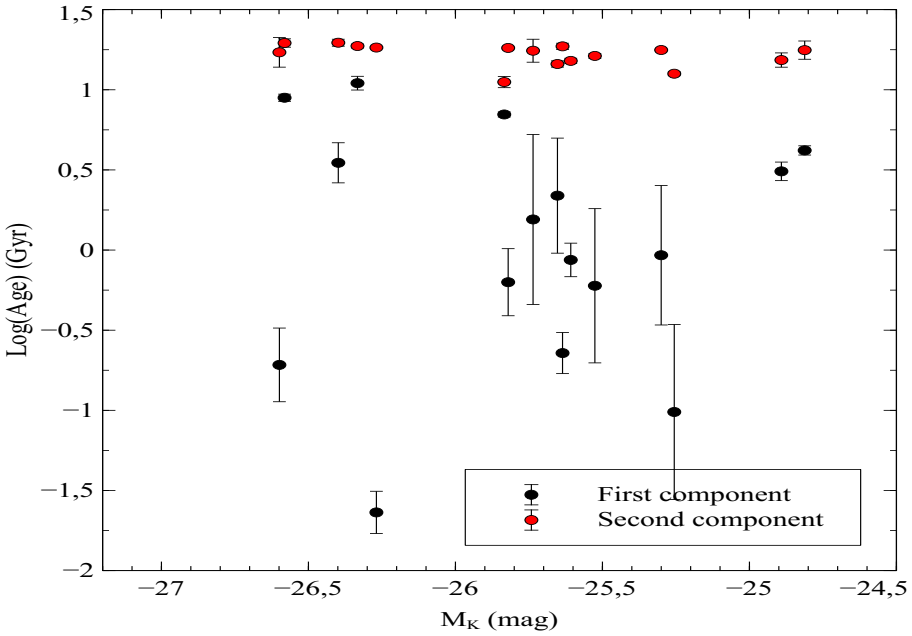

(a) Age – M_K

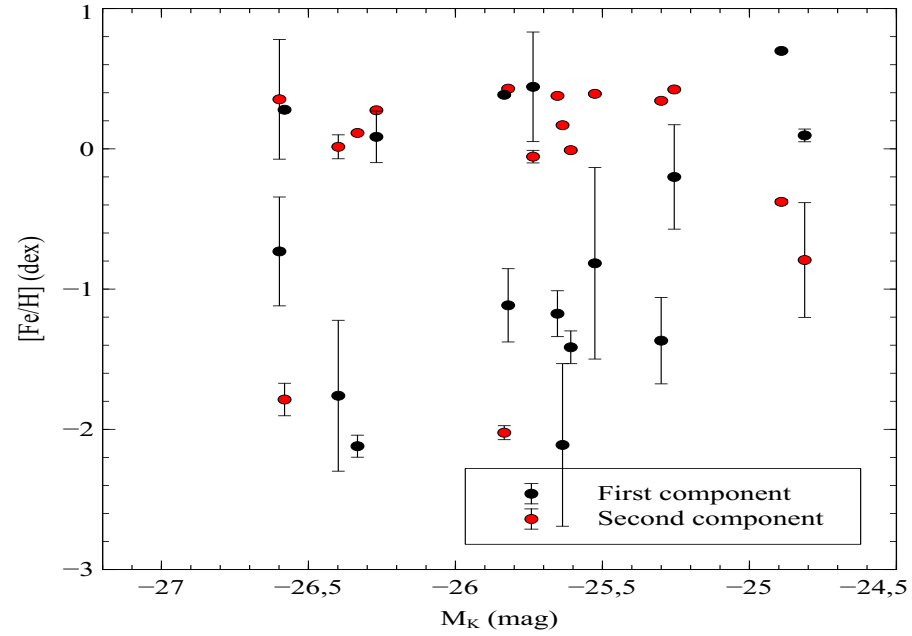

(b) [Fe/H] – M_K

Figure A.22: Shown here is the age and [Fe/H] against the M_K for the BCGs which had a SFH of 2 SSP. The black dots represents the first component of the 2 SSPs while the red dots represents the second component.

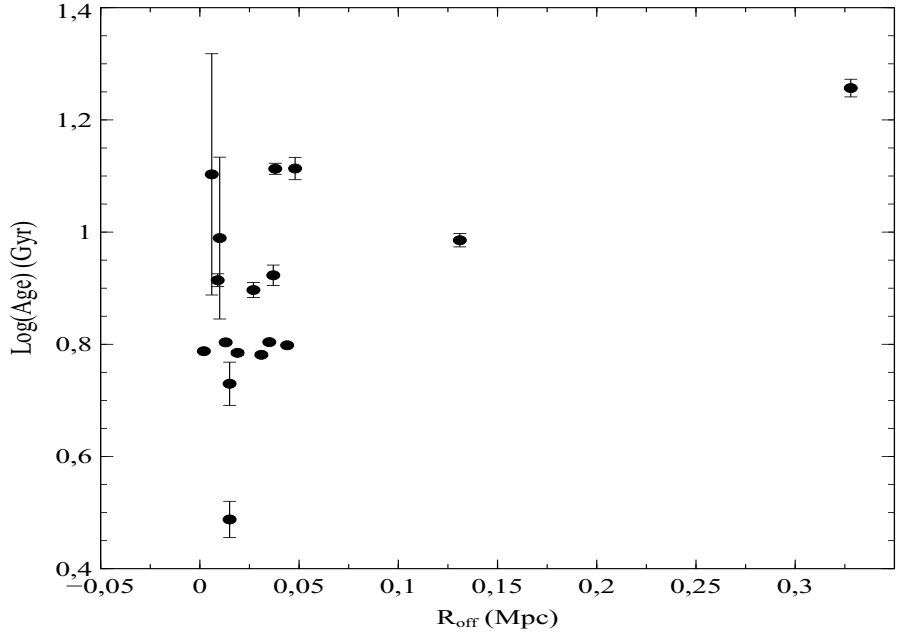

(a) Age – R_{off}

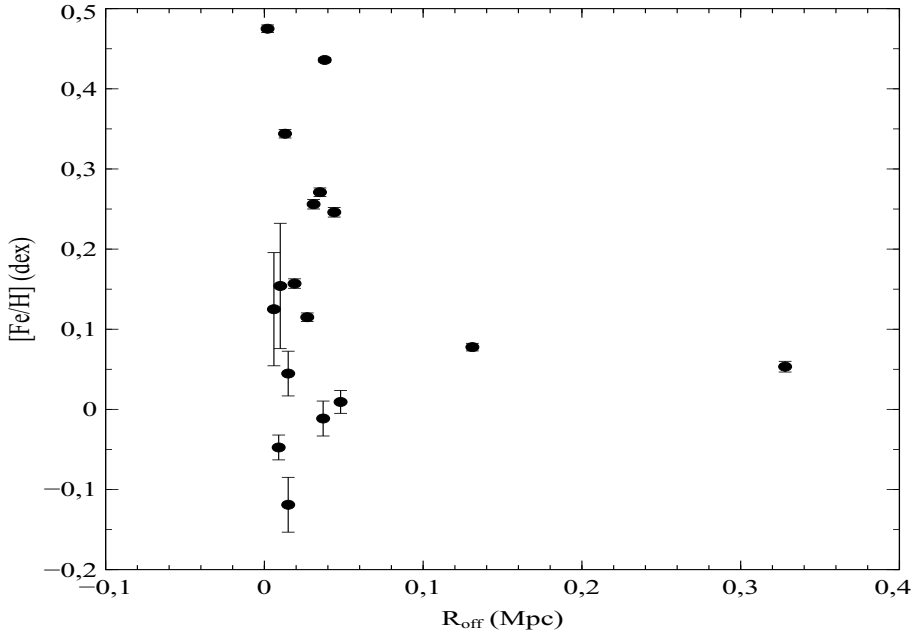

(b) [Fe/H] – R_{off}

Figure A.23: Shown here is the age and [Fe/H] against the R_{off} for the BCGs which had a SFH of 1 SSP.

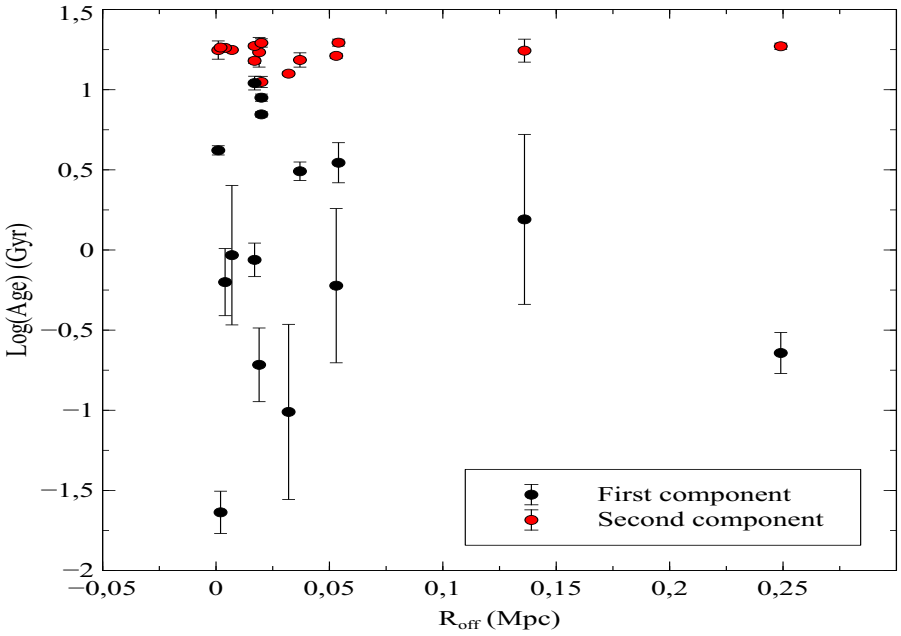

(a) Age – R_{off}

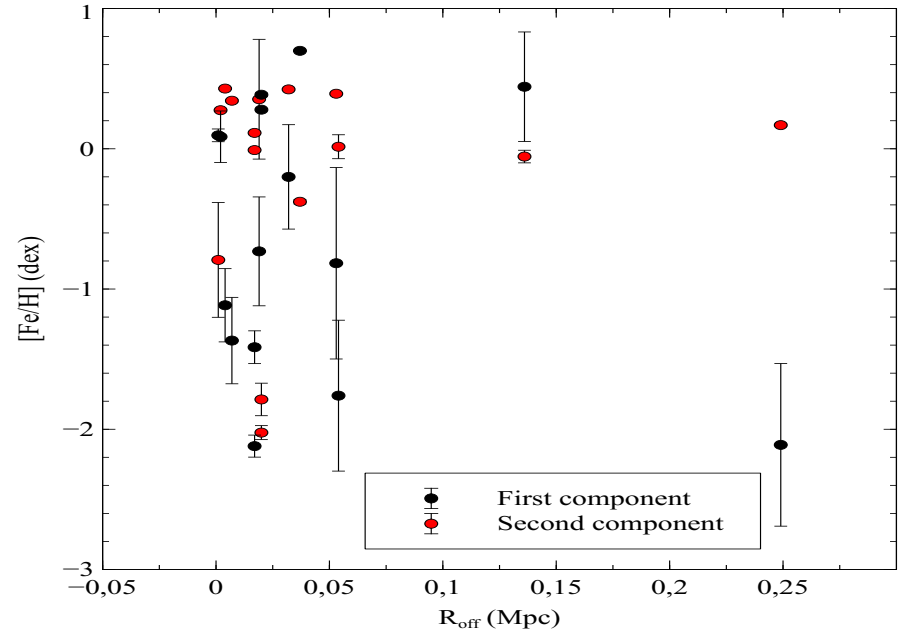

(b) [Fe/H] – R_{off}

Figure A.24: Shown here is the age and [Fe/H] against the R_{off} for the BCGs which had a SFH of 2 SSP. The black dots represents the first component of the 2 SSPs while the red dots represents the second component.

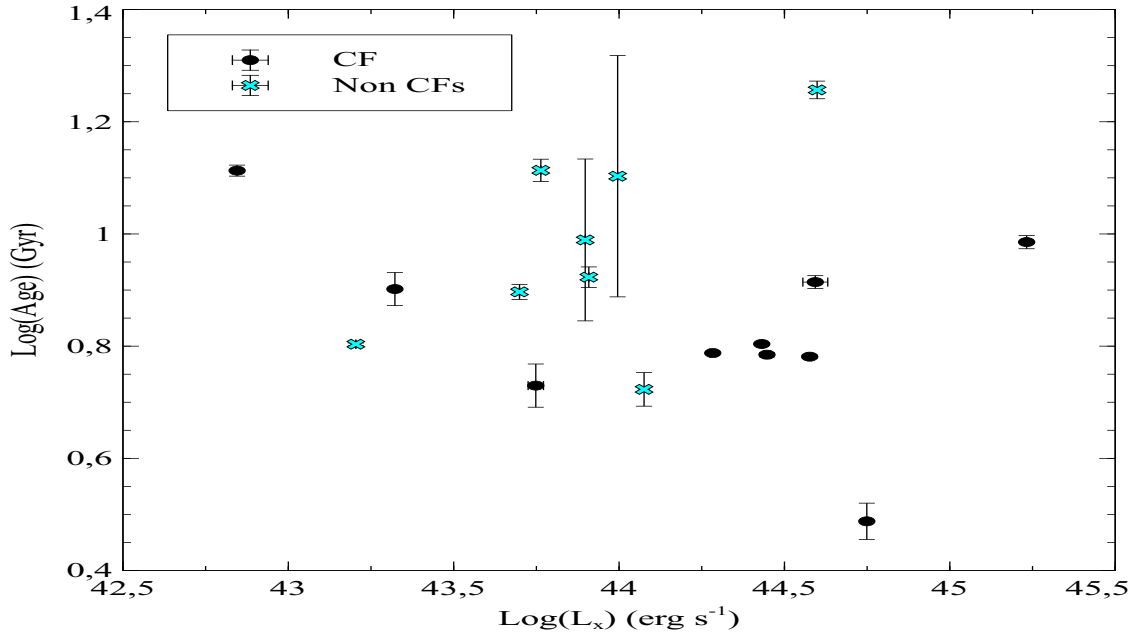

(a) Age – Log(L_X) of CFs and non-CFs.

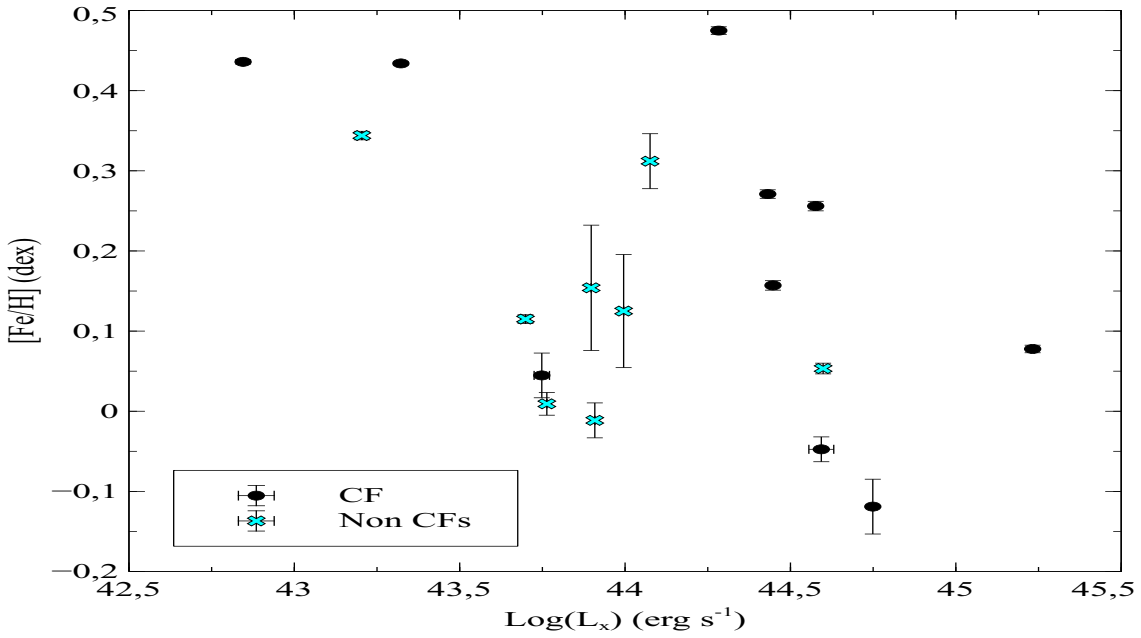

(b) [Fe/H] – Log(L_X) of CFs and non-CFs.

Figure A.25: Shown here is the ages and [Fe/H] against the Log(L_X) for the BCGs that had SFHs of 1 SSP and contained in CF and non-CF clusters. The CF and non-CF clusters are respectively indicated in the black dots and cyan crosses.

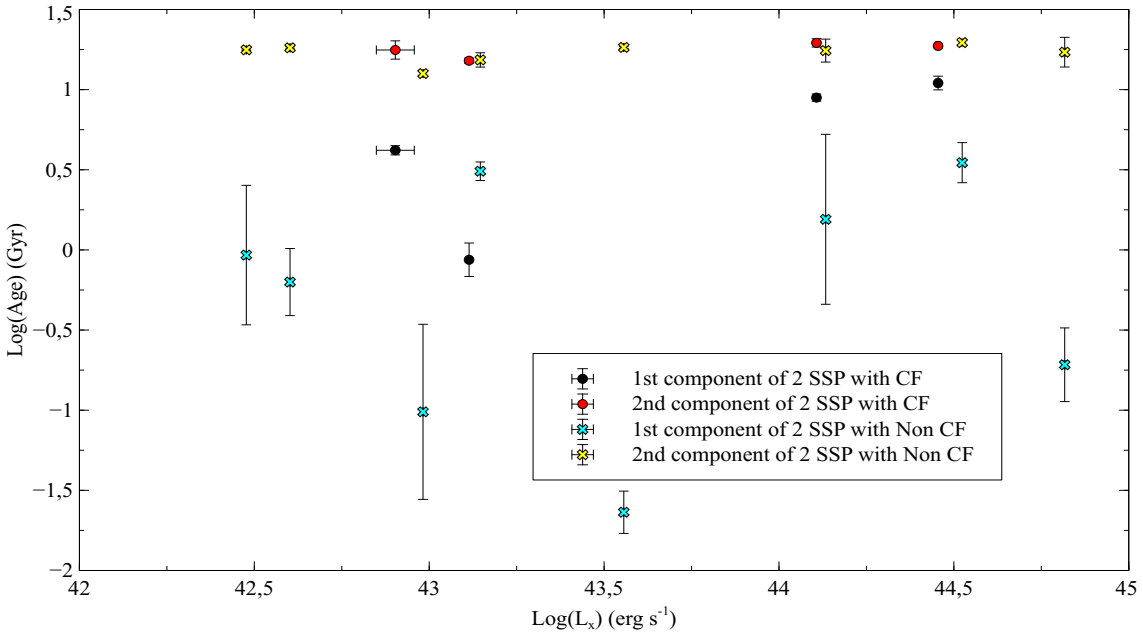

(a) Age – Log(L_X)

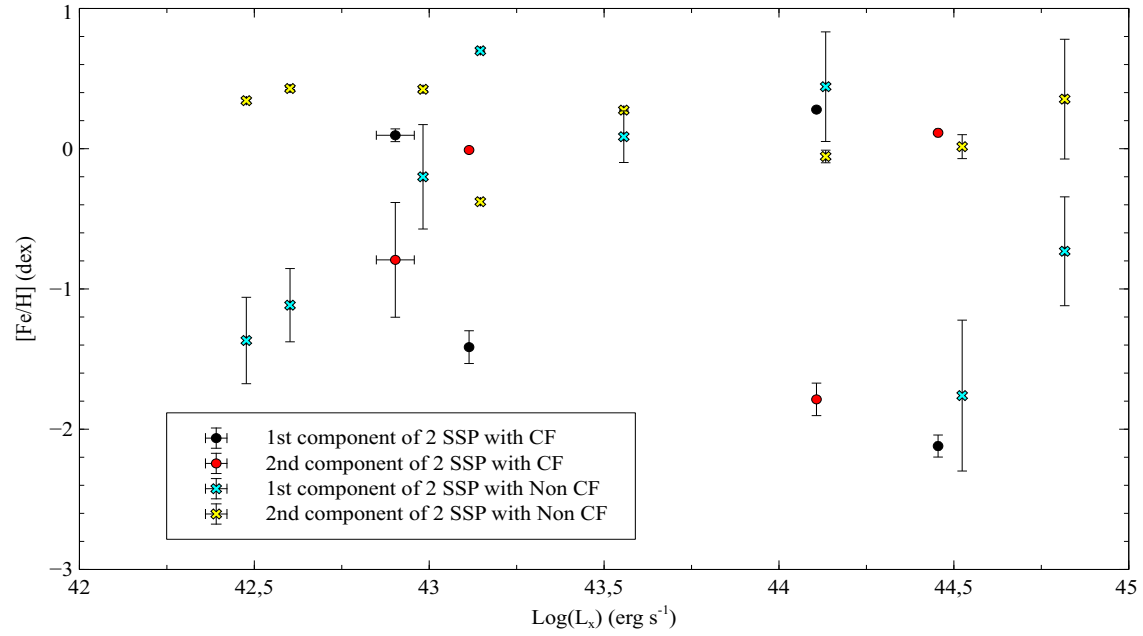

(b) [Fe/H] – Log(L_X)

Figure A.26: Shown here is the ages and [Fe/H] against the Log(L_X) for the BCGs that had SFHs of 2 SSPs and contained in CF and non-CF clusters. The 2 SSP galaxies, contained in CF clusters are indicated with the black and red dots, while the 2 SSP galaxies, contained in non-CF clusters are indicated with the cyan and yellow crosses.

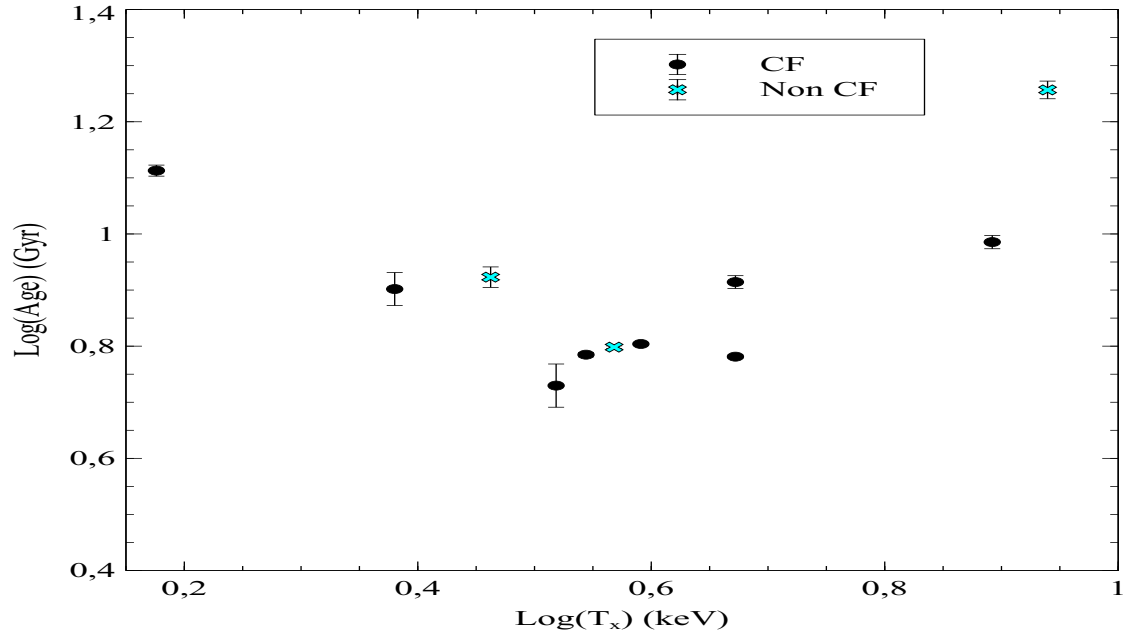

(a) Age – Log(T_X)

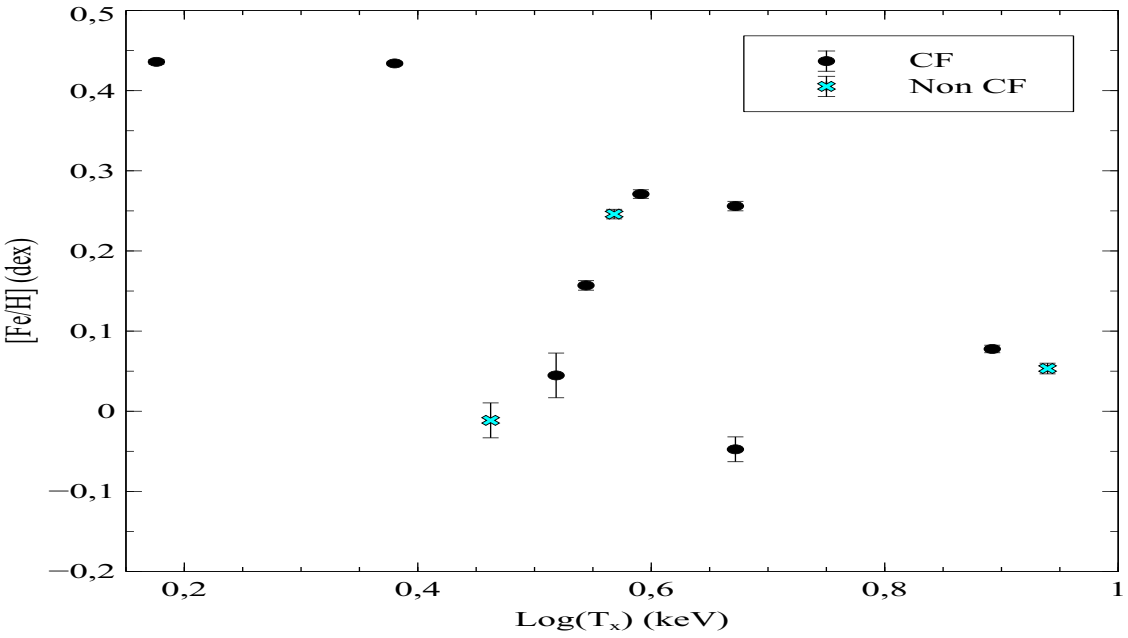

(b) [Fe/H] – Log(T_X)

Figure A.27: Shown here is the age and [Fe/H] against the Log(T_X) for the BCGs that had SFHs of 1 SSP and contained in CF and non-CF clusters. The CF and non-CF clusters are respectively indicated in the black dots and cyan crosses.

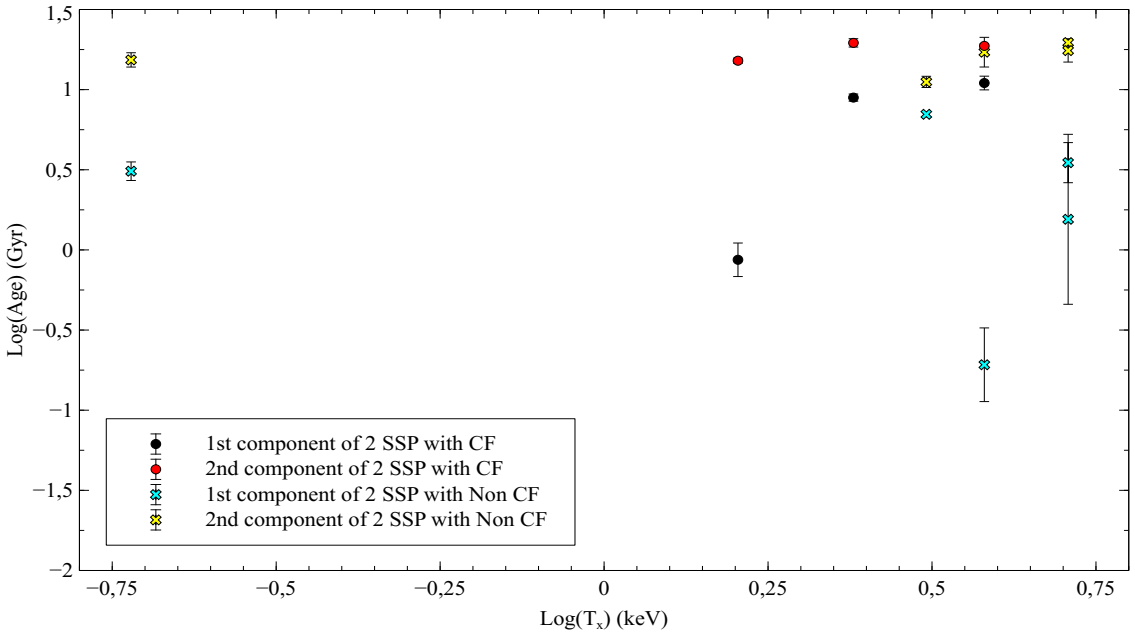

(a) Age – Log(T_X)

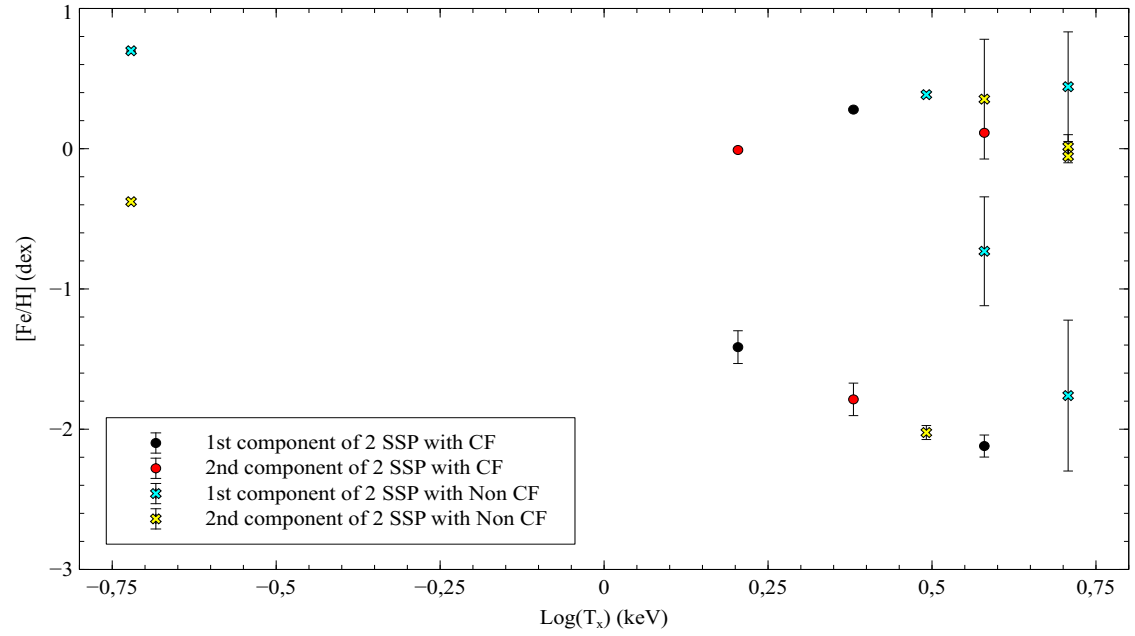

(b) [Fe/H] – Log(T_X)

Figure A.28: Shown here is the ages and [Fe/H] against the Log(T_X) for the BCGs that had SFHs of 2 SSPs and contained in CF and non-CF clusters. The 2 SSP galaxies, contained in CF clusters are indicated with the black and red dots, while the 2 SSP galaxies, contained in non-CF clusters are indicated with the cyan and yellow crosses.

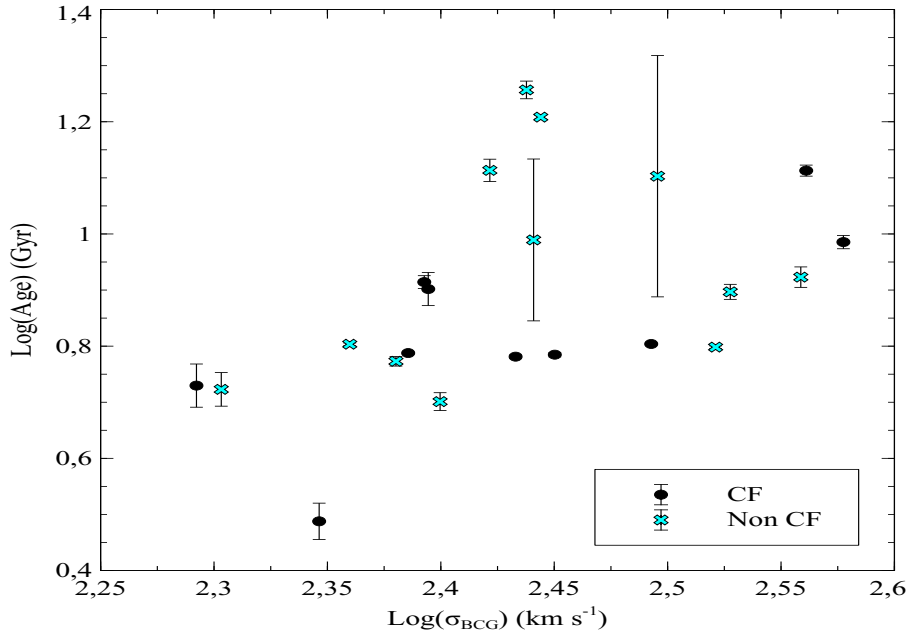

(a) Age – Log(σ_{BCG})

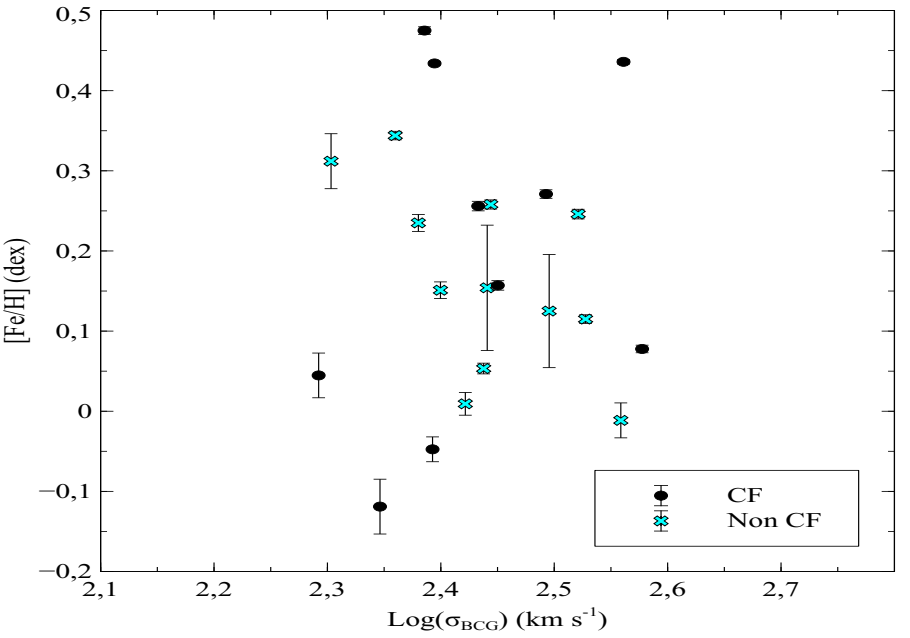

(b) [Fe/H] – Log(σ_{BCG})

Figure A.29: Shown here is the ages and [Fe/H] against the Log(σ_{BCG}) ffor the BCGs that had SFHs of 1 SSP and contained in CF and non-CF clusters. The CF and non-CF clusters are respectively indicated in the black dots and cyan crosses.

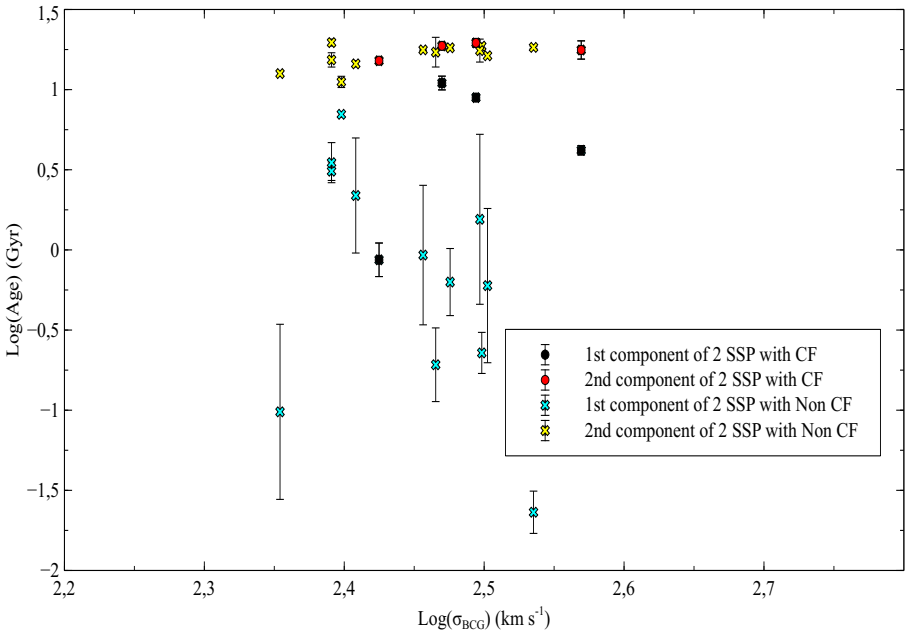

(a) Age – Log(σ_{BCG})

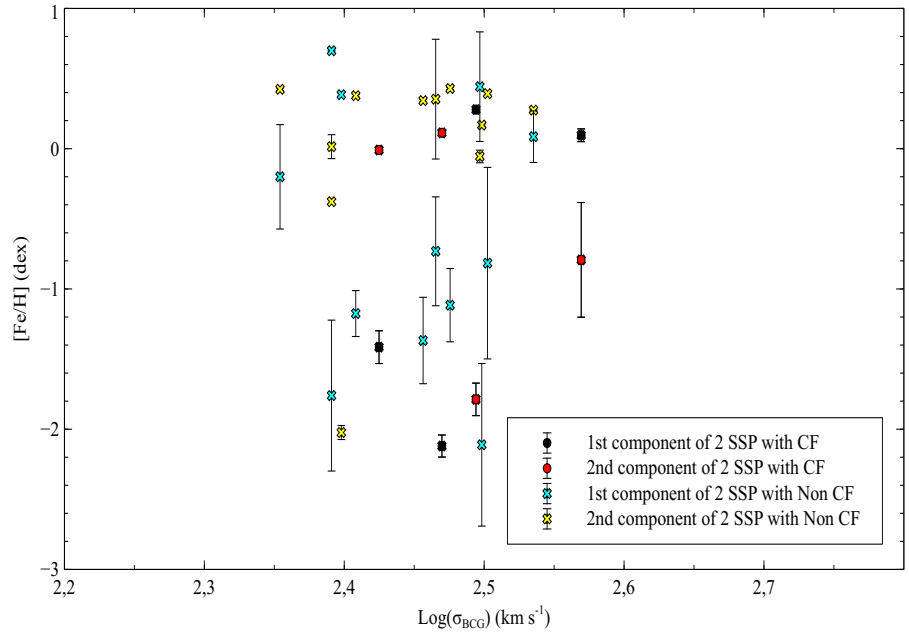

(b) [Fe/H] – Log(σ_{BCG})

Figure A.30: Shown here is the ages and [Fe/H] against the Log(σ_{BCG}) for the BCGs that had SFHs of 2 SSPs and contained in CF and non-CF clusters. The 2 SSP galaxies, contained in CF clusters are indicated with the black and red dots, while the 2 SSP galaxies, contained in non-CF clusters are indicated with the cyan and yellow crosses.

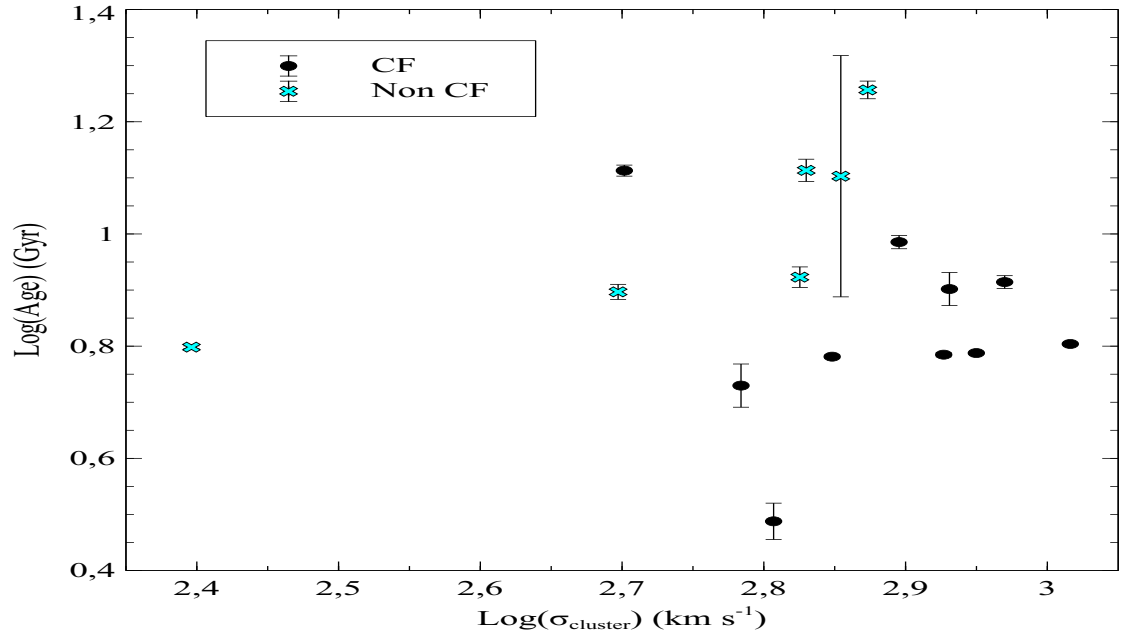

(a) Age – Log(σ_{cluster})

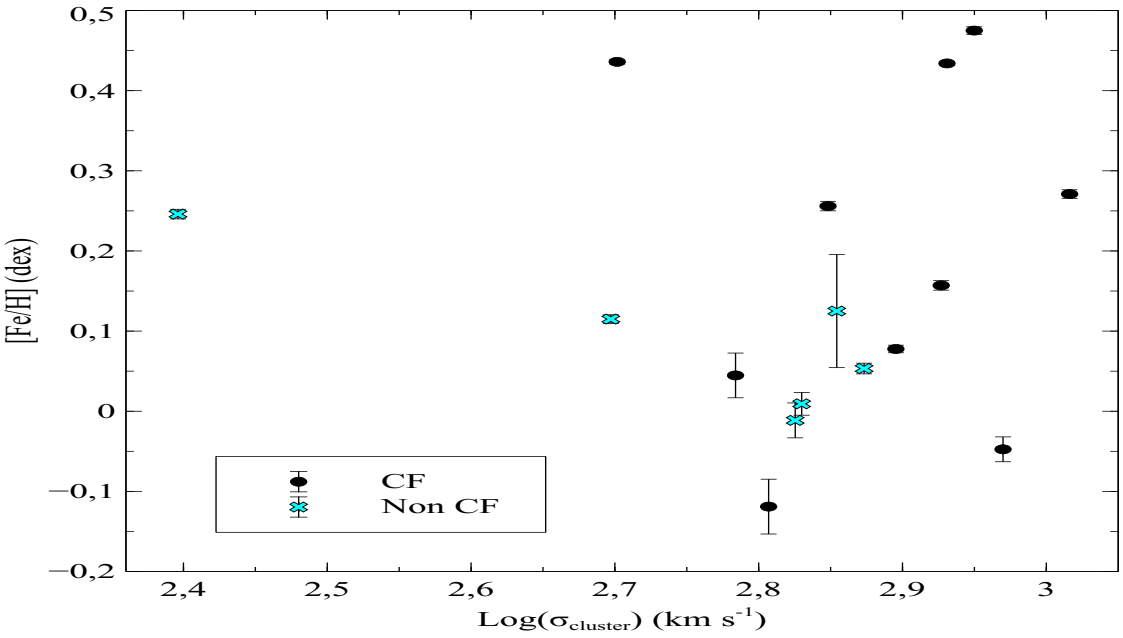

(b) [Fe/H] – Log(σ_{cluster})

Figure A.31: Shown here is the ages and [Fe/H] against the Log(σ_{cluster}) for the BCGs that had SFHs of 1 SSP and contained in CF and non-CF clusters. The CF and non-CF clusters are respectively indicated in the black dots and cyan crosses.

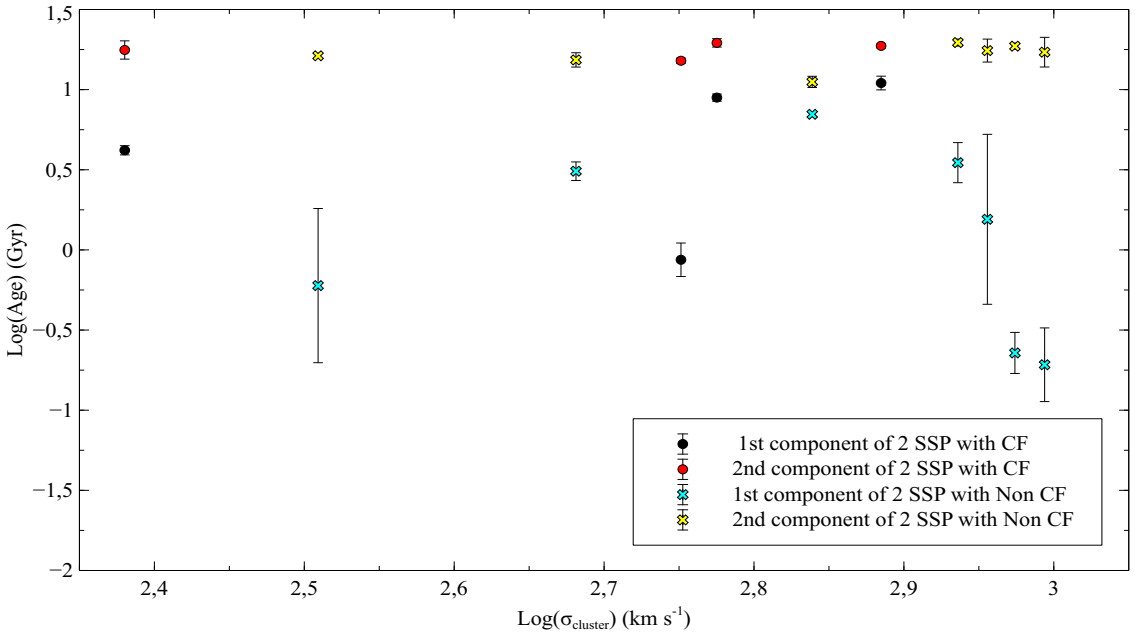

(a) Age – Log(σ_{cluster})

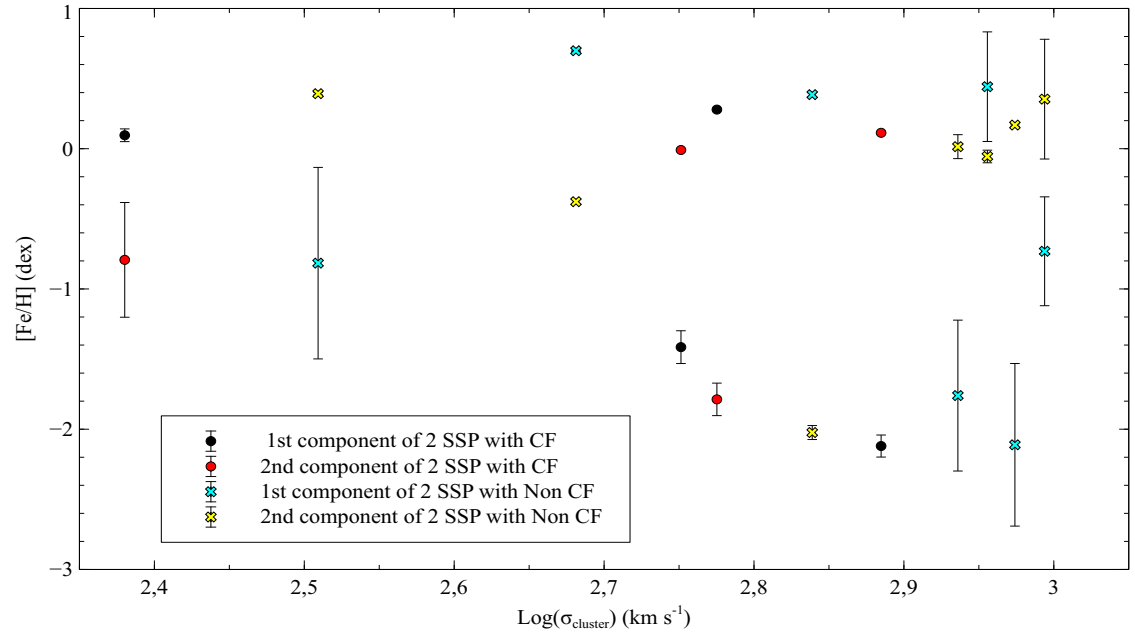

(b) [Fe/H] – Log(σ_{cluster})

Figure A.32: Shown here is the ages and [Fe/H] against the Log(σ_{cluster}) for the BCGs that had SFHs of 2 SSPs and contained in CF and non-CF clusters. The 2 SSP galaxies, contained in CF clusters are indicated with the black and red dots, while the 2 SSP galaxies, contained in non-CF clusters are indicated with the cyan and yellow crosses.

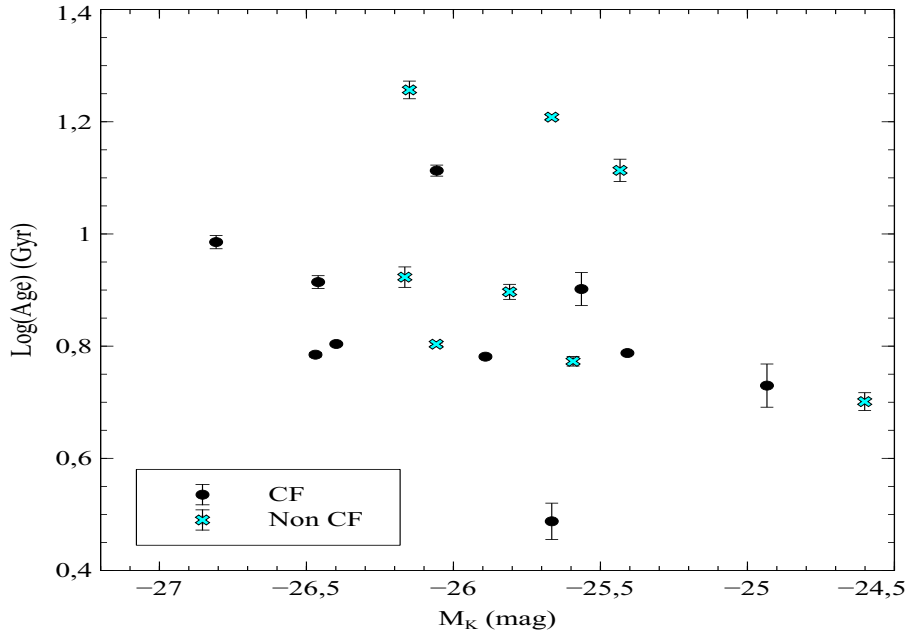

(a) Age – M_K

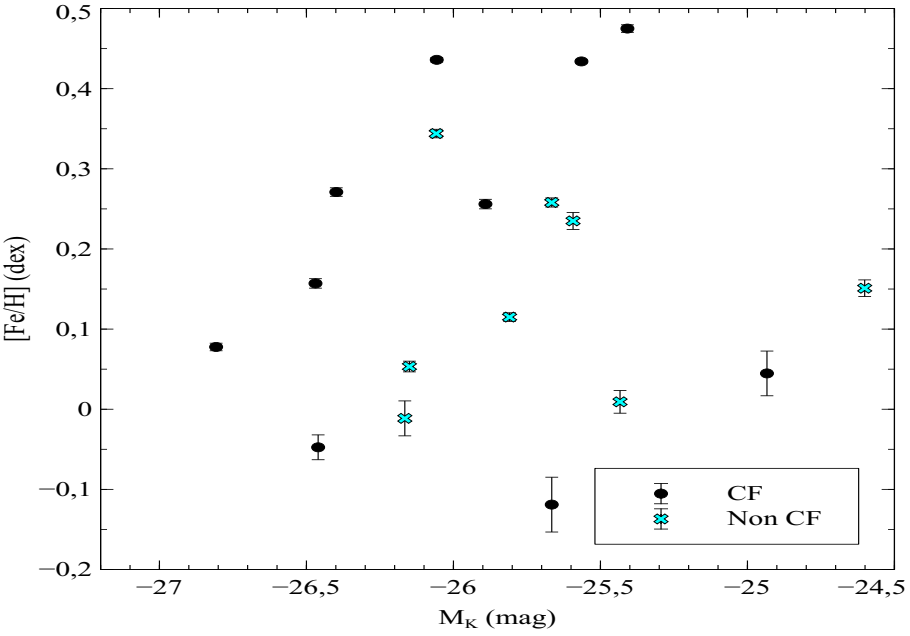

(b) [Fe/H] – M_K

Figure A.33: Shown here is the ages and [Fe/H] against the M_K for the BCGs that had SFHs of 1 SSP and contained in CF and non-CF clusters. The CF and non-CF clusters are respectively indicated in the black dots and cyan crosses.

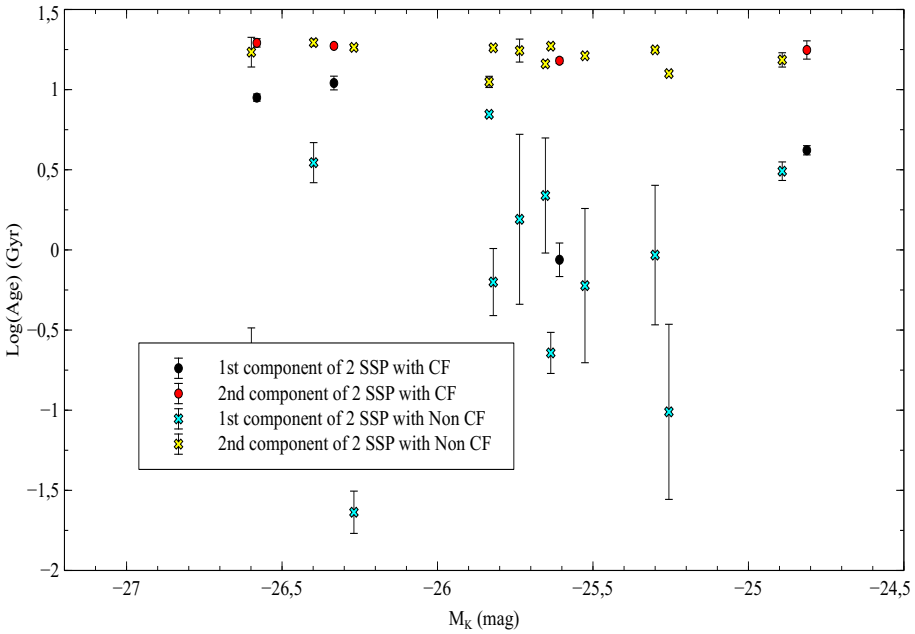

(a) Age – M_K

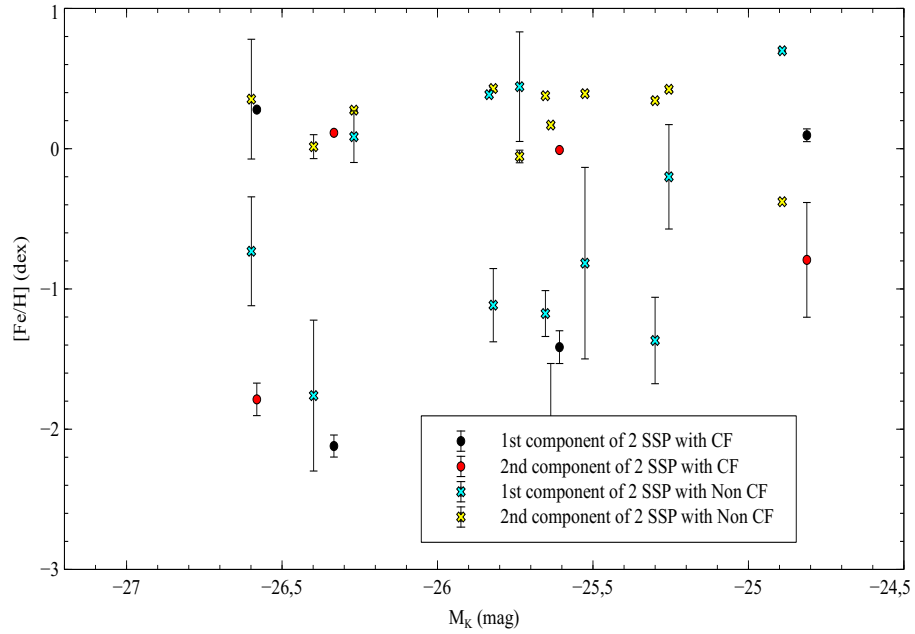

(b) [Fe/H] – M_K

Figure A.34: Shown here is the ages and [Fe/H] against the M_K for the BCGs that had SFHs of 2 SSPs and contained in CF and non-CF clusters. The 2 SSP galaxies, contained in CF clusters are indicated with the black and red dots, while the 2 SSP galaxies, contained in non-CF clusters are indicated with the cyan and yellow crosses.

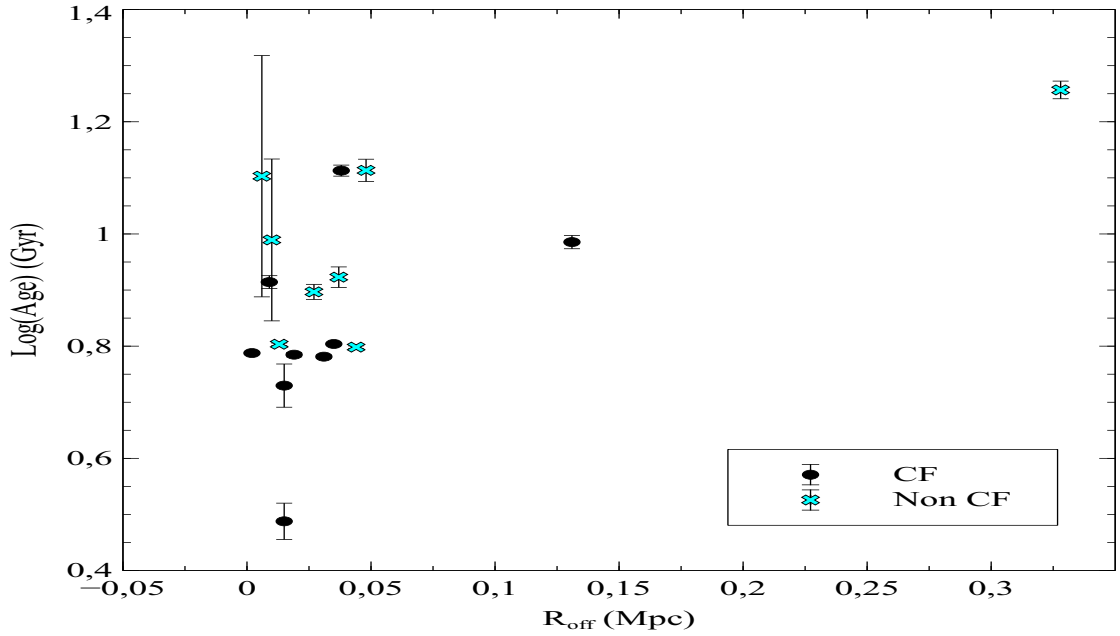

(a) Age – R_{off}

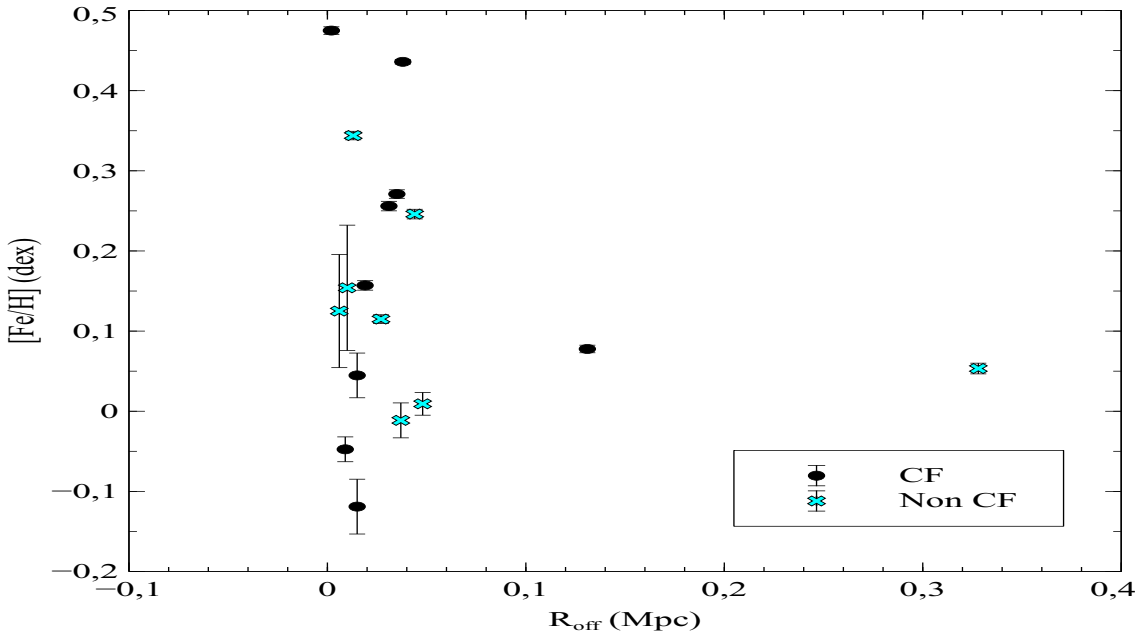

(b) [Fe/H] – R_{off}

Figure A.35: Shown here is the ages and [Fe/H] against the R_{off} for the BCGs that had SFHs of 1 SSP and contained in CF and non-CF clusters. The CF and non-CF clusters are respectively indicated in the black dots and cyan crosses.

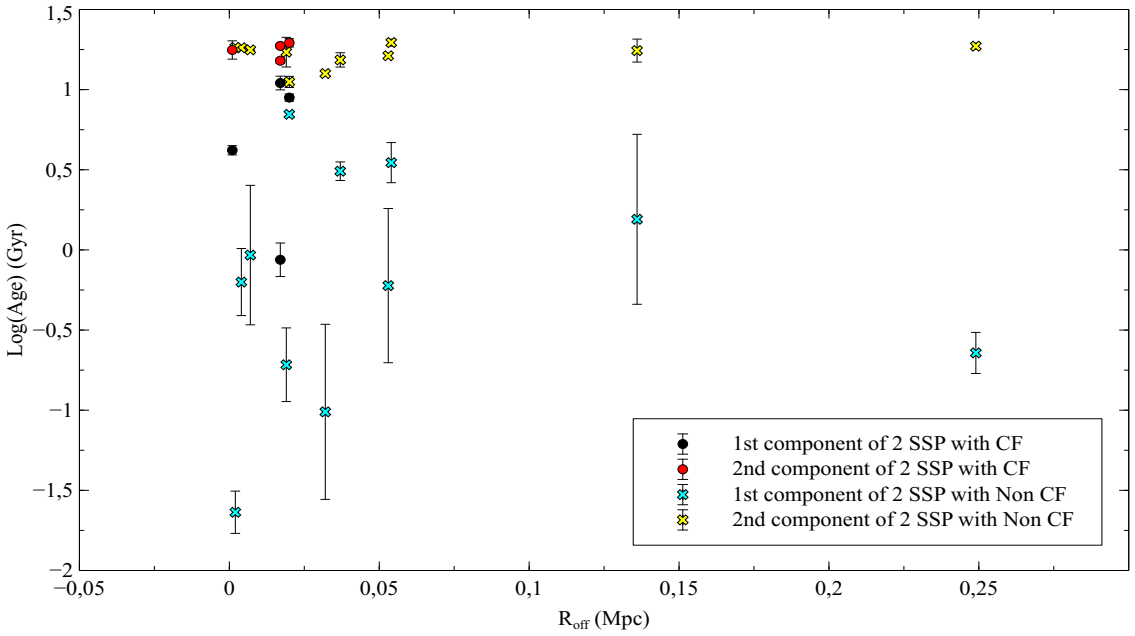

(a) Age – R_{off}

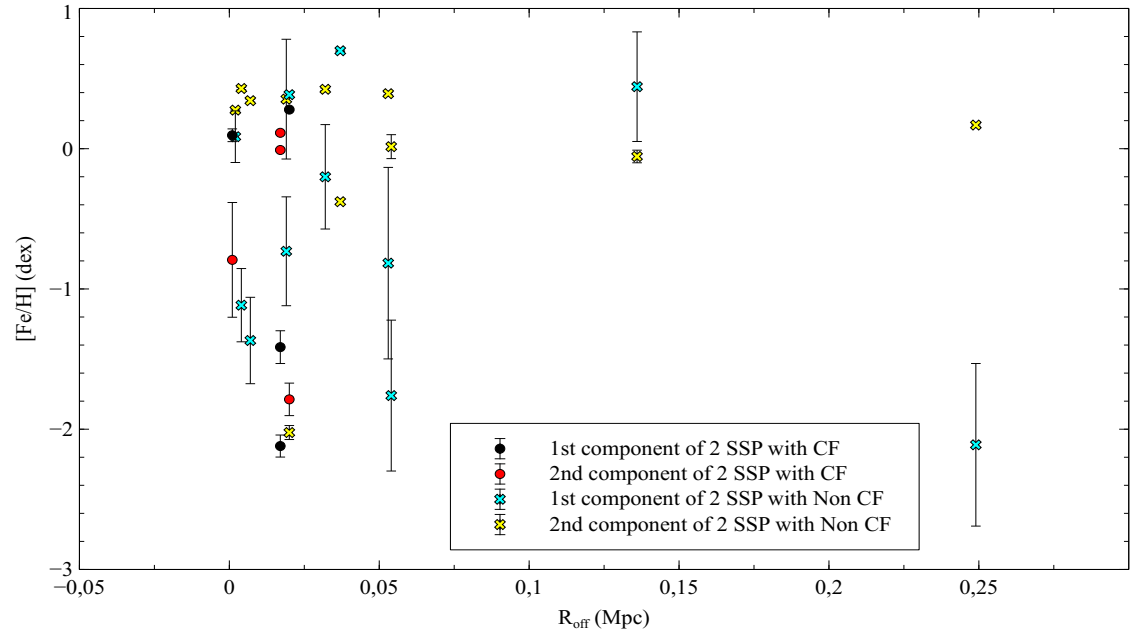

(b) [Fe/H] – R_{off}

Figure A.36: Shown here is the ages and [Fe/H] against the R_{off} for the BCGs that had SFHs of 2 SSPs and contained in CF and non-CF clusters. The 2 SSP galaxies, contained in CF clusters are indicated with the black and red dots, while the 2 SSP galaxies, contained in non-CF clusters are indicated with the cyan and yellow crosses.

BIBLIOGRAPHY

Avila-Reese, V. 2006, [arXiv: astro–ph/0605212]

Bacon, R., Monnet, G. & Simen, F. 1985, *A&A*, **152**, 315

Barrena, R., Girardi, M., Boschin, W. & Mardirossian, F. 2012, *A&A*, **540**, A90

Bertelli, G., Bressan, A., Chiosi, C., Fagotto, F. & Nasi, E. 1994, *A&AS*, **106**, 275

Best, P.N., Kaiser, C.R., Heckman, T.M. & Kauffmann, G. 2006, *MNRAS*, **368**, L67

Best, P.N., Kaiser, C.R., Heckman, T.M. & Kauffmann, G. 2007, *MNRAS*, **379**, 894

Bildfell, C., Hoekstra, H., Babul, A. & Mahdavi, A. 2008, *MNRAS*, **389**, 1637

Bîrzan, L., Rafferty, D.A., McNamara, B.R., Wise, M.W. & Nulsen, P.E.J. 2004, *ApJ*, **607**, 800

Böhringer, H., Voges, W. & Huchra, J.P., McLean, B., Giacconi, R., Rosati, P., Burg, R., Mader, J., Schuecker, P., Simig, D., Komossa, S., Reiprich, T.H., Retzlaff, J. & Trumper, J. 2000, *ApJS*, **129**, 435

Böhringer, H., Schuecker, P., Guzzo, L., Collins, C.A., Voges, W., Cruddace, R.G., Ortiz-Gil, A., Chincarini, G., De Grandi, S., Edge, A.C., MacGillivray, H.T., Neumann, D.M., Schindler, S. & Shaver, P. 2004, *A&A*, **425**, 367

Boksenberg, A. 1985, *Vistas in Astronomy*, **28**, 531

Bosma, A. 1981, *AJ*, **86**, 1825

Bouchard, A., Prugniel, Ph., Koleva, M. & Sharina, M. 2010, *A&A*, **513**, 54

Brough, S., Collins, C.A., Burke, D.J., Mann, R.G. & Lynam, P.D. 2002, *MNRAS*, **329**, 533

Brough, S., Proctor, R., Forbes, D.A., Couch, W.J., Collins, C.A., Burke, D.J. & Mann, R.G. 2007, *MNRAS*, **378**, 1507

Bruzual, G. & Charlot, S. 2003, *MNRAS*, **344**, 1000

Burbidge, E.M. & Burbidge, G.R. 1975, *Galaxies in the Universe* (Chicago: Chicago Univ. Press)

Burbidge, E.M., Burbidge, G.R., Fowler, W.A. & Hoyle, F. 1975, *Rev. Mod. Phys.*, **29**, 547

Burns, J.O. 1990, *AJ*, **99**, 14

Cappellari, M., Emsellem, E., Krajnovi, D., McDermid, R.M., Serra, P., Alatalo, K., Blitz, L., Bois, M., Bournaud, F., Bureau, M., Davies, R.L., Davis, T.A., de Zeeuw, P.T., Khochfar, S., Kuntschner, H., Lablanche, P., Morganti, R., Naab, T., Oosterloo, T., Sarzi, M., Scott, N., Weijmans, A. & Young, L.M. 2011, *MNRAS*, **416**, 1680

Cavagnolo, K.W., Donahue, M., Voit, G.M. & Sun, M. 2009, *ApJS*, **182**, 12

Chaisson, E. & McMillan, S. 2008, *Astronomy Today, 6th ed.* (Harlow: Addison-Wesley, Pearson International ed.)

Chen, Y., Reiprich, T.H., Böhringer, H., Ikebe, Y. & Zhang, Y.Y. 2007, *A&A*, **466**, 805

Ciotti, L. & Ostriker, J.P. 1997, *ApJ*, **487**, L105

Coccato, L., Gerhard, O., Arnaboldi, M. & Ventimiglia, G. 2011, *A&A*, **533**, A138

Coelho, P., Barbuy, B., Meléndez, J., Schiavon, R.P. & Castilho, B.V. 2005, *A&A*, **443**, 735

Coelho, P., Bruzual, G., Charlot, S., Weiss, A., Barbuy, B. & Ferguson, J.W. 2007, *MNRAS*, **382**, 498

Collins, C.A., Stott, J.P., Hilton, M., Kay, S.T., Stanford, S.A., Davidson, M., Hosmer, M., Hoyle, B., Liddle, A., Lloyd-Davies, E., Mann, R.G., Mehrtens, N., Miller, C.J., Nichol, R.C., Romer, A.K., Sahlén, M., Viana, P.T.P & West, M.J. 2009, *Nature*, **458**, 603

Cowie, L.L. 1988, in *The Post–Recombination Universe*, Proceedings of the NATO Advanced Study Institute held in Cambridge, England, 27 July – 7 Aug 1987, Eds. N. Kaiser & A.N. Lasenby (Dordrecht: Kluwer Academic Publishers)

Cruddace, R., Voges, W., Böhringer, H., Collins, C.A., Romer, A.K., MacGillivray, H., Yentis, D., Schuecker, P., Ebeling, H. & de Grandi, S. 2002, *ApJS*, **140**, 239

De Lucia, G. 2010, [arXiv: astro–ph/1012.3326v1]

De Lucia, G. & Blaizot, J. 2007, *MNRAS*, **375**, 2

De Lucia, G. & Borgani, S. 2012, *MNRAS*, **426**, L61

Donahue, M., Voit, G.M., O'Dea, C.P., Baum, S.A. & Sparks, W.B. 2005, *ApJ*, **630**, L13

Dressler, A. 1980a, *ApJ*, **236**, 351

Dressler, A. 1980b, *Astronomy and Astrophysics Encyclopedia: Short Essays — Galaxies, Properties in relation to Enviroment*, Ed. S.P. Maran

Dressler, A. 1984, *ARA&A*, **22**, 185

Du, W., Luo, A.L., Prugniel, Ph., Liang, Y.C. & Zhao, Y.H. 2010, *MNRAS*, **409**, 567

Dubinski, J. 1998, *ApJ*, **502**, 141

Edge, A.C., Stewart, G.C. & Fabian, A.C. 1992, *MNRAS*, **258**, 177

Edwards, L.O.V., Hudson, M.J., Balogh, M.L. & Smith, R.J. 2007, *MNRAS*, **379**, 100

Eggen O.J., Lynden-Bell D. & Sandage A.R. 1962, *ApJ*, **136**, 748

Faber, S.M. & Gallagher, J.S. 1979, *ARA&A*, **17**, 135

Faber, S.M., Friel, E.D., Burstein, D. & Gaskell, C.M. 1985, *ApJS*, **57**, 711

Fabian, A.C. 1994, *ARA&A*, **32**, 277

Gao, L., Loeb, A., Peebles, P.J.E., White, S.D.M. & Jenkins, A. 2004, *ApJ*, **614**, 17

Giovannini, G., Liuzzo, E. & Giroletti, M. 2008, *Approaching Micro–Arcsecond Resolution with VSOP–2: Astrophysics and Technology*, Eds. Y. Hagiwara, E. Fomalont, M. Tsuboi & Y. Murata.

Girardi, L., Bressan, A., Bertelli, G. & Chiosi, C. 2000, *A&AS*, **141**, 371

Henry, J.P., Briel, U.G. & Böhringer, H. 1998, *Sci. Am.*, **279**, 52

Howell, D.A., Sullivan, M., Brown, E.F., Conley, A., Borgne, D.L., Hsiao, E.Y., Astier, P., Balam, D., Balland, C., Basa, S., Carlberg, R.G., Fouchez, D., Guy, J., Hardin, D., Hook, I.M., Pain, R., Perrett, K., Pritchet, C.J., Regnault, N., Baumont, S., Du, J.L., Lidman, C., Perlmutter, S., Suzuki, N., Walker, E.S. & Wheeler, J.C. 2009, *ApJ*, **691**, 661

Inglis, M. 2007, *Astrophysics is easy* (London: Springer)

Jones, M.H. & Lambourne, R.J. 2003, *An Introduction to Galaxies and Cosmology* (Cambridge: Cambridge Univ. Press)

Kaler, J.B. 1989, *Stars and their Spectra* (Cambridge: Cambridge Univ. Press)

Katayama, H., Hayashida, K.I., Takahara, F. & Fujita, Y. 2003, *ApJ*, **585**, 687

Katz, D., Soubiran, C., Cayrel, R., Adda, M. & Cautain, R. 1998, *A&A*, **338**, 151

Kauffmann, G., White, S.D.M., Heckman, T.M., Ménard, B., Brinchmann, J., Charlot, S., Tremonti, C. & Brinkmann, J. 2004, *MNRAS*, **353**, 713

Keel, W.C. 2007, *The Road to Galaxy Formation, 2nd ed.* (Chichester: Springer)

King, I.R. & Minkowski, R. 1972, IAU 44, *Symposium, A Mass–Luminosity Ratios and Sizes of Giant Elliptical Galaxies*, Eds. D.S. Evans, D. Wills, & B.J. Wills

Koleva, M., Prugniel, P., Ocvirk, P., Le Borgne, D. & Soubiran, C. 2008, *MNRAS*, **385**, 1998

Koleva, M., Prugniel, Ph., Bouchard, A. & Wu, Y. 2009, *A&A*, **501**, 1269

Kong, X. & Cheng, F.Z. 2008, *MNRAS*, **3235**, 1035

Kormendy, J. 1989, *ARA&A*, **27**, 235

Kraan-Korteweg, R.C. & Lahav, O. 1998, *Sci. Am.*, **279**, 50

Lauer, T.R., Faber, S.M., Richstone, D., Gebhardt, K., Tremaine, S., Postman, M., Dressler, A., Aller, M.C., Filippenko, A.V., Green, R., Ho, L.C., Kormendy, J., Magorrian, J. & Pinkney, J. 2007, *ApJ*, **662**, 808

Le Borgne, D., Rocca-Volmerange, B., Prugniel, Ph., Lançon, A., Fioc, M. & Soubiran, C. 2004, *A&A*, **425**, 881

Leblanc, F. 2010, *An Introduction to Stellar Astrophysics* (England: Wiley & Sons)

Ledlow, M.J., Voges, W., Owen, F.N. & Burns, J.O. 2003, *AJ*, **126**, 2740

Li, Z. & Han, Z. 2007, *A&A*, **471**, 795

Liu, F.S., Mao, S. & Meng, X.M. 2012, *MNRAS*, **423**, 422

Longair, M.S. 2008, *Galaxy Formation* (Heidelberg: Springer)

Loubser, S.I. 2009a, Kinematics and stellar population in brightest cluster galaxies, Ph.D. thesis, Jeremiah Horrocks Institute for Astrophysics and Supercomputing, School of Computing, Engineering and Physical Sciences, University of Central Lancashire.

Loubser, S.I., Sansom, A.E., Sánchez-Blázquez, P., Soechting, I.K. & Bromage, G.E. 2008, *MNRAS*, **391**, 113

Loubser, S.I., Sansom, A.E., Sánchez-Blázquez, P. & Soechting, I.K. 2009b, *MNRAS*, **398**, 1009

Madau, P., Ferguson, H.C., Dickinson, M.E., Giavalisco, M., Steidel, C.C. & Fruchter, A. 1996, *MNRAS*, **283**, 1388

Mahdavi, A. & Geller, M.J. 2001, *ApJ*, **554**, 129

Maraston, C. & Strömbäck, G. 2011, *MNRAS*, **418**, 2785

Martizzi, D., Teyssier, R. & Moore, B. 2012, *MNRAS*, **420**, 2859

McCarthy, I.G., Balogh, M.L., Babul, A., Poole, G.B. & Horner, D.J. 2004, *ApJ*, **613**, 811

Menanteau, F., Abraham, R.G. & Ellis, R.S. 2001, *MNRAS*, **322**, 1

Merritt, D. 1983, *ApJ*, **264**, 24

Merritt, D. 1985, *ApJ*, **289**, 18

Mo, H., van den Bosch, F. & White S. 2010, *Galaxy Formation and Evolution* (New York: Cambridge Univ. Press)

Moultaka, J., Ilovaisky, S.A., Prugniel, P. & Soubiran, C. 2004, *PASP*, **116**, 693

Niederste-Ostholt, M., Strauss, M.A., Dong, F., Koester, B.P. & McKay, T.A. 2010, *MNRAS*, **693**, 2023

Ocvirk, P., Pichon, C., Lançon, A. & Thiébaut, E. 2006, *MNRAS*, **365**, 74

Ostriker, J.P. & Peebles, P.J.E. 1973, *ApJ*, **186**, 467

Ostriker, J.P. & Tremaine, S.D. 1975, *ApJ*, **202**, L113

Ostriker, J.P. & Hausman, M.A. 1977, *ApJ*, **217**, L125

Patel, P., Maddox, S., Pearce, F.R., Araǵon-Salamanca, A. & Conway, E. 2006, *MNRAS*, **370**, 851

Pearson K. 1900, *Phil. Mag. Series 5*, **50**, 157

Peres, C.B., Fabian, A.C., Edge, A.C., Allen, S.W., Johnstone, R.M. & White, D.A. 1998, *MNRAS*, **298**, 416

Podeva, A. 1958, *Bol. Obs. Tonantzintla y Tacubava*, **17**, 3

Prugniel, Ph. & Soubiran, C. 2001, *A&A*, **369**, 1048

Prugniel, Ph. & Koleva, M. 2011, IAU 284 Symposium, *Spectral models of stellar populations resolved in chemical abundances*, Eds. R.J. Tuffs & C.C. Popescu

Prugniel, Ph., Koleva, M., Ocvirk, P., Le Borgne, D. & Soubiran, C. 2007a, IAU 241, *Symposium, Analysis of stellar populations with large empirical libraries at high spectral resolution*, Eds. A. Vazdekis & R.F. Peletier

Prugniel, Ph., Soubiran, C., Koleva, M. & Le Borgne, D. 2007b, [arXiv:astro–ph/0703658]

Rafferty, D.A., McNamara, B.R., Nulsen, P.E.J. & Wise, M.W. 2006, *ApJ*, **652**, 216

Rafferty, D.A., McNamara, B.R. & Nulsen, P.E.J. 2008, *ApJ*, **687**, 899

Rawle, T.D., Edge, A.C., Egami, E., Rex, M., Smith, G.P., Altieri, B., Fiedler, A., Haines, C.P., Pereira, M.J.; Pérez-González, P.G., Portouw, J., Valtchanov, I., Walth, G., van der Werf, P.P. & Zemcov, M. 2012, *ApJ*, **747**, 29

Recio-Blanco, A., Bijaoui, A. & de Laverny, P. 2006, *MNRAS*, **370**, 141

Rudolph, A.L., Fich, M., Bell, G.R., Norsen, T., Simpson, J.P., Haas, M.R. & Erickson, E.F. 2006, *ApJS*, **162**, 346

Salaris, M. & Cassisi, S. 2005, *Evolution of Stars and Stellar Populations* (England: Wiley & Sons)

Salpeter, E.E. 1955, *ApJ*, **121**, 161

Sánchez-Blázquez, P., Peletier, R.F., Jiménez-Vicente, J., Cardiel, N., Cenarro, A.J., Falcón-Barroso, J., Gorgas, J., Selam, S. & Vazdekis, A. 2006, *MNRAS*, **371**, 703

Sarzi, M., Falcón-Barroso, J., Davies, R.L., Bacon, R., Bureau, M., Cappellari, M., de Zeeuw, P.T., Emsellem, E., Fathi, K., Krajnović, D., Kuntschner, H., McDermid, R.M. & Peletier, R.M. 2006, *MNRAS*, **366**, 1151

Schaivon, R.A. 2010, [arXiv: astro–ph/1009.0967]

Schechter, P. 1976, *ApJ*, **203**, 297

Schombert, J. 1986, *ApJS*, **60**, 603

Seeds, M.A. & Backman, D.E. 2007, *Stars and Galaxies* (Canada: Brooks/Cole)

Serra, P. & Trager, S.C. 2007, *MNRAS*, **374**, 769

Smith, R.C. 1995, *Observational Astrophysics* (Cambridge: Cambridge Univ. Press)

Sparke, L.S. & Gallagher, J.S. 2007, *Galaxies in the Universe: An Introduction* (New York: Cambridge Univ. Press)

Spinrad, H. 2005, *Galaxy Formation and Evolution* (Berlin: Springer)

Springel, V., White, S.D.M., Jenkins, A., Frenk, C.S., Yoshida, N., Gao, L., Navarro, J., Thacker, R., Croton, D., Helly, J., Peacock, J.A., Cole, S., Thomas, P., Couchman, H., Evrard, A., Colberg, J. & Pearce, F. 2005, *Nature*, **435**, 629

Struble, M.F. & Rood, H.J. 1991, *ApJS*, **77**, 363

Struble, M.F. & Rood, H.J. 1999, *ApJS*, **125**, 35

Tantalo, R., Chiosi, C. & Bressan, A. 1998, *A&A*, **333**, 419

Tayler, R.J. 1994, *The Stars: Their Structure and Evolution* (England: Cambridge Univ. Press)

Thomas, D., Maraston, C. & Bender, R. 2003, *MNRAS*, **339**, 897

Thomas, D., Maraston, C., Bender, R. & Mendes de Oliveira, C. 2005, *ApJ*, **621**, 673

Tojeiro, R., Heavens, A.F., Jimenez, R. & Panter, B. 2007, *MNRAS*, **381**, 1252

Tonry, J.L. & Davis, M. 1981, *ApJ*, **246**, 666

Trager, S.C., Worthey, G., Faber, S.M., Burstein, D. & González, J.J. 1998, *ApJS*, **116**, 1

Trager, S.C., Faber, S.M. & Dressler, A. 2008, *MNRAS*, **386**, 715

Vaisanen, P. 2009, *Quest*, **5**, 22

Von der Linden, A., Best, P.N., Kauffmann, G. & White, S.D.M. 2007, *MNRAS*, **379**, 867

Wall, J.V. & Jenkins, C.R. 2003, *Practical statistics for Astronomers* (New York: Cambridge Univ. Press)

White, S.D.M. & Rees, M.J. 1978, *MNRAS*, **183**, 341

White, D.A., Jones, C. & Forman, W. 1997, *MNRAS*, **292**, 419

Worthey, G. 1994, *ApJS*, **95**, 107

Worthey, G., Faber, S.M., González, J.J. & Burstein, D. 1994, *ApJS*, **94**, 687

Worthey, G. & Ottaviani, D.L. 1997, *ApJS*, **111**, 377